Conference Proceedings of the Society for Experimental Mechanics Series

Meredith Silberstein · Alireza Amirkhizi · Xia Shuman
Allison Beese · Ryan B. Berke · Garrett Pataky *Editors*

Challenges in Mechanics of Time Dependent Materials, Fracture, Fatigue, Failure and Damage Evolution, Volume 2

Proceedings of the 2019 Annual Conference on Experimental and Applied Mechanics

SEM

Springer

Conference Proceedings of the Society for Experimental Mechanics Series

Series Editor

Kristin B. Zimmerman, Ph.D.
Society for Experimental Mechanics, Inc.,
Bethel, CT, USA

The Conference Proceedings of the Society for Experimental Mechanics Series presents early findings and case studies from a wide range of fundamental and applied work across the broad range of fields that comprise Experimental Mechanics. Series volumes follow the principle tracks or focus topics featured in each of the Society's two annual conferences: IMAC, A Conference and Exposition on Structural Dynamics, and the Society's Annual Conference & Exposition and will address critical areas of interest to researchers and design engineers working in all areas of Structural Dynamics, Solid Mechanics and Materials Research.

More information about this series at http://www.springer.com/series/8922

Meredith Silberstein • Alireza Amirkhizi • Xia Shuman • Allison Beese
Ryan B. Berke • Garrett Pataky
Editors

Challenges in Mechanics of Time Dependent Materials, Fracture, Fatigue, Failure and Damage Evolution, Volume 2

Proceedings of the 2019 Annual Conference on Experimental and Applied Mechanics

Springer

Editors
Meredith Silberstein
Department of Mechanical & Aerospace Engineering
Cornell University
Ithaca, NY, USA

Xia Shuman
Georgia Institute of Technology
Atlanta, GA, USA

Ryan B. Berke
Utah State University
Logan, UT, USA

Alireza Amirkhizi
University of Massachusetts Lowell
Lowell, MA, USA

Allison Beese
Pennsylvania State University
University Park, PA, USA

Garrett Pataky
Clemson University
Clemson, SC, USA

ISSN 2191-5644 ISSN 2191-5652 (electronic)
Conference Proceedings of the Society for Experimental Mechanics Series
ISBN 978-3-030-29985-9 ISBN 978-3-030-29986-6 (eBook)
https://doi.org/10.1007/978-3-030-29986-6

This Springer imprint is published by the registered company Springer Nature Switzerland AG.
The registered company address is: Gewerbestrasse 11, 6330 Cham, Switzerland

Preface

Challenges in Mechanics of Time-Dependent Materials, Fracture, Fatigue, Failure and Damage Evolution, represents one of six volumes of technical papers presented at the 2019 SEM Annual Conference and Exposition on Experimental and Applied Mechanics organized by the Society for Experimental Mechanics and held in Reno, NV, June 3–6, 2019. The complete proceedings also include volumes on *Dynamic Behavior of Materials; Advancement of Optical Methods & Digital Image Correlation in Experimental Mechanics; Mechanics of Biological Systems and Materials & Micro- and Nanomechanics; Mechanics of Composite, Hybrid and Multifunctional Materials; and Residual Stress, Thermomechanics & Infrared Imaging and Inverse Problems.*

Each collection presents early findings from experimental and computational investigations on an important area within Experimental Mechanics, the Mechanics of Time-Dependent Materials, Fracture, Fatigue, Failure and Damage Evolution being some of these areas.

The Time-Dependent Materials track was organized to address time (or rate)-dependent constitutive and fracture/failure behavior of a broad range of materials systems, including prominent research in progress in both experimental and applied mechanics. Papers concentrating on both modeling and experimental aspects of Time-Dependent Materials are included.

Fatigue and fracture tracks are two of the most critical considerations in engineering design. Understanding and characterizing fatigue and fracture has remained as one of the primary focus areas of experimental mechanics for several decades. Advances in experimental techniques, such as digital image correlation, acoustic emissions, and electron microscopy, have allowed for deeper study of phenomena related to fatigue and fracture. This volume contains the results of investigations of several aspects of fatigue and fracture such as microstructural effects, the behavior of interfaces, the behavior of different and/or complex materials such as composites, and environmental and loading effects. The collection of experimental mechanics research included here represents another step toward solving the long-term challenges associated with fatigue and fracture.

The track organizers thank the presenters, authors, and session chairs for their participation and contribution to these tracks. The support and assistance from the SEM staff is also greatly appreciated.

Ithaca, NY — Meredith Silberstein
Lowell, MA — Alireza Amirkhizi
Atlanta, GA — Xia Shuman
State College, PA — Allison Beese
Logan, UT — Ryan B. Berke
Clemson, SC — Garrett Pataky

Contents

Dynamic Analysis of Vehicle Performance for Changes to Rear Axle Housing

Diane L. Peters, Yaomin Dong, and Vimal Patel

Abstract This paper explores the performance improvements of a 2013 Ford Mustang Shelby GT500 resulting from changes to the rear axle housing. In previous work, described in (Peters et al., In *Optimal Design of an Automotive Rear Axle Housing. Proceedings of the 2018 IAJC International Conference*, Orlando, FL, 2018; Patel, In *Design, Analysis, & Optimization of 8.8 Inch Rear Axle Differential Housing*, MS Thesis, Kettering University, Flint, MI, 2017), the rear axle housing was optimized in order to minimize its weight. It was expected that the decrease in weight would lead to improved fuel economy; in this work, the vehicle was simulated for the EPA highway drive cycle (HWFET) both before and after the optimization of the housing, in order to quantify the changes in fuel economy. It was found that the optimization of the housing did produce a modest improvement in the chassis energy demand and in the fuel energy demand.

Keywords Automotive axle · Dynamic analysis · Vehicle performance

Introduction

It is generally known that, if all other factors are held constant, a vehicle with lower mass will have greater fuel economy than one with a greater mass. Therefore, lightweighting of vehicles is of strong interest, both in practical terms and in theoretical studies. There are many approaches to lightweighting, some involving new and innovative materials and others involving new configurations or designs. Yet another approach is to simply optimize existing components in a vehicle, with the goal of reducing them to the minimum mass that will still allow them to satisfy all of the specifications for those components. In previous work, a specific vehicle component, the rear axle housing, was optimized to minimize weight while still meeting stress and deflection constraints, and it was found that the weight could be reduced by 47% [1, 2]. It was stated that the reduction in weight should improve fuel economy; however, that improvement was not quantified in that work. In this work, the vehicle is modeled in Simulink, and the model is run with the EPA highway cycle (HWFET), for both the original vehicle and the vehicle with the optimized rear axle housing.

The paper is organized as follows: in the next section, background is given, including an overview of some of the usage of dynamic modeling for the analysis of different types of vehicles. Next, the equations for the dynamic model are presented, along with details of the implementation in Simulink. The section after that gives the results, followed by a conclusion.

Background

Determining the performance of a vehicle, and analyzing the possible effects of changes to the vehicle, is an important part of the development process. With the high expense and time commitment involved in developing prototypes, the use of dynamic models of sufficient fidelity to provide meaningful results will benefit the development process.

Dynamic modeling has been used extensively to analyze vehicle performance. In [3–5], a dynamic model was used to analyze and determine a control algorithm for a hybrid electric vehicle powertrain. The integration of sensors, actuators, and vehicle dynamics into a single model was presented in [6], with the model used in that case to develop controllers for vehicle safety. In [7], a vehicle configuration with four motorized wheels was analyzed. While the models were of varying complexity, in each case they were able to provide results of sufficient fidelity to provide some degree of confidence in the

D. L. Peters · Y. Dong (✉) · V. Patel
Department of Mechanical Engineering, Kettering University, Flint, MI, USA
e-mail: ydong@kettering.edu

M. Silberstein et al. (eds.), *Challenges in Mechanics of Time Dependent Materials, Fracture, Fatigue, Failure and Damage Evolution, Volume 2*, Conference Proceedings of the Society for Experimental Mechanics Series, https://doi.org/10.1007/978-3-030-29986-6_1

predicted performance, and to ensure that the vehicle performance would meet the specified criteria. As vehicles increase in complexity, appropriate models are used for a variety of different analysis tasks.

Dynamic Modeling

Prior to implementation in MATLAB/Simulink, a mathematical model was developed for the vehicle. This model is based on a simple force balance of the various loads on the vehicle, and is drawn from commonly available information on vehicle modeling.

The propulsion force to move the vehicle forward is the tractive or driving force; it is opposed by various road loads. The various road loads on the vehicle are shown in Fig. 1, taken from [8]. They are the rolling resistance F_{rr}, the aerodynamic drag F_{ad}, and the climbing resistance force F_{hc} (the component of the vehicle's weight acting down the slope). There could also be a force required to accelerate the vehicle, depending on whether or not the velocity is being held constant.

In the absence of acceleration, the road load is given by the equation

$$F_{RL} = F_{rr} + F_{ad} + F_{hc} \tag{1}$$

The rolling resistance depends on the coefficient of rolling friction between the tire and the road, μ_{rr}, and the normal force between the vehicle and the road, which depends on both the vehicle's weight, $m_v g$, and on the road gradient, θ.

$$F_{rr} = \mu_{rr} m_v g \cos\theta \tag{2}$$

The aerodynamic drag depends on air density, ρ; drag coefficient, C_d; frontal area of the vehicle, A_f; and the vehicle speed, v.

$$F_{ad} = \frac{1}{2}\rho C_d A_f v^2 \tag{3}$$

The frontal area of the vehicle can be calculated based on the the height and weight of the vehicle, and is given by

$$A_f = 0.8HW \tag{4}$$

The force due to the road grade is simply the component of the weight that opposes the forward motion of the vehicle:

$$F_{hc} = m_v g \sin\theta \tag{5}$$

Values for vehicle parameters are given in Table 1 [9].

The power required by the vehicle at any point in the drive cycle can be found once the tractive force is found, by multiplying force and velocity of the vehicle. However, this does not correspond to the power output of the engine, due to various losses in the system. While detailed models can be developed for all of the components in the system, in this analysis

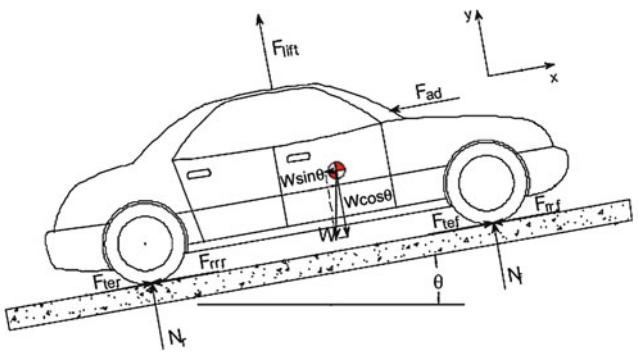

Fig. 1 Road load reaction forces [8]

Table 1 Vehicle parameters [9]

Description	Symbol	Units	Value
Vehicle height, per SAE J1263	H	m	1.392
Vehicle width, per SAE J1263	W	m	1.877
Vehicle length	L	m	4.780
Wheelbase	W_b	m	2.720
Curb weight of the vehicle	W_{curb}	kN	17.132
EPA test weight	W_{test}	kN	1.334
Drag coefficient	C_d	–	0.35
Tire rolling resistance	μ_{rr}	–	0.0125
Engine power	P_{eng}	kW	493.7
Total vehicle mass for original vehicle (corresponding to curb weight plus EPA test weight)	m_v	kg	1882.41
Total vehicle mass for vehicle with optimized rear axle housing	m_{opt}	kg	1873.34
Density of air	ρ	kg/m^3	1.225
Frontal area of vehicle	A_f	m^2	2.090

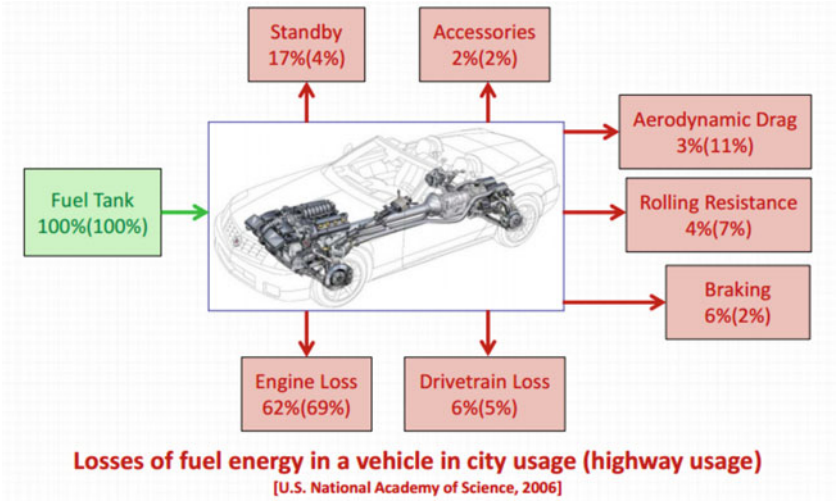

Fig. 2 Typical vehicle losses [10]

the losses were assumed to take on typical values for vehicles of this type. The typical losses for a vehicle are shown in Fig. 2, taken from [10].

In this analysis, it was assumed that there is no grade, i.e., $\theta = 0$, which eliminates the force due to road grade from the equations. It is also assumed that the drive cycle used is the EPA highway cycle, shown in Fig. 3 [11].

Two Simulink models were created, one for the chassis power and energy demand and one for the fuel demand, based on the mathematical model that was developed. These are shown in Figs. 4 and 5, respectively.

In the development of the model for fuel demand, the efficiency of the internal combustion engine must be considered. Again, it is possible to develop highly complex models for various types of applications. For this application, a simple model was used which considers the various efficiencies of the engine and powertrain. The engine is assumed to have a constant efficiency of 35%, and the axle and transmission efficiencies are assumed to be 95% efficient, with these values taken from [8].

These models were run for both the original vehicle parameters and for the vehicle after the optimization of the rear axle housing [2].

Results

The optimization detailed in [1, 2] resulted in a decrease in weight of 87.8 N, or approximately 20 lb. Over the full drive cycle, this decrease in vehicle weight resulted in a decrease of 6.12% in the chassis energy demand, and a decrease of 1.96%

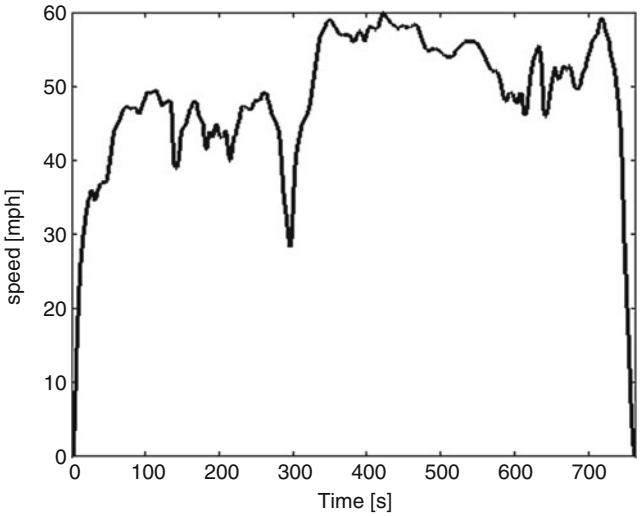

Fig. 3 EPA highway drive cycle [11]

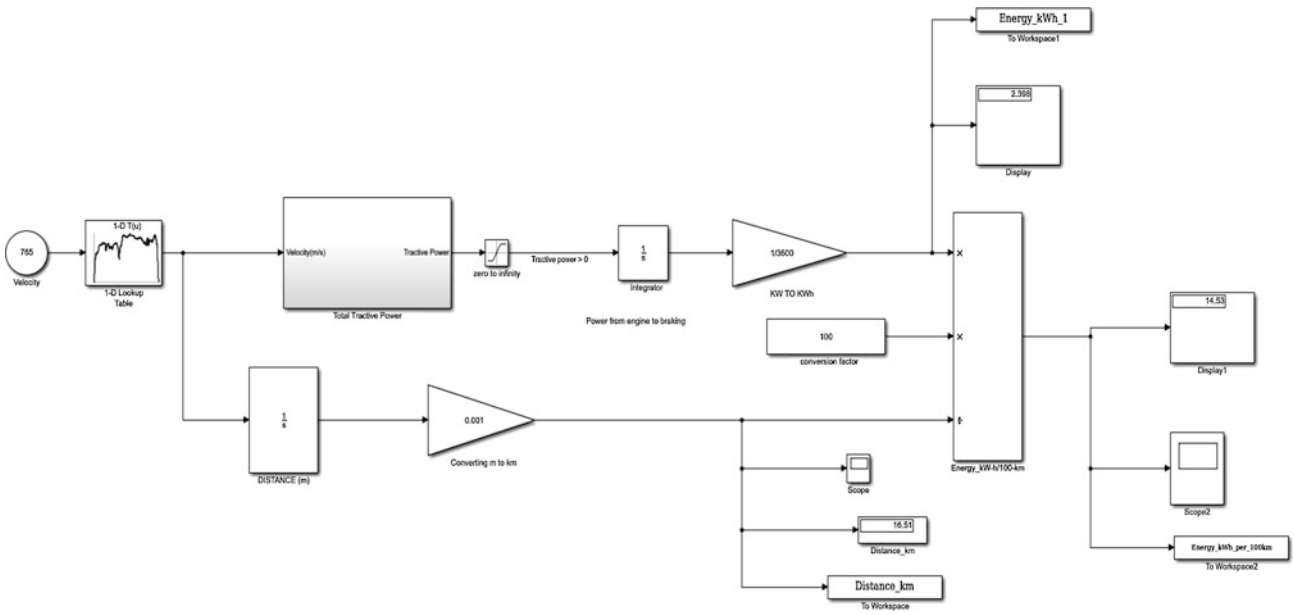

Fig. 4 Simulink model for chassis power & energy demand [2]

in the fuel demand. This drive cycle is relatively short, however, so a longer trip of 100 km was also considered. For this longer trip, there was a decrease of 10% in the chassis energy demand, and a decrease of 3.3% in the total fuel required [2], as shown in Table 2.

The cumulative energy usage and fuel requirement over the full drive cycle are shown in Figs. 6 and 7, respectively. Each graph is shown in its entirety, followed by a view of only the last 165 seconds, in order to better see the distinction between the curves. It can be seen, in both figures, that there is a small but noticeable difference between the energy demands before and after optimization of the rear axle housing. As expected, the new, lighter rear axle housing does result in a lower demand for energy to move the vehicle, and consequently will provide a fuel savings. The extent of the fuel savings will depend on the length and type of the trip, with longer trips showing a greater fuel savings.

Even with the relatively short trip corresponding to the highway drive cycle, however, there is a noticeable savings in the fuel required for the vehicle.

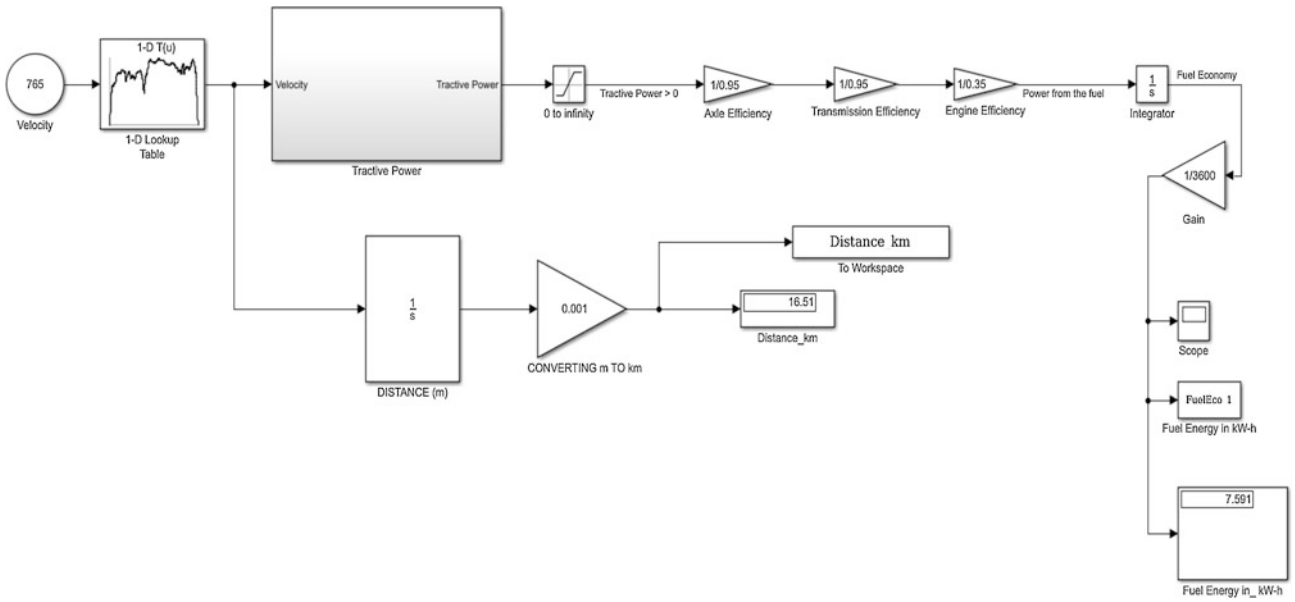

Fig. 5 Simulink model for fuel demand [2]

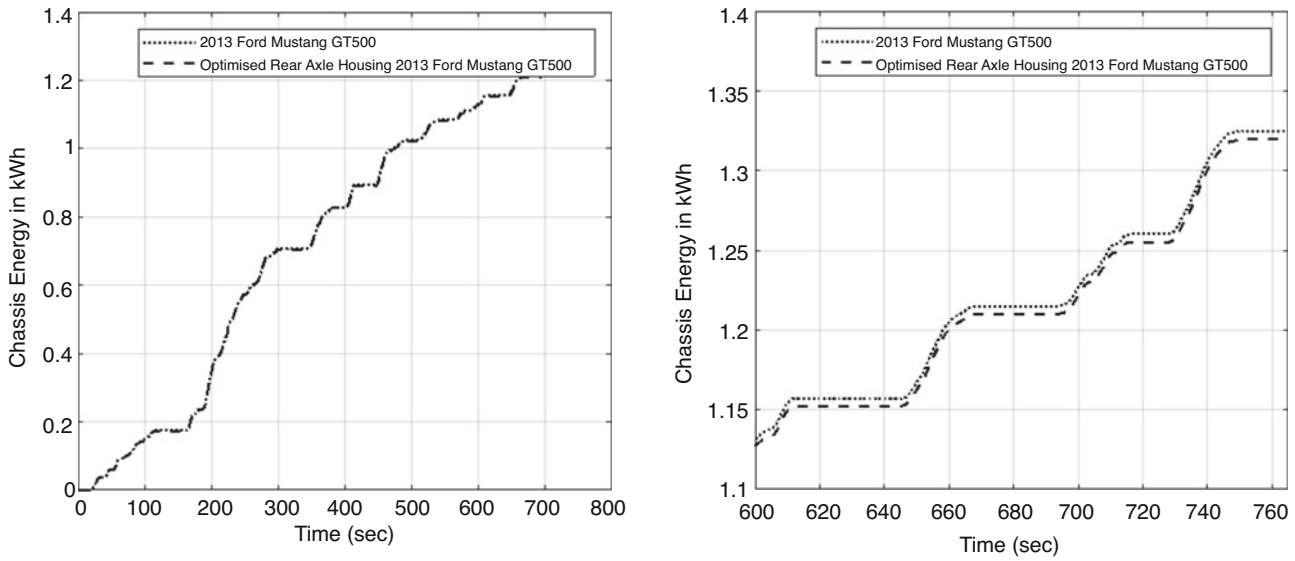

Fig. 6 Chassis energy demand for EPA highway drive cycle [2]

Table 2 Simulation results for original and optimized designs

Description	Energy demand for drive cycle (kWh)	Energy demand for 100 km trip (kWh)	% Change for 100 km trip
Chassis Energy Demand before optimization of rear axle housing	2.45	15.0	10%
Chassis Energy Demand after optimization of rear axle housing	2.30	13.5	
Fuel Energy Demand before optimization of rear axle housing	7.65	46.5	3.3%
Fuel Energy Demand after optimization of rear axle housing	7.50	45.0	

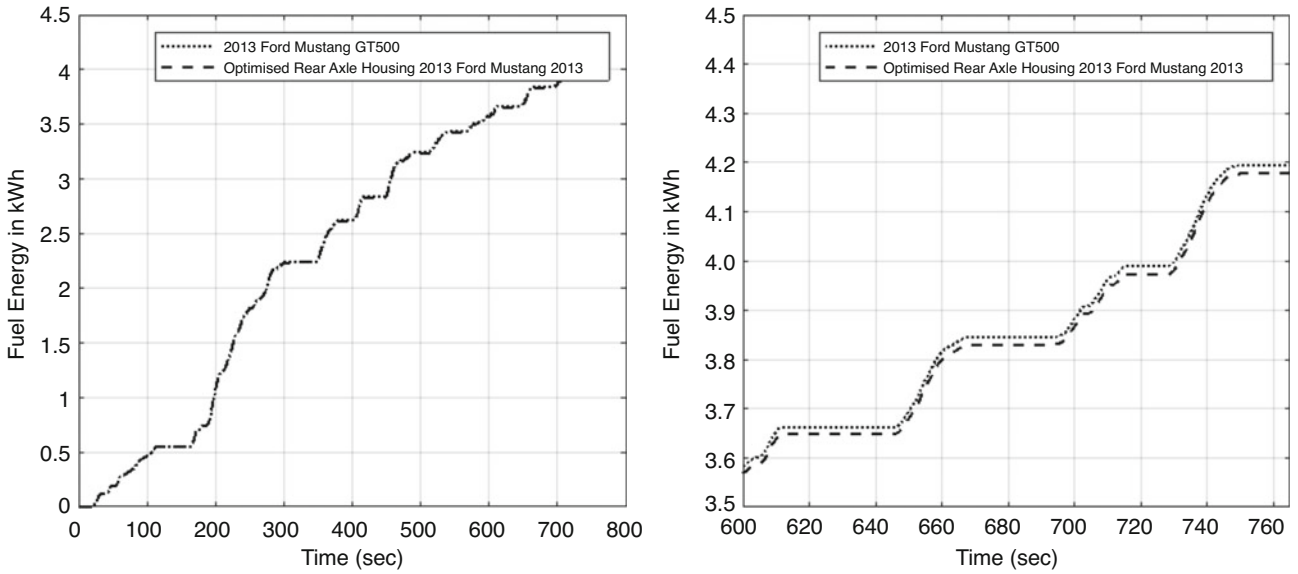

Fig. 7 Fuel energy demand for EPA highway drive cycle [2]

Conclusion

In previous work, described in [1], an optimization was carried out in order to reduce the weight of a rear axle housing on a vehicle. It was expected that the reduced weight would result in a fuel savings for the vehicle, compared to the original design. Based on dynamic modeling and simulation of the vehicle, the expected fuel savings was seen. While the decrease in fuel usage is relatively modest, with a 3.3% reduction in fuel usage for a 100-km trip, this small reduction over a long period of operation for the automobile will result in substantial fuel savings.

The fuel savings indicated by the modeling and simulation result from a single optimized component, the rear axle housing. Automobiles include many other components, however, which may be suitable targets for a similar optimization; such an approach could result in a substantially lower fuel demand, due to the effect of many small improvements.

In addition, experimental validation should be carried out. The vehicle model developed in this paper has not been validated; ensuring that the model is, in fact, an accurate predictor for the actual system. This experimental validation should consist of two stages. In the first stage, the work carried out in [1, 2] should be validated, ensuring that the optimized design will in fact meet the criteria for the component. In the second stage, the dynamic model described in this paper should be validated, through comparisons of these results and the output of the model. Such a validation would provide an additional degree of confidence in the model output, and would allow the model developed in this paper to be used for development of the critical aspects of the project.

Acknowledgements The authors would like to thank the Graduate School of Kettering University for providing the graduate assistantships during this work, and Dr. Arnaldo Mazzei for serving as a committee member of the graduate student's research.

References

1. D.L. Peters, Y. Dong, V. Patel, in *Optimal Design of an Automotive Rear Axle Housing. Proceedings of the 2018 IAJC International Conference*, (Orlando, FL, 2018)
2. V.B. Patel, Design, Analysis, & Optimization of 8.8 Inch Rear Axle Differential Housing, MS Thesis, Kettering University, Flint, MI, 2017
3. B.K. Powell, K.E. Bailey, S.R. Cikanek, Dynamic modeling and control of hybrid electric vehicle powertrain systems. IEEE Control. Syst. **18**(5), 17–33 (1998)
4. S.R. Cikanek, K.E. Bailey, B.K. Powell, in *Parallel Hybrid Electric Vehicle Dynamic Model and Powertrain Control*. American Control Conference, Proceedings of the 1997, vol. 1 (IEEE, 1997), pp. 684–688
5. K.E. Bailey, B.K. Powell, in *A Hybrid Electric Vehicle Powertrain Dynamic Model*. American Control Conference, Proceedings of the 1995, vol. 3 (IEEE, 1995), pp. 1677-1682

6. D. Margolis, T. Shim, A bond graph model incorporating sensors, actuators, and vehicle dynamics for developing controllers for vehicle safety. Journal of the Franklin Institute **338**(1), 21–34 (2001)
7. E. Esmailzadeh, G.R. Vossoughi, A. Goodarzi, Dynamic modeling and analysis of a four motorized wheels electric vehicle. Veh. Syst. Dyn. **35**(3), 163–194 (2001)
8. G. Davis, C. Hoff, *Introduction to Automotive Powertrain*. (2003)
9. Data panel archive (2012), http://paws.kettering.edu/~amazzei/Road_Track.htm. Accessed 24 Aug 2017
10. Where the energy goes: gasoline vehicles (n.d.), https://www.fueleconomy.gov/feg/atv.shtml. Accessed 16 Oct 2017
11. Dynamometer drive schedules (n.d.), https://www.epa.gov/vehicle-and-fuel-emissions-testing/dynamometer-drive-schedules. Accessed 2 Mar 2018

A Comparative Study of Crack Branching in Glass Using Photoelasticity, Digital Image Correlation and Digital Gradient Sensing Techniques

Sivareddy Dondeti and Hareesh V. Tippur

Abstract Fracture behavior of high-stiffness and low-toughness materials such as soda-lime glass typically involves crack branching, a phenomenon which has not been well-understood. Attempts to shed light on this issue via full-field optical investigation has been hampered by numerous spatio-temporal experimental challenges as crack speeds in these materials reach upwards of 1500 m/s accompanied by highly localized small deformations. In this work, three different optical techniques—transmission photoelasticity, 2D Digital Image Correlation (DIC) and transmission-mode Digital Gradient Sensing (DGS)—are separately implemented to comparatively assess their efficacy to study crack growth and branching in soda-lime glass plates. Each method is implemented in conjunction with ultrahigh-speed photography (1–2 Mfps), flash/pulse illumination and a modified-Hopkinson pressure bar on nominally identical wedge impact experiments. Visualization of results from these experiments along with preliminary observations on their pros and cons of each approach for this material system are presented.

Keywords Photoelasticity · Digital Image Correlation · Digital Gradient Sensing · Dynamic fracture · Crack branching · Transparent structures

Introduction

Brittle materials such as soda-lime glass are widely used in many civilian and military structures. Due to their high-stiffness and low-toughness characteristics, they pose prohibitive experimental challenges to dynamic fracture investigations as typical crack-tip opening displacements are in the range of 80 nm whereas crack speeds tend to be in excess of ~1500 m/s. Accordingly, the past works have primarily considered polymeric materials to understand high-speed fracture and the associated phenomenon. Some examples include, dynamic crack growth in polymers studied by Dally and Kobayashi [1, 2] separately using photoelasticity to visualize and quantify the fracture parameters. Ravi-Chandar and Knauss [3, 4] investigated some of the underlying mechanics in Homalite using the method of optical caustics. They noted the occurrence of the micro cracks ahead of the running main crack besides quantifying dynamic fracture parameters. Nigam and Shukla [5] compared two optical methods, photoelasticity and caustics, under static and dynamic conditions using Homalite. They reported good agreement under static conditions but large differences for dynamic conditions. Kirugulige and Tippur were the first to study [6] rapidly growing cracks in brittle epoxy-based syntactic foam sheets using Digital Image Correlation technique (DIC). More recently, Sundaram and Tippur [7, 8] demonstrated the feasibility of using DGS [9] to tackle this problem in polymers as well as glasses. The present work aims to comparatively evaluate the pros and cons of studying dynamic crack growth and branching in soda-lime glass using some of these popular methods and demonstrate possible new avenues.

Experimental Details

Three prominent full filed optical investigations were performed to study dynamic crack propagation in v-notched specimens (Fig. 1) made of soda-lime glass plates. The machined v-notch was extended by 8 mm with diamond impregnated circular saw. The experimental setup employed a modified Hopkinson pressure bar to load the specimen, shown schematically in

S. Dondeti · H. V. Tippur (✉)
Department of Mechanical Engineering, Auburn University, Auburn, AL, USA
e-mail: htippur@eng.auburn.edu

M. Silberstein et al. (eds.), *Challenges in Mechanics of Time Dependent Materials, Fracture, Fatigue, Failure and Damage Evolution, Volume 2*, Conference Proceedings of the Society for Experimental Mechanics Series, https://doi.org/10.1007/978-3-030-29986-6_2

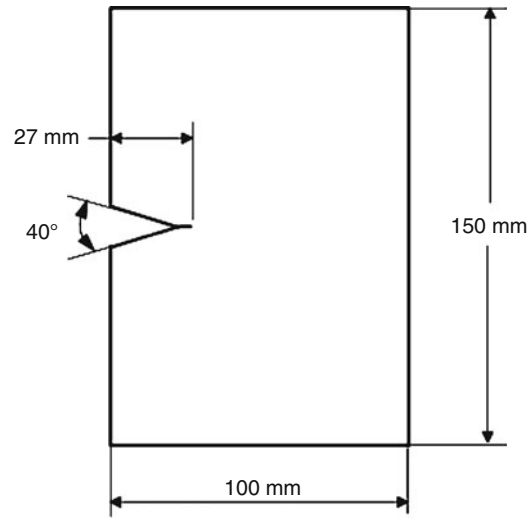

Fig. 1 V-notched soda-lime glass specimen geometry with an extended notch

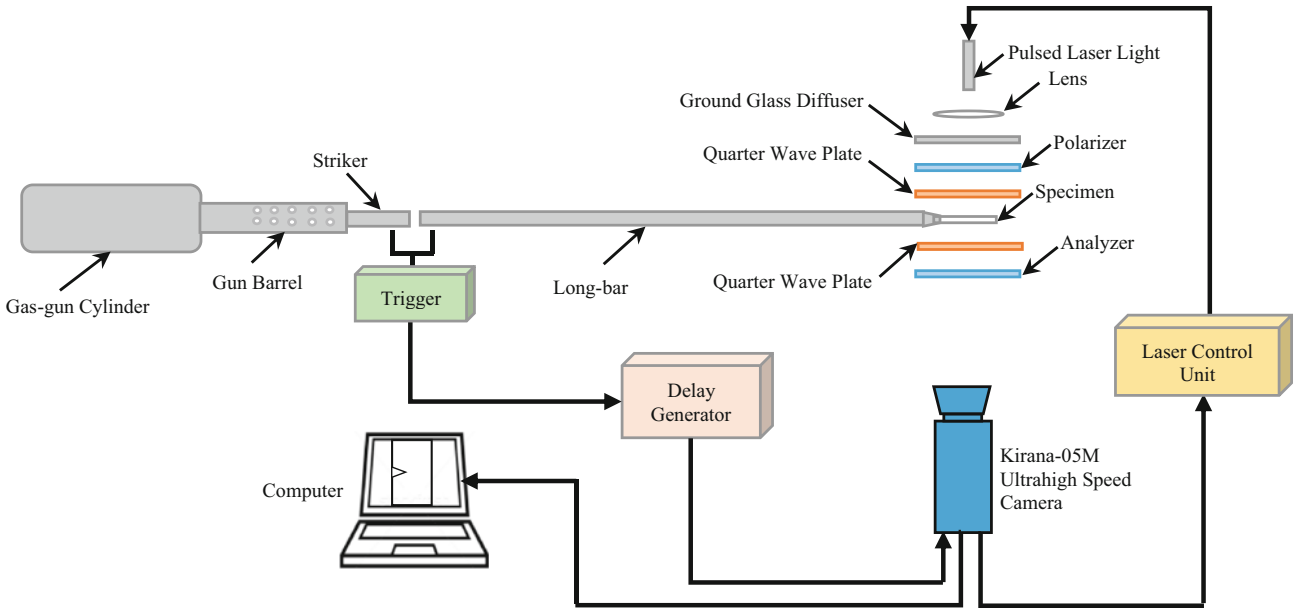

Fig. 2 Photoelasticity experimental setup

Fig. 2. A 305 mm long striker (25.4 mm diameter) aligned co-axially with a long-bar (1830 mm long, 25.4 mm diameter) was used to subject the specimen to stress waves. Both the striker and the long-bars were made of maraging steel. The long-bar was tapered at one end to match the v-notch cut into the specimen. When the striker was launched by a gas gun, the impact between the striker and the long-bar produced a compressive stress wave that loaded the specimen on the upper and lower flanks. Simultaneously, a trigger pulse was also generated which initiated camera to capture images. During the photoelastic investigation, the specimen was situated in a standard circular polariscope (see Fig. 2) with a 640 nm wavelength pulse laser as the light source. The impact event triggered the laser unit to emit 160 ns light pulses. The fracture event was recorded using a Kirana-05 single sensor (924 × 768 pixels) high-speed camera capable of recording up to 180 images.

Next, a nominally identical dynamic fracture experiment was performed using another popular method, 2D Digital Image correlation (DIC). Figure 3 shows the schematic representation of the experimental setup, which is similar to the one used for photoelasticity but for the modifications to capture the sprayed-on random speckles on the specimen surface. That is, the v-notched specimen was initially sprayed with alternate mists of black and white paints to create random but uniform speckles on one of the surfaces. The illumination used here was from a pair of high-intensity xenon flash lamps.

Lastly, a relatively new full-field optical measurement technique, transmission-mode DGS [9] was attempted to study dynamic fracture in soda-lime glass. This method, based on 2D DIC and elasto-optic effects, is able to evaluate two

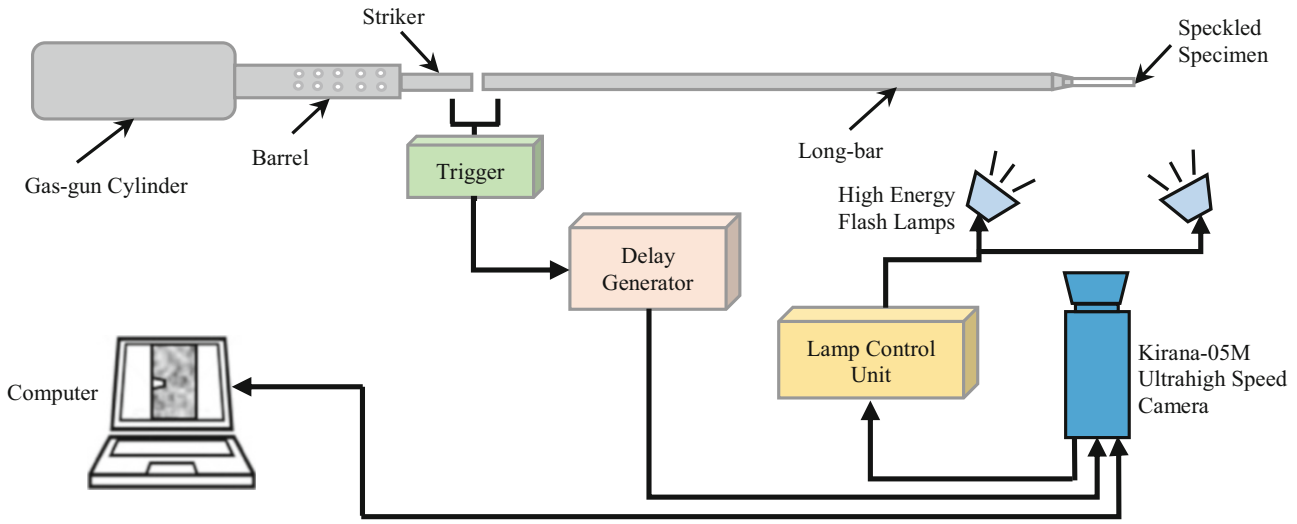

Fig. 3 DIC experimental setup

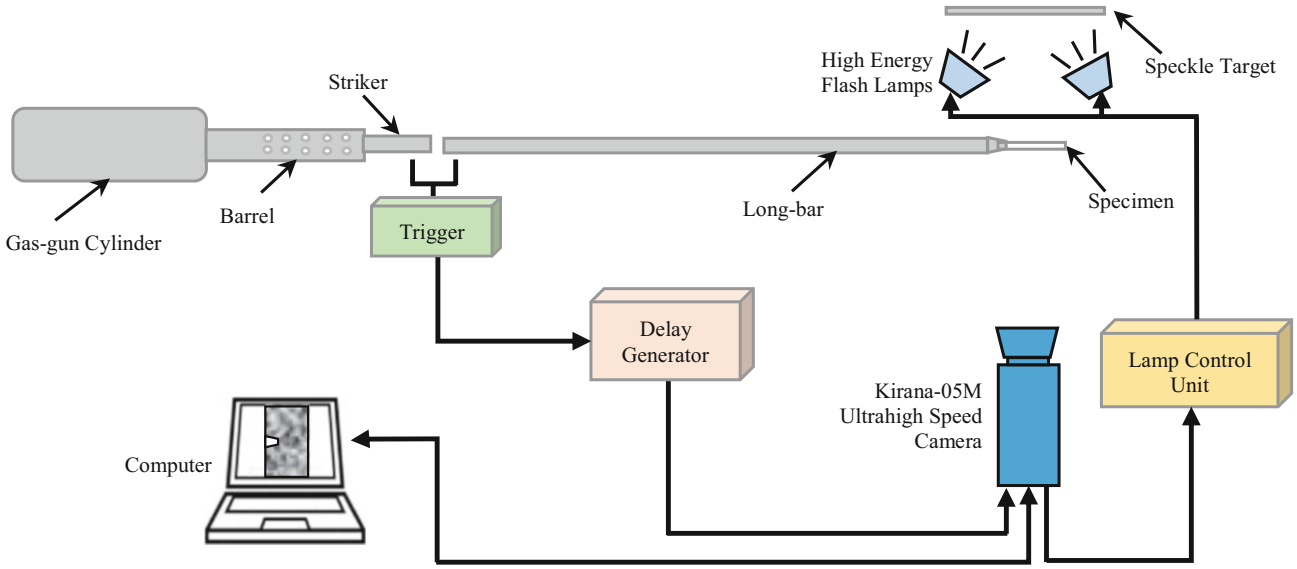

Fig. 4 DGS experimental setup

orthogonal stress gradients in the whole field. The experimental setup for DGS is shown in Fig. 4, which is similar to the ones used for photoelasticity and DIC. In this apparatus, however, the camera is made to photograph random speckles on a planar target plate located at a known distance behind the optically transparent soda-lime glass specimen being investigated.

Optical Measurements

The photoelastic fringes proportional to the in-plane shear stresses in soda-lime glass were obtained using the dark-field polariscope. Two select fringe patterns from the complete fracture event are shown in Fig. 5. Figure 5(a, b) depict isochromatic fringes before and after crack branching (into two daughter cracks), respectively, following mode-I crack propagation from the original notch tip. The images show well-formed fringes associated with the long-bar and specimen contact stresses. However, the growing mode-I crack-tip of the mother crack or mixed-mode crack-tips of the daughter cracks do not show discernable fringes.

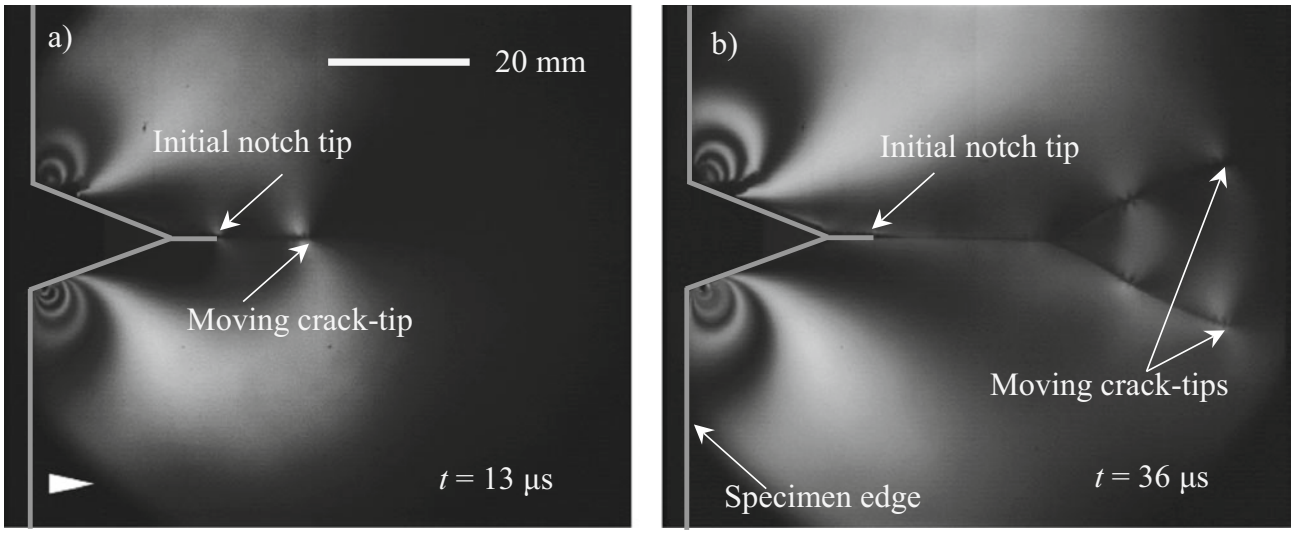

Fig. 5 Photoelastic fringes (dark field setup) subjected dynamic wedge loading (**a**) before and (**b**) after crack branching, respectively. Time t is relative to crack initiation at the original notch tip; the arrowhead indicates crack growth direction

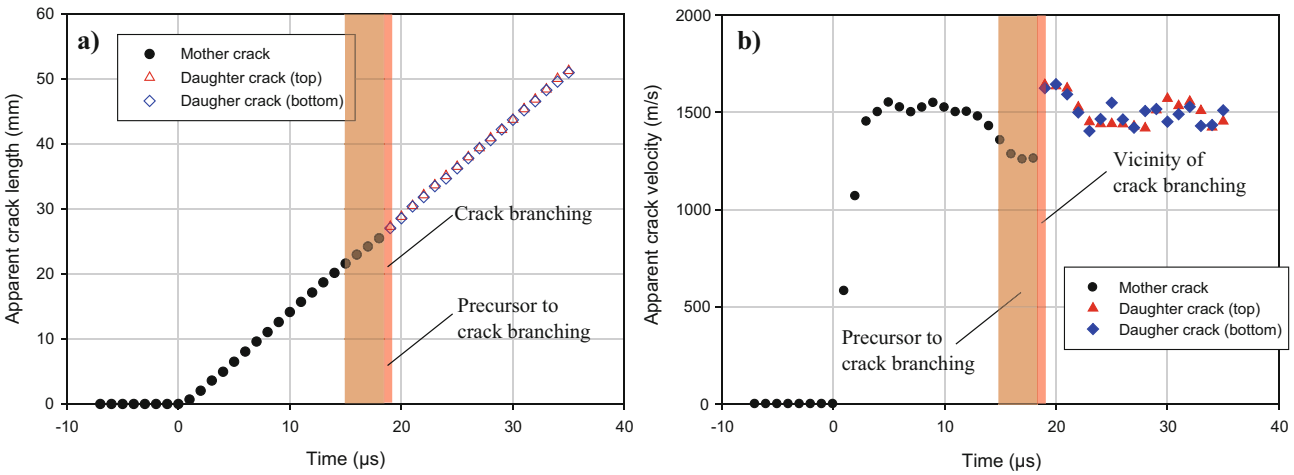

Fig. 6 Apparent (**a**) crack length and (**b**) crack velocity histories from photoelasticity

The crack-tip locations were measured from the interferograms for evaluating crack length and velocity histories shown in Fig. 6. The crack lengths increased steadily until branching and continued propagation in the same manner until the end of the observation window as shown in Fig. 6(a). The data points for the two daughter cracks show excellent symmetry in terms of the branching event. Subsequently the apparent crack velocities were evaluated and are shown in Fig. 6(b). The crack velocity of dynamically propagating mode-I crack increased steadily from 0 to ~1400 m/s in ~3 μs, before attaining a constant velocity in the range of 1400–1600 m/s for a duration of ~10 μs. The apparent velocity decreased gradually to ~1200 m/s as the mode-I crack approached the branching phase. Following branching there was an instantaneous rise in velocity to ~1600 m/s. Finally, the two mixed-mode daughter cracks travelled with an average velocity in the range of 1400–1600 m/s, same as the mode-I mother crack.

After the photoelasticity experiment, the dynamic crack branching was studied by another popular full-field method DIC. The speckle images in the deformed state were correlated with the one the undeformed state prior to the arrival of the stress waves. The speckle images were segmented into 30 × 30 pixel sub-images and a sub-image overlap of 10 pixels (scale factor, 1 pixel = 95 μm on the specimen). The resulting crack-opening displacement contours u_y are shown in Fig. 7 at two time instants, $t = 5$ μs and $t = 26$ μs, corresponds to pre- and post-crack branching phases, respectively. It should be noted that as the displacements are non-singular and do not converge to a single point, which in turn made the crack-tip location indeed a challenge using this method given the extremely small crack opening displacements in soda-lime glass. The best estimates of the apparent crack length based on displacement jump across the crack tip and the corresponding velocity history are

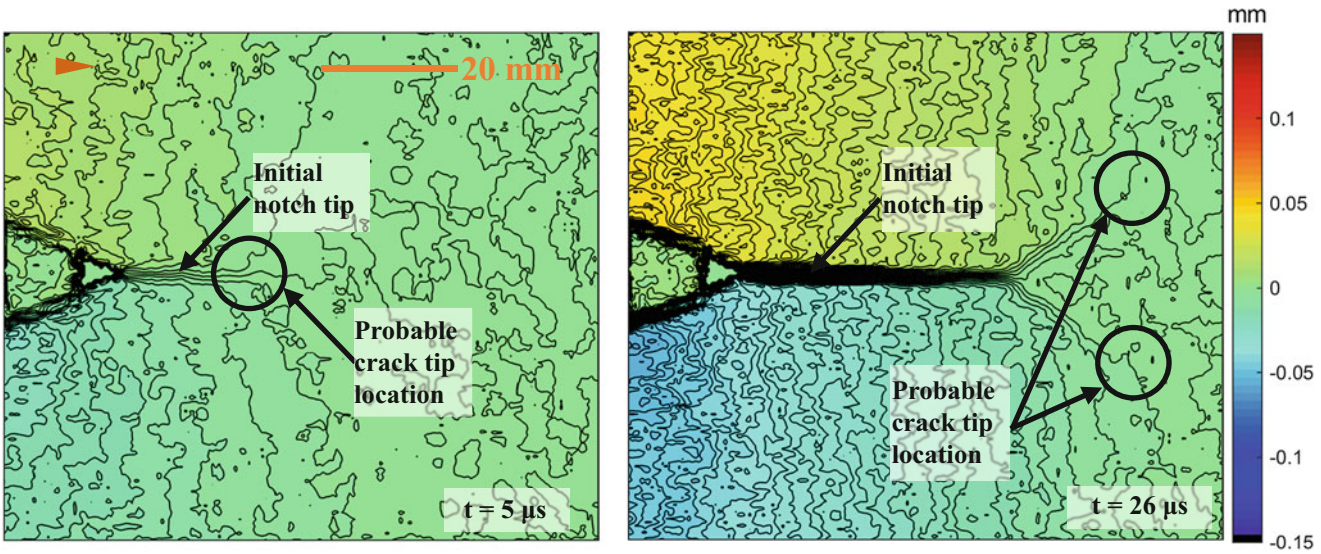

Fig. 7 Displacement contours on soda-lime glass specimen surface from DIC

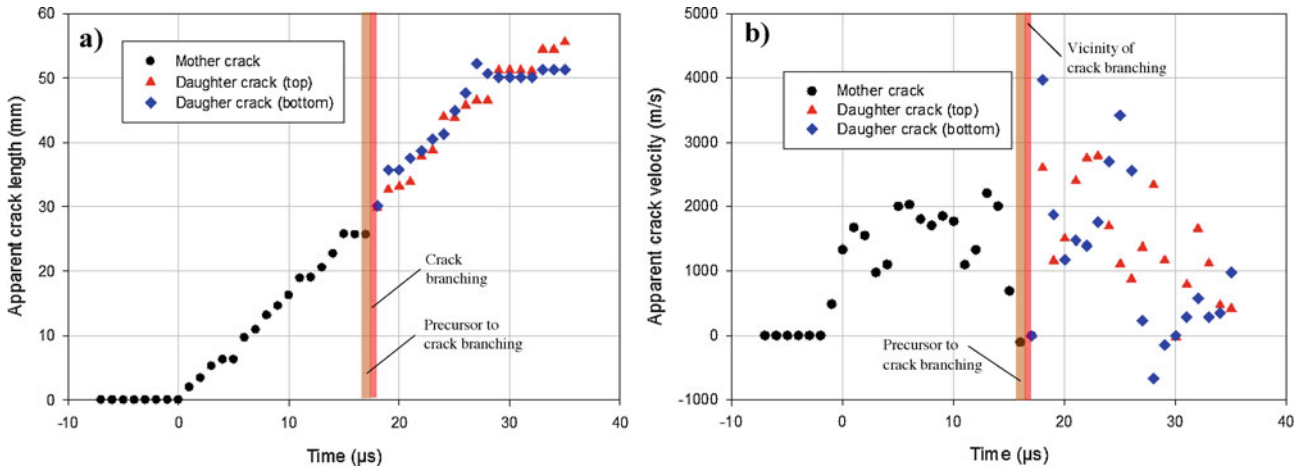

Fig. 8 Apparent (**a**) crack length and (**b**) crack velocity histories from DIC

shown in Fig. 8(a, b). The crack length history, though similar to the one in Fig. 8(a), it is very noisy relative to the one from the photoelastic measurements. The crack velocity histories (shown in Fig. 8(b)) evaluated from crack length history is extremely noisy with little evidence of any discernable pattern seen in the photoelastic experiments.

Finally, the dynamic crack branching of soda-lime glass was studied by using a newer method, DGS. Speckle images captured using the Kirana-05 M high speed camera during the fracture event were correlated with the one in the undeformed or reference state to quantify angular deflections of light rays (ϕ_x and ϕ_y) that are proportional to in-plane gradients of stress ($\sigma_x + \sigma_y$) in the x- and y-directions, respectively. Two results, corresponding to pre-crack branching and post-crack branching phases of the experiment, are plotted in Fig. 9. Due to the singular nature of the crack-tip fields measured by DGS, locating the crack-tip is relatively easy when compared to DIC, as evident from the contour plots. Figure 10 depicts the apparent crack length and crack velocity histories evaluated from DGS measurements. As in the case of photoelastic experiment the apparent crack length increased monotonically in the entire observation window. The apparent crack velocity steadily increased to ~1500 m/s after crack initiation followed a relatively steady growth at 1450–1550 m/s for the next ~9 µs. The apparent crack velocity dropped gradually before entering the branching phase. Once the branching occurred, it increased abruptly to ~1700 m/s before dropping back to an average velocity in the 1450–1600 m/s range until the end of the observation window.

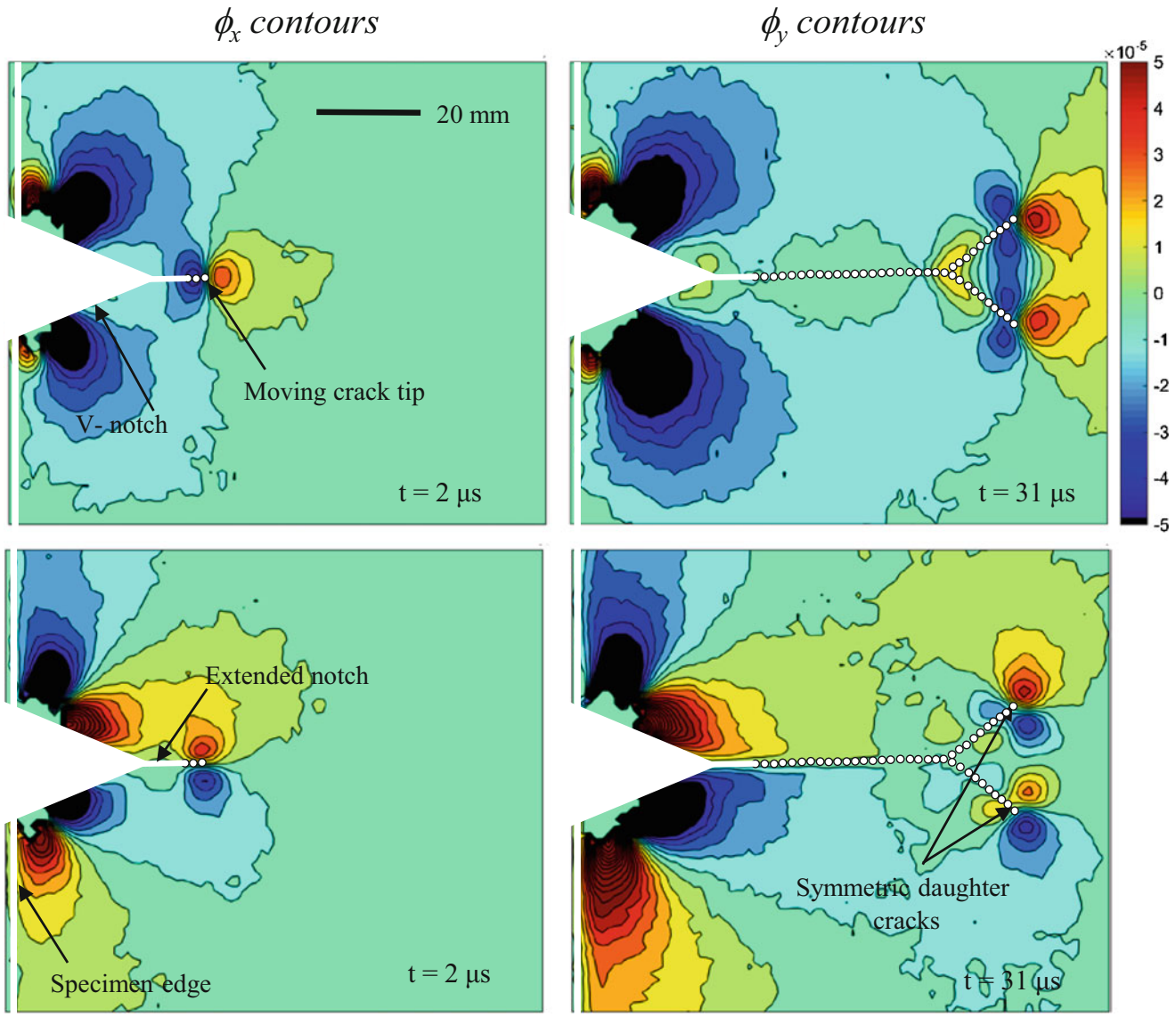

Fig. 9 Angular deflection contours on soda-lime glass specimen surface from DGS. Open circles show the past approximate crack-tip positions during the event

Work-In-Progress

Using the displacement contours obtained from DIC and stress gradient contours from DGS experiments in conjunction with the elasto-dynamic asymptotic crack-tip fields, the fracture parameters such as the dynamic stress intensity factor, strain energy release rates are being quantified [10]. The normal forces acting on the crack flanks are also being evaluated from photoelasticity and DGS methods.

Summary

Three full-field optical methods, photoelasticity, 2D-DIC and transmission-mode DGS were implemented in conjunction with ultrahigh-speed photography to visualize and quantify dynamic crack growth and branching phenomenon in soda-lime glass plates by mapping crack-tip fields. The results indicate that photoelasticity could be used to visualize the events

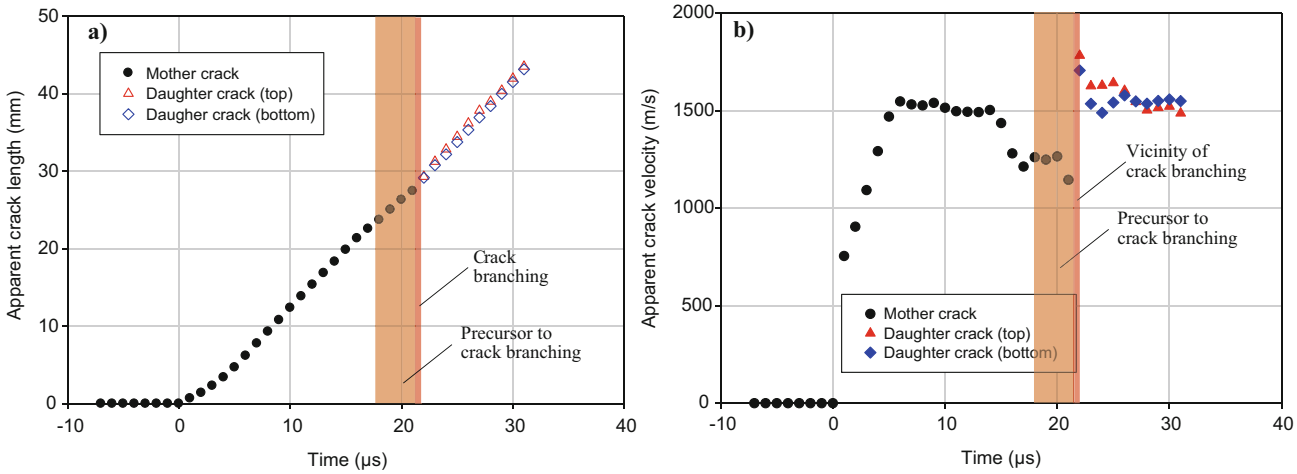

Fig. 10 Apparent (**a**) crack length and (**b**) velocity histories measured from DGS

in terms of precise crack-tip location and velocity measurement. However, in-plane max, shear stress contours could not be visualized due to low strain-to-failure and weak birefringence of the material to extract fracture parameters. The DIC-based measurement of in-plane displacement fields, particularly the crack opening displacement jump location, resulted in very noisy crack length history and was unable to map displacements accurately near the crack-tip. The apparent velocity histories in turn resulted in poor quantification necessary for precise evaluation of dynamic fracture parameters. Finally, due to the singular nature of the crack-tip fields measured by DGS, results provided relatively accurate crack length and velocity histories when compared to DIC counterparts. Furthermore, unlike photoelasticity, the stress gradients in DGS were discernable during the entire event suggesting it to be an effective optical tool for studying high-stiffness and low-toughness materials such as soda-lime glass and potentially other similar ceramics and glasses.

Acknowledgments Partial support of this research from the U.S. Army grants W911NF-15-1-0357 (DURIP) and ARMY-W911NF-17-1-0355 are gratefully acknowledged.

References

1. J.W. Dally, Dynamic photoelastic studies of fracture. Exp. Mech. **10**, 349–361 (1979)
2. A.S. Kobayashi, S. Mall, Rapid crack propagation and arrest in polymers. Polym. Eng. Sci. **19**(2), 131–135 (1979)
3. K. Ravi-Chandar, W.G. Knauss, An experimental investigation into dynamic fracture: II. Microstructural aspects. Int. J. Fract. **26**, 65–80 (1984)
4. K. Ravi-Chandar, W.G. Knauss, An experimental investigation into dynamic fracture: III. On steady-state crack propagation and crack branching. Int. J. Fract. **26**, 141–154 (1984)
5. H. Nigam, A. Shukla, Comparison of the techniques of transmitted caustics and photoelasticity as applied to fracture. Exp. Mech. **28**(2), 123–131 (1988)
6. M.S. Kirugulige, H.V. Tippur, Measurement of fracture parameters for a mixed-mode crack driven by stress waves using image correlation technique and high-speed digital photography. Strain **45**(2), 108–122 (2009)
7. B.M. Sundaram, H.V. Tippur, Dynamics of crack penetration vs. branching at a weak interface: An experimental study. J. Mech. Phys. Solids **96**, 312–332 (2016)
8. B.M. Sundaram, H.V. Tippur, Dynamic fracture of soda-lime glass: A full-field optical investigation of crack initiation, propagation and branching. J. Mech. Phys. Solids **120**, 132–153 (2018)
9. C. Periasamy, H.V. Tippur, Full-field digital gradient sensing method for evaluating stress gradients in transparent solids. Appl. Opt. **51**, 2088–2097 (2012)
10. K. Ravi-Chandar, *Dynamic Fracture* (Elsevier, Amsterdam, 2004)

Attenuation of Hand-Transmitted Vibration Application on Weed Wacker

Ammar Mohammed, John Miller, Jassim Alhamid, and Changki Mo

Abstract Many syndrome and disorders have been reported by worker due to long time use of the hand tools. These disorders have been collected by the International Standard Organization (ISO) to help workers maintain safe operation. Anti-vibration gloves have been proposed to attenuate vibrations that transfer from hand tools to the human body, but these gloves are not effective for this purpose. Here we report experimental work and calculations done on the weed wacker to devise a method to attenuate the vibration of this hand tools. An absorber was fabricated by 3D printing and installed on the shaft between the engine and the handle. The location of the absorber on the shaft was investigated to find the optimum location of vibrational attenuation. Because the absorber is designed as a ring, it can absorb the vibration in all three directions. The optimized absorber reduced vibration by about 75% compared to the vibration of weed wacker without an absorber. Our results also indicate that the location of the absorber is very important to optimize its effectiveness. We found that the best position is close to the engine and away from the handle.

Keywords Hand-transmitted vibration · Tuned vibration absorber · Vibration attenuation

Introduction

Extensive longtime exposure to hand-transmitted vibration can cause many disorders in the vascular and musculoskeletal structures of the human hand–arm system, (Griffin et al. [1], Pelmear et al. [2]). The ISO collects data reported by labor and establishes standards for measurement of exposure and affects. Mechanical vibration that arises from powered tools and enters the body at the hands is called hand-transmitted vibration (HTV). Hao et al. [3] worked on an electric grass trimmer in an attempt to attenuate the HTV using a tuned vibration absorber (TVA) and concluded that the location of the TVA was very important and should be closer to the handle than the engine. Ewins [4], suggested that calculations of an absorber's effectiveness do n't require knowledge of the mass, stiffness, and damping of the original structure because the natural frequency of the TVA should be the same as the frequency of the excitation source. TVAs are particularly effective when the excitation frequency of the machine is close to the natural frequency of the absorber, which maximizes transfer the energy from the machine to the absorber mass because of reactive forces created by the disturbance. Dong et al. [5] performed experimental works on anti-vibration air bladder gloves. They suggested two approaches to measuring the effectiveness of these gloves. First, measure the glove's vibration transmissibility and second, use a palm adapter equipped with a miniature accelerometer to measure the vibration. These measurements were carried out as recommended in the ISO 10819. This work aims to propose a TVA and to demonstrate it's effectiveness of the atenuation of HTV on a weed wacker.

Methods and Results

The absorber is designed as a plastic ring made on a 3D-printer and placed around the weed wackers shaft, as shown in the Fig. 1.

The absorber was analyzed using a spring-mass model system. The ring is represented as four equal masses in a circular shape connected to each other by spring k1, as shown in the Fig. 2. The internal beam is connected to the circle by spring k2.

A. Mohammed (✉) · J. Miller · J. Alhamid · C. Mo
School of Mechanical and Material Engineering, Washington State University, Tri-Cities, Richland, WA, USA
e-mail: ammar.mohammed@wsu.edu

M. Silberstein et al. (eds.), *Challenges in Mechanics of Time Dependent Materials, Fracture, Fatigue, Failure and Damage Evolution, Volume 2*, Conference Proceedings of the Society for Experimental Mechanics Series, https://doi.org/10.1007/978-3-030-29986-6_3

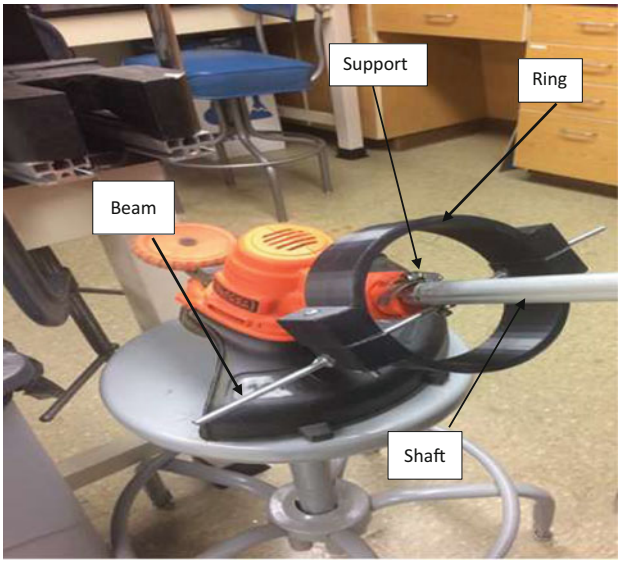

Fig. 1 Vibration absorber attenuation for the weed wacker

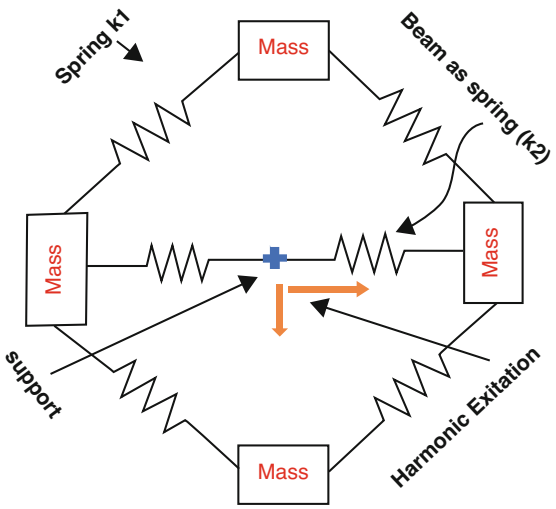

Fig. 2 Modeling the structure of the absorber as a spring-mass system

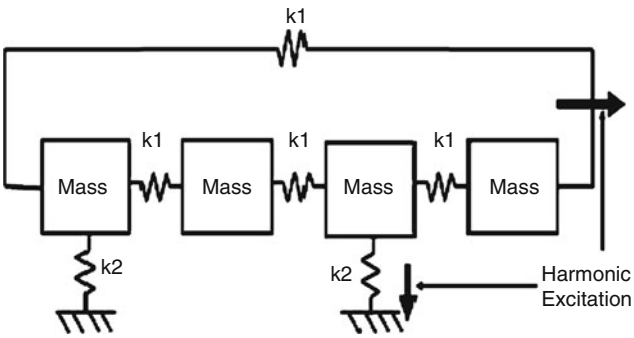

Fig. 3 The model in Fig. 2 is opened and represented in the x-y direction

By cutting the absorber in half and opening it, the system can be redrawn as shown in Fig. 3. From Fig. 3 it can be seen that the excitation force is parallel on the spring stiffness for both k1 and k2.

In x-direction the equations of motion of the masses can be written in matrix form as

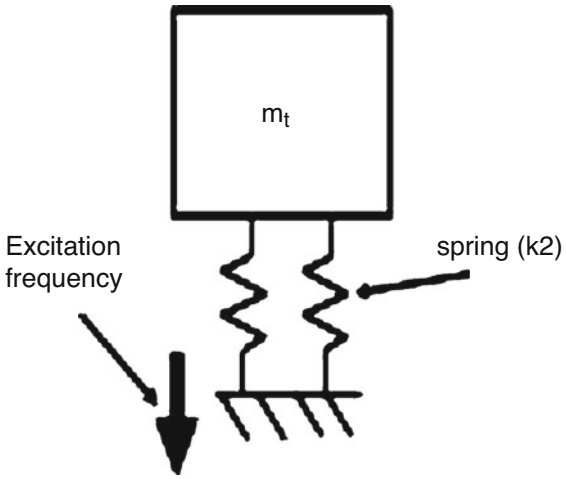

Fig. 4 Mass-spring model for motion in the y-direction

$$\begin{bmatrix} m & 0 & 0 & 0 \\ 0 & m & 0 & 0 \\ 0 & 0 & m & 0 \\ 0 & 0 & 0 & m \end{bmatrix} \begin{Bmatrix} \ddot{x_1} \\ \ddot{x_2} \\ \ddot{x_3} \\ \ddot{x_4} \end{Bmatrix} + \begin{bmatrix} 2k1 & -k_1 & 0 & -k_1 \\ -k_1 & 2k_1 & -k_1 & 0 \\ 0 & -k_1 & 2k_1 & -k_1 \\ -k_1 & 0 & -k_1 & 2k_1 \end{bmatrix} \begin{Bmatrix} x_1 \\ x_2 \\ x_3 \\ x_4 \end{Bmatrix} = \begin{bmatrix} F \\ F \\ F \\ F \end{bmatrix} \tag{1}$$

In the y-direction the absorber can be modeled by one mass only with two springs k2 because all four masses move the same displacement in the y direction.

So, the natural frequency of Fig. 4 is

$$\omega_{n1} = \sqrt{\frac{2k_2}{m_t}} \tag{2}$$

which leads to $k_2 = m_t {\omega_{n1}}^2/2$, where, m_t is the absorber's total mass.

To find the natural frequency of the system first we need to find the transmissibility of the system. Rao [6] suggest that the transmissibility of the system should be bigger than $\sqrt{2}$ to achieve minimum transmissibility (maximum isolation). Hence, we assume that

$$\omega_{n1} = \sqrt{2}\omega \tag{3}$$

where ω is the system frequency, which we measured to be $\omega = 120 \times 2\pi = 240\pi$ rad/sec. With the value of ω and a measured value of $m_t = 0.36$ kgm, we calculate $\omega_{n1} = 240\pi\ \sqrt{2} = 1066.3\ rad/s$ and $k_2 = \frac{1066.3^2 \times 0.36}{2} = 20459.2\ N/m$. These results suggest that k_2 has a high value, so a rigid beam.

The radius (R) of the ring absorber can be found from the following equation

$$Power = V \times I = Torque \times \omega = (k1 \times \Delta x) \times R \times \omega \tag{4}$$

where Δx is the absorber deflection that can be found through the strain $\varepsilon = \frac{\sigma}{E}$. The values of σ *and* E come from the 3D printer wire specification. Using $\varepsilon = \frac{\Delta x}{x}$ and $x = 2\pi R$ leads to $\Delta x = \varepsilon 2\pi R$. Substituting the expression for Δx into Eq. (4) yields result in Eq. (5) for R.

$$R = \sqrt{\frac{V \times I}{k1 * 2\pi \times \varepsilon \times \omega}} \tag{5}$$

To complete the calculation of R, we use Dynkerley's method to find the value of k_1.

$$\frac{1}{{\omega_n}^2} = \frac{1}{{\omega_{n1}}^2} + \frac{1}{{\omega_{n2}}^2} \tag{6}$$

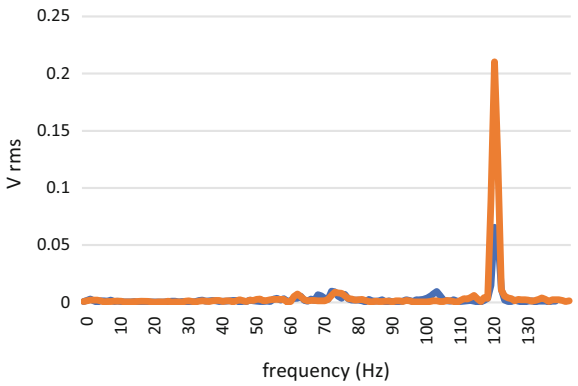

Fig. 5 The blue line is the weed wacker after adding the absorber

$$\omega_{n2} = 3.52\sqrt{\frac{E \times I_{beam}}{m_b \times {l_b}^3}} \tag{7}$$

$$I_{beam} = \frac{\pi \times r^4}{4} \tag{8}$$

where r is the radius of the beam equal to 3 mm and ω_n has the measured value of 240π rad/s reported above. m_b and I_b mean the mass and moment of inertia for the beam.

Applying Eq. (7) with half of the beam length only because the support catches the beam from the middle yields a value of ω_{n2} equal to 904.1206 rad/s. Using the value of ω_n and ω_{n2} in Eq. (6) we can calculate $\omega_{n1} = 140$ Hz. Using this value of ω_{n1} in MATLAB software for the x-direction equations of motions in Eq. (1), we find that k1 equal to 888 N/m when the frequency is matching ω_{n2} equal to 904.1206 rad/s. With a value for k1, we can complete the calculation for R using Eq. (5) and find that $R = 70$ mm.

After adding the absorber meeting the design specification above and a sensor on the weed-wacker handle, we measured the vibrational amplitude with respect to frequency shown by the blue curve in Fig. 5. The orange curve is a similar measurement for the weed wacker without an absorber. After adding the absorber, the vibration is reduce as shown by the smaller peak at about 120 Hz.

During measurements, like those shown in Fig. 5, the absorber was moved on the shaft to find the optimal location for vibration reduction. We found that the best location is close to the motor and away from the handle.

Conclusions

A circular absorber to attenuate hand vibrations by a weed wacker has been designed, assembled, and tested. The shape helps to absorb the vibration in three directions. The vibration at the handle was reduced by about 75% compared with the vibration of weed wacker without absorber. The same absorber can attenuate the torsional vibration as well as the horizontal and vertical vibrations.

References

1. M.J. Griffin, *Handbook of Human Vibration* (Academic, London, 1990)
2. P.L. Pelmear, D. Leong, W. Taylor, M. Nagalingam, D. Fung, Measurement of vibration of hand-held tools: weighted or unweighted? J. Occup. Environ. Med. **31**, 902–908 (1989)
3. K.Y. Hao et al., Tuned vibration absorber for suppression of hand-arm vibration in electric grass trimmer. Int. J. Ind. Ergon. **41**, 494–508 (2011)
4. D.J. Ewins, *Modal Testing: Theory and Practical* (John Wiley & Sons Inc, London, 1984)
5. R.G. Dong et al., A method for assessing the effectiveness of anti-vibration gloves using biodynamic responses of the hand–arm system. J. Sound Vib. **282**, 1101–1118 (2005)
6. S.S. Rao, *Mechanical Vibrations*, 5th edn. (Pearson Education, Inc/Prentic Hall, London/Upper Saddle River, NJ, 2011)

Effect of Loading Rate on Fracture Behavior of Carbon Fiber Reinforced Polymer Composites

Chengyun Miao and Hareesh V. Tippur

Abstract The crack initiation and growth in single-edge notched unidirectional T800s/3900-2 carbon fiber reinforced polymer composites (CFRP) are studied under stress wave and quasi-static loading conditions. The reflection-mode Digital Gradient Sensing (or, r-DGS) is extended here to study fracture mechanics of fiber reinforced composites by using it in conjunction with ultrahigh-speed photography to perform full-field measurement of crack-tip deformations in the pre- and post-crack initiation regimes. The optical method is capable of measuring two orthogonal surface slopes in the crack-tip vicinity as angular deflections of light rays in two mutually perpendicular planes due to crack-tip deformations. The effect of fiber orientation of 0°–60° relative to the initial notch in different composite coupons and the effect of different loading rates are investigated. Nominally mode-I fracture occurs when the fiber orientation is 0° whereas mixed-mode (mode-I and -II) fracture ensues in others. The fiber bridging effects are quite evident in the energy release rate histories, which conveys that fracture behavior of CFRP with dynamic loading producing a weaker post-initiation response relative to the quasi-static counterparts.

Keywords Carbon fiber reinforced polymer composites · Loading rate effects · Dynamic fracture · Crack growth behavior · Digital Gradient Sensing

Introduction

Carbon fiber reinforced polymer (CFRP) composites have been widely used as multifunctional structural materials in aerospace and automotive systems [1, 2]. The high strength, high stiffness, impact resistant and lightweight characteristics make them popular in these and other applications. However, it is highly possible that crack-like defects evolve in these materials during service. As a result, fracture may ensue differently from such defects when subjected to different loading rates.

Non-contact full-field optical methods have distinctive advantages in terms of providing mechanical quantities in the region-of-interest and are preferable to study fracture mechanics of various materials including fiber reinforced composites. Liu et al. applied the method of Coherent Gradient Sensing (CGS) [3] to study static and dynamic fracture behaviors of unidirectional fiber-reinforced composites [4, 5]. Lee et al. [6, 7] investigate crack growth in unidirectional composite coupons subjected to dynamic and quasi-static loadings using Digital Image Correlation (DIC). The same optical technique was adopted by Isaac and Tippur to study quasi-static and dynamic fracture behaviors of additively printed ABS [8]. Difficulty of identifying the crack-tip location for an accurate evaluation of fracture parameters is an issue for investigations [6] which employ speckle decoration on the specimen surface. In this regard, advanced ultrahigh-speed imaging technology coupled with modified vision-based techniques could be helpful. Recently, a full-field optical method called Digital Gradient Sensing (DGS) has been introduced for measuring two orthogonal angular deflections of light rays caused by stresses in transparent materials [9] and out-of-plane deformation of reflective objects [10]. Miao et al. [11–14] extended the reflection-mode DGS (r-DGS) by coupling it with a 2D least-squares integration scheme to map surface topography of thin structures and sub-micron deformations and stresses in laterally impacted plates. Subsequently, these DGS methods have been combined to further enhance the measurement sensitivity by three-fold [15]. Being a very sensitive full-field optical method, DGS has not been applied to study fracture mechanics of opaque structural materials such as CFRP. Hence, a successful demonstration could not only provide a complementary experimental tool for the composites community and provide insight into the fracture characteristics.

C. Miao · H. V. Tippur (✉)
Department of Mechanical Engineering, Auburn University, Auburn, AL, USA
e-mail: htippur@eng.auburn.edu

M. Silberstein et al. (eds.), *Challenges in Mechanics of Time Dependent Materials, Fracture, Fatigue, Failure and Damage Evolution, Volume 2*, Conference Proceedings of the Society for Experimental Mechanics Series, https://doi.org/10.1007/978-3-030-29986-6_4

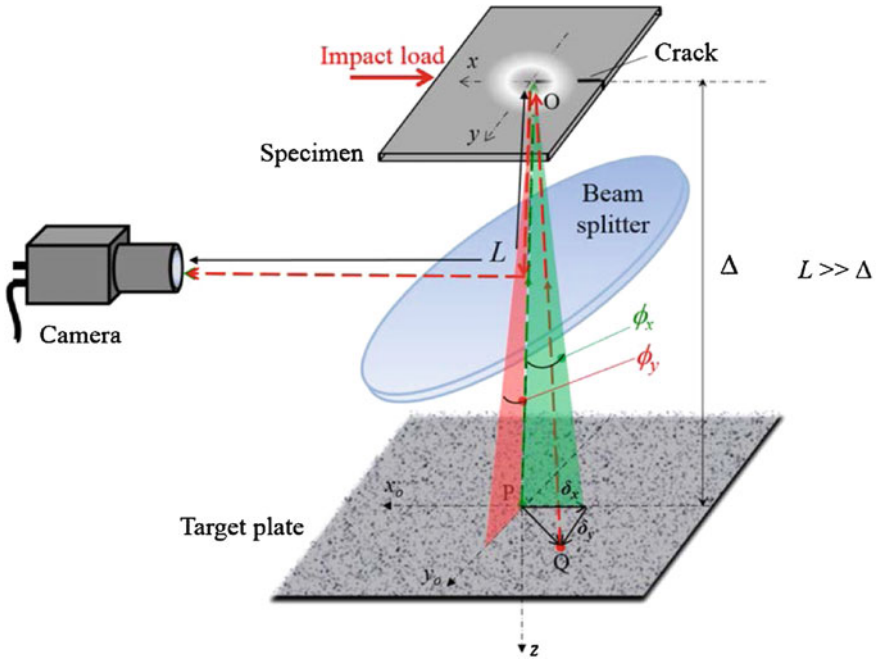

Fig. 1 Schematic of experimental setup for reflection DGS (r-DGS)

Optical Method

A schematic of the optical setup for reflection-mode Digital Gradient Sensing (r-DGS) is shown in Fig. 1. A camera is used to record random speckles on a target plane via the specular specimen surface. Typically, this is achieved by placing the specimen plane and the target plane parallel to each other and a 50/50 beam splitter at 45° relative to both. The target plate is sprayed with black and white paints to create random speckles. To facilitate recording of the speckles via the specimen surface, the specimen is made reflective by depositing an aluminum film. Other details of working principle of r-DGS can be found in Ref. [10].

Dynamic Fracture of CFRP

CFRP plates made of T800s/3900-2 unidirectional laminate with a $[0_{36}]$ lay-up (Toray Composite America, Inc.) were studied. The specimens were cut into 152 mm × 76 mm × 6.8 mm plates of five different fiber orientations, $\alpha = 0°$, 15°, 30°, 45° and 60°, with respect to the initial edge crack direction, as shown in Fig. 2. The impact load is at the middle of the edge opposite to the cracked edge. That is, when $\alpha = 0°$, mode-I fracture conditions occur whereas mixed-mode fracture occurs for the other angles. One of the two 152 mm × 76 mm faces of each specimen was made reflective by using the aluminum film transfer technique to implement r-DGS.

The schematic of the experimental setup used is shown in Fig. 3. A modified Hopkinson pressure bar, or simply a 'long-bar', was used for loading the edge-cracked composite specimens. The long-bar was a 1.83 m steel rod of 25.4 mm diameter with a polished wedge-shaped tip for impacting an unconstrained CFRP plate on the edge opposite to the cracked edge. A 305 mm long, 25.4 mm diameter steel striker placed in the barrel of a gas-gun was launched towards the long-bar at a velocity of approx. 6 m/s during tests. At the same time, the speckle images were photographed by a Kirana-05 M ultrahigh-speed digital camera at 500 K frames per second (inter frame period 2 μs). The distance between the specimen and the camera lens plane (L) was ~780 mm and the one between the specimen mid-plane and the target plane (Δ) was ~70 mm.

Measured surface slopes of $\frac{\partial w}{\partial x}$ around the dynamically loaded cracks for $\alpha = 15°$, 45° are shown in Fig. 4 at a few select time instants, the surface slopes of other fiber orientations can be found in Ref. [16]. It should be noted that, all the contours are plotted in the global coordinates (x, y), shown in Fig. 4a. The mixed-mode fracture behaviors can be observed here due to the fiber orientations being not along the loading direction namely -x-axis. Figure 4a, b correspond to $\frac{\partial w}{\partial x}$ of each specimen

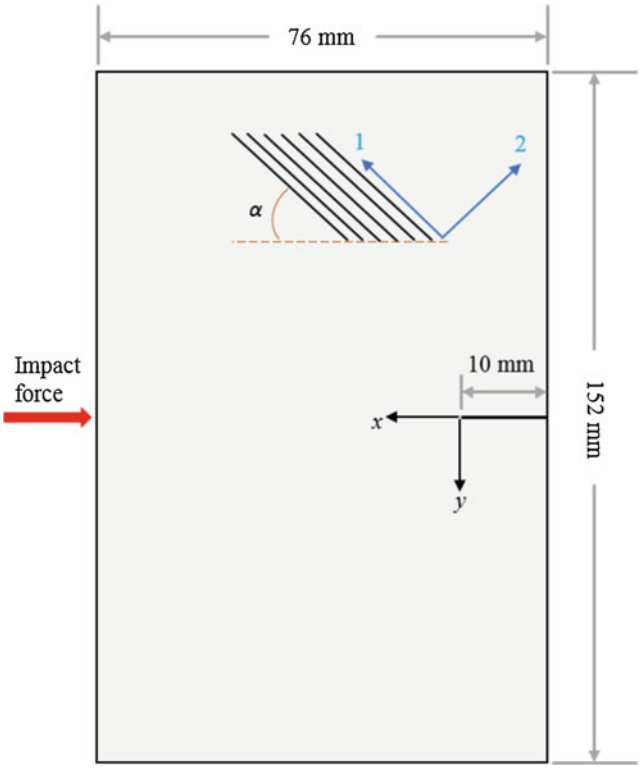

Fig. 2 Specimen configuration

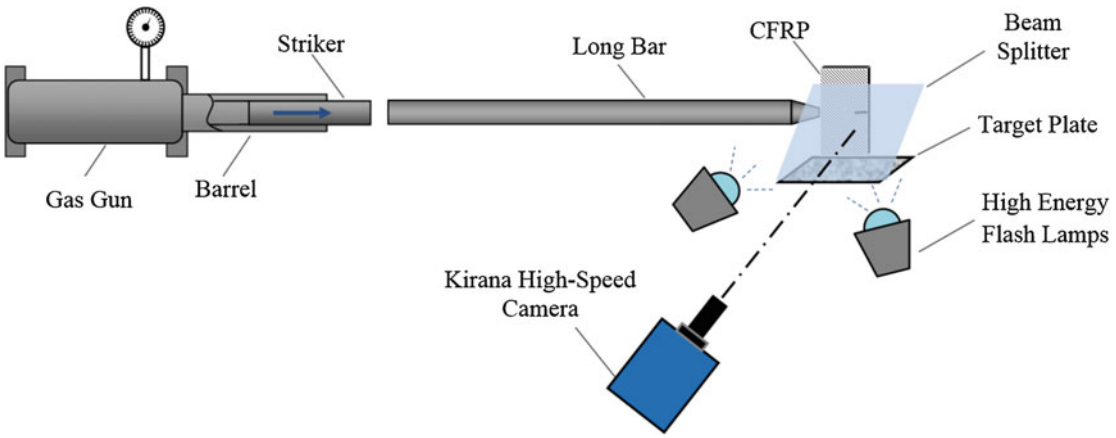

Fig. 3 Schematic of the experimental setup used to study dynamic fracture behavior of CFRP

at $t = 0\,\mu s$ or just before crack initiation; it can be observed in these plots that the contours are not symmetric relative to the initial crack orientation and are increasingly tilted as the fiber orientation increases. Figure 4c, d correspond to $\frac{\partial w}{\partial x}$ of each specimen at $t = 20\,\mu s$, which indicate that cracks have propagated for 20 μs following crack initiation in each case. The dominant contours are the current crack-tip whereas the contours at the original notch tip represent residual deformations. The dotted lines indicate the crack path and solid lines indicate the initial crack direction in these plots. It can be observed that as expected crack propagation occurs along the fiber direction although they are all subjected to the same geometrically symmetric impact. Furthermore, the specimen with $\alpha = 15°$ has a longer crack at $t = 20\,\mu s$ and the crack length decreases with increasing angles of fiber orientation relative to loading direction due to different crack speeds in each case.

The crack growth histories during dynamic fracture of CFRP are plotted in Fig. 5. It can be observed that for $\alpha = 0°$, 15° and 30°, the crack speeds are rather close to each other within the experimental accuracy. However, for $\alpha = 45°$, a significant drop in speed is evident. For $\alpha = 60°$, the crack grows at the lowest speed following initiation.

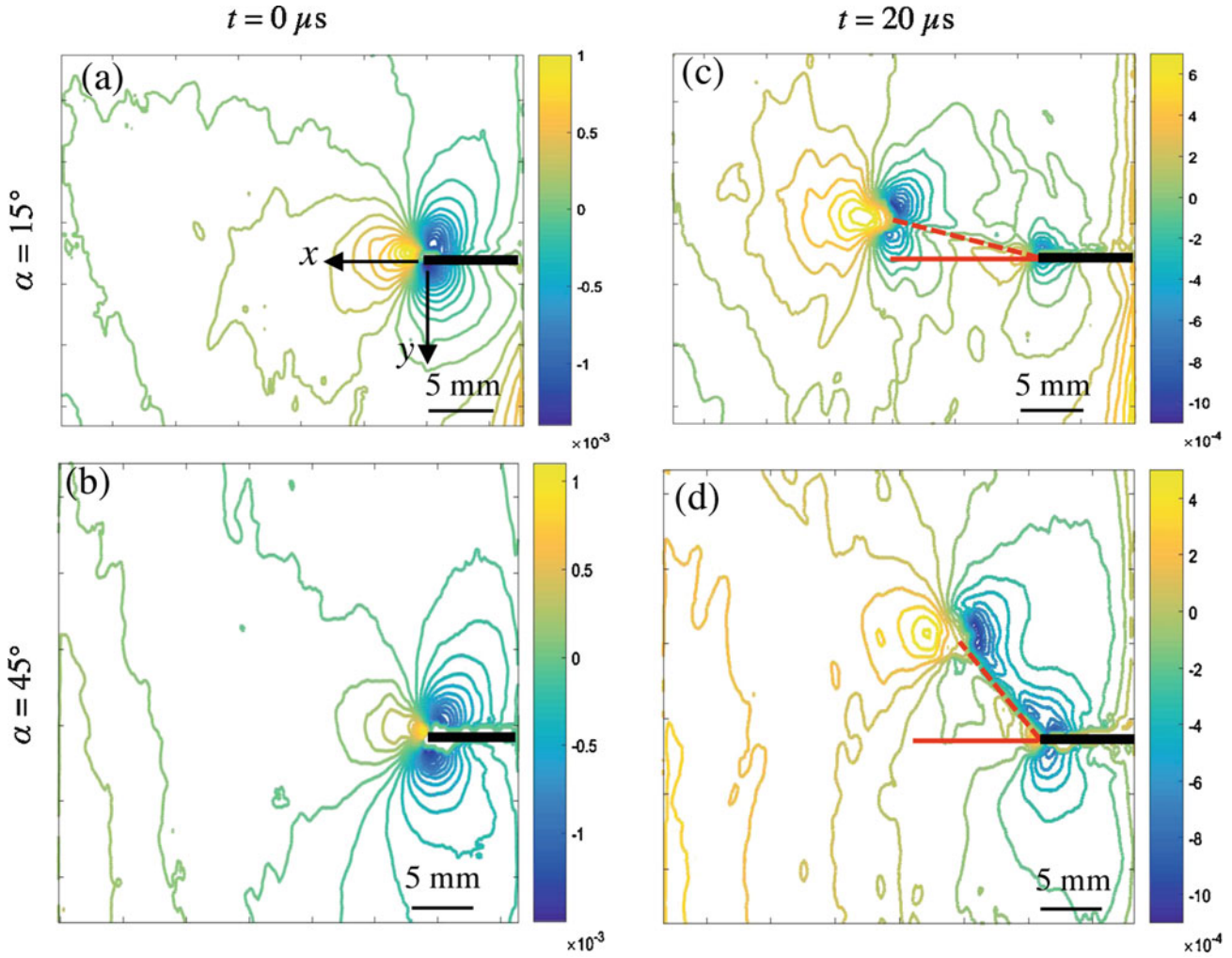

Fig. 4 Measured surface slopes $w_{,x}$ contours for CFRP of mixed-mode dynamic fracture. Contour increments $= 1 \times 10^{-4}$ rad. (Black strips are overlaid on the plots to highlight the crack; broken red line suggests kinked crack path)

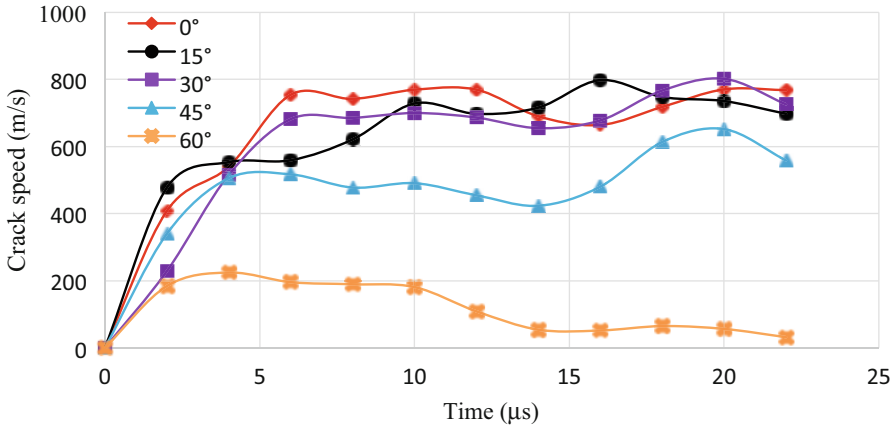

Fig. 5 Crack velocity histories during dynamic fracture of CFRP with different fiber orientation

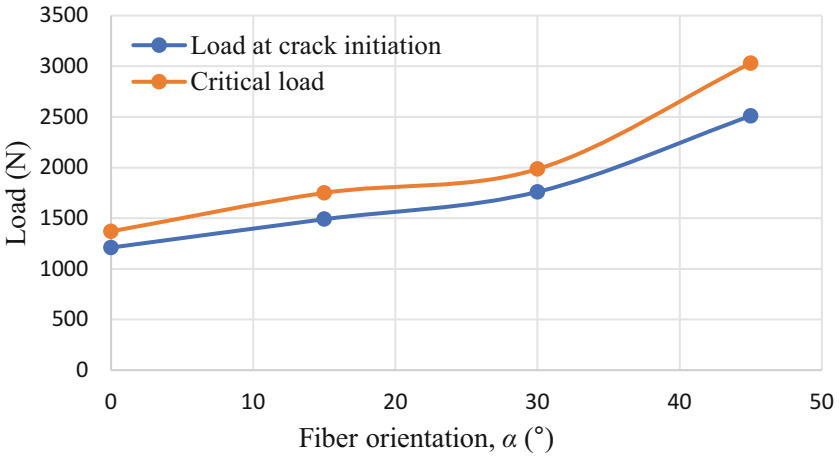

Fig. 6 Fracture load variations for different fiber orientations

Quasi-Static Fracture of CFRP

To study the loading rate effect on fracture behaviors of CFRP, symmetric quasi-static 3-point bending experiments were performed on edge notched coupons, again using r-DGS. Rectangular specimens of dimensions 152 mm × 56 mm × 6.8 mm with an initial crack of length 10 mm were used. As in the dynamic experiments, the specimens had different fiber orientations, $\alpha = 0°$, 15°, 30° and 45°, with respect to the initial crack direction, (the load required to initiate the crack in the specimen with $\alpha = 60°$ exceeded the limit of the loading device and hence static fracture of the specimen with $\alpha = 60°$ was not studied). The specimens supported on two anvils (span 127 mm) were loaded using an Instron 4465 universal testing machine operating in displacement-controlled mode (crosshead speed = 0.007 mm/s). The fracture behaviors of CFRP was also studied using r-DGS. A Nikon D100 digital SLR camera fitted with a 70–300 mm macro lens and an adjustable bellows was used to record images at a rate of 0.5 frames per second. The distance between the specimen and the camera lens plane (L) was ~1200 mm and the one between the specimen mid-plane and the target plane (Δ) was ~70 mm.

The failure load histories for quasi-static fracture of CFRP are plotted as a function of fiber orientation, α, in Fig. 6. It includes two graphs, one for the load at crack initiation and the other for the critical load corresponding to visible crack growth. Interestingly, it can be observed that the load at crack initiation for each CFRP coupon is lower than the corresponding critical load. This is attributed to fiber bridging of the crack faces causing additional load bearing after crack initiation. The crack bridges are evident from the micrographs of the failed samples shown in Fig. 7.

Results and Discussion

Using an over-deterministic least-squares regression of optical measurements used in conjunction with the crack-tip fields for orthotropic materials, the stress intensity factors (SIFs) of all CFRP coupons under dynamic and quasi-static loadings were calculated first, and then the energy release rates, G, were determined from SIFs as detailed in Ref. [16].

The energy release rate, G, histories for both high- and low-rate loading conditions and the results are compiled in Fig. 8. In the pre-initiation regime, the G histories monotonically increase up to crack initiation with higher fiber orientation producing higher values at initiation. In the dynamic loading cases (Fig. 8a), the peak value of G (340–590 N/m) occurred either at $t = 0$ or one time step (2 μs) after that, possibly due to the fiber bridging effects noted earlier. Aside this, the G values drop in all dynamic fracture cases after crack initiation and show a tendency to attain separate plateau values in different cases. The plateau values for different fiber orientations vary between ~145 N/m for $\alpha = 0°$ to ~300 N/m for $\alpha = 45°$, nearly a half of the peak values at crack initiation. In the quasi-static loading cases (Fig. 8b), the values of G show noticeably different trend in the post-initiation regime although they increase monotonically up to crack initiation for all fiber orientations as in the dynamic cases. Again, the values of G corresponding to crack initiation increases with fiber angle and are higher than the corresponding dynamic counterparts. A striking difference in the quasi-static G histories is in the post-initiation regime where (1) a significant increase in G values are seen following crack initiation and, (2) the G values continue to increase, though at a reduced rate, during the window of observation suggesting a relatively graceful failure. This difference relative

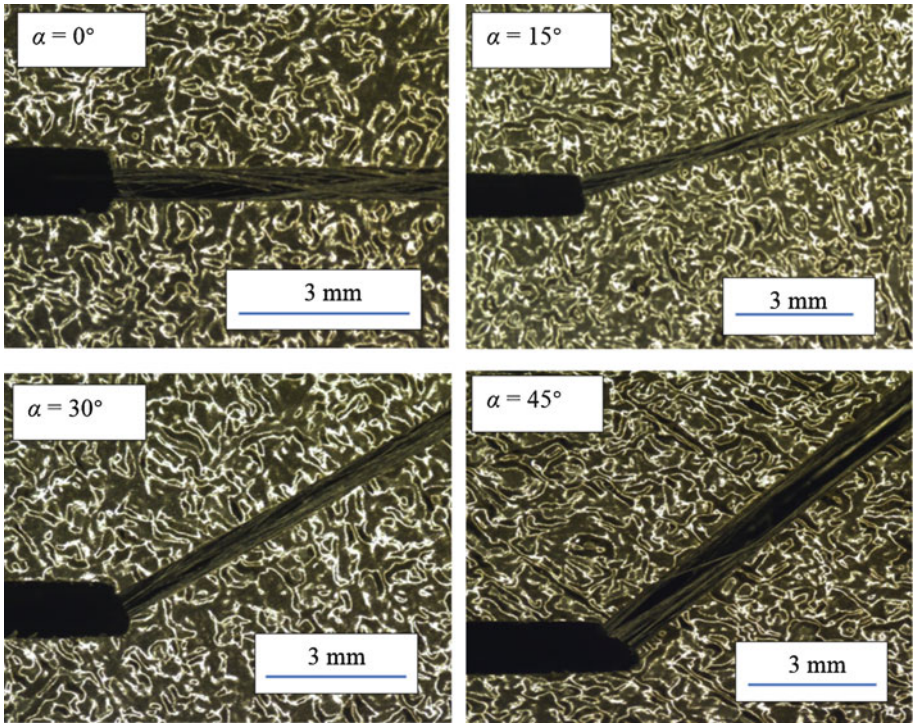

Fig. 7 Cracked faces bridged by fibers in quasi-static experiments. (The random pattern elsewhere is due to the surface texture and angular illumination and are not coated speckles)

to the dynamic counterpart is significant as it conveys an important loading rate dependent post-initiation behavior of this CFRP namely dynamic loading produced a weaker post-initiation response relative to the quasi-static counterparts.

Conclusions

In this paper, static and dynamic fracture behaviors of unidirectional CFRP laminates made of T800s/3900-2 are studied. A vision-based full-field optical method called reflection-mode Digital Gradient Sensing or r-DGS is also extended to study fracture behavior and evaluate the fracture parameters in fiber reinforced plastics. Based on the measurements, the following observations are made:

- The inclined fiber orientation relative to the crack direction have forced the crack-tip deformations and crack growth to occur under mixed-mode conditions in geometrically symmetric loading configurations.
- Under quasi-static loading conditions, crack initiation occurred at a load that continued to increase until a peak/critical load was reached. This is due to the formation of fiber bridges across the crack flanks.
- The energy release rate (G) variations show monotonic increase until crack initiation in both quasi-static and dynamic conditions. In the post-initiation regime, an abrupt drop in G followed by steady values in the dynamic cases contrast with increasing trends in the static cases. A weaker post-initiation crack growth could cause sudden failure under dynamic conditions whereas static loading result in a more graceful failure.

Acknowledgement Partial support of this research from the U.S. Army grants W31P4Q-14-C-0049, W911NF-16-1-0093 and W911NF-15-1-0357 (DURIP) are gratefully acknowledged. The authors are also grateful to Dr. Dongyeon Lee, Toray Composite Materials America, Inc., for providing the CFRP laminates studied in this work.

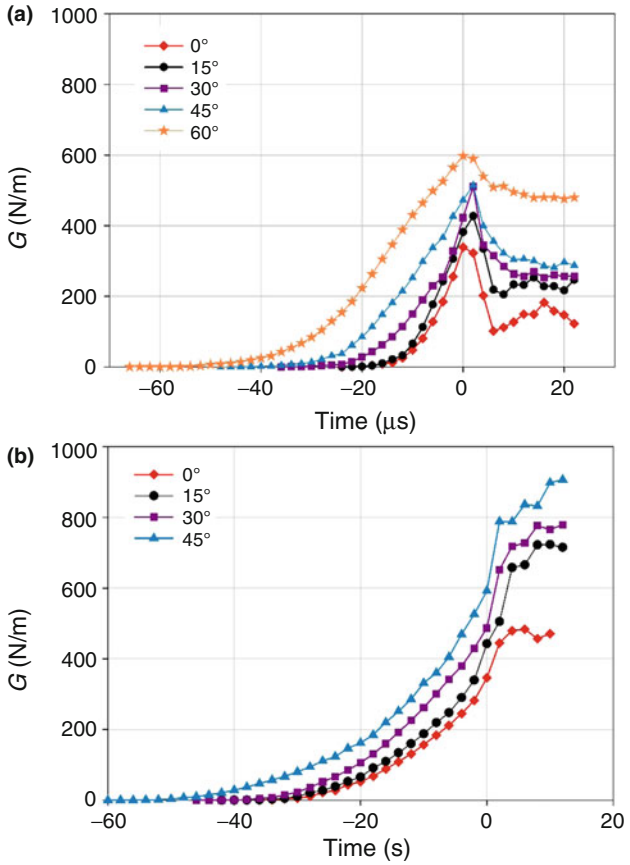

Fig. 8 Energy release rate histories for CFRP with different fiber orientations (**a**) dynamic fracture and (**b**) quasi-static fracture. ($t = 0$ corresponds to crack initiation)

References

1. R.F. Gibson, A review of recent research on mechanics of multifunctional composite materials and stractures. Compos. Struct. **92**, 2793–2810 (2010)
2. T. Pereira, Z. Guo, S. Nieh, J. Arias, H.T. Hahn, Energy storage structural composites: a review. J. Compos. Mater. **43**, 549–560 (2009)
3. H.V. Tippur, S. Krishnaswamy, A.J. Rosakis, Optical mapping of crack tip deformations using the methods of transmission and reflection coherent gradient sensing: a study of crack tip K-dominance. Int. J. Fract. **52**, 91–117 (1991)
4. C. Liu, A.J. Rosakis, M.G. Stout, Dynamic fracture toughness of a unidirectional graphite/epoxy composite, in *Proceedings of the Symposium on "Dynamic Effects in Composite Structures"*, (IMECE, New York, 2001)
5. C. Liu, A.J. Rosakis, R.W. Ellis, M.G. Stout, A study of the fracture behavior of unindirectional fiber- reinforced composite using coherent gradient sensing (CGS) interferometry. Int. J. Fract. **90**, 355–382 (1998)
6. D. Lee, H. Tippur, P. Bogert, Quasi-static and dynamic fracture of graphite/epoxy composites: an optical study of loading-rate effects. Compos. Part B **41**, 462–474 (2010)
7. D. Lee, H. Tippur, M. Kirugulige, Experimental study of dynamic crack growth in unidirectional graphite/epoxy composites using digital image correlation method and high-speed photography. J. Compos. Mater. **43**, 2081–2108 (2009)
8. J.P. Isaac, H.V. Tippur, Quasi-static and dynamic fracture behaviors of additively printed ABS coupons studied using DIC: role of build architecture and loading rate. Mechan. Addit. Adv. Manuf. **8**, 11–19 (2019)
9. C. Periasamy, H.V. Tippur, Full-field Digital Gradient Sensing method for evaluating stress gradients in transparent solids. Appl. Opt. **51**(12), 2088–2097 (2012)
10. C. Periasamy, H.V. Tippur, A full-field reflection-mode Digital Gradient Sensing method for measuring orthogonal slopes and curvatures of thin structures. Meas. Sci. Technol. **24**, 025202 (2013)
11. C. Miao, B.M. Sundaram, L. Huang, H.V. Tippur, Surface profile and stress field evaluation using Digital Gradient Sensing method. Meas. Sci. Technol. **27**, 095203 (2016)
12. C. Miao, H.V. Tippur, Measurement of sub-micron deformations and stresses at microsecond intervals in laterally impacted composite plates using Digital Gradient Sensing. J. Dyn. Behav. Mater. **4**, 336–358 (2018)
13. C. Miao, H.V. Tippur, Quantitative visualization of sub-micron deformations and stresses at sub-microsecond intervals in soda-lime glass plates. Dyn. Behav. Mater. **1**, 315–321 (2019)

14. C. Miao, H.V. Tippur, Measurement of orthogonal surface gradients and reconstruction of surface topography from Digital Gradient Sensing method, in *Advancement of Optical Methods in Experimental Mechanics*, (Springer, Cham, 2017), pp. 203–206
15. C. Miao, H.V. Tippur, Higher sensitivity Digital Gradient Sensing configurations for quantitative visualization of stress gradients in transparent solids. Opt. Lasers Eng. **108**, 54–67 (2018)
16. C. Miao, H.V. Tippur, Fracture behavior of carbon fiber reinforced polymer composites: an optical study of loading rate effects. Eng. Fract. Mech. **207**, 203–221 (2019)

Experimental Measurements of Overload and Underloads on Fatigue Crack Growth Using Digital Image Correlation

Paul A. Lara, Hugh A. Bruck, and Felix J. Fillafer

Abstract Aluminum materials are utilized across many industries, spanning from the cycling, automotive, aerospace, and the marine industry. In the latter, marine grade aluminum materials are utilized to construct the hull, appendages, and/or specific components. In particular, 5xxx series aluminum materials are relied on by the marine industry for these purposes, where their material properties are advantageous to reducing the overall weight of naval platforms and reducing their operational cost. During its lifetime, a marine vessel will experience a multitude of variable amplitude loading conditions, with occasional overloads and underloads depending on the sea environment encountered. In some cases, these overloads/underloads result affect the catastrophic failure of the structure and associated design lifetime due to changes in the crack growth rate in 5xxx aluminum materials. Existing models, like the Wheeler, Willemborg, and variations of these, have been utilized to predict the crack growth behavior with varying degrees of success. In this study, we created experimental matrices to explore the effects of overload/underload combinations on fatigue crack growth in 5xxx aluminum. Both visual inspection of crack tip location and Digital Image Correlation (DIC) characterization of the crack tip deformation fields were used to characterize the crack growth in center crack tension (CCT) panel specimens. DIC also enabled additional analysis of strain fields to elucidate on the conditions responsible for the change in the crack growth behavior. Future phases of this work will utilize this data to develop new models for fatigue crack growth.

Keywords Aluminum crack growth · Digital Image Correlation · Center crack tension · Overload · Underload · Plastic zone

Introduction

Embedded high frequency signal effects derived from wave impacts on ships can affect failure mechanisms on the structures and have an adverse impact on the fatigue life of the vessel. While operating in a sea environment, ship structures can be subject to many operational loads (wind, pressure, temperature, etc.), one of which is the structural effects derived from the surrounding sea environment. Typically, the wave environment applies an ordinary wave component which drives the primary bending stress of the vessel, along with a more stochastically driven element that manifest itself as wave impacts. This dynamic wave impacts results in a high frequency vibratory response signals load applied to ship structures. The vibratory nature of these high frequency responses makes the design of structures increasingly complex in nature due to their uncertainty, designers and naval design rule societies have relied on methods such as safety factors and/or margins of safety to account for its effects. A typical wave impact on a Naval Structure imparts a time dependent pulse load that exhibits a higher frequency logarithmic decaying sinusoidal response when measured via experimental means and captured utilizing data acquisition systems. The figure below displays one of these signals, where the measured signal can be decomposed into its different components by applying filtering techniques.

P. A. Lara (✉)
Carderock Division, Naval Surface Warfare Center, West Bethesda, MD, USA
e-mail: paul.lara@navy.mil

H. A. Bruck
Mechanical Engineering Department, University of Maryland, College Park, MD, USA

F. J. Fillafer
Mannheim University of Applied Science, Mannheim, Germany

M. Silberstein et al. (eds.), *Challenges in Mechanics of Time Dependent Materials, Fracture, Fatigue, Failure and Damage Evolution, Volume 2*, Conference Proceedings of the Society for Experimental Mechanics Series, https://doi.org/10.1007/978-3-030-29986-6_5

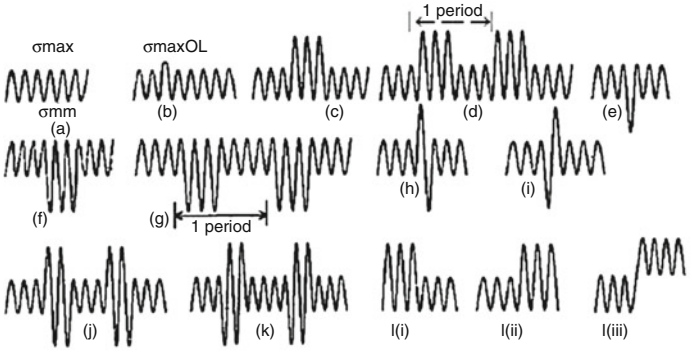

(a) CAL;typical VAL sequences; (b) single Ol; (c) block of OL; (d) period blocks of OL; (e) single UL; (f) block of UL; (g) period blocks of UL; (h) single OL-UL; (i) single UL-OL; (j) periodic OL-UL blocks; (k) periodic UL-OL blocks; and (l) two-level block loading -l(i) high-low; (ii) low-high; and l(iii) both maximum and minimum load

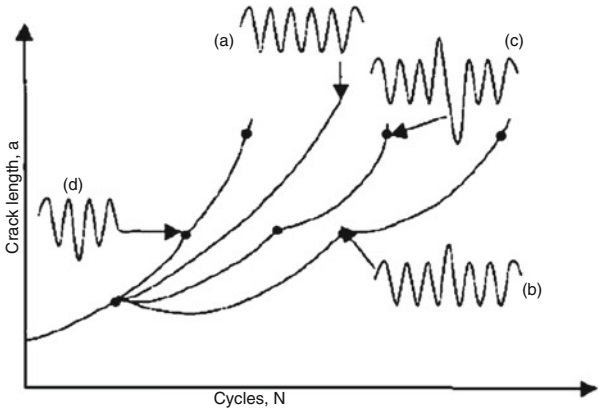

Figure 3 Transient effects on crack growth produced by (a) CAL; (b) single overload; (c) tensile-compressive overload sequence; and (d) single underload

Fig. 1 Load Sequencing [2]

Under the current practices, the peaks of these responses are utilized to compare to the quasi-static design stresses, as well as evaluate the fatigue life of the structures either under constant or variable amplitude experimentation. Figure 1 above displays this kind of behavior, where underloads and underloads affect the crack growth rate behavior of material under a simplified signal approach [1].

But there are additional higher frequency characteristics to these high frequency signals are not currently taken into consideration. Existing academic research has been centered on capturing a simplified sinusoidal response associated with this slamming event and embedded high frequency response, but has not addressed logarithmic decay, signal frequency, or frequency of occurrence. Work by Sumi et al. has centered on more complex signals, where bounding functions where used to predict crack growth behavior [2], and the results show an influence of crack length predictions based on utilizing these bounding functions.

All these factors have associated uncertainty and cause impact on fatigue life and failure mechanisms exhibited by ship structures, work by researchers such as Fricke et al. has shown damage variation as related to amplitude of high frequency signals [3]. The work presented is a multiphase task that looks to gather fundamental understanding of the effects of this high frequency loading on Aluminum 5xxx material, accounting for some of the signal's characteristics, and through an experimental evaluation assess its impact on the local failure mechanism and life cycle models. The foundational findings of this research, can then be used in future investigative efforts to develop analytical models addressing heat affected zones, provide underpinnings for high fidelity numerical modelling, eventually providing broader toolsets to designers that can be used to reduce the dependency on safety factors and introduce more rigorous failure mechanism design criterion. The presented work has the following two basic research objectives: develop and execute an experimental evaluation matrix to investigate a bound set of effects of embedded high frequency signals on fatigue crack growth and associated initiation of failure, and develop failure models that incorporate uncertainty in signal parameters variation and their associated influence on material failure. The first is presented as part of this work, and the latter to be presented as part of future efforts.

Experiment Design

This work builds and complements on existing work developed by Hart and Bruck [4] where the investigators looked at failure of aluminum 5052-H32 and the applications of composite patches to aluminum and the effects of crack growth. Whereas their work centered on the utilization of a composite laminate to mitigate crack growth on ultimate failure, this work looks at the effects of crack growth based on loading condition. Figure 2 below displays the aluminum material properties that Hart and Bruck obtained utilizing ATSM 8 [5] and ASTM E466 [6], as well as the layout of their center crack panel specimens. The Modulus listed for the material is 70.9 MPa, the yield at 2% offset is 116 MPa, and the parameters α and n at 9.9 and 0.22 respectively.

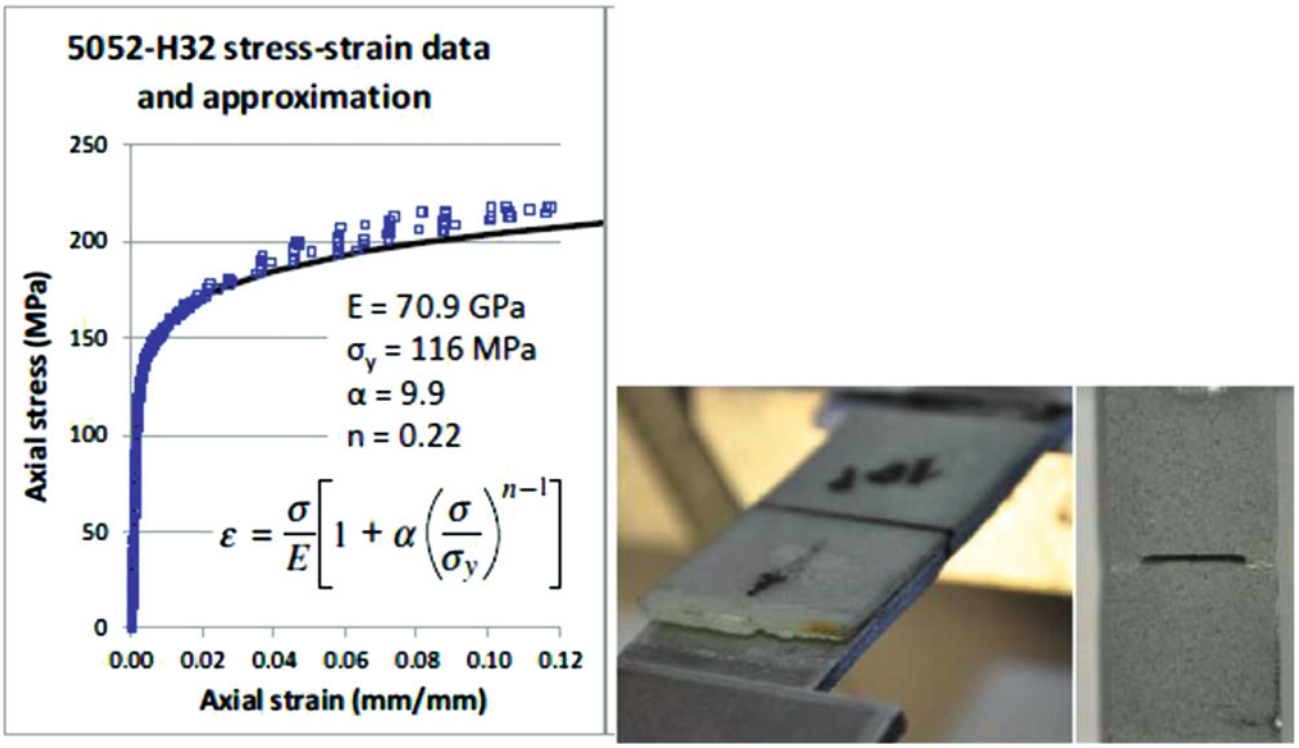

Fig. 2 5052-H32 Material properties and Specimen Failure [5]

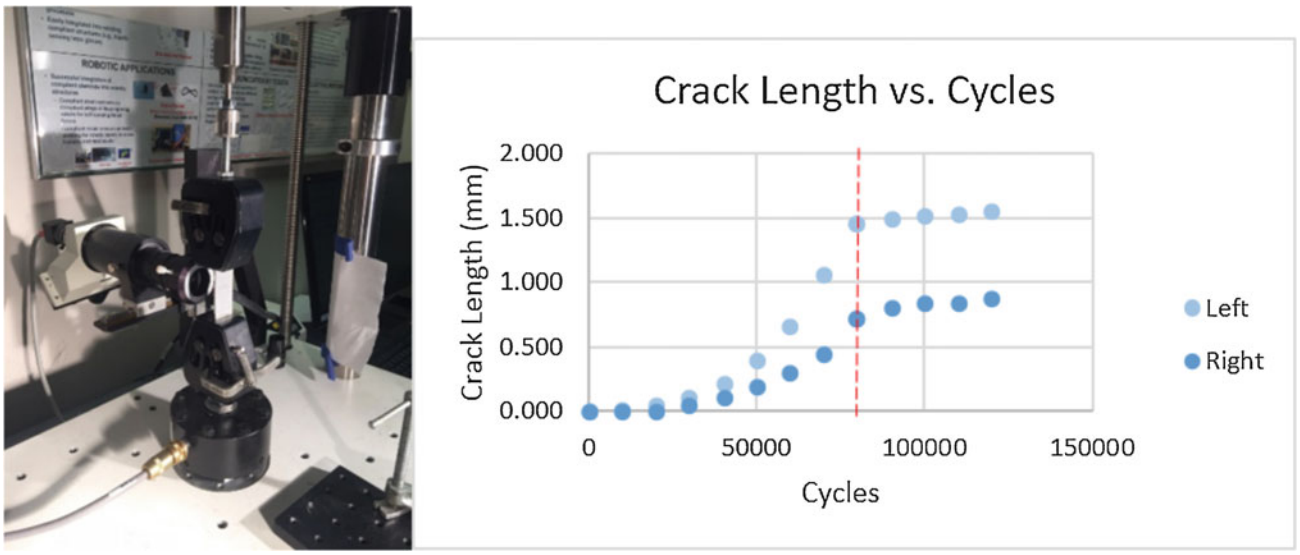

Fig. 3 Initial Specimen Setup

Initial experiments were carried out on this setup for this work, but the results indicated that there was an imbalance of crack growth between the left and right cracks growing from the notch during fatigue loading. Figure 3 above displays the friction wedge grip setup, as well as the crack length visually captured via microscope measurements, the left and right cracks shows differences over 0.5 mm at 80 k cycles. However, one of the promising results from these experiments was that the setup captured effects of crack growth when a high frequency pulse was applied at 80 K cycles, the crack growth shows a variation of the crack growth rate (Da/DN) before and after the pulse is applied.

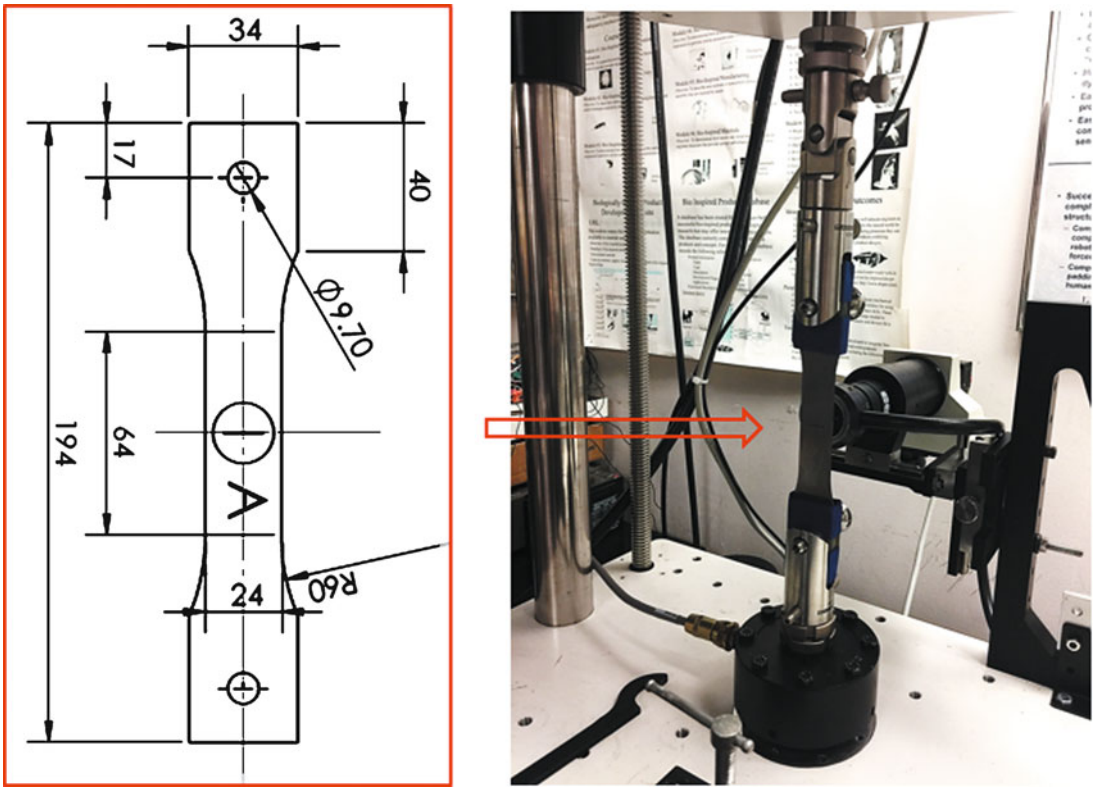

Fig. 4 Clevis Pin Specimen and Setup

It is important to mention that whereas the experiments by Hart and Bruck utilized a four post MTS servo hydraulic setup since they were interested in the ultimate loading capacity, this work work required flexibility to apply smaller loads with different characteristics, hence a two post Bose ElectroForce frame was used, which has the capacity of applying loadings up to 100 Hz and 3000 N. This device has a built in displacement meter with errors of less than 5 μm, and it has a block waveform generation software that allows for the implementation of unique load signals. Fast Fourier Transforms methods were utilized to ensure that the programmed signal and the applied signals displayed the required frequencies.

The specimen configuration shown in Fig. 4 was developed and it is an amalgamation of several ASTM methods, this was conducted to address the significant asymmetry observed with crack growth as previously described. ASTM E8 [5] guidance was utilized to develop the specimen tapers towards test region, while ASTM E647 [7] middle tension specimen configuration was utilized to size the center notch and test region, maintaining the configuration carried out by Hart and Bruck. Since a clevis pin was utilized, ASTM E338 [8] was utilized to develop end reinforcements and alignment tabs for the end pin connections to ensure the failure would not occur in or adjacent to the clevis pin area. Electrical Discharge Machining (EDM) techniques were utilized to manufacture the specimens, providing a stable level of accuracy for the component geometry, it was also critical to ensure alignment of end pins and size and location of center notch. Several test were carried out in this setup, along with finite element analysis, and microscope evaluations of the clevis pin areas and tapers to ensure no failure was visible and that crack growth would be focused towards the test region and adjacent to the notch. The material for the specimen in marine grade aluminum 5052-H32, with a nominal thickness of 2.29 mm (0.09in) Fig 4. Also shows how the clevis pins were utilized in the loading train, and end adaptors that were used to interface with the Bose frame and to help with specimen load alignment, Universal Grip LLC. components were utilized for this setup: Adapter—Male Bolt 5/8″-18 w/1″ length, Universal Joint Adapter; in addition, Mark-10 G1090 high capacity clevis grip (pair) were utilized. The load capacity of the members was at a minimal load of 9KN, hence far exceeding the capacity of the Bose equipment of 3KN, and ensuring no failure could be accidentally induced to the Bose fixture from a failure of the adapters under load.

The experimental setup consisted of several components setup to achieve two goals: observe/capture the crack growth on the back of the specimens using a microscope, and to capture the surface strains on the front face of the specimen utilizing digital image correlation techniques. Figure 5 below details the setup utilized for these experiments.

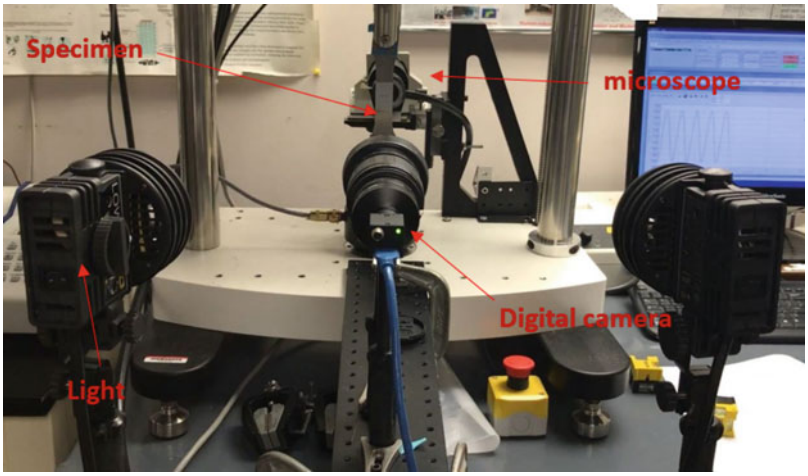

Fig. 5 Experiment Setup

In the back face of the specimens, an optics zoom inspection microscope head by Edmunds Optics was used, along with a Dolan-Jenner MI-150 fiber optic illuminator with a fiber optic ring light accessory, was utilized to capture the crack growth on the back side of the specimen. The setup was connected with a rack and pinion positioning system that allowed movement of the microscope along three axis via a hand knob, hence allowing the positioning of the microscope in different locations to capture crack growth. The microscope was able to visualize square areas of 0.5 mm on each side. Several digital pictures were taken on each crack emanating from each notch, which overlapped, and then were stitched together to form an overall view of the crack of the specimen.

In the front face of the specimen, a Point Gray Flea FL3-U3-88S2C-C digital camera attached to a Tamron 28–80 mm f/3.5–22 lens and adapter was used to capture static pictures of the surface of the specimen. In addition, two 250 W halogen Lowel Pro Lights were utilized to provide lighting to the specimen. The lights were not directly aimed at the specimens, but instead aimed at locations adjacent to the mid-point of the specimen, and focused as to provide evenly dispersed light flooding on the specimen. Digital Image Correlation (DIC) was utilized on the front face of the specimens to capture field surface strains [9], in order to capture these images, the area had to be prepped to generate distinct patterns that can be captured with PointGrey FlyCap 2 V2.11.3 and processed utilizing VIC-2D Ver6.0.6 by Correlated Solutions (Lexington, SC).

The figure below shows the typical DIC pattern applied, the generation of this pattern is achieved by first applying a coat of flat white paint as the background, and the black speckle patterns was developed by not directly applying paint, but instead relying on lightweight particles that slowly settle over the specimen. This procedure requires practice as the specimens needs to be rotated over multiple passes, ending with a specimen that has an adequate gray scaling and consistent patterns that would allow for acceptable DIC measurements. Several references were utilized to obtain best practices and recommendations on acceptable DIC techniques to obtain feasible results, one such body of work in conducted by the internationals digital image correlation society [10] (Fig. 6).

Experiment Protocol and Matrix

In order to explore the variability of the high frequency pulses, a couple of items das to be developed, first was a consistent process/protocol that was repeatable across experiments, and second was an experimental matrix that varied certain parameters to determine their influence on the response. Figure 7 below outlines the experimental process utilized. It is worth noting that each step below is a top level overview, as there are substantial details on each step that are needed for consistency, i.e. the number of photographs taken during measurements, camera settings, etc.

The specimen preparation was the initial step in the configuration, the back side of the specimens that faced the microscope was polished to a mirror type finish, this aided in the identification of the crack tip. The front of the specimens received a DIC spackle pattern that had a sigma level equal or below 0.001 [9]. The sigma level was tested during the baseline measurements stages until the desired value was achieved. Prepping the specimens several times was required in some cases to achieve

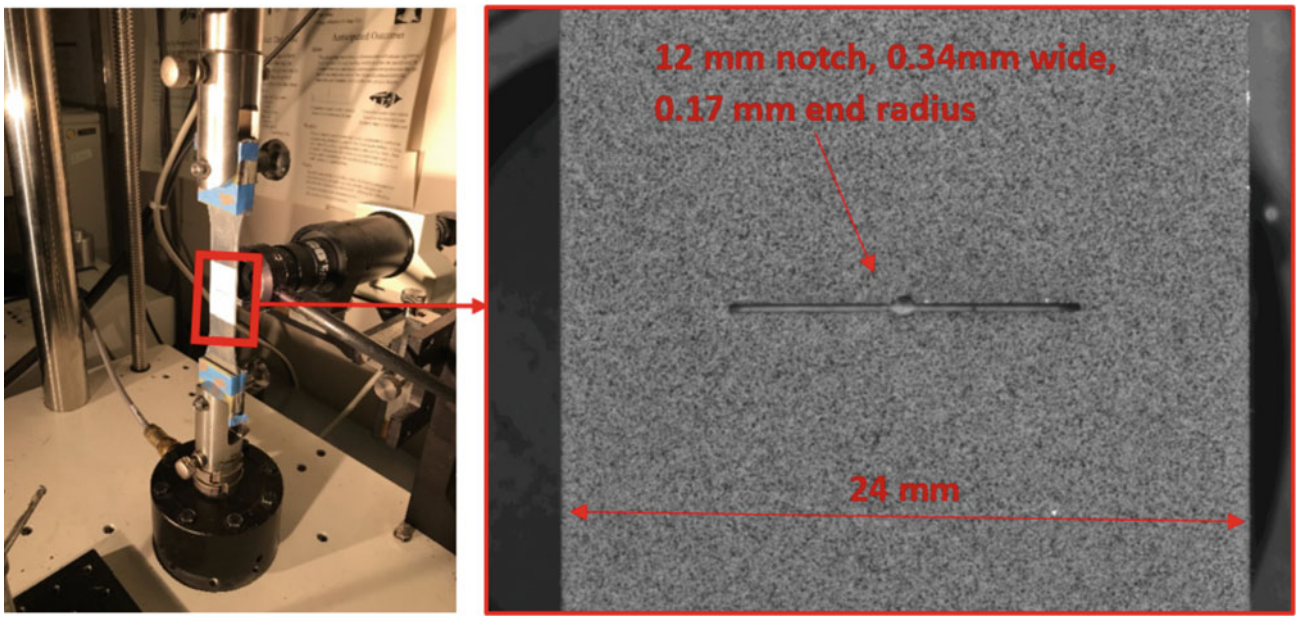

Fig. 6 Specimen and Speckle Pattern

Fig. 7 Experimental Process

the desired values, as inconsistent baseline measurements would result in unpredictable data during the later stages of the experiments. The baseline measurements also consisted on utilizing DIC to evaluate the displacement of the fixture. i.e. if the load frame indicated a 0.2 mm displacement, do the DIC measurements also show a similar value? This was done by only pining the stationary end of the specimen and comparing the displacement between the load frame and DIC calculations. Additional baseline measurements included static DIC measurements at 200, 1100, and 2000 N, as well as microscope crack measurements at no load and 2000 N. The initial crack growth was a step used to develop a crack and go outside the envelope of the stress-strain effects of the notch radius [11]. The notch radius was 0.17 mm, and an initial starter crack was developed to be around 0.5 mm in length. The HF pulse was applied at 40 K cycles, subsequent measurements monitored the crack growth rates after the HF pulse was applied to evaluate the recovery. It is important to note that the load ranged from 200 N to 2000 N, where the stress ratio $R = 0.1$, the frequency used for fatigue was 5 Hz, and the nominal Stress intensity $\Delta K = 6.07$ MPa-m$^{0.5}$.

The experimental matrix utilized is shown in the table below, it consists of a baseline test where no HF pulse is applied, and a 3×3 matrix with three level and two factors (amplitude, frequency), resulting in nine treatments, where the amplitude of the pulse is increased in 1/3 amplitude increments, and frequencies that range between 4 and 10 times the baseline frequency i.e. specimen 3C had a peak amplitude of 2900 N, and an HF pulse with a frequency of 50 Hz.

For this matrix, the HF pulse was only applied at the peak of the ordinary wave of 5 Hz, hence the phase shift was held constant, as well as the log decrement of the function as maintained at 0.21. Introduction of other factors would increase the matrix size to a 3^3 design resulting in 27 treatments.

Initial Results

The initial results provided adequate results, but also highlighted areas of the experiments that required tuning to capture the desired data. Figure 8 below outlines the crack length results of three experiments and the baseline. The frequency is contact at 20 Hz, but the amplitude is varied for each experiment. It can be seen that after the HF pulse is applied at 40 K cycles, the

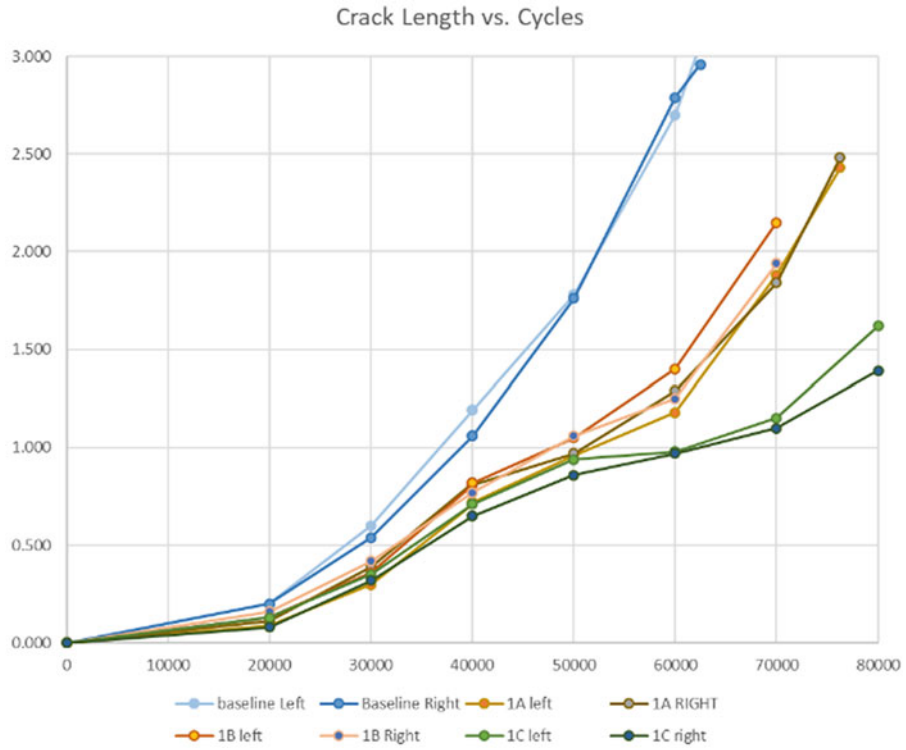

Fig. 8 Initial Results, Amplitude Variability, 20 Hz

crack growth rate is different over time as compared to the baseline, with block 1C (20 Hz, 2900 N) displaying the longest recovery. These measurements are based on microscope measurements of the crack length on the left and right side of the crack.

Reviewing the DIC measurements with Vic2D on the front side of the specimens, one can see variation on the strain fields and crack length and dA/dn as shown in Fig. 9 below.

The data results indicate that a higher fidelity was needed in order to capture the behavior, the data acquisition of every 10 K cycles does not provide sufficient fidelity to address the underlying behavior observed. At the core of this work, models by Wheeler [12] and Willemborg [13]. These models look at the plastic zone behavior, Wheeler relying on crack growth rates, and Willemborg utilizing stress intensity for the calculation, as follows (Fig. 10).

More recent research work by Mehrzadi & Taheri [14], and Chen [15] outline the behavior of the plastic zone ahead of the crack tip.

The common thread of all these models is that an overload plastic zone is created once an overload/underload occurs, and the magnitude of this region has an effect on the crack growth rate as long as the cyclic plastic zone stays within its boundaries. In our case, the data obtained indicated that an overload zone is created, but the fidelity of the data does not support the identification of its progression over time. In addition, it is critical to identify the location of the crack tip with respect to the plastic zones around it.

Data Processing

Of the two limitations outlined above, data fidelity improvements can be addressed by capturing a higher number of data points, instead of capturing data every 10 K cycles, capturing data ever 2 K cycles. The drawback of this approach is that the data required for processing increases in magnitude for each test, hence a more robust/automated method of identifying the crack tip location and plastic zone behavior is needed. A unique method for using DIC for crack detection was developed by Bruck [16] while utilizing curve fitting to locate the crack tip location based on the vertical displacement field. Other researchers have tackled this problem, such as Yates who evaluated the vertical displacement field ahead of the crack tip

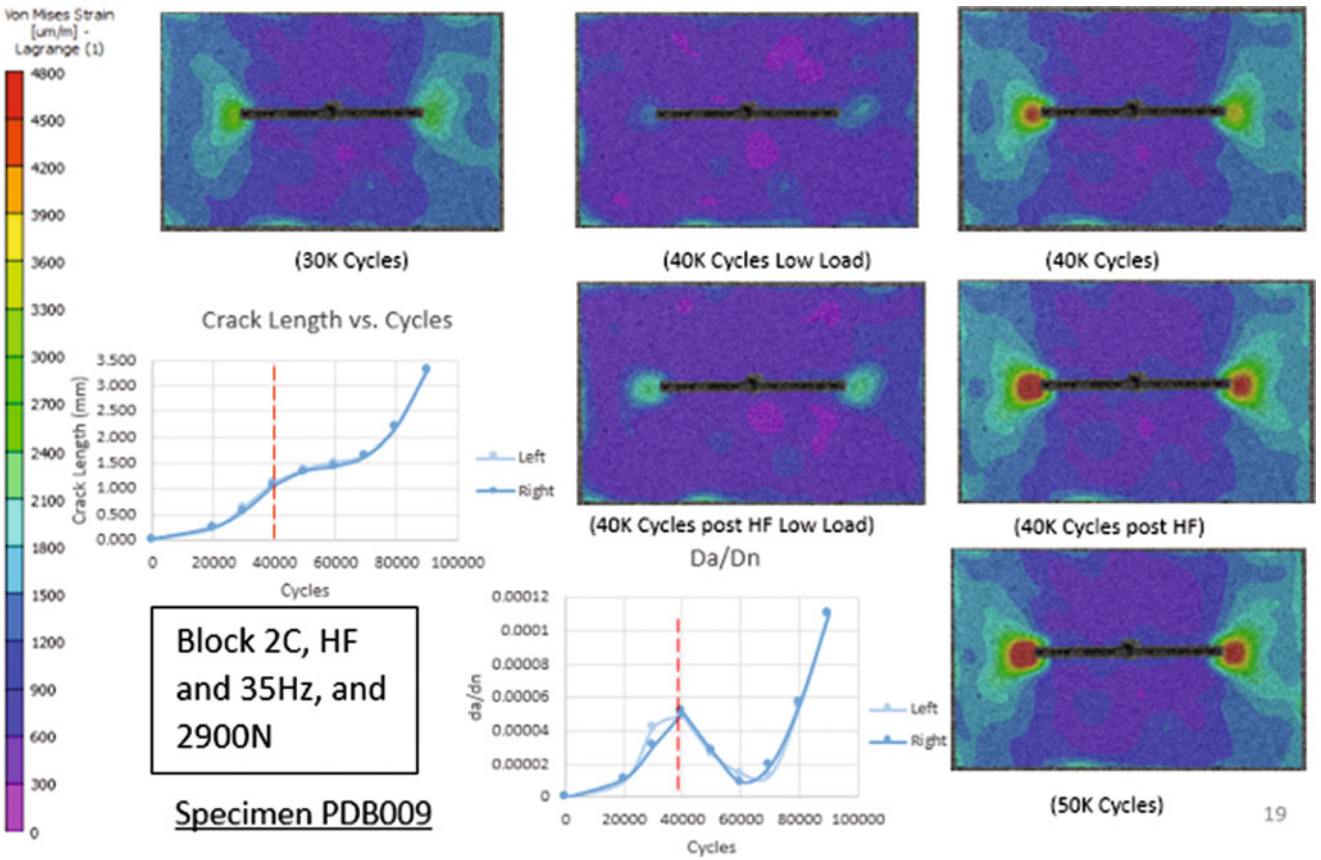

Fig. 9 Block 2C at HF of 35 Hz and Peak Amplitude of 2900 N

Wheeler:

$$\frac{da}{dN} = \Phi_R \left(\frac{da}{dN}\right)_{CAL}$$

$$\text{where}: \Phi_R = \begin{cases} \left[\frac{r_{p,i}}{a_{OL}+r_{p,OL}-a_i}\right]^m & \text{when} \quad a_i + r_{p,i} < a_{OL} + r_{p,OL} \\ 1 & \text{when} \quad a_i + r_{p,i} > a_{OL} + r_{p,OL} \end{cases}$$

Willemborg:

$$\frac{da}{dN_i} = \frac{C(\Delta K_{eff})_i^m}{[(1-R_{eff})_i]K_c - (\Delta K_{eff})_i}$$

Fig. 10 Wheeler and Willemborg Models

[17]. Since the vertical displacement gradient ahead of the crack tip is much higher than other zones, a threshold can be set based on the gradient, and hence, a crack tip location can be obtained.

This work included extracting DIC output data to MATLAB in order to program algorithms to find the crack tip location. The process for this extraction included exporting output vectors (x, y, V, U, Von Mises strain) from DIC at various pixel locations, for each load set (200, 1100, & 2000 N), and time step (30 K, 32 K cycles, etc.). This data was then brought into MATLAB, where it was arranged in matrix form, and the gradient of V along the vertical direction was calculated. Once this was completed, data could be processed for visualization, where the maximum gradient can be picked from each slide of the notch in the vertical direction. The figure below shows the gradient calculated plotted along the Z axis, hence providing a unique method to visualize the behavior around the crack tip by. Figure 11 below outlines how the data can be plotted in 3D, and then filtered to show a specific range.

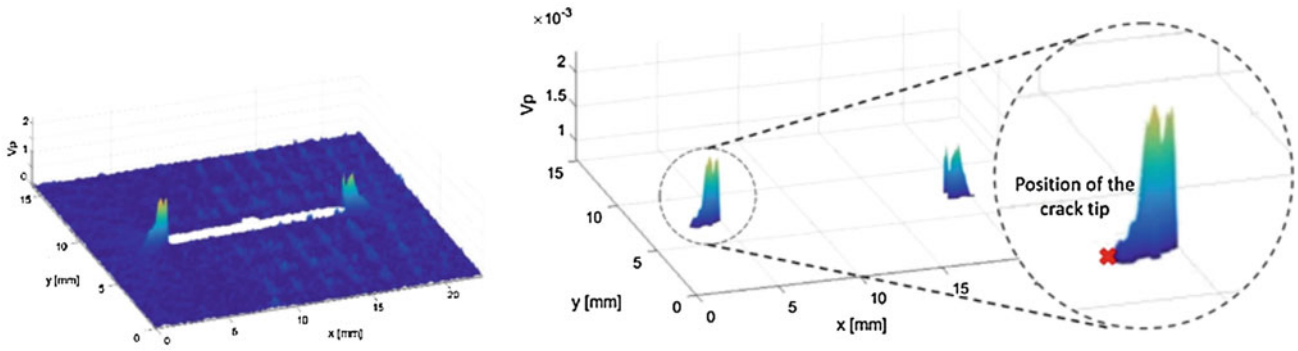

Fig. 11 Vertical Gradient Vp

This data can also be used to determine the crack path and other output vectors further analyzed to automatically show Von misses strains when compared with the crack tip location. This is a unique way to visualize the behavior shown by Yates et al., uniquely developed to process the output experimental data.

This methods also provides a unique process for the identification of the plastic zone areas and begin the comparison with theoretical models [18] where the approximate size of the plastic zone as a function of angular position, r(ϑ), can be estimated by formulations that are based on yield criterion, as follows:

$$r\left(\theta\right) = \frac{1}{4\pi}\left(\frac{K_I}{\sigma_y}\right)^2\left(\frac{3}{2}\sin^2\theta + \cos\theta + 1\right)$$

$$r\left(\theta\right) = \frac{1}{4\pi}\left(\frac{K_I}{\sigma_y}\right)^2\left(\frac{3}{2}\sin^2\theta + \left(1-\nu^2\right)^2\left(1+\cos\theta\right)\right)$$

While the work on outlined above displays the complex shapes of the plastic zones under plane stress and plan strain conditions, these items can be simplified to a circular zone ahead of the crack, as shown by Chen [15].

Experimental Results & Follow on Work

The data captured now allows a visualization of the evolution of plastic zones with respect to the crack tip location, Fig. 12 below shows the effects of block 2C which had a HF pulse of 35 Hz and 2900 N in magnitude. The application of this small pulse showed a change is the residual strain ahead of the crack tip and the loaded strain paths. It also allows the inclusion of the calculated crack path using the strain gradient value in the system.

Work was carried out to compare the error values obtained between microscope measurement and DIC calculated values. Figure 13 below displays the horizontal crack length measurements for the crack propagating form each notch (left and right). The timeline of interest ranges from 36 K cycles to 62 K cycles.

Another aspect of the work is evaluating the failure mechanism observed, while the microscope measurements provide a view of the crack propagation, a Barker's etch method [19] was used for anodizing the aluminum alloy, and then utilizing optical microscopy with polarized lights to observe the grain boundary and the propagated crack. Figure 14 below displays results at 500 μm, 100 μm, and 20 μm magnification levels, allowing the evaluation of the crack propagation through the grain, and the investigation of shielding effects such as contact and deflection on crack growth [20].

The work presented has resulted in procedures utilizing DIC for capturing and quantifying details of the fatigue crack growth associated with HF pulse loading. In future work, the dimensions of the HF pulse plastic zone can be captured, and then further utilizing the DIC data, it will be possible to show the plastic zone progression and change over time to evaluate the applicability of failure models such as Willemborg. Another important aspect will be how the added definition of the plastic zone observed affects the crack path. There are several instances, such as the data in Fig. 13, where there is a

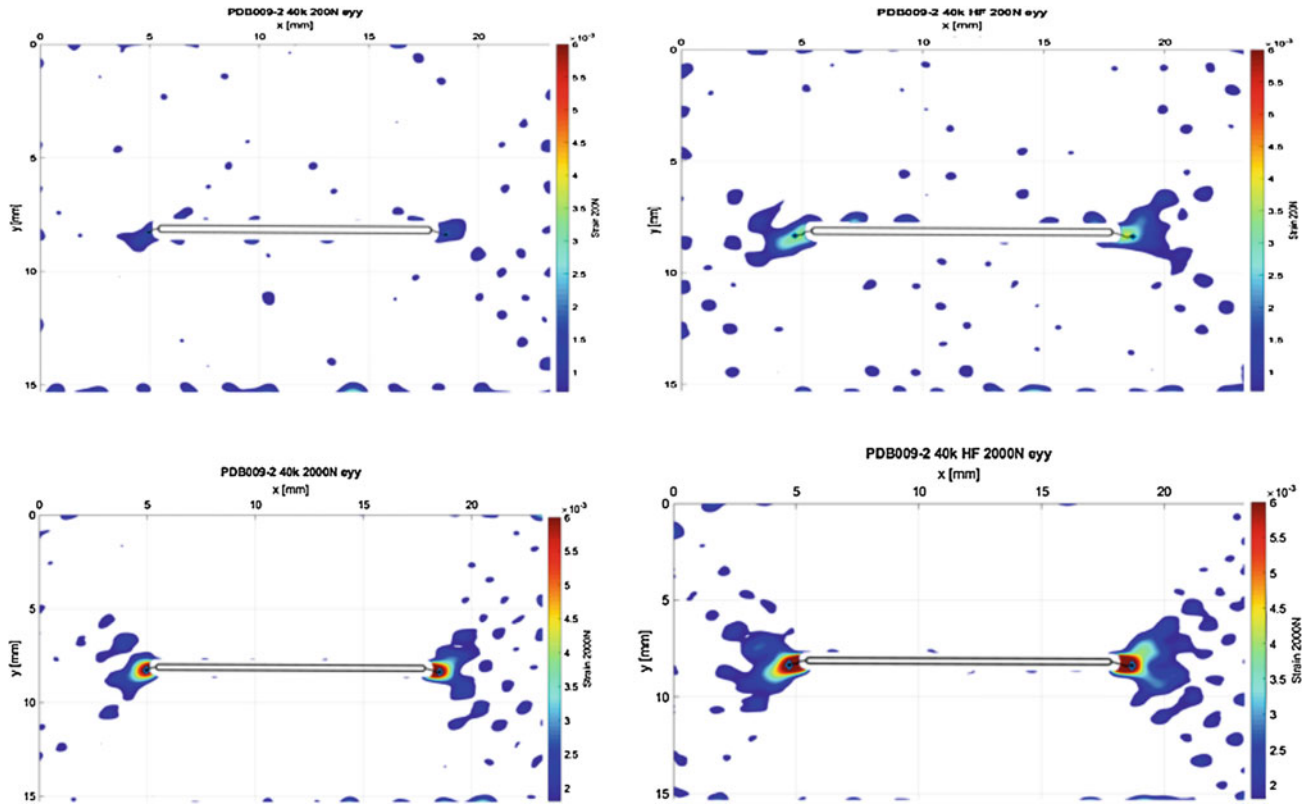

Fig. 12 *eyy* strain pre and post Block 2C at HF of 35 Hz and Peak Amplitude of 2900 N

Table 1 Experimental matrix

		High Frequency Pulse Amplitude (N)		
	Baseline, No Effects	1/3 Peak Amplitude 2300	2/3 Peak Amplitude 2600	Peak Amplitude 2900
High Frequency Pulse Frequency (Hz)	4× Main Wave 20	1A	1B	1C
	7× Main Wave 35	2A	2B	2C
	10× Main Wave 50	3A	3B	3C

deviation of the crack path direction following the occurrence of the HF pulse, where strain fields surrounding the crack tip can be taken into consideration to understand the origin of the deviation. Finally, the experiments in Table 1 can be expanded to obtain higher fidelity of data post the application of the high frequency pulse.

Conclusions

Existing models, like the Wheeler, Willemborg, and variations of these, have been utilized to predict the crack growth behavior with varying degrees of success. In this study, we created experimental matrices to explore the effects of overload/underload combinations on fatigue crack growth in 5xxx aluminum, typically used in marine applications. Both visual inspection of crack tip location, and using Digital Image Correlation (DIC) techniques for characterization of the crack tip deformation fields. These techniques were used on a designed center crack tension (CCT) panel specimens to measure

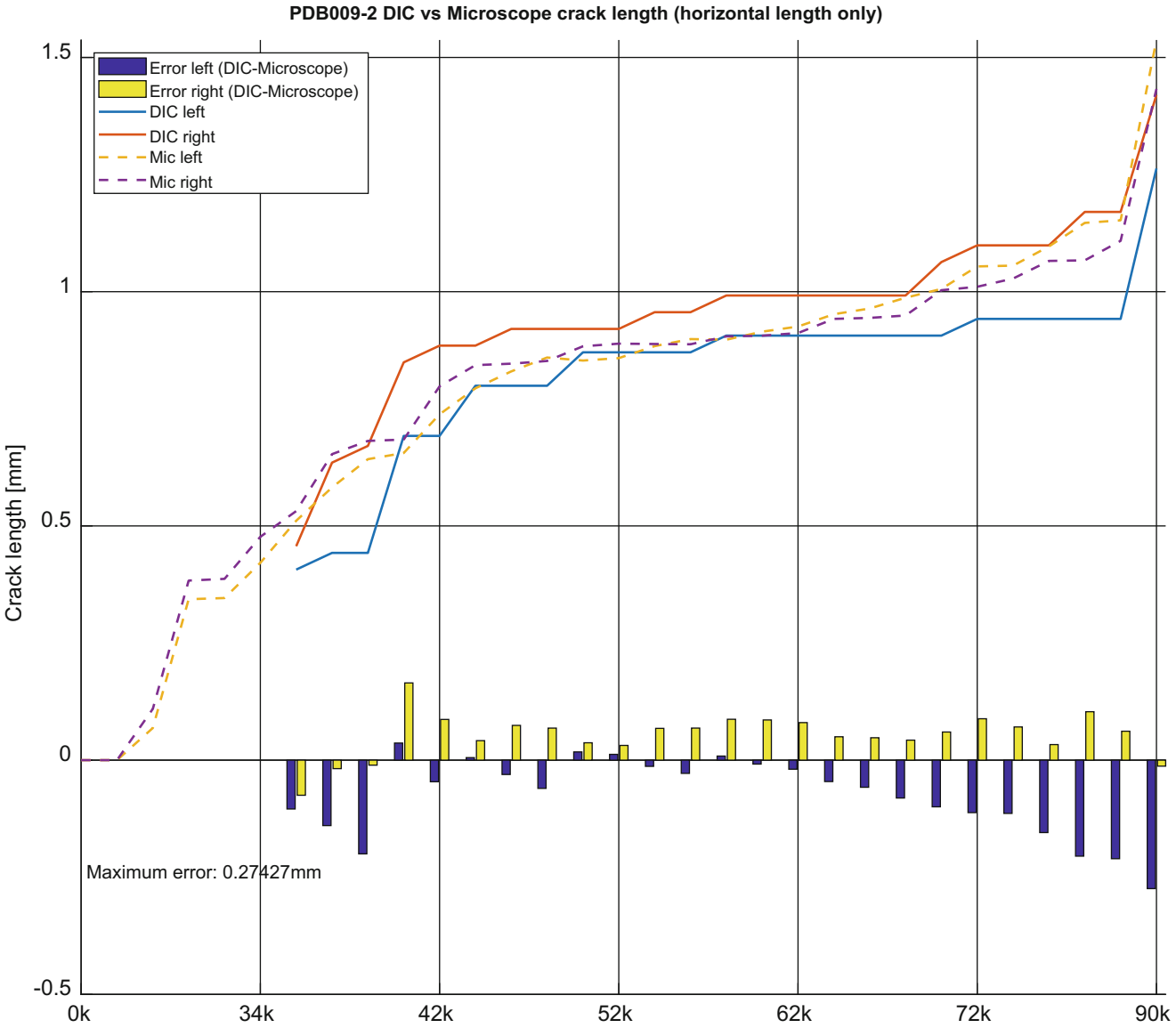

Fig. 13 comparison of DIC and microscope crack length, Block 2C at HF of 35 Hz and Peak Amplitude of 2900 N

crack growth. DIC techniques also enabled additional analysis of strain fields to elucidate on the conditions responsible for the change in the crack growth behavior. The development of the experimental protocol was critical for capturing the desired output data for DIC and microscope measurements, and observe the behavior of the plastic zones surrounding the crack tip. Several experiments were conducted until a finalized methods that captured the required data was developed. Unique MATLAB algorithms provided a means to develop innovative approaches to automatically capture the crack tip location and display it along with observed behavior around the crack tip. The next phase of this work includes utilizing this observed data to elucidate the mechanics of crack growth behavior when affected by an embedded high frequency load models for fatigue crack growth.

Acknowledgements Work described was performed by the Naval Surface Warfare Center Carderock Division's Survivability, Structures, Materials Department, and University of Maryland College Park's Department of Mechanical Engineering. Financial and technical support was provided by an NSWCCD In-house Laboratory Independent Research (ILIR) program under Dr. Jack Price, and a grant provided to UMD by program officer Dr. Paul Hess of the Office of Naval Research Code 331 under grant number N000141812016.

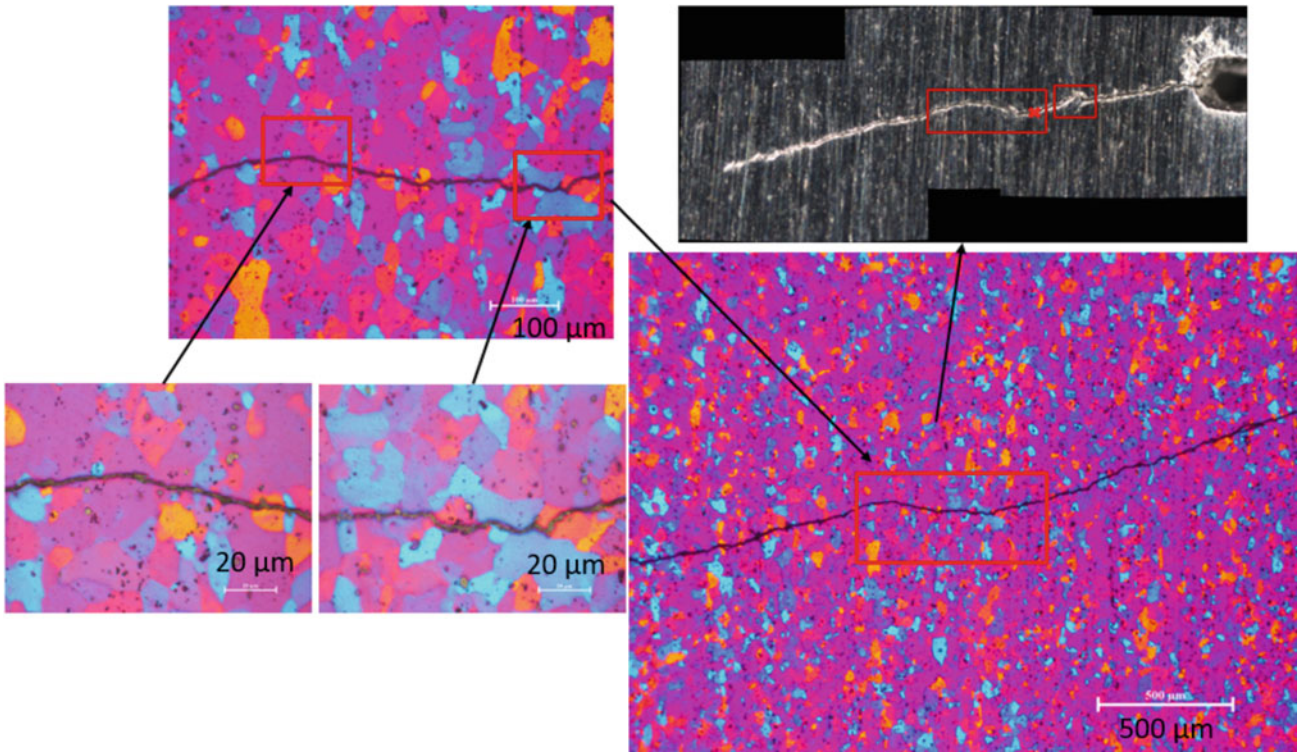

Fig. 14 Barkers Etch of Specimen, Block 2C, HF at 35 Hz and 2900 N

References

1. R. Murthy, G. Palani, N. Iyer, State-of-the-art review on fatigue crack growth analysis under variable amplitude loading. J Inst Eng (India) **85**, 118–129 (2004)
2. Y. Sumi, Fatigue crack propagation in marine structures under seaway loading. Int. J. Fatigue **58**, 218–224 (2014)
3. W. Fricke, H. Paetzold, Experimental Investigations on Fatigue Damage of Ship Structures Caused by Whipping Stresses, in *PRADS*, (Korean Society of Naval Architects, Changwon City, 2013)
4. D. Hart, H. Bruck, Characterization and modeling of low modulus composite patched center crack tension specimen using DIC surface. Fracture Fatigue Failure Damage Evolution **6**, 31–43 (2018). in Society of Expermiental Mechanics
5. ASTM-E8, *ASTM E8M-08: Standard Test Methods for Tension Testing of Metallic Materials* (ASTM International, Conshohocken, 2008)
6. ASTM-E466, *ASTM E466–07: Standard Practice for Conducting Force Controlled Constant Amplitude Axial Fatigue Tests of Metallic Materials* (ASTM International, Conshohocken, 2007)
7. ASTM-E647, *Standard test method for measuring fatigue crack growth rates* (ASTM International, Conshohocken, 2015)
8. ASTM-E338, *Standard Test Method of Sharp-Notch Tension Testing of High-Strength Sheet Materials* (ASTM International, Conshohocken, 2003)
9. M. Sutton, J.-J. Orteu, H. Schreier, *Image Correlation for Shape, Motion, and Deformation Measurements* (Springer LLC, New York, NY, 2009)
10. E. Jones, *Good Practices Guide for Digital Image Correllation* (International Digital Image Correllation Society, Portland, OR, 2018)
11. J. Bannantine, J. Comer, J. Handrock, *Fundamentals of Metal Fatigue Analysis* (Prentice Hall Inc, Upper Saddle River, NJ, 1990)
12. O. Wheeler, Spectrum loading and crack growth. J. Basic Eng. **94**, 181–186 (1972)
13. J. Willenborg, R. Engle, H. Wood, *A crack growth retardation model using an effective stress concept, AFFDL TM-71-1-FBR, Jan 1971*, (1971)
14. M. Mehrzadi, F. Taheri, A material sensitive modified wheeler model for predicting the retardation in fatigue response of AM60B due to an overload. Int. J. Fatigue **5**, 220–229 (2013)
15. F. Chen, F. Wang, W. Cui, Fatigue life prediction of engineering structures subjected to variable amplitude loading using the improved crack growth rate model. Fatigue Fract Eng Mater Structures **35**, 278–290 (2012)
16. H. Bruck, *Analysis of 3-D Effects near the Crack Tip on Rice's 2-D J-Integral Using Digital Image Correllation and Smoothing Techniques*, M.S. Thesis, Univeristy of South Carolina, (1989)
17. J. Yates, Y. Zanganeh, Quantifying crack tip displacement fields with DIC. Eng. Fract. Mech. **77**, 2063–2076 (2010)
18. E. Gdoutos, *Fracture Mechanics, An Introduction, Second Edition* (Springer, Minneapolis, 2005)
19. E. Cerri, E. Evangelista, *Metallography of Aluminum Alloys* (Mechanical Engineering Department, European Aluminum Association, Ancona-Italy, 1999)
20. R. Ritchie, Mechanisms of fatigue crack propagation in metals, ceramics and composites: role of crack tip shielding. Mater. Sci. Eng. **A103**, 14 (1988)

Exploring Microstructural Descriptors in Elastomeric Foams Using Digital Image Correlation and Statistical Analysis

Robert F. Waymel, Sharlotte L. B. Kramer, Dan S. Bolintineanu, Enrico C. Quintana, and Kevin N. Long

Abstract In this work, we investigated microstructural features of elastomeric foam with the goal of identifying descriptors other than porosity that have a significant effect on the macroscale mechanical response. X-ray computed tomography (XCT) provided three-dimensional images of several flexible polyurethane foam samples prior to mechanical testing. The samples were then compressed to approximately 80% engineering strain. Stereo digital image correlation was used to measure the three-dimensional surface displacement data, from which strain was determined. The strain data, which were calculated with respect to the undeformed coordinates, were then overlaid on the corresponding surface generated from XCT. Heterogeneities in the strain-field were cross-correlated with topological quantities such as pore size distribution. A statistically significant correlation was identified between the distance transform of the pore phase and strain fluctuations.

Keywords Flexible polyurethane foam · x-ray computed tomography · Stereo digital image correlation · Microstructural analysis · Cross-correlation

Introduction

Elastomeric foams, defined as cellular solids that operate well above the glass transition temperature of their polymer matrix, are used for impact protection in applications ranging from sports equipment to packaging. A thorough understanding of elastomeric foams at large deformations and different strain rates is necessary to ensure adequate protection. The relative density of the foam, that is, the density of the foam divided by the density of the solid polymer matrix material, is considered the most important structural characteristic of foams. While the relative density provides general insight into cell wall thickness, it does not precisely indicate when the deformation mode (which affects the overall mechanical response) of the cell wall transitions (e.g. from bending to buckling). Current models for elastomeric foams are generally empirical and assume an isotropic strain energy function. Yet, many foams exhibit mechanical anisotropy since their cells are elongated along the foam rise direction during fabrication. In this work, we seek microstructural descriptors besides the relative density that significantly influence the macroscopic mechanical response with the eventual goal of developing a physically motivated constitutive relationship.

Methods and Analysis

General Plastics supplied the LAST-A-FOAM® TF6070 series flexible polyurethane foam tested in this work. Cubical samples with dimensions 25.4 × 25.4 × 25.4 mm^3 were manufactured via water jet cutter from a sheet with thickness 25.4 mm. Prior to loading, x-ray computed tomography (XCT) generated volumetric images of the samples with a resolution of 29 μm/voxel. Black spray paint was used to speckle the samples, so they could be analyzed with digital image correlation. The samples were then compressed in an MTS Bionix Tabletop Test System to 80% engineering strain and two Point Grey cameras recorded the deformation. Stereo digital image correlation (DIC) measured the 3D surface displacement, from which the full-field strain was calculated with respect to the undeformed coordinates (i.e., Lagrangian description). Figure 1a shows the axial (i.e., aligned with the axis of compression) strain field at 70% engineering strain on the deformed specimen while Fig. 1b displays the strain field on the undeformed sample. The virtual strain gage size, the area over which strain is averaged

R. F. Waymel (✉) · S. L. B. Kramer · D. S. Bolintineanu · E. C. Quintana · K. N. Long
Sandia National Laboratories, Albuquerque, NM, USA
e-mail: rwaymel@sandia.gov

M. Silberstein et al. (eds.), *Challenges in Mechanics of Time Dependent Materials, Fracture, Fatigue, Failure and Damage Evolution, Volume 2*, Conference Proceedings of the Society for Experimental Mechanics Series, https://doi.org/10.1007/978-3-030-29986-6_6

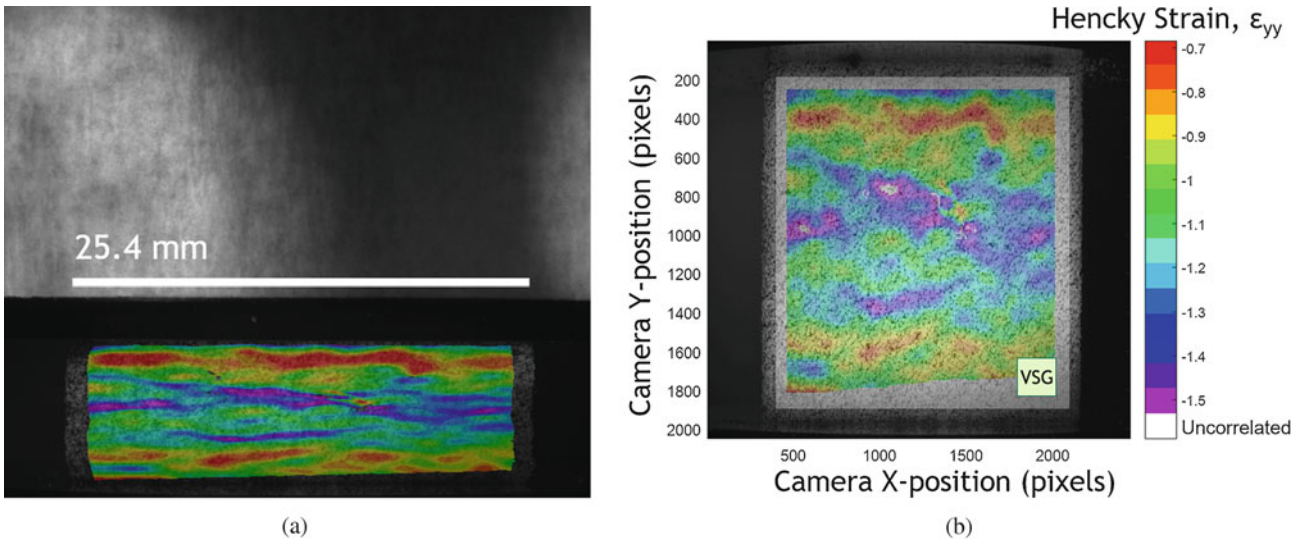

Fig. 1 Axial strain field at 70% engineering strain overlaid on the (**a**) deformed sample and (**b**) reference image. The color bar represents the same values in (**a**) and (**b**)

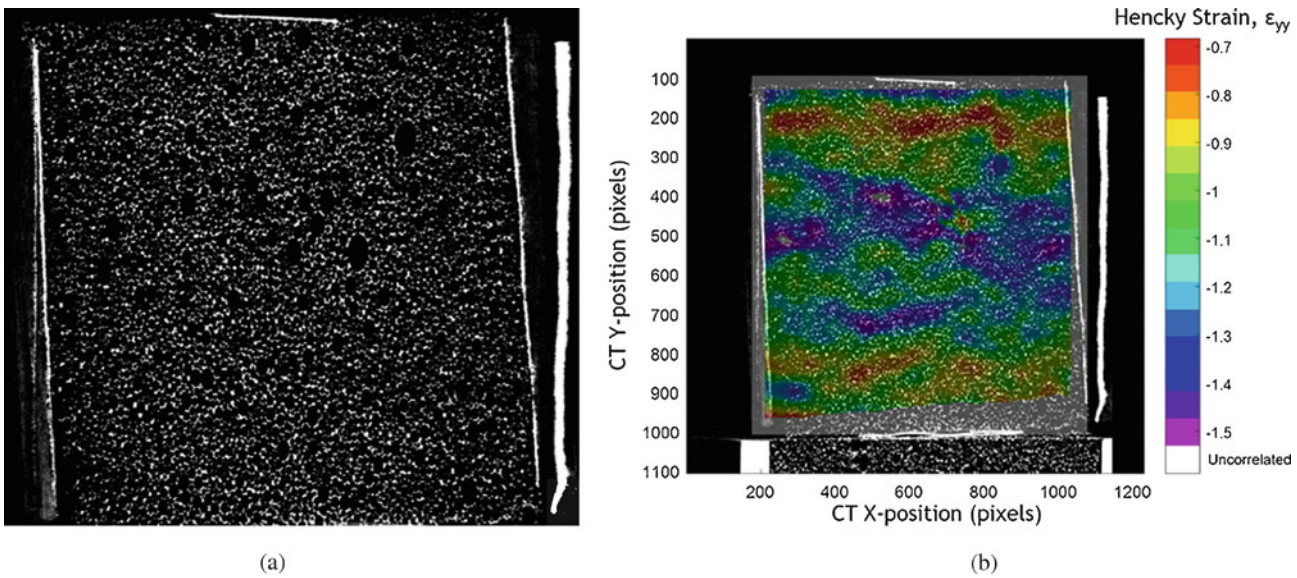

Fig. 2 (**a**) XCT generated slice shows the microstructure of the surface where strain data was captured. (**b**) Strain data overlaid on the slice

in DIC, is displayed in Fig. 1b and is 191 × 191 px^2, which is equivalent to 2.66 × 2.66 mm^2. The strain field in Fig. 1 is represented in terms of the Hencky, or logarithmic, strain.

Figure 2a shows one slice from XCT that corresponds to the surface where the DIC analysis occurred. The coordinates of the DIC contour map and the XCT slice are different due to a translation offset and a difference in resolutions, so the DIC coordinates were altered such that the strain map could be plotted on top of the CT slice, as is done in Fig. 2b. Once the strain data and the XCT-generated volumetric image shared common coordinates, statistical analysis was performed to determine if the axial strain was correlated with any microstructural descriptors.

A common practice in statistical analysis is to standardize the data set in which the mean of the data set is subtracted and the difference is then divided by the standard deviation. Subtracting the mean allows us to investigate the fluctuations in the data while dividing by the standard deviation non-dimensionalizes the quantity of interest and allows for a better comparison with some other quantity that would otherwise have different units (e.g., comparison of strain fluctuation with pore size fluctuation). The standardized strain was compared with microstructural features such as the distance transform of the pore phase. The distance transform is an operation that modifies a digital image such that points that are further from a

border (the polymer matrix phase in the case of polyurethane foams) have higher intensity than regions closer to a border. A distance transform of the pore phase in a foam would assign higher intensities to the interior of large pores than the interior of small pores. A statistically significant correlation was identified between the strain field and the distance transform in which regions surrounding large pores exhibited larger compressive strains than regions around smaller pores.

Conclusion

Statistical analysis was used to cross-correlate features imaged by XCT with strain fields calculating with stereo DIC. The cross-correlation revealed statistically significant correlations between the strain field and the distance transform whereby larger pores corresponded to greater negative strain and smaller pores correlated to smaller negative strain.

Acknowledgements Sandia National Laboratories is a multi-mission laboratory managed and operated by National Technology & Engineering Solutions of Sandia, LLC, a wholly owned subsidiary of Honeywell International, Inc., for the U.S. Department of Energy's National Nuclear Security Administration under contract DE-NA0003525.

Effect of Crystallization on Mechanical Properties of CFRTP

Takenobu Sakai and Nur Safiah Binti Shamsudim

Abstract Carbon fiber reinforced thermoplastics are consisted with the carbon fiber and thermos plastics such as PP, PA6, PI, and PC and so on. Mechanical properties, especially viscoelasticity, of CFRTP were depended on the matrix resin, therefore, if the mechanical properties of matrix resin has changed, CFRTP's properties will be also changed. In this study, carbon fiber reinforced polyamide 6 was used for evaluate the effect of crystallization. The materials were heat treated for crystallization, and the crystallization was controlled by heat treatment time. As the result of dynamic mechanical analysis, storage modulus was decreased with the increase in the heat treatment time, however, longer heat treatment time made the storage modulus increased. As the results of DSC measurement, the peak shape of melting point was different each other. The double peak was observed with the longer heat treatment time, however, the single peak was observed with the short heat treatment time. This is because the mechanical properties of CFRTP was dominated by the peak shape and peak area of the melting point.

Keywords Carbon Fiber Reinforced Thermoplastics · Polyamide 6 · DSC · DMA · Crystallization

Introduction

The carbon fiber reinforced thermosetting composite material is CFRP, which is a composite material of carbon fiber and resin and uses a thermosetting resin as a base material. On the other hand, the carbon fiber reinforced thermoplastic composite material is CFRTP, using a thermoplastic resin as a base material. Although CFRTP has the disadvantage of low heat resistance, it has the advantage that it can be remolded and the molding cost is low. Taking advantage of these characteristics, CFRTP attracts attention in various fields such as electric and electronic industry, automobile industry, home appliance manufacturer and furniture manufacturer, medical technology, sporting goods manufacturer, shoe manufacturer and baggage industry.

Among the resins of CFRTP which have been used in recent years, Polyamide 6 (PA6) is a crystalline polymer, a resin which crystallizes. In general, it is known that when crystallized, the strength and elastic modulus change as the degree of crystallinity increases, but the influence of not only crystallinity but also crystal state on the mechanical properties of CFRTP has not been clarified.

Background

Klata et al. reported the DSC investigation of Polyamide 6 with the glass fibers, and the results show that the Polyamide 6 and their composites have the two types of different crystal conditions as α and γ forms [1]. Therefore, the mechanical behavior also affected by the different crystal conditions. Hyo et al. investigated the mechanical and thermal properties of long carbon fiber-reinforced polyamide 6 composites. They showed the results of tensile properties and dynamic viscoelastic properties, however, they had not been related to the different crystal conditions [2].

Therefore, in this study, in order to understand the influence of crystallization of CFRTP using PA6 as a base material on the static and dynamic bending property, a static 3-point bending test and a dynamic mechanical analysis (DMA) were conducted on various heat treated test pieces, and the effect of crystallization is evaluated on static and dynamic bending properties using strength and each modulus.

T. Sakai (✉) · N. S. B. Shamsudim
Graduate School of Science and Engineering, Saitama University, Saitama, Japan
e-mail: sakai@mech.saitama-u.ac.jp

M. Silberstein et al. (eds.), *Challenges in Mechanics of Time Dependent Materials, Fracture, Fatigue, Failure and Damage Evolution, Volume 2*, Conference Proceedings of the Society for Experimental Mechanics Series, https://doi.org/10.1007/978-3-030-29986-6_7

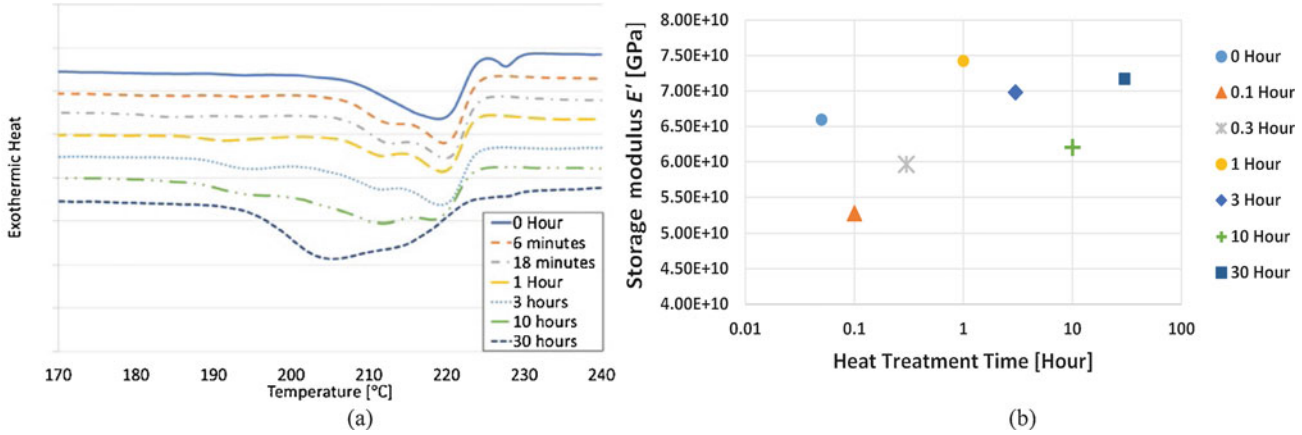

Fig. 1 DSC results (**a**) and storage modulus E′ (**b**) of CFRTP with different heat treatment time

DSC Results

DSC measurement was carried out using DSC-60 Plus (SHIMADZU) in order to ascertain the crystalline state. Figure 1(a) shows the melting point of DSC measurement results of CFRTP subjected to various heat treatments. The vertical axes are translated in the direction of the vertical axis and are displayed side by side. It was confirmed that the DSC curve of CFRTP not subjected to heat treatment has a peak only at 220 °C and the crystal structure shows a single structure. The same tendency is observed in the heat treatment for 0.1 h, but a slight peak is observed around 210 °C, indicating a secondary crystal structure. It was similar to the tendency of heat treatment for 0.1 h even in heat treatment for 0.3 h and 1 h. However, in the heat treatment for 1 h, a slight peak was observed at around 190 °C, and it was confirmed that it showed a tertiary crystal structure. In the heat treatment at 3 h and 10 h, it was the same as 1 h of heat treatment. In the heat treatment for 30 h, a peak was observed at 205 °C unlike other heat treatment time. This result is different from the pure PA6's data, therefore, existence of carbon fiber made the crystal structure of PA6 as different structure.

A graph of storage modulus at 50 °C is shown in Fig. 1(b). The vertical axis shows the storage modulus and the horizontal axis shows the logarithm of heat treatment time. From this graph, it shows that the storage Modulus decreased in the heat treatment condition up to 0.3 h, then increased once in the heat treatment for 1 h, then decreased again. Finally, the value increased again for 30 h. As explained in the previous section, the crystal structure changes with primary crystal, secondary crystal and tertiary crystal by heat treatment. The results of the static three-point bending test corresponded well with the change of the crystal structure.

Conclusion

In this study, we investigated the effect of crystal structure on the dynamic viscoelastic property. The crystal structure was changed with the heat treatment, and the existence of carbon fiber made the crystal structure as different from PA6. The value of storage modulus was changed with the crystal structure changed, therefore, the viscoelastic properties of CFRTP was effected by their crystal structure of matrix resins.

References

1. E. Klata, K.V. de Velde, I. Krucinska, DSC investigations of polyamide 6 in hybrid GF/PA 6 yarns and composites. Polym. Test. **22**, 929–937 (2003)
2. H. An, J. Kim, K.-Y. Kim, et al., Mechanical and thermal properties of long carbon fiber-reinforced polyamide 6 composites. Fiber Polym **15**, 2355–2359 (2014)

Mode I Traction-Separation Relationship of Sylgard 184: Aluminum Interface Using Rigid Double Cantilever Beam Analysis

Sreehari Rajan, Michael A. Sutton, William McMakin, Mike Steinzig, Laura Inkret, Elsa Compton, and Amanda Olsen

Abstract For soft adhesives, a Rigid Double Cantilever Beam (RDCB) experiment has recently been shown to be a convenient way for extracting traction-separation (σ-δ) relationships. An implicit expression of the σ-δ relationship is derived by Brock et al. (J. Adhesion, 2018) assuming small rotation of the beams and a linear traction separation relationship in the compressive zone. In this work, an explicit expression of the σ-δ relationship for a Rigid Double Cantilever beam (RDCB) for large deformation of the adhesive including the effect of a compressive zone ahead of the cohesive zone is used for direct extraction of σ-δ relationship. The expression for the σ-δ relationship is in terms of quantities that can be directly measured using the full-field deformation measurement technique, StereoDIC. Using RDCB analysis, the traction at the Sylgard 184-aluminum interface where adhesive failure occurs is obtained by simultaneous measurement of separation of the adherends at the crack tip, separation at the end of the compressive zone (far end of the beam ahead of the crack tip) and load. The true separation of the crack surfaces at the interface is obtained by measuring δ, the relative displacement of two points separated by 0.05 mm across the interface. It is shown that the compressive zone in the adhesive has a significant effect on the σ-δ relationship. The maximum traction and maximum separation are found to be 0.33 MPa and 5.5 μm respectively. The energy release rate obtained by calculating the area under the σ-δ curve is 1.13 J/m^2.

Keywords Rigid Double Cantilever beam · Traction-separation · Cohesive zone · Soft adhesive · Sylgard · StereoDIC

Introduction

Cohesive zone modelling (CZM) is extensively used in the simulation of nonlinear fracture processes for adhesives due to its effectiveness in modeling adhesive fracture where the process zone size is much larger than the transverse dimensions of the fracture specimen. The concept of CZM was introduced in the independent work of Dugdale [1] and Barenblatt [2]. The works of Needleman [3] and Knauss [4] describing the process of void nucleation and decohesion in an isotropically hardening, elastic-viscoplastic matrix were instrumental in development of finite element based CZMs to describe the process of void nucleation and decohesion in an isotropically hardening, elastic-viscoplastic matrix. In the CZM approach, the stress singularity at the crack tip is eliminated by considering cohesive tractions acting on fictitious cohesive surfaces to close the crack faces. The constitutive law required in modeling of fracture using a CZM is the relation between traction on the cohesive surfaces, σ, and relative separation between the surfaces, δ, and are commonly known as σ-δ relationships. A variety of test methods such as blister tests, peel tests and double cantilever beam experiments are used for deriving energy release rate and the σ-δ relationship for a variety of adhesives. Due to its simplicity and the existence of a closed form solution for the J integral, the DCB test geometry is commonly used for measurement of energy release rate and σ-δ. For example, Sorensen et al. [5] showed that the J integral for the DCB geometry can be obtained by simultaneous measurement of load and root rotation of the DCB at the crack tip location. The σ-δ relationship can then be obtained by numerical differentiation of the J integral with respect to δ. The closed form expression of the J integral in term of the experimentally measurable

S. Rajan (✉) · M. A. Sutton · W. McMakin · E. Compton
Department of Mechanical Engineering, University of South Carolina, Columbia, SC, USA
e-mail: sreehari@email.sc.edu

M. Steinzig · L. Inkret · A. Olsen
Los Alamos National Laboratory, Los Alamos, NM, USA

M. Silberstein et al. (eds.), *Challenges in Mechanics of Time Dependent Materials, Fracture, Fatigue, Failure and Damage Evolution, Volume 2*, Conference Proceedings of the Society for Experimental Mechanics Series, https://doi.org/10.1007/978-3-030-29986-6_8

quantities[1] such as load, root rotation and opening displacement has made this a popular method for direct extraction of traction-separation relation of structural adhesives.

One of the assumptions used in the derivation of J integral expression is that the far end of the beam away from the crack tip remains unloaded, which is true for most structural adhesives when the length of the beam is sufficiently long. However, when stiff adherends are used with soft biological adhesives and elastomers having very low modulus, the far end of the beam may experience finite displacements and the far end of the beam cannot be assumed to be stress free. Dastjerdi et al. [7, 8] has shown an alternate approach for extraction of σ-δ relationships for soft biological adhesives using a rigid double cantilever beam assumption. In their work the authors assumed the beam to be rigid, with all the energy stored in the adhesive. They have shown that using the RDCB analysis, the σ-δ relationship can be obtained using simultaneous measurement of the load and load point displacement. In their work, the authors did not include the effect of a small compressive zone at the end of the beam. For their studies, exclusion of the effect of a compressive zone does not significantly affect the accuracy of their results for either of very thin adhesives or soft biological materials which has negligible resistance to compression.

Brock et al. [9] further extended the RDCB analysis by considering the effect of compression of the adhesive at the end of the beam. In their analysis of the RDCB, the authors considered a point of rotation of the beam to define the tensile to compressive transition point and derived an implicit expression for obtaining σ-δ relationship and solved numerically. The derivation of a σ-δ law using their analysis requires knowledge of σ-δ relationship in the compressive region. In our work, we have derived an explicit form for the σ-δ relationship in terms of the end displacements of the beam[2] (at the crack tip and far end of the beam) and load. The derivation is based on an arbitrary σ-δ relationship while making no assumption of the form of σ-δ in the compressive zone, except that the σ-δ response of the material is continuous from compression to tension. The effect of large rotation of the beams is also included in the derivation and an expression for small rotations similar to the expression in [8] is deduced, where it is shown that the presence of a compressive zone can be expressed as a correction term added to Eq. (1) in [8].

$$\sigma\left(\delta\right) = \frac{L}{\left(L-a\right)^2}\left\{\delta\frac{dP}{d\delta} + 2P\right\} \tag{1}$$

Section "Explicit Form of σ-δ Relationship for RDCB Specimen" of this paper discussed the details of the derivation of the explicit form of the σ-δ relationship for Mode I loading. Then the σ-δ relationship for a soft elastomer (Sylgard-184) obtained using the RDCB methods is presented in section "Experimental Method" followed by conclusion and acknowledgements.

Explicit Form of σ-δ Relationship for RDCB Specimen

Derivation of the σ-δ relationship for the RDCB specimen shown in Fig. 1 is based on the same principles as in [8] and [9], using statics to obtain force and moment equilibrium equations.

Details of the derivation can be found in our recently published work on σ-δ relationship of uncured thermoset flows [12].

The general expression of σ-δ relationship including large angle of rotation of the beams and compressive stresses at the far end of the beam is given in Eq. (2).

where δ is the separation of the adherend interface at the crack tip and δ_c is the relative displacement of the adherend interface in the negative y direction at the far end of the beam, L is the length of the beam from far end to load point, a is the initial crack length and θ is the average rotation of the top and bottom beam.

$$\sigma\left(\delta\right) = \frac{L}{L-a}\left\{\tan\theta\frac{dP}{d\delta} + \frac{P}{\cos^2\theta}\frac{d\theta}{d\delta}\right\} + \frac{P}{\delta+\delta_c}\tan\theta\frac{d\Delta}{d\delta} \tag{2}$$

When the rotation of the beam is small, the angle θ can be approximated by, $\theta \sim \frac{\delta+\delta_c}{L-a}$, hence for small rotation of the beam the σ-δ relationship in Eq. (2) can be approximated as shown in Eq. (3).

$$\sigma\left(\delta\right) = \frac{L}{\left(L-a\right)^2}\left\{\delta\frac{dP}{d\delta} + 2P\right\} + \frac{L}{\left(L-a\right)^2}\left\{\frac{d\left(P\delta_c\right)}{d\delta} + \frac{Pa}{L}\frac{d\delta_c}{d\delta}\right\} \tag{3}$$

[1] It has been shown that the root rotation and opening displacement can be measured using StereoDIC [6].

[2] Using digital image correlation full filed information of displacement and rotation of the beam can be obtained [10–11].

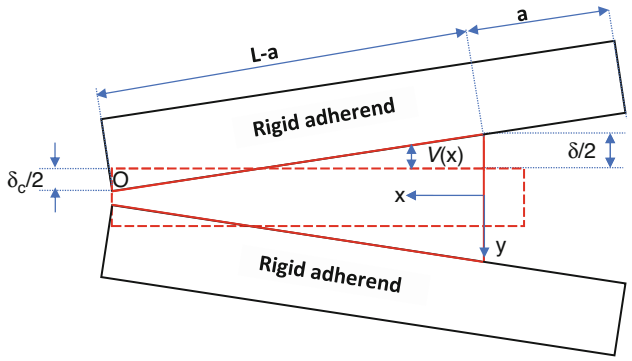

Fig. 1 Schematic of the RDCB specimen showing deformation of the adhesive layer; the red dotted line represents reference position of the adhesive layer and solid line shows the deformed position of the adhesive layer

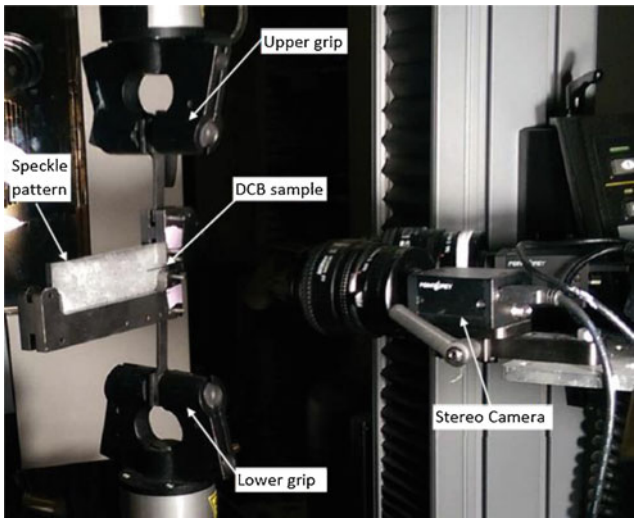

Fig. 2 Mode 1 rigid DCB Experimental set up

The first term in the bracket on RHS of Eq. (3) is the exact expression for $\sigma(\delta)$ as derived in [8] assuming zero compressive zone length ahead of the cohesive zone. Hence the second term in Eq. (3) can be viewed as a correction term due to a finite compressive zone ahead of the cohesive zone. Equation (3) gives an explicit representation of the σ-δ relationship in the cohesive zone in term of the geometric dimensions of the beam, load and displacement at the crack tip and far end of the beam.

Experimental Method

The fracture experiment is conducted for nominally Mode I loading with a load line displacement rate of 5 μm/s using an Instron 5566 test frame with a 5 kN load cell. A photograph of the complete experimental set up is shown in Fig. 2. The RDCB consists of two aluminum 6061 adherends, and SYLGARD™ 184 (manufactured by Dow Corning Corporation) joining the two adherends. The aluminum beam has a Young's Modulus of 70 GPa, height of 19 mm, width of 6.5 mm and length of 127 mm. The bonded length of the adhesive is 120 mm, initial crack length $a = 0$, and thickness of the adhesive is 0.5 mm. The stiffness of the aluminum adherend is at least four orders of magnitude higher than the adhesive, hence a rigid beam analysis is employed to determine σ-δ for the material.

Sample Preparation

The DCB samples are manufactured after preparing the faying surfaces of the aluminum adherends. Initially, the adherends' faying surfaces are polished using 600-grit sand paper. Followed by cleaning in acetone and then isopropyl alcohol to remove residues left after polishing. Compressed air is used to remove excess cleaning solution. After surface preparation, a 0.500 mm thick shim is placed between the top and bottom adherends and laid horizontally on a flat plate. The shims serve to obtain a uniform thickness of adhesive. The adhesive (SYLGARD™ 184) is prepared by mixing constituents and then degassing in a vacuum chamber. After degassing, the adhesive is immediately poured in the gap between the adherends using a syringe. The adhesive flows in the gap with the aid of gravity. A fixture is used to press the adherents tightly in place while pouring the adhesive to prevent them from being separated due to the pressure of the adhesive in the gap. The adhesive is then cured for 12 h at room temperature.

StereoDIC Set Up

After the adhesive has been cured, a random speckle pattern is applied to one side of the surface of the adherends for DIC measurements. The speckle pattern is applied by initially coating the surface with a thin layer of white paint using an airbrush and then applying an overcoat of black paint using the airbrush with a 0.2 mm tip. This resulted in an average speckle size of 0.25 mm. Two 5 MP CCD cameras with pixel size of 3.45 μm manufacture by Point Grey and 28 mm Nikon lens are used to capture synchronized stereo images of the speckle pattern along with load measurement. An LED lighting with intensity of 4000 lumens is used to illuminate the sample. The magnification of the stereo vision system is 20 μm/pixel. Thus, each average speckle is sampled by 12 pixels, providing more than adequate oversampling for accurate measurements. The position of the cameras is arranged so that crack tip is approximately at the center of the field of view. The subset size, step size and strain filter size used in all the DIC analyses are 29 pixels, 1 pixel, and 5 × 5 data points respectively. The commercial DIC software from correlated solutions (VIC 3D) [13] is used in all the DIC analysis.

Results and Discussion

Variation of load with δ at the crack tip (P vs. δ), separation of the adherends at the far end, δ_c, versus separation at the crack tip (δc vs. δ) and average in-plane rotation of the top and bottom adherends versus separation at the crack tip are shown in Fig. 3a–c respectively. The derivative of these variables with δ is also plotted in Fig. 3. From Fig. 3a, it is observed that $\frac{d\delta_c}{d\delta}$ decreases with δ indicating that the cohesive zone size is increasing with increase in δ. Also, the point of rotation of the beam moves towards the far end of the beam. Figure 3c shows that the angle of rotation of the beam is less than 6×10^{-4} rad. Hence Eq. (3) with small angle approximation is used to determine the traction along the crack surface. Since separation is observed occur at the interface between the aluminum and Sylgard interface, the crack opening displacement for the material, δ_*, can be obtained by subtracting the elastic deformation of the Sylgard from separation of the adherends (δ). In this work, δ_* is obtained by measuring the relative displacement of two points separated by a distance of 0.05 mm across the interface. The traction versus separation of the crack surfaces, is shown in Fig. 4. The maximum traction is shown to be 0.33 MPa and the maximum separation at the end of the cohesive zone is 5.5 μm. The σ-δ relationship obtained *without* considering the compressive zone (Eq. (1)) is significantly different from the value obtained using Eq. (3). Using Eq. (1), the maximum traction obtained is 50% lower than that from Eq. (3).

The area under the σ-δ curve gives the critical energy release rate, $J_c = 1.13$ J/m^2. Such a low value of the interface toughness of the Sylgard (PDMS) is also observed by Sofla et al. [14] where they observed a nominal toughness of 0.2 J/m^2 for PDMS-glass interface from blister experiments. It is conjectured that the higher value of J_c for the Sylgard -Aluminum interface compared to the Sylgard-glass interface could be due to aluminum surface roughness.

Conclusion

An explicit expression for the σ-δ relationship is derived for the RDCB specimen for a general case of large rotation of the adherends and the presence of a compressive zone ahead of the cohesive zone region. It is also shown that the constitutive

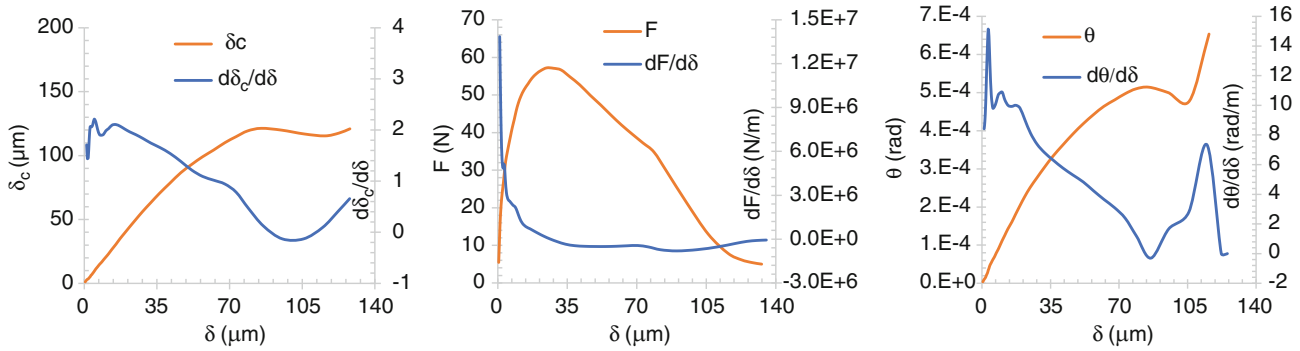

Fig. 3 (**a**) Variation of δ_c vs. δ, and derivative of δ_c vs. δ (**b**) F vs. δ and derivative of F vs. δ, (**c**) θ vs. δ and derivative of θ vs. δ

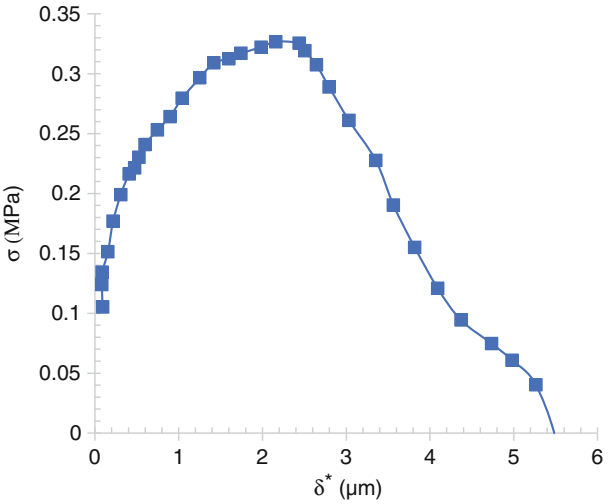

Fig. 4 Traction-separation relationship of the Sylgard 184- aluminum interface obtained using RDCB analysis

relationship of the adhesive for both tensile and compressive region in the adhesive can be simultaneously obtained from a single experiment. Prior knowledge of the shape of the σ-δ relationship or the stiffness of the adhesive is not required for determination of the σ-δ relationship. The σ-δ relationship can be obtained from simultaneous measurement of separation of the adherends at the crack tip, separation at the far end of the beam ahead of the crack tip, and load. Using the RDCB analysis, the σ-δ relationship for a Sylgard -aluminum interface is obtained, with the maximum traction $\sigma = 0.33$ MPa. For interface crack growth, the crack surface opening displacement is obtained by measuring the relative displacement of two points that are separated by a distance of 0.05 mm across the separation interface. The critical energy release is measured to be 1.13 J/m^2 which is found to be six times higher than the interface toughness of Sylgard-glass interface obtained previously via a blister test [14]. The higher energy release rate for the Sylgard -aluminum interface is conjectured to be related to the surface roughness of the aluminum surface when compared to glass.

References

1. D.S. Dugdale, Yielding of steel sheets containing slits. J. Mech. Phys. Solids **8**(2), 100–104 (1960). https://doi.org/10.1016/0022-5096(60)90013-2
2. G.I. Barenblatt, The mathematical theory of equilibrium cracks in brittle fracture. Adv. Appl. Mech. **7**, 55–129 (1962). https://doi.org/10.1016/S0065-2156(08)70121-2
3. A. Needleman, A continuum model for void nucleation by inclusion debonding. J. Appl. Mech. **54**(3), 525–531 (1987). https://doi.org/10.1115/1.3173064
4. T. Ungsuwarungsri, W.G. Knauss, The role of damage-softened material behavior in the fracture of composites and adhesives. Int. J. Fract. **35**(3), 221–241 (1987). https://doi.org/10.1007/BF00015590

5. B.F. Sørensen, T.K. Jacobsen, Determination of cohesive laws by the J integral approach. Eng. Fract. Mech. **70**, 1841–1858 (2003). https://doi.org/10.1016/S0013-7944(03)00127-9
6. S. Rajan, M.A. Sutton, R. Fuerte, A. Kidane, Traction-separation relationship for polymer-modified bitumen under mode I loading: double cantilever beam experiment with stereo digital image correlation. Eng. Fract. Mech. **187**, 404–421 (2018). https://doi.org/10.1016/j.engfracmech.2017.12.031
7. A.K. Dastjerdi, M. Pagano, M.T. Kaartinen, M.D. McKee, F. Barthelat, Cohesive behavior of soft biological adhesives: experiments and modeling. Acta Biomater. **8**, 3349–3359 (2012)
8. A.K. Dastjerdi, E. Tan, F. Barthelat, Direct measurement of the cohesive law of adhesives using a rigid double cantilever beam technique. Exp. Mech. **53**(9), 1763–1772 (2013)
9. W. Brock, L. Chi-Hsiang, J.W. Michael, S.C. Duane, Mode I traction-separation measured using rigid double cantilever beam applied to structural adhesive. J. Adhesion. (2018). https://doi.org/10.1080/00218464.2018.1502666
10. M.A. Sutton, S.R. McNeill, J.D. Helm, Y.J. Chao, Advances in two-dimensional and three-dimensional computer vision, in *Photomechanics. Topics in Applied Physics*, ed. by P. K. Rastogi, (Springer, Berlin, Heidelberg, 2000), pp. 323–372. https://doi.org/10.1007/3-540-48800-6_10
11. M.A. S utton, F. Matta, D. Rizos, R. Ghorbani, S. Rajan, D.H. Mollenhauer, et al., Recent progress in digital image correlation: background and developments since the 2013 W M Murray Lecture. Exp. Mech. **57**(1), 1–30 (2017). https://doi.org/10.1007/s11340-016-0233-3
12. S. Rajan, M.A. Sutton, W. McMarkin, E. Compton, A. Kidane, et al., Out-of-plane Wrinkle formation in automated fiber placement: characterization of Mode I and Mode II traction-separation laws for cohesive separation of uncured thermoset fows. Int. J. Fract. (in review)
13. correlatedsolutions.com [internet]. Irmo: Correlated Solutions Incorporated, 120 Dutchman Blvd, Irmo, SC 29063. www.correlatedsolutions.com. Accessed 25 Feb 2019
14. A. Sofla, E. Seker, J.P. Landers, M.R. Begley, PDMS-glass interface adhesion energy determined via comprehensive solutions for thin film bulge/blister tests. ASME. J. Appl. Mech. **77**(3), 031007–031007-5 (2010). https://doi.org/10.1115/1.4000428

Solid Cylindrical Bar Torsion for Characterizing Shear Plastic Deformation and Failure

Wei-Yang Lu, Helena Jin, Jay Foulk, and Jakob Ostien

Abstract The method of thin-wall tube torsion to characterize metal's shear response is well-known. Unfortunately, the thin wall tube specimen tends to buckle before reaching large shear deformation and failure. An alternative technique, which has rarely been considered, is Nadai's surface stress method (Nadai, Theory of Flow and Fracture of Solids. McGraw-Hill, New York, 1950). It derives shear stress-strain curve from the torque-twist relationship of a solid bar. Although the analysis is more complex due to nonlinear shear stress distribution along the radius, the deformation is stable through large shear deformation to failure.

Solid bar torsion experiments were conducted to study large shear deformation of Al6061-T6. Two experiments were described in this study. Since few tests were available in the literature, these experiments were to explore the large deformation behaviors of an engineering alloy and the application of modern measurement techniques, such as 3D DIC method, under torsion. Results show during twisting, the surface shear strain distribution was uniform initially and then localized on a narrow band; eventually, the specimen was cracked and failed within the band. Depending on the specimen size, the twist could be greater than 360°. Details are discussed.

Keywords Ductile failure · Large deformation · Digital image correlation · Shear stress-strain curve · Torsion

Introduction

Numerous examples have shown that ductile failure of metals is not fully understood. Especially at low triaxial stress state, i.e. shear dominated failure, experimental data are little and inconsistent. Also, stress-strain curves used in computational or hybrid studies are based on tensile data. The shear stress-strain curve and pure shear failure of a metal have hardly been investigated experimentally.

It is well known that large shear deformation and failure are important pieces of information needed in characterizing and modeling engineering metals. Available experimental data in the area, however, are surprisingly limited. Large strain torsion tests and related problems were discussed in detail by Wu et al. [2]. The major issue mentioned was the deformation uniformity at the gage section. A well-controlled homogeneous material had to be selected to satisfy the requirement. Little progress has been made since. Motivated by its potential applications, preliminary experiments of solid bar torsion were conducted to observe the deformation and gauge possible challenges and solutions of the test. The first was to explore large deformation torsion qualitatively, focusing on surface deformation uniformity, rotation and torque ranges, etc. In the second experiment, 3D DIC method and IR camera were utilized for quantitative deformation and temperature measurements.

Experiment I

The torsion test was performed on a hydraulic axial-torsional testing system. It has the capacities of ±100 mm displacement and ±140° rotation; the system load cell is rated at ±15 kN (3.3 kips) force and ±170 N-m (1,500 in-lb) torque. A pair of hydraulic grips allow quick installing and releasing specimens.

A Al6061-T6 bar stock was used in this investigation. The specimen geometry is shown in Fig. 1. The gage section dimensions are: 7.62 mm (0.3 in) diameter and 12.7 mm (0.5 in) long. There were six vertical lines painted on the surface of

W.-Y. Lu (✉) · H. Jin · J. Foulk · J. Ostien
Sandia National Laboratories, Livermore, CA, USA
e-mail: wlu@sandia.gov

M. Silberstein et al. (eds.), *Challenges in Mechanics of Time Dependent Materials, Fracture, Fatigue, Failure and Damage Evolution, Volume 2*, Conference Proceedings of the Society for Experimental Mechanics Series, https://doi.org/10.1007/978-3-030-29986-6_9

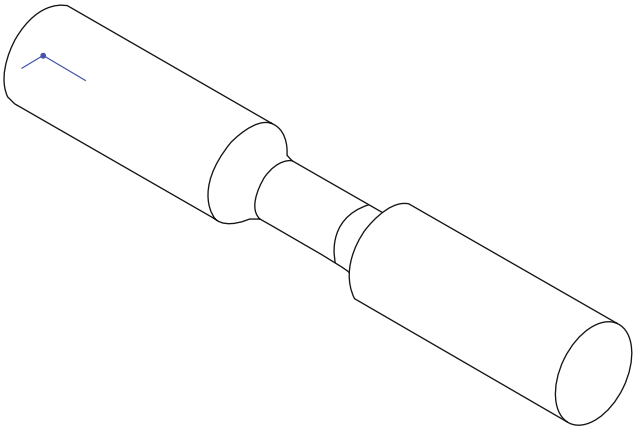

Fig. 1 The shape of solid torsion specimen

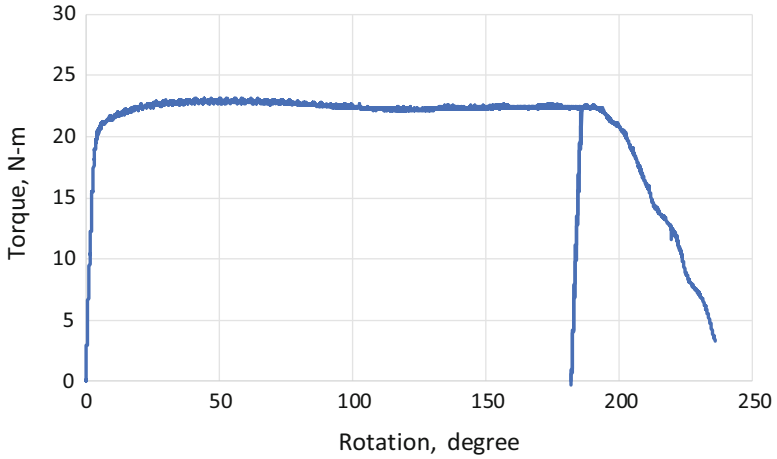

Fig. 2 Torque-rotation curve of Specimen Solid_Torsion_1

the specimen, which were approximately equally spaced around the circumference. The purpose of these lines was to help visualizing the deformation.

The test was under biaxial control. The axial control mode was force, which was kept at zero load, $F = 0$ N, throughout the test. At the same time, the torsion went through a loading-unloading cycle. During loading, the control mode was rotation Ω, where the actuator was programmed to rotate 180°, from −90° to 90°, at a constant rate of $\dot{\Omega} = 0.05°$ per second. When loading was done, the torsional control mode was switched to torque T and unloaded to zero torque.

The torque-rotation T-Ω curve of Specimen Solid_Torsion_1 is shown in Fig. 2. The specimen did not fail during the first cycle. After the torque was unloaded to zero at the end of a cycle, the operator manually released the hydraulic grip on the actuator side, returned the actuator to −90° position, regripped specimen, and restarted the program for another loading-unloading cycle. The specimen began to fail at total rotation $\Omega = 194°$, i.e. about 14° into the second cycle.

Images were taken at every 5 s to record the deformation. Figure 3 shows the solid cylinder specimen at selected deformation stages. At $\Omega = 0°$, which was the undeformed state, all marked lines were straight and vertical. At $\Omega = 40°$, inclined straight lines within the gage section indicated uniform deformation. Lines were kinked at upper part of the gage section at $\Omega = 80°$, which denoted surface deformation was not uniform and localization had occurred. The transition from uniform to localization was gradual; it started approximately at $\Omega = 60°$. For further rotation, the deformation was evidently concentrated at the localized zone as shown in $\Omega = 120°$ and 180° images. Finally, the specimen cracked within the localized zone and separated the cracked cross-section. The system stroke showed a maximum 0.013 mm axial displacement. It corresponds to about 0.1% axial strain if all elongation is from the gage section. Change of radius at the shear localized zone was not detectable form this nonquantitative observation.

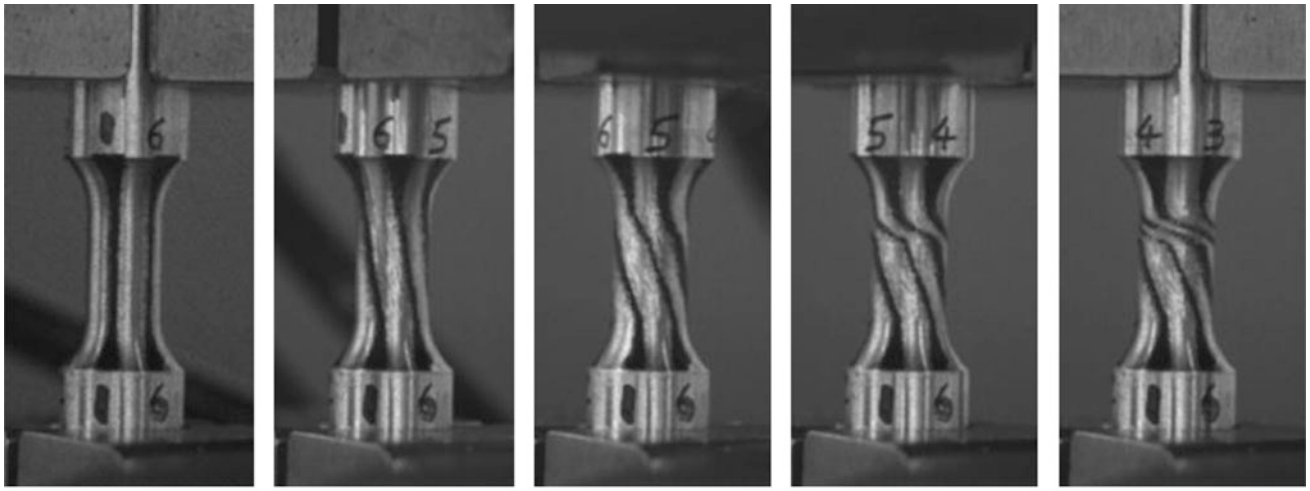

Fig. 3 Deformation images of Specimen Solid_Torsion_1

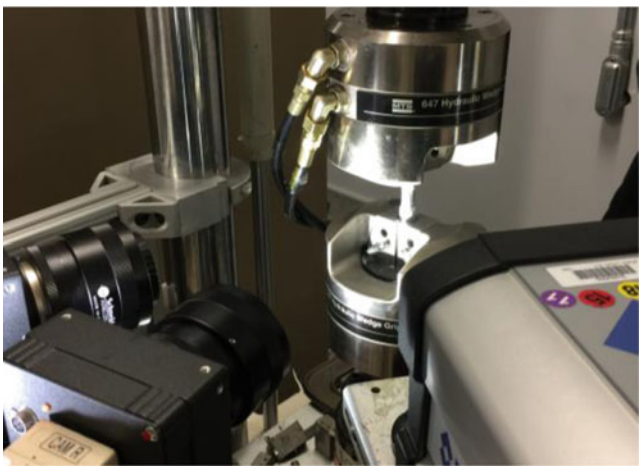

Fig. 4 Test setup for Solid_Torsion_3

Experiment II

The setup is shown in Fig. 4. A pair of DIC cameras and IR camera are on the left and right side of the specimen, respectively. Specimen Solid_Torsion_3 was painted with speckles for 3D DIC analysis but left with a vertical unpainted window for IR temperature measurement. The test control was the same as Solid_Torsion_1 except the torsion loading was running at a faster rate of $\dot{\Omega} = 6.67$ degree per second and the camera frame rate was 10 Hz.

The torque history *T-t* curve is shown in Fig. 5. The specimen failed within the first loading cycle. The shear strain field e_{xy} of selected stages are shown in Fig. 6, where Stage 75, 145, 186 and 198 correspond to rotations, approximately, 0°, 42°, 72° and 80°, respectively. The deformation was clearly localized at Stage 145 and beyond. The figure also shows that the measurable area became smaller and smaller since speckles gradually rotated out of the camera view. At Stage 198, $\Omega = 80°$, all top half and most of the localized zone were without data. The specimen failed at rotation $\Omega = 160°$. Unfortunately, only the strain data between 0° and 80° are available. Using the average shear strain of localized zone for Nadia's analysis, the initial portion of engineering stress-strain curve is shown in Fig. 7, no data for $\Omega > 80°$. The estimated strain rate is about 0.15 s^{-1}. Same as Solid_Torsion_1, the separation was in the localized zone, shown in Fig. 8. The width of the localized zone is estimated to be about 1–2 mm. IR data show negligible temperature changes.

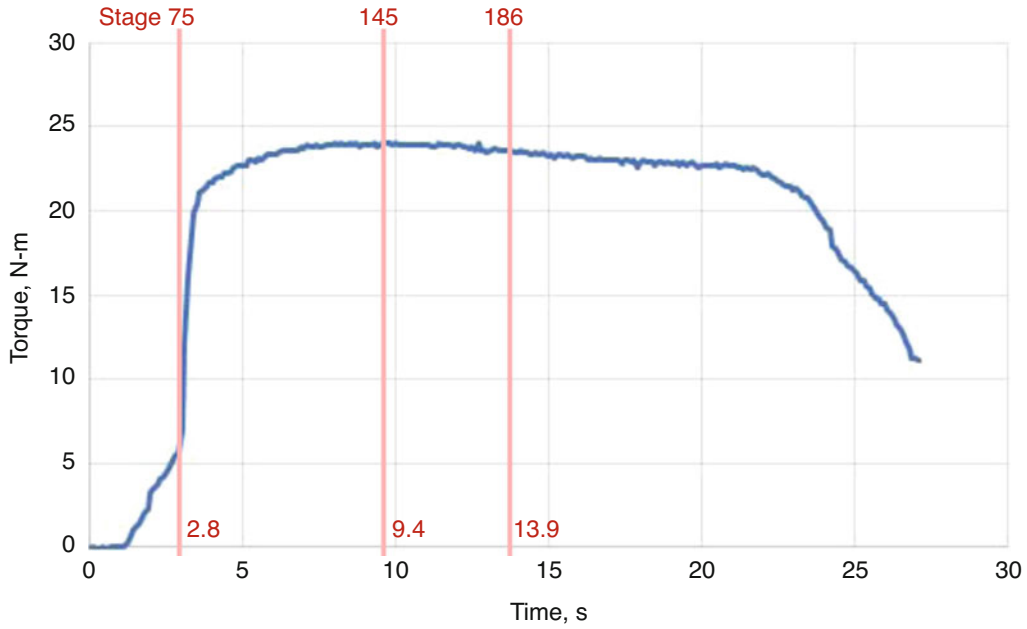

Fig. 5 Torque history of Specimen Solid_Torsion_3

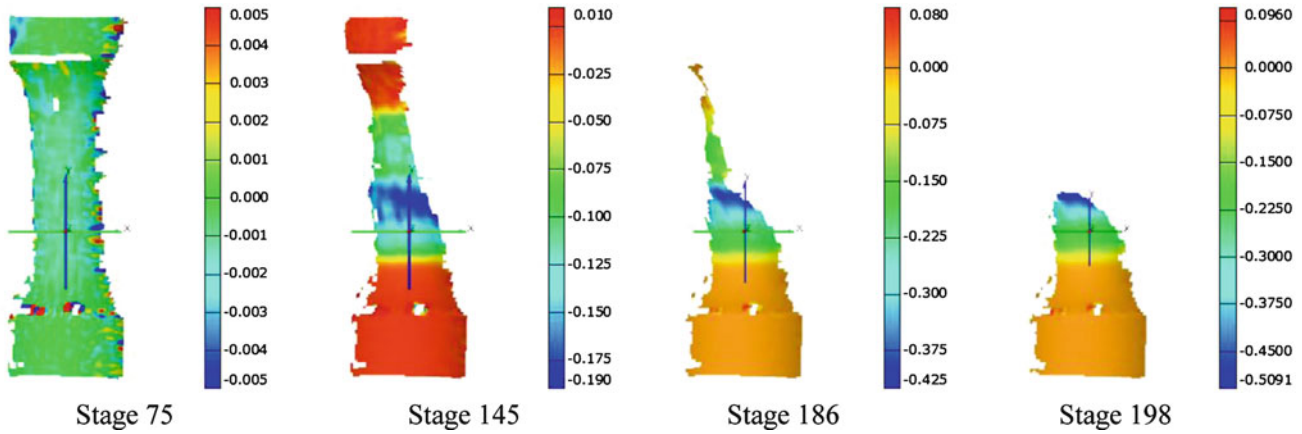

Fig. 6 Solid_Torsion_3 shear strain e_{xy} distributions of selected DIC stages

Conclusion

For Al6061-T6, solid bar torsion is stable and do not buckle. It can achieve large shear deformation up to failure. Within the gage section, the deformation is uniform in the beginning, it gradually transitions to deform further in a localized zone, and eventually a crack forms within the zone.

Solid bar torsion analyses are no longer limited to the experiments with uniform deformation. Modern 3D DIC method makes up the shortcomings of the mechanical extensometer. Strain fields clearly reveal the deformation uniformity of the gage section. One great advantage of the technique is that the area of interest (AOI) does not need to be identified or guessed before the test, selecting the necessary data to construct shear stress-strain curve are done afterward.

The rotation could be very large. The whole gage section should be painted with DIC speckles; also, the DIC analysis needs to re-establish the reference frame periodically to avoid the reference AOI deforms out of the camera view. Take the current setup for example, about every 60° (i.e. less than 80°) rotation is recommended. The re-referenced analyses results need to map back to the original reference frame.

No significant temperature change is observed. Numerical modeling will help to understand and improve the torsion experiment.

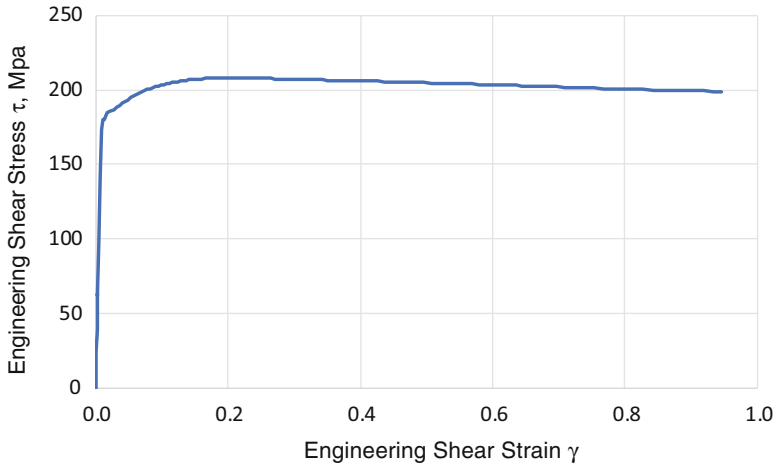

Fig. 7 Shear stress-strain curve of Al6061-T6

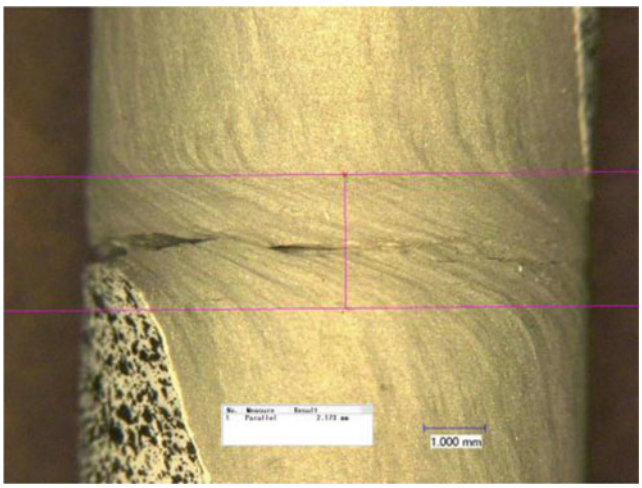

Fig. 8 Failed Specimen Solid_torsion_3

Acknowledgements Sandia National Laboratories is a multimission laboratory managed and operated by National Technology and Engineering Solutions of Sandia, LLC., a wholly owned subsidiary of Honeywell International, Inc., for the U.S. Department of Energy's National Nuclear Security Administration under contract DE-NA-0003525. The views expressed in the article do not necessarily represent the views of the U.S. Department of Energy or the United States Government.

References

1. A. Nadai, *Theory of Flow and Fracture of Solids*, 3rd edn. (McGraw-Hill, New York, 1950)
2. H.C. Wu, Z. Xu, P.T. Wang, The shear stress-strain curve determination from torsion test in the large strain range. J. Test. Eval. **20**, 396–402 (1992)

Mixed Mode (Mode I/III) Dynamic Fracture Initiation Toughness of Aluminum Alloy

Ali F. Fahem and Addis Kidane

Abstract In this study, a hybrid experimental-numerical approach is used to determine the mixed mode (mode I/III) dynamic fracture initiation toughness of aluminum alloy. Cylindrical specimens with spiral v-notch at a revolution angle of 360°and pitch angles 22.5°(inclined angles) are fabricated from aluminum rod. A torsional Hopkinson bar apparatus is used to generate and apply a dynamic torsional load on the specimens. A stereo digital image correlation is used to measure full-field displacements around the crack tip and to estimate the fracture initiation time. A commercial finite element software (ABAQUS) is used to extract a dynamic stress intensity factors based on interaction integral method. The stress distribution, full-field deformation with time, and the mixed mode fracture toughness are discussed.

Keywords Mixed Mode I/III · Spiral crack · Torsional load · TSHB · FE solution

Introduction

There are enough standard experimental methods to measure the fracture toughness of materials in Mode I, Mode II and Mode III under quasi-static loading condition. However, the method is very scarce when it comes to dynamic fracture. On the other hand, dynamic fracture mechanics has been an important subject due to the criticality of structures subjected to dynamic load condition [1, 2]. There are several efforts focused on investigating the dynamic fracture of materials under mixed mode loading. For instance, Nishioka and Atluri, 1983, used the J-integral method for determining the mixed mode fracture parameters [3]. Chandar, 1995, investigated the dynamic fracture of polycarbonate materials under mixed mode condition [4]. The dynamic mixed mode fracture of isotropic and graded materials subjected to thermomechanical load were investigated by Kidane [5, 6]. To minimize the effect of inertia force on the dynamic loading of materials, recently, a cylindrical specimen with spiral v-notch at 45° an inclined angle was proposed and used to measure the Mode I of dynamic fracture initiation toughness of materials [7, 8]. In this work, the proposed method has been extended and used for measuring the dynamic fracture of materials under mixed mode (mode I/III). Cylindrical specimens with spiral v-notch at inclined angles 22.5° were used to determine the mixed mode I/III dynamic initiation toughness of materials. The experimental procedure including material used, specimen dimensions, and, the finite element model and the resulted dynamic stress intensity factors and fracture toughness are presented in detail.

Experimental Setup

Material and Specimen

A total of three cylindrical specimens with spiral v-notch at an angle of 22.5^{o} were prepared from Aluminum 2024-T3. The specimens, as shown in Fig. 1, have 19 *mm* outer diameter, 12.7 *mm* inner diameter, and *2.15 mm* crack depth. More details

A. F. Fahem (✉)
Department of Mechanical Engineering, The University of South Carolina, Columbia, SC, USA

Department of Mechanical Engineering, The University of Al-Qadisiyah, Al-Qadisiyah, Iraq
e-mail: afahem@email.sc.edu

A. Kidane
Department of Mechanical Engineering, The University of South Carolina, Columbia, SC, USA

M. Silberstein et al. (eds.), *Challenges in Mechanics of Time Dependent Materials, Fracture, Fatigue, Failure and Damage Evolution, Volume 2*, Conference Proceedings of the Society for Experimental Mechanics Series, https://doi.org/10.1007/978-3-030-29986-6_10

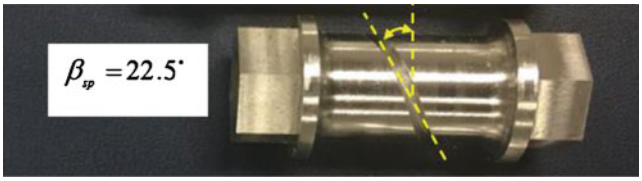

Fig. 1 Mixed mode spiral specimen

Table 1 Spiral crack specimens dimensions

Out radius r_o (*mm*)	Spiral angle (degree)	Spiral pitch h(*mm*)	Spiral length L(*mm*)	Crack depth c(*mm*)	Crack ligament a(*mm*)	Fracture mode
9.5	22.50	24.71	64.57	2.15	1.0	I + III

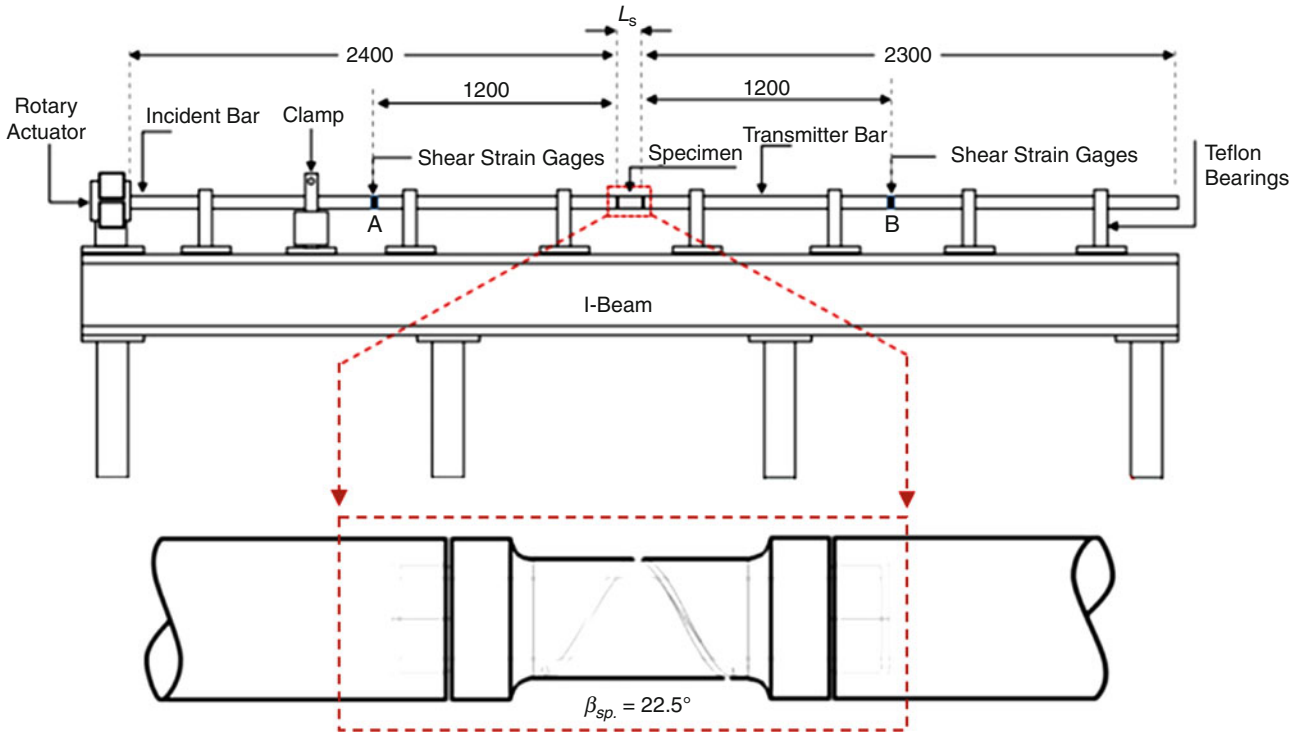

Fig. 2 Schematic of torsional split Hopkinson bar (TSHP) and specimen (mm)

of the specimen's dimension are listed in Table 1. Four-Dimensions Milling machine and a G- tool was used to manufacture the spiral crack path.

Torsional Split Hopkinson Bar (TSHB) Setup

The torsional Hopkinson bar THB was used in this work to generate torsional impulse load as a far-field load [9]. The THB used in this work has two long incident and transmitter bars, respectively, made of *25.4 mm* diameter high-strength grade 5 Titanium (ASTM B348). The bars are supported in a horizontal plane and are free to rotate around their central axis. An internal hexagonal groove was manufactured at the end of the incident and transmitted bar. The spiral notch specimen was sandwiched between the two bars via hexagonal joint and a thin layer of JB-Weld epoxy. The epoxy is used around the hexagonal interface to reduce slip due to tiny space between the specimen and the bars. The assembly provides a reliable connection that can be used to load the samples even at higher loading rate. Two pairs of shear strain gauge were used to measure the torsional impels as a far-field load at a position A and B, Fig. 2.

During loading, a hydraulic driven rotary actuator is used to apply and store shear strain in the part of the incident bar between the rotary actuator and the clamp system, Fig. 2. Thus, the stored shear strain is suddenly released by breaking a brittle notched bolt installed in the clamping mechanism. During this time, half of the stored shear strain propagates towards the specimen through the incident bar. When the incident wave reached the specimen, some of the waves will transmit to the output bar through the specimen, and the rest will reflect the incident bar. The incident, transmitted and reflected shear strain data would be acquired by using two pairs of shear strain gauge the processed repeated three time for each spiral specimen as shown in a schematic Fig. 2. The incident torsional impulse wave Eq. (1), was measured at position A, is used as input far field load to the finite element model [10], furthermore the reflected and transmitted measured shear waves V_r *and* V_t respectively, show and indicated the time of the crack initiation time.

$$T_i(t) = \frac{GD^3\pi}{16} \times \gamma_I(t) \tag{1}$$

Numerical Solution of DSIF

A numerical method is performed to calculate the dynamic stress intensity factor as presented in Eqs. (2–5), and full details of these equations are available in Fahem [11, 12]. A commercial finite element software ABAQUS-dynamic implicit, was used to solve a finite element model of a quarter spiral crack specimen and the complete incident and transmitter bar assembly of a torsional Hopkinson bar. Typical finite element model and mesh for the spiral crack angle is shown in Fig. 3. For the specimen's model has a circular tube with a *19 mm* and *12.7 mm* external and internal diameter respectively. A shell revolve was used to make a spiral seam crack with all models. Since the J-integral, path independent is the base of the interaction integral method, the refine mesh around the crack tip is not required. The middle volume of the solid cylinder was divided into a sufficient number of elements, that generated a robust mesh around the crack tip as shown in Fig. 3. The model was built with a 3D solid structure quadratic hexahedral C3D20R element.

The incident torque measured experimentally was used as input to the finite element model, and appropriate boundary conditions are applied [13]. The stress, strain, and displacement are calculated numerically around the crack tip and assemble to calculated J-interaction and the dynamic stress intensity factor as well, Eqs. (2–5).

$$\overline{J}^{\alpha}_{Inter.}(t) = \int_V \left(\sigma_{ij}(t)\left(u^{aux}_{i,1}(t)\right)^{\alpha} + \left(\sigma^{aux}_{ij}(t)\right)^{\alpha} u_{i,1}(t)\right) q_{,j}\, dV - \frac{1}{2}\int_V \left(\sigma_{ij}(t)\left(\varepsilon^{aux}_{ij}(t)\right)^{\alpha} + \left(\sigma^{aux}_{ij}(t)\right)^{\alpha} \varepsilon_{ij}(t)\right) q_{,j}\, dV \tag{2}$$

$$K_{III}(t) = \frac{E}{2\,(1+\upsilon)} ave.\left(\sum_{i=1}^{n} J^{III}_{Intre.}(t)\right) \tag{3}$$

$$K_I(t) = \frac{E}{2\left(1-\upsilon^2\right)} \times ave.\left(\sum_{i=1}^{n} J^{I}_{Intre.}(t)\right) \tag{4}$$

$$K_J(t) = \frac{E}{2\,(1+\upsilon)} \frac{1}{n} \sqrt{\left(\sum_{i=1}^{n} J^{I}_{Intre.}(t)\right)^2 + \left(\sum_{i=1}^{n} J^{III}_{Intre.}(t)\right)^2} \tag{5}$$

Results and Discussions

Stress Around Crack Tip

The numerical result of a stress contour distribution around the crack tip is shown in Fig. 4a. Figure 4a shows a full field of the stress result at the time of crack initiation which is similar to the static stress profile under plane strain condition. The

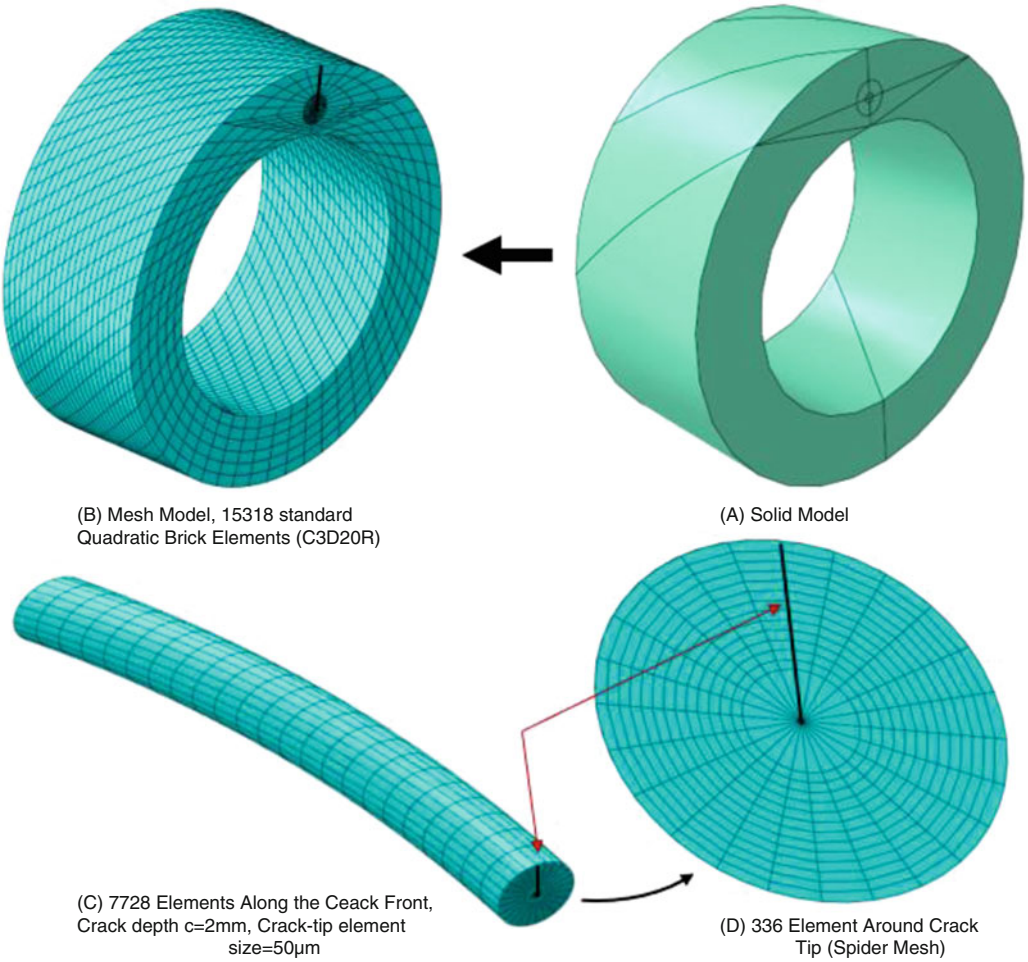

Fig. 3 Typical finite element model of spiral crack under mixed mode (I/III) with a highlight of the crack front and crack tip elements [14]

Table 2 Dynamic mixed mode (I/III) fracture initiation toughness of Alu. 2024-T3

Fracture mode	Spiral angle (degree)	Dynamic initiation toughness $\left(MPa\sqrt{m}\right)$		
		K_{Id}	K_{IIId}	$K_{(I/III)d}$
I + III	22.50	22.49	8.60	23.40

normalized stress, (von Mises stress, σ_v/Far-Field Stress, σ_{ff}), versus normalized distance from the crack tip along the crack ligament, a, are illustrates in Fig. 4b.

Dynamic Stress Intensity Factor and Fracture Toughness

The dynamic stress intensity factor (DSIF) values of Alu. 2024-T3 was calculated numerically by using a finite element method in Abaqus package as shown in Fig. 5.

As shown in Fig. 5, the Mode I is higher compared to Mode III. Table 2 has a summary of the result.

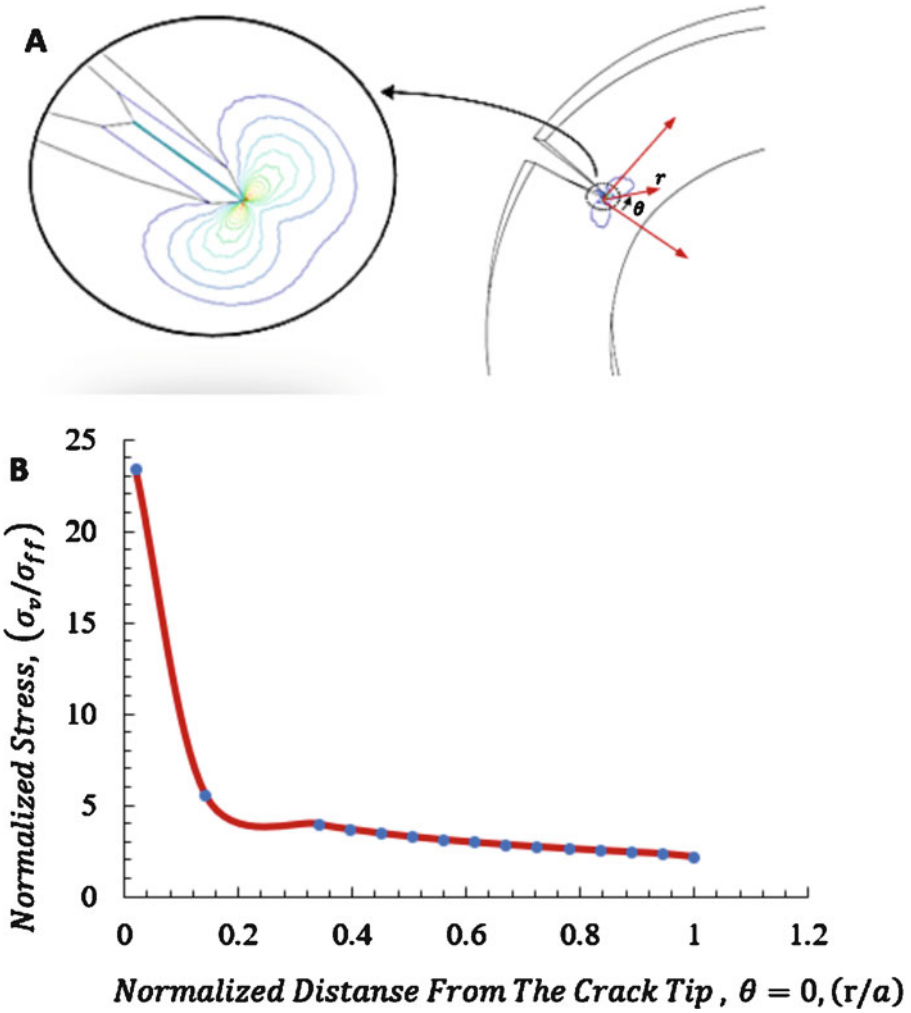

Fig. 4 Typical stress profile around the crack tip at $t = t_f$

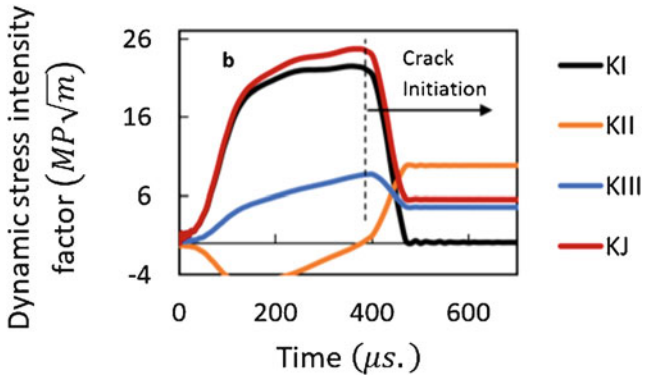

Fig. 5 Dynamic stress intensity factor, (mixed mode (I/III) ($\beta_{sp} = 22.5°$)

Summary

To understand the dynamic mixed mode (I/III) fracture of aluminum alloys, experiments were performed on cylinder specimens with spiral v-notch at inclined angle subjected to a dynamic torsional load. A torsional Hopkinson Bar apparatus was used to generate dynamic torsional load. A 3D-DIC method was used to measure the crack mouth opening displacement

(CMOD) and estimate the fracture initiation time. The mixed mode (I/III) dynamic stress intensity factor of aluminum was calculated numerically following the dynamic interaction integral method. The value of the mixed mode dynamic fracture toughness was very close to the Mode I dynamic fracture toughness, only 4% higher.

References

1. L.B. Freund, *Dynamic Fracture Mechanics* (Cambridge University Press, Cambridge, 1990)
2. K. Ravi-Chandar, *Dynamic Fracture*, 1st edn. (Elsevier Ltd, Netherlands, 2004)
3. T. Nishioka, S.N. Atluri, Path-independent integrals, energy release rates, and general solutions of near-tip fields in mixed-mode dynamic fracture mechanics. Eng. Fract. Mech. **18**, 1–22 (1983)
4. K. Ravi-Chandar, On the failure mode transitions in polycarbonate under dynamic mixed-mode loading. Int. J. Solids Struct. **32**, 925–938 (1995)
5. A. Kidane, V.B. Chalivendra, A. Shukla, R. Chona, Mixed-mode dynamic crack propagation in graded materials under thermo-mechanical loading. Eng. Fract. Mech. **77**, 2864–2880 (2010)
6. A. Kidane, V.B. Chalivendra, A. Shukla, Thermo-mechanical stress fields and strain energy associated with a mixed-mode propagating crack. Acta Mech. **215**, 57–69 (2010)
7. A.F. Fahem, A. Kidane, A general approach to evaluate the dynamic fracture toughness of materials, in *Dynamic Behavior of Materials*, ed. by D. Casem, L. Lamberson, J. Kimberley, vol. 1, (Springer, Cham, 2017), pp. 185–194. https://doi.org/10.1007/978-3-319-41132-3_26
8. A.F. Fahem, A. Kidane, Modification of Benthem solution for mode I fracture of cylinder with spiral crack subjected to torsion, in *Fracture, Fatigue, Failure, and Damage Evolution, vol. 6, the Proceedings of the SEM Annual Conference & Exposition on Experimental and Applied Mechanics, Greenville, SC*, (Springer, Cham, 2019), pp. 57–63. https://doi.org/10.1007/978-3-319-95879-8_10
9. S. Mallon, B. Koohbor, A. Kidane, A.P. Reynolds, On the effect of microstructure on the torsional response of AA7050-T7651 at elevated strain rates. Mater. Sci. Eng. A **639**, 280–287 (2015)
10. N.K. Naik, A. Asmelash, V.R. Kavala, V. Ch, Interlaminar shear properties of polymer matrix composites: strain rate effect. Mech. Mater. **39**, 1043–1052 (2007)
11. A. Fahem, A. Kidane, M. Sutton, Geometry factors for Mode I stress intensity factor of a cylindrical specimen with spiral crack subjected to torsion. Eng. Fract. Mech. 214, 79–94 (2019). https://doi.org/10.1016/j.engfracmech.2019.04.007
12. A. Fahem, A. Kidane, M. Sutton, Mode-I dynamic fracture initiation toughness using torsion load. Eng. Fract. Mech. 213, 53–71 (2019). https://doi.org/10.1016/j.engfracmech.2019.03.039
13. A. Fahem, A. Kidane, A progression on the determination of dynamic fracture initiation toughness using spiral crack, in *Fracture, Fatigue, Failure, and Damage Evolution. The Proceedings of the SEM Annual Conference & Exposition on Experimental and Applied Mechanics, vol. 6, Greenville, SC*, (Springer, Cham, 2019), pp. 89–95. https://doi.org/10.1007/978-3-319-95879-8_15
14. A. Fahem, A. Kidane, Hybrid computational and experimental approach to identify the dynamic initiation fracture toughness at high loading rate, in *Dynamic Behavior of Materials*, vol. 1, (Springer, Cham, 2018), pp. 141–146. https://doi.org/10.1007/978-3-319-62956-8_24

Incremental 1D Viscoelastic Model for Residual Stress and Shape Distortion Analysis During Composite Manufacturing Processes

Sibin Saseendran, Daniel Berglund, Janis Varna, and Patrik Fernberg

Abstract The present contribution is toward the systematic characterization and development of a one-dimensional incremental viscoelastic (VE) model for thermo-rheologically complex materials (called "VisCoR") for the prediction of residual stresses and shape distortions in composites. Traditionally, models that have been developed for this purpose within the composites industry are based on incremental linear elastic methods. While these methods are robust, they fall short in predicting exact behaviour of large composite parts and high temperature composites where relaxation effects also play a vital role in the final shape of the part. Moreover, these models also do not consider the dependency of stresses on temperature and degree of cure. Although viscoelastic models have been formulated, they are not in an incremental form (which is suitable for Finite Element (FE) simulations), hence requiring higher computational efforts. The presented model is an incremental form and requires lesser computational cost and characterization efforts and most importantly takes into account the effect of temperature and degree of cure. Preliminary studies indicate that the incremental 1D viscoelastic model can accurately model VE stress relaxation behaviour when compared to exact solutions.

Keywords Viscoelasticity · Residual stress · Strain recovery · Process simulation · Incremental formulation

Introduction

The manufacturing techniques and processes to produce optimized reinforced polymer composite parts are rapidly evolving and refined, but modelling of these processes is yet to mature. Prediction of process-induced residual stresses and deformations that occur during composite manufacturing requires special attention. It is vital to have a final composite component that matches up to specifications dimensionally and meet design criteria for strength.

Usually, in the beginning of the process the resin is an uncured liquid. During the manufacturing, the resin undergoes phase changes from a liquid to a solid. The phase changes induce volumetric shrinkage of the resin as it solidifies; change its thermo-mechanical properties. Adding external constraints and influences, like interaction between the tool and the part, thermal, thermal gradients, results in stress build-up and in strains different from free expansion strains in the composite part. This causes undesired shape distortions and the composite part deviating from the design specifications [1]. The ability to simulate these phenomena is crucial in order to employ methods for compensation and for suggesting corrective methods for minimization of shape distortions based on optimizing post-cure time and temperature, thus significantly influencing the spring-in angles [2].

The existing numerical methods for prediction of residual stresses and shape distortions can be grouped under two approaches assuming; (a) linear elastic material behaviour and (b) viscoelastic (VE) behaviour respectively. Both approaches have their advantages and disadvantages. While the number of input parameters for an elastic model is small and it can be easily implemented in a numerical code, the prediction accuracy may be questionable. VE models provide a more accurate description of the material behaviour and can render better predictions. However, the characterization is time consuming and the codes are computationally expensive. Hence, the goal in predicting process-induced deformations and residual stresses is to find a balance developing models, ideally viscoelastic and viscoplastic, with low characterization effort and computational costs and with acceptable accuracy. The changing temperature (T) and degree of cure (DoC) makes the VE computation rather expensive and hence currently this type of models is not frequently used for shape distortion analysis in composites.

S. Saseendran (✉) · D. Berglund · P. Fernberg
RISE SICOMP AB, Piteå, Sweden
e-mail: sibin.saseendran@ri.se

J. Varna
Luleå University of Technology, Luleå, Sweden

M. Silberstein et al. (eds.), *Challenges in Mechanics of Time Dependent Materials, Fracture, Fatigue, Failure and Damage Evolution, Volume 2*, Conference Proceedings of the Society for Experimental Mechanics Series, https://doi.org/10.1007/978-3-030-29986-6_11

Among elastic approaches, the Cure Hardening Instantaneously Linear Elastic (CHILE) model [3] is one of the most frequently used: the assumed properties are linear elastic within each material phase. Under certain conditions, this model can predict the spring-in angle and the warpage with a reasonable accuracy. However, the so-called "frozen-in" strains occurring during curing and their release during phase transitions that actually is VE strain recovery cannot be accounted for.

Svanberg and Holmberg in [4] proposed so-called "linear elastic path-dependent model", which was derived as a limiting case of the linear VE model formulated by Zocher et al. [5]. In fact, model [4] is not viscoelastic: in the rubbery state the stress relaxation is instant whereas in the glassy state there is no relaxation. Nevertheless, the model has some "memory": during the glassy state a special term, allowing the "frozen-in" strain release at T_g, is accumulated. Since the VE relaxation/recovery at high temperatures below T_g is not accounted for, the predicted stresses and strains may be greatly overestimated.

Experimental work to validate an incremental thermo-rheologically simple VE constitutive model is reported by Machado et al. [6] applying it to various thermoplastic composite materials. Benavente et al. [2] used a similar model to study VE relaxation during cure of a 3D interlock woven fabric reinforced epoxy.

In the aforementioned VE models, only the DoC and T affect the time shift factor. The shifting mechanism is based on the time-temperature-cure-superposition (TTCS) principle. According to TTCS, high temperature and/or low DoC shorten the VE relaxation times. Kim and White [7] determined the temperature shift factor at various DoCs. Simon et al. [8] used the DiBenedetto function to calculate the glass transition temperature, T_g as a function of the DoC and used the T_g so determined as the reference temperature in the temperature shift factor. O'Brien et al. [9] analysed the effect of DoC on VE parameters using a combination of rheometry and three-point bending testing in a DMA. In recent studies [10, 11] the VE models were improved by assuming the glassy and rubbery stiffness dependent on DoC and T. Curtois et al. [12] used a generalized form of the model developed by Machado et al. with stiffness in the glassy state dependent on the DoC. Ding et al. [13] simulated complex VE behaviour using a T-dependent factor as a multiplier for Prony series. The multiplier was calculated as the ratio of stiffness at a given temperature to the reference temperature.

The above-discussed thermo-rheological models are rather empirical: flexibility in the model in the model is introduced without being concerned about thermodynamic consistency. In the presented work, a thermodynamically consistent, rheologically complex VE model, derived from Helmholtz free energy systematically using simplifying assumptions, is used. The material model has the rubbery modulus and glassy modulus dependent on DoC and T. The dependence is represented by three functions. The first is the current value of the rubbery modulus, the second one in front of the convolution integral is a weight factor characterizing the current instant of the T- and DoC state. The final one (as a derivative under the sign of the integral) defines the way the strain history affects the stress. The material model, written in an incremental form with more accurate approximation of functions in the time increment than usually, is used to analyse residual stress build up in comparison with results from the path-dependent model [4].

Thermo-Rheologically Complex Viscoelastic Material Model (VISCOR)

The VE thermo-rheologically complex behavior model used in this paper uses the following assumptions:

- The cross-linking and the T changes may have the same time scale as the mechanical loading. Therefore, time derivatives of the material functions in the model cannot be neglected.
- The material is linear viscoelastic.
- Free thermal expansion and curing shrinkage strains are not explicitly shown in the derived expressions. This means that in the following expressions, strain ε is, in fact,

$$\varepsilon = \varepsilon_{applied} - \varepsilon_{thermal}^{free} - \varepsilon_{curing}^{free} \tag{1}$$

The derivation of this model, using the thermodynamics-based routine suggested by Schapery [14] for nonlinear VE materials is given in detail in [15]: the Helmholtz free energy function is expanded with respect to applied strain ε and internal state variables related to viscoelasticity. Using a systematic sequence of simplifying assumptions, the following constitutive model was obtained

$$\sigma = E_r(\alpha, T)\,\varepsilon + h_1(\alpha, T)\int_0^t \Delta C\left(\psi - \psi'\right)\frac{d\left(h_2(\alpha, T)\,\varepsilon\right)}{d\tau'}d\tau' \tag{2}$$

$$\Delta C(\psi) = \sum_i C^i \exp\left(-\frac{\psi}{\tau_i}\right) \tag{3}$$

In (2) α is the degree of cure and T is the temperature. The reduced time ψ is defined by expression

$$\psi(t) = \int_0^t \frac{1}{a(\alpha, T)} d\zeta \tag{4}$$

In Prony series (3) C^i are constants and τ_i are constant relaxation times. In (2) $E_r(\alpha, T)$ has the meaning of the rubbery modulus; $h_1(\alpha, T)$ is a weight factor in front of the convolution integral. The stress value in a particular time instant depends on the value of this function in that instant, $h_2(\alpha, T)$ under the sign of the derivative, is a "weight factor for strains in the fading memory", determining the importance of strains at different stages during the loading history. For thermo-rheologically simple materials E_r is independent on DoC and T and $h_1 = h_2 = 1$ [9].

Derivation of the Incremental Form

Stress Increment

The used notation for variables and their derivatives in the time increment $\Delta t_{k+1} = t_{k+1} - t_k$ is as follows. Function f in time instant t_k is $f^k = f(t_k)$. Increment of this function is $\Delta f^{k+1} = f(t_{k+1}) - f(t_k)$. Hence, increments of the reduced time, strain, shift factor a, h_2 and h_1 are $\Delta\psi_{k+1}$, $\Delta\varepsilon^{k+1}$, Δa^{k+1}, Δh_2^{k+1}, Δh_1^{k+1}. Derivatives (slope) of these parameters in the increment are denoted d_a^{k+1}, d_{h2}^{k+1}, d_{h1}^{k+1}, d_ε^{k+1}.

We substitute in (2) the transient compliance expression (3) and rewrite (2) for time instants t_k and t_{k+1}

$$\sigma^k = E_r^k \varepsilon^k + h_1^k \int_0^{t_k} \sum_i C^i \exp\left(-\frac{\psi_k - \psi'}{\tau_i}\right) \frac{d(h_2 \varepsilon(\tau))}{d\tau} d\tau \tag{5}$$

$$\sigma^{k+1} = E_r^{k+1} \varepsilon^{k+1} + h_1^{k+1} \int_0^{t_{k+1}} \sum_i C^i \exp\left(-\frac{\psi_{k+1} - \psi'}{\tau_i}\right) \frac{d(h_2 \varepsilon(\tau))}{d\tau} d\tau \tag{6}$$

The integral in (6) can be written as a sum of an integral from 0 to t_k and from t_k to t_{k+1}

$$\sigma^{k+1} = E_r^{k+1} \varepsilon^{k+1} + h_1^{k+1} \left(\sum_i C^i \int_0^{t_k} \exp\left(-\frac{\psi_{k+1} - \psi'}{\tau_i}\right) \frac{d(h_2(\tau)\varepsilon(\tau))}{d\tau} d\tau + \sum_i C^i \int_{t_k}^{t_{k+1}} \exp\left(-\frac{\psi_{k+1} - \psi'}{\tau_i}\right) \frac{d(h_2 \varepsilon)}{d\tau} d\tau \right) \tag{7}$$

Subtracting (5) from expression (7), and performing some rearrangements, we obtain

$$\Delta\sigma^{k+1} = \Delta E_r^{k+1} \varepsilon^{k+1} + E_r^k \Delta\varepsilon^{k+1} + h_1^{k+1} \sum_i C^i Q_i^{k+1} + \Delta h_1^{k+1} \sum_i C^i S_i^k + h_1^{k+1} \sum_i C^i \Delta\Theta_i^{k+1} \tag{8}$$

In (8) the following notation is used

$$\Delta\Theta_i^{k+1} = \int_{t_k}^{t_{k+1}} \exp\left(-\frac{\psi_{k+1} - \psi'}{\tau_i}\right) \frac{d(h_2 \varepsilon)}{d\tau} d\tau \tag{9}$$

$$S_i^k = \int_0^{t_k} \exp\left(-\frac{\psi_k - \psi'}{\tau_i}\right) \frac{d(h_2 \varepsilon)}{d\tau} d\tau \tag{10}$$

$$Q_i^{k+1} = \int_0^{t_k} \left[\exp\left(-\frac{\psi_{k+1} - \psi'}{\tau_i} \right) - \exp\left(-\frac{\psi_k - \psi'}{\tau_i} \right) \right] \frac{d\left(h_2 \varepsilon\left(\tau\right)\right)}{d\tau} d\tau \tag{11}$$

S_i^k and $\Delta\Theta_i^k$ defined by (9), and (10) are analysed in the following sections. A closer examination of expression (11) shows that Q_i^{k+1} is not an independent function

$$Q_i^{k+1} = -S_i^k \left(1 - \exp\left(-\frac{\Delta\psi_{k+1}}{\tau_i} \right) \right) \tag{12}$$

Using (12) and

$$\Delta E_{\mathrm{r}}^{k+1} \varepsilon^{k+1} + E_{\mathrm{r}}^k \Delta\varepsilon^{k+1} = \Delta E_{\mathrm{r}}^{k+1} \varepsilon^k + E_{\mathrm{r}}^{k+1} \Delta\varepsilon^{k+1} \tag{13}$$

Expression (8) can be written in a different form, which is used in all following derivations

$$\Delta\sigma^{k+1} = \Delta E_{\mathrm{r}}^{k+1} \varepsilon^k + E_{\mathrm{r}}^{k+1} \Delta\varepsilon^{k+1} + \sum_i C^i \mathrm{S}_i^k \left(h_1^{k+1} \exp\left(-\frac{\Delta\psi_{k+1}}{\tau_i} \right) - h_1^k \right) + h_1^{k+1} \sum_i C^i \Delta\Theta_i^{k+1} \tag{14}$$

Assumption About Parameter Change in the Interval

We assume that in the small interval $\Delta \mathrm{t}_{k+1}$ the VE shift factor $a$is a linear function of time τ.

$$\mathrm{a} = \mathrm{a}^{\mathrm{k}} + \mathrm{d}_{\mathrm{a}}^{\mathrm{k}+1} \left(\tau - \mathrm{t}_{\mathrm{k}} \right), \text{ where } \mathrm{d}_{\mathrm{a}}^{\mathrm{k}+1} = \frac{\mathrm{a}^{\mathrm{k}+1} - \mathrm{a}^{\mathrm{k}}}{\mathrm{t}_{\mathrm{k}+1} - \mathrm{t}_{\mathrm{k}}} \tag{15}$$

We also assume linear dependence of $h_2(\alpha, T)$ on time τ in the interval $\tau \in [t_k, t_{k+1}]$

$$h_2\left(\tau\right) = h_2\left(t_k - 0\right) + d_{h2}^{k+1} \left(\tau - t_k\right) H\left(\tau - t_k\right), \text{ where } d_{h2}^{k+1} = \frac{h_2^{k+1} - h_2^k}{t_{k+1} - t_k} \tag{16}$$

We also assume a linear time dependence of the strain change in the interval

$$\varepsilon\left(\tau\right) = \varepsilon\left(t_k - 0\right) + d_{\varepsilon}^{k+1} \left(\tau - t_k\right) H\left(\tau - t_k\right), \text{ where } d_{\varepsilon}^{k+1} = \frac{\varepsilon^{k+1} - \varepsilon^k}{t_{k+1} - t_k} \tag{17}$$

In (16) and (17) H is the Heaviside step function. The calculation scheme based on linear approximation in each increment leads to faster convergence, than common schemes using the values of parameters in the starting point of the increment. In contrast to most common representations, the time increment does not have to be constant. For example, large regions where the parameter change and the strain change is linear can be treated in a single time step.

Expression for $\Delta\psi_{k+1}$

According to (4), $\Delta\psi_{k+1}$ is not a linear function of $\Delta \mathrm{t}_{k+1}$ For finite increments and assumption (15) in the previous section

$$\psi^k = \int_0^{t_k} \frac{dt'}{a}, \; \psi^{k+1} = \int_0^{t_{k+1}} \frac{dt'}{a}, \; \Delta\psi_{k+1} = \int_{t_k}^{t_{k+1}} \frac{d\tau}{a} \tag{18}$$

Substituting (15) in (18) and integrating we obtain

$$\Delta\psi_{k+1} = \frac{1}{d_a^{k+1}} \ln\left(1 + \frac{d_a^{k+1}}{a^k}\Delta t_{k+1}\right) \tag{19}$$

Direct substitution of d_a^{k+1} defined by (15) in (19) yields

$$\Delta\psi_{k+1} = \frac{\Delta t_{k+1}}{\Delta a^{k+1}} \ln\left(1 + \frac{\Delta a^{k+1}}{a^k}\right) \tag{20}$$

In regions where a is not changing or changing slowly ($d_a^{k+1} \Rightarrow 0$) expressions (19) and (20) can lead to numerical inaccuracies. Expansion $ln(1 + x) \approx x$ can be used instead, leading to

$$\Delta\psi_{k+1} = \frac{\Delta t_{k+1}}{a^k} \tag{21}$$

Keeping also the second term in expansion of the logarithm, a more accurate expression is obtained

$$\Delta\psi_{k+1} = \frac{\Delta t_{k+1}}{a^k}\left(1 - \frac{1}{2}\frac{\Delta a^{k+1}}{a^k}\right) \tag{22}$$

Linear Approximation of h_2, ε and the Derivative of their Product

The integral in (2) contains the $\frac{d}{d\tau}(h_2\varepsilon)$ term. From (16) and (17) (and keeping in mind that $H * H = H$)

$$h_2\varepsilon = h_2^k\varepsilon^k + \left\{h_2^k\left[d_\varepsilon^{k+1}(\tau - t_k)\right] + d_{h2}^{k+1}(\tau - t_k)\left[\varepsilon^k + d_\varepsilon^{k+1}(\tau - t_k)\right]\right\} H(\tau - t_k) \tag{23}$$

The derivative of the Heaviside step function is the Dirac's delta-function. Hence,

$$\begin{aligned}\frac{d}{d\tau}(h_2\varepsilon) = &\left\{h_2^k\left[d_\varepsilon^{k+1}(\tau - t_k)\right] + d_{h2}^{k+1}(\tau - t_k)\left[\varepsilon^k + d_\varepsilon^{k+1}(\tau - t_k)\right]\right\}\delta(\tau - t_k)\\ &+ \left[h_2^k d_\varepsilon^{k+1} + d_{h2}^{k+1}\left(\varepsilon^k\right) + 2d_{h2}^{k+1}d_\varepsilon^{k+1}(\tau - t_k)\right] H(\tau - t_k)\end{aligned} \tag{24}$$

The numerical value of an integral involving delta-function is equal to the function under the sign of integral at $\tau = t_k$. This means that after integration all terms containing $\tau - t_k$ will be equal to null. The remaining (relevant) terms are

$$\frac{d}{d\tau}(h_2\varepsilon) = \left[h_2^k d_\varepsilon^{k+1} + d_{h2}^{k+1}\left(\varepsilon^k\right) + 2d_{h2}^{k+1}d_\varepsilon^{k+1}(\tau - t_k)\right] H(\tau - t_k) \tag{25}$$

Determination of $\Delta\Theta_i^{k+1}$

$\Delta\Theta_i^{k+1}$ is defined by Eq. (9). Substituting expression (25) into (9) we obtain

$$\Delta\Theta_i^{k+1} = \left[h_2^k d_\varepsilon^{k+1} + d_{h2}^{k+1}\varepsilon^k\right]\Delta I_i^{k+1} + 2d_{h2}^{k+1}d_\varepsilon^{k+1}\Delta N_i^{k+1} \tag{26}$$

$$\Delta I_i^{k+1} = \int_{t_k}^{t_{k+1}}\left[\exp\left(-\frac{\psi_{k+1} - \psi'}{\tau_i}\right)\right]d\tau,\ \Delta N_i^{k+1} = \int_{t_k}^{t_{k+1}}\exp\left(-\frac{\psi_{k+1} - \psi'}{\tau_i}\right)(\tau - t_k)\,d\tau \tag{27}$$

Expressions for integrals ΔI_i^{k+1} and ΔN_i^{k+1} have been derived in [15].

$$\Delta \mathrm{I}_i^{k+1} = \frac{a^k}{d_a^{k+1} + \frac{1}{\tau_i}} \left(1 + \frac{\Delta a^{k+1}}{a^k} - \exp\left(-\frac{\Delta \psi_{k+1}}{\tau_i}\right)\right) \tag{28}$$

$$\Delta N_i^{k+1} = \frac{1}{2d_a^{k+1} + \frac{1}{\tau_i}} \left[\Delta t_{k+1} a^{k+1} - a^k \frac{a^{k+1} - a^k \exp\left(-\frac{\Delta \psi_{k+1}}{\tau_i}\right)}{\left(d_a^{k+1} + \frac{1}{\tau_i}\right)}\right] \tag{29}$$

Recursive Expression for S_i^k

Expression (10) for S_i^k can be written as a sum of two integrals

$$S_i^k = \exp\left(-\frac{\Delta \psi_k}{\tau_i}\right) \int_0^{t_{k-1}} \exp\left(-\frac{\psi_{k-1} - \psi'}{\tau_i}\right) \frac{d\,(h_2 \varepsilon)}{d\tau} d\tau + \int_{t_{k-1}}^{t_k} \exp\left(-\frac{\psi_k - \psi'}{\tau_i}\right) \frac{d\,(h_2 \varepsilon)}{d\tau} d\tau \tag{30}$$

The second integral in (30) is $\Delta \Theta_i^k$ defined by (26) and (28), (29). According to definition (10) the first integral in (30) is S_i^{k-1}. Therefore (30) can be rewritten as

$$S_i^k = S_i^{k-1} \exp\left(-\frac{\Delta \psi_k}{\tau_i}\right) + \Delta \Theta_i^k \tag{31}$$

Summary of the Derived Incremental Expressions

$$\Delta \sigma^{k+1} = \Delta E_{\mathrm{r}}^{k+1} \varepsilon^k + E_{\mathrm{r}}^{k+1} \Delta \varepsilon^{k+1} + \sum_i C^i \mathrm{S}_i^k \left(h_1^{k+1} \exp\left(-\frac{\Delta \psi_{k+1}}{\tau_i}\right) - h_1^k\right) + h_1^{k+1} \sum_i C^i \Delta \Theta_i^{k+1} \tag{32}$$

$$\Delta \psi_{k+1} = \frac{\Delta t_{k+1}}{\Delta a^{k+1}} \ln\left(1 + \frac{\Delta a^{k+1}}{a^k}\right) \text{ or } \Delta \psi_{k+1} = \frac{1}{d_a^{k+1}} \ln\left(1 + \frac{d_a^{k+1}}{a^k} \Delta t_{k+1}\right) \tag{33}$$

We redefine $\Delta \mathrm{I}_i^{k+1}$ and ΔN_i^{k+1} given by (28) and (29) as follows

$$\Delta \mathrm{I}_{\mathrm{i}}^{\mathrm{k+1}} = \Delta \mathrm{t}_{\mathrm{k+1}} \Delta \hat{\mathrm{I}}_{\mathrm{i}}^{\mathrm{k+1}} \text{ and } \Delta \mathrm{N}_{\mathrm{i}}^{\mathrm{k+1}} = \Delta \mathrm{t}_{\mathrm{k+1}}^2 \Delta \hat{\mathrm{N}}_{\mathrm{i}}^{\mathrm{k+1}} \tag{34}$$

Substituting (34) in (26) and (26) in (31) we have

$$\Delta \Theta_i^{k+1} = \left[h_2^k \Delta \varepsilon^{k+1} + \Delta h_2^{k+1} \varepsilon^k\right] \Delta \hat{I}_i^{k+1} + 2 \Delta h_2^{k+1} \Delta \varepsilon^{k+1} \Delta \hat{N}_i^{k+1} \tag{35}$$

$$S_i^k = S_i^{k-1} \exp\left(-\frac{\Delta \psi_k}{\tau_i}\right) + \left[h_2^{k-1} \cdot \Delta \hat{I}_i^k + 2 \Delta h_2^k \cdot \Delta \hat{N}_i^k\right] \cdot \Delta \varepsilon^k + \Delta h_2^k \cdot \Delta \hat{I}_i^k \cdot \varepsilon^{k-1} \tag{36}$$

$$\Delta \hat{I}_i^k = \frac{1}{d_a^k + \frac{1}{\tau_i}} \left(d_a^k + \frac{1 - \exp\left(-\frac{\Delta\psi_k}{\tau_i}\right)}{\Delta t_k / a^{k-1}} \right) \tag{37}$$

$$\Delta \hat{N}_i^k = \frac{1}{2d_a^k + \frac{1}{\tau_i}} \left\{ \frac{a^k}{\Delta t_k} - \frac{a^{k-1}}{\Delta t_k \left(d_a^k + \frac{1}{\tau_i}\right)} \frac{a^k - a^{k-1}\exp\left(-\frac{\Delta\psi_k}{\tau_i}\right)}{\Delta t_k} \right\} \tag{38}$$

Incremental Form for Implementation in Software

The equations described in the previous section can be rewritten in a different form:

$$\Delta\sigma^{k+1} = \Delta C^{k+1} \cdot \Delta\varepsilon^{k+1} + \Delta\sigma_R^k \tag{39}$$

In (39)

$$\Delta\sigma_R^k = \Delta E_r^{k+1} \cdot \varepsilon^k + h_1^{k+1} \cdot \Delta h_2^{k+1} \cdot \varepsilon^k \cdot \sum_i C^i \cdot \Delta \hat{I}_i^{k+1} + \Delta h_1^{k+1} \sum_i C^i S_i^k$$

$$-h_1^{k+1} \sum_i C^i S_i^k \left[1 - \exp\left(-\frac{\Delta\psi_{k+1}}{\tau_i}\right) \right] \tag{40}$$

In (40) $\Delta\sigma_R^k$ depends on strain in time instant t_k and before.

$$\Delta C^{k+1} = E_r^{k+1} + h_1^{k+1} \sum_i C^i \left[h_2^k \cdot \Delta \hat{I}_i^{k+1} + 2\Delta h_2^{k+1} \cdot \Delta \hat{N}_i^{k+1} \right] \tag{41}$$

The reduced time is calculated using (33), $\Delta\hat{I}_i^{k+1}$ and $\Delta\hat{N}_i^{k+1}$ are obtained using (37) and (38), and finally S_i^k are calculated using (36).

Numerical Instability

Numerical accuracy problems may be encountered while calculating $1 - \exp\left(-\frac{\Delta\psi_k}{\tau_i}\right)$ for small values of $\frac{\Delta\psi_k}{\tau_i}$. Therefore, if $\frac{\Delta\psi_k}{\tau_i} < \delta$ where δ is small, we must use the general expansion of $1 - \exp(-x) \approx x - \frac{x^2}{2}$ in (40). Substituting this expression in (37) and (38) we obtain

$$\Delta \hat{I}_i^k = \frac{1}{d_a^k + \frac{1}{\tau_i}} \left(d_a^k + \frac{\Delta\psi_k}{\tau_i} \frac{a^{k-1}}{\Delta t_k} \left[1 - \frac{\Delta\psi_k}{2\tau_i} \right] \right) \tag{42}$$

$$\Delta \hat{N}_i^k = \frac{1}{\left(2d_a^k + \frac{1}{\tau_i}\right)\left(d_a^k + \frac{1}{\tau_i}\right)} \left\{ \left(d_a^k\right)^2 + \frac{a^k}{\Delta t_k \tau_i} - \left(\frac{a^{k-1}}{\Delta t_k}\right)^2 \frac{\Delta\psi_k}{\tau_i} \left[1 - \frac{\Delta\psi_k}{2\tau_i} \right] \right\} \tag{43}$$

If, in addition, the term $\frac{\Delta a^k}{a^{k-1}}$ is also very small, approximate expressions (21) and (22) can be used to calculate $\Delta\psi_k$ leading to

$$\Delta\hat{I}_i^k = 1 \tag{44}$$

$$\Delta\hat{N}_i^k = \frac{1}{\left(2d_a^k + \frac{1}{\tau_i}\right)\left(d_a^k + \frac{1}{\tau_i}\right)}\left\{\left(d_a^k\right)^2 + \frac{d_a^k}{\tau_i} + \frac{1}{2\tau_i^2}\right\} \tag{45}$$

Validation of the Viscor Model

We will analyse an example used in [4] to calculate residual stresses and "frozen-in strains" by the path-dependent model. Svanberg et al. [4] obtained the properties of the epoxy system LY5052/HY5052 utilised in this section and presented in Table 1. The shift factor $a(T,\alpha)$ in (32–38) is presented as a product of temperature and DoC dependent functions [10, 11]. In doing so, it becomes possible to decouple the temperature and cure effects on the VE behavior, which is useful if one wishes to study the effects of temperature or cure separately.

$$a\,(T,\alpha) = a_C\,(\alpha)\cdot a_T(T) \tag{46}$$

The a_T, is calculated using the WLF equation and the cure shift factor obtained from [10].

$$\log \mathrm{a_T} = -\frac{\mathrm{c_1\,(T-T_{ref})}}{\mathrm{c_2 + (T-T_{ref})}}, \text{ where } \mathrm{T_{ref}} = 30^{\circ}\mathrm{C}, \mathrm{c_1} = 131.4 \text{ and } \mathrm{c_2} = 614.9\mathrm{K} \tag{47}$$

$$\log a_C = \begin{cases} \left[0.0026\cdot T^2 - 0.0903\cdot T + 1.39\right]\frac{t-100}{60} & 0 < t < t_0 \\ 0 & t_0 \le t \end{cases} \tag{48}$$

In (48) t_0 is the time for full cure at a given temperature. The path-dependent model, is a particular case of the VisCoR model, obtained assuming extreme values of the shift factor above and below the glass T_g, i.e. by redefining (46) as

$$a = \begin{cases} 1\cdot 10^8, & T < T_g \\ 1\cdot 10^{-8}, & T \ge T_g \end{cases} \tag{49}$$

The coefficients in the Prony series are given in Table 2 and the rubbery modulus $E_r = 28\ MPa$. Since Svanberg et al. [4] worked with a thermo-rheologically simple material, we set $h_1 = h_2 = 1$ in the VisCoR model.

Table 1 Material properties used in the simulations [4]

Property	Symbol	Value
Coefficient of chemical shrinkage[a] (CCS) [%]	CCS	$-7/3$
Degree of cure at gelation [−]	α_{gel}	0.5
Uncured glass transition temperature [$^{\circ}C$]	T_g^0	-41
Fully cured glass transition temperature [$^{\circ}C$]	T_g^{∞}	136
Glassy state properties		
Young's modulus [GPa]	E_g	2.6
Coefficient of thermal expansion [$^{\circ}C^{-1}$]	CTE	$71\cdot 10^{-6}$
Rubbery state properties		
Young's modulus [MPa]	E_r	28
Coefficient of thermal expansion [$^{\circ}C^{-1}$]	CTE	$178\cdot 10^{-6}$

[a]Chemical shrinkage is assumed to be the same in both glassy and rubbery state

Table 2 Parameters in the Prony series [16]

τ_i (min)	C_i (MPa)
2.922E01	152.091
2.921E03	170.074
1.824E05	212.677
1.103E07	288.871
2.830E08	393.693
7.943E09	673.423
1.955E11	472.114
3.315E12	152.240
4.917E14	64.880

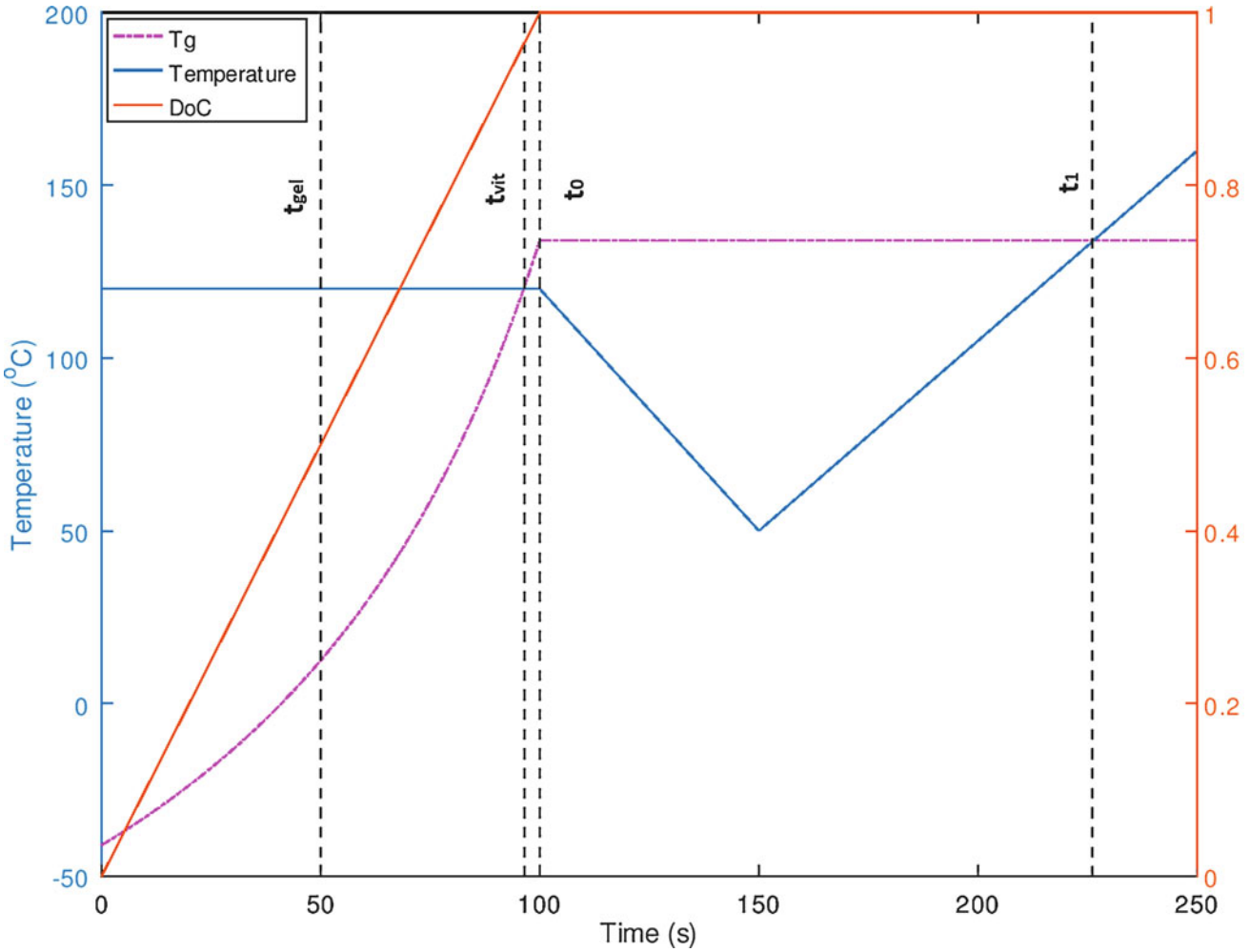

Fig. 1 The DoC and T_g development due to imposed temperature changes. The vertical lines indicate instants for gelation, vitrification, the full cure and the instant when applied temperature goes above the glass transition temperature

In this example, an initially uncured polymer is cured at constant temperature in a closed mould that fully suppresses free expansion/shrinkage. Large stresses build up when the polymer after the curing is cooled down in a closed mould. After that, the polymer is released from the mould leading to zero stresses and "frozen in" strains. The strain recovery (release of "frozen-in" strains) takes place in subsequent heating ramp. The thermal conditions and the DoC profile along with the change of the T_g with cure are shown in Fig. 1. The free expansion strains are $\varepsilon_{thermal}^{free} = CTE \cdot \Delta T$, $\varepsilon_{curing}^{free} = CCS \cdot \Delta\alpha$. The mechanical constraints during the in-mould cure with release after cooling down are described as zero applied strain when the polymer is in the mould and as zero applied stress when it is out of the mould

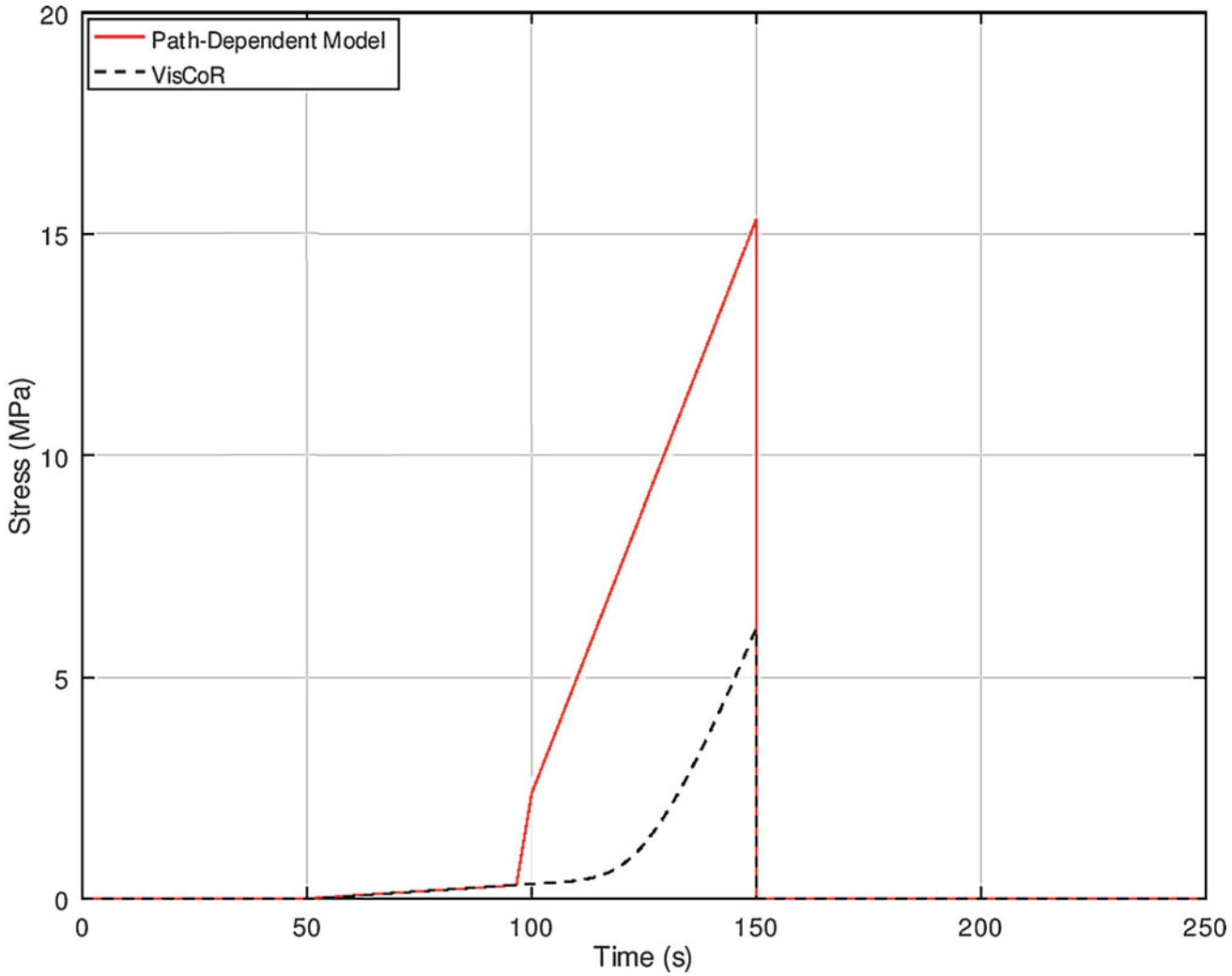

Fig. 2 Stress build up in a polymer during curing and cooling in a closed mold, $\varepsilon_{applied} = 0$, according to (**a**) VisCoR-simple model and (**b**) path dependent model

$$\varepsilon_{applied} = 0, t < 150s \text{ and } \sigma = 0, t \geq 150s \tag{50}$$

As in [4] we assume that the DoC is a linear function of time, with $\alpha = 1$ at $t = t_0$ ($t_0 = 100s$ for curing at $=120^{\circ} C$).

$$\alpha = \left\{ \begin{array}{ll} 0.01 \cdot t, & t < t_0 \\ 1, & t \geq t_0 \end{array} \right\} \tag{51}$$

Parameters in the VisCoR model do not depend on the glass transition temperature, T_g; they depend on DoC and temperature. Nevertheless, $T_g$is a part of the path-dependent model and therefore its increase with time is calculated using

$$T_g = \frac{77 \cdot \alpha}{1 - 0.56 \cdot \alpha} - 41 \tag{52}$$

which is obtained using the DiBenedetto expression [4].

In (46) the $a_T = 1$ at $T_{ref} = 30^{\circ} C$; the cure shift factor $a_C = 1$ when the material is fully cured ($t_0 \geq 100s$).

The build-up of stresses according to the path-dependent model and the VisCoR model is shown in Fig. 2. During the first 100 sec the temperature is kept constant at 120 $^{\circ} C$ and the DoC increases linearly with respect to time. At $t = t_{gel} = 50s$ the degree of cure reaches the gel-point (first vertical line in Fig. 1) and transformation from a liquid to a rubbery state takes

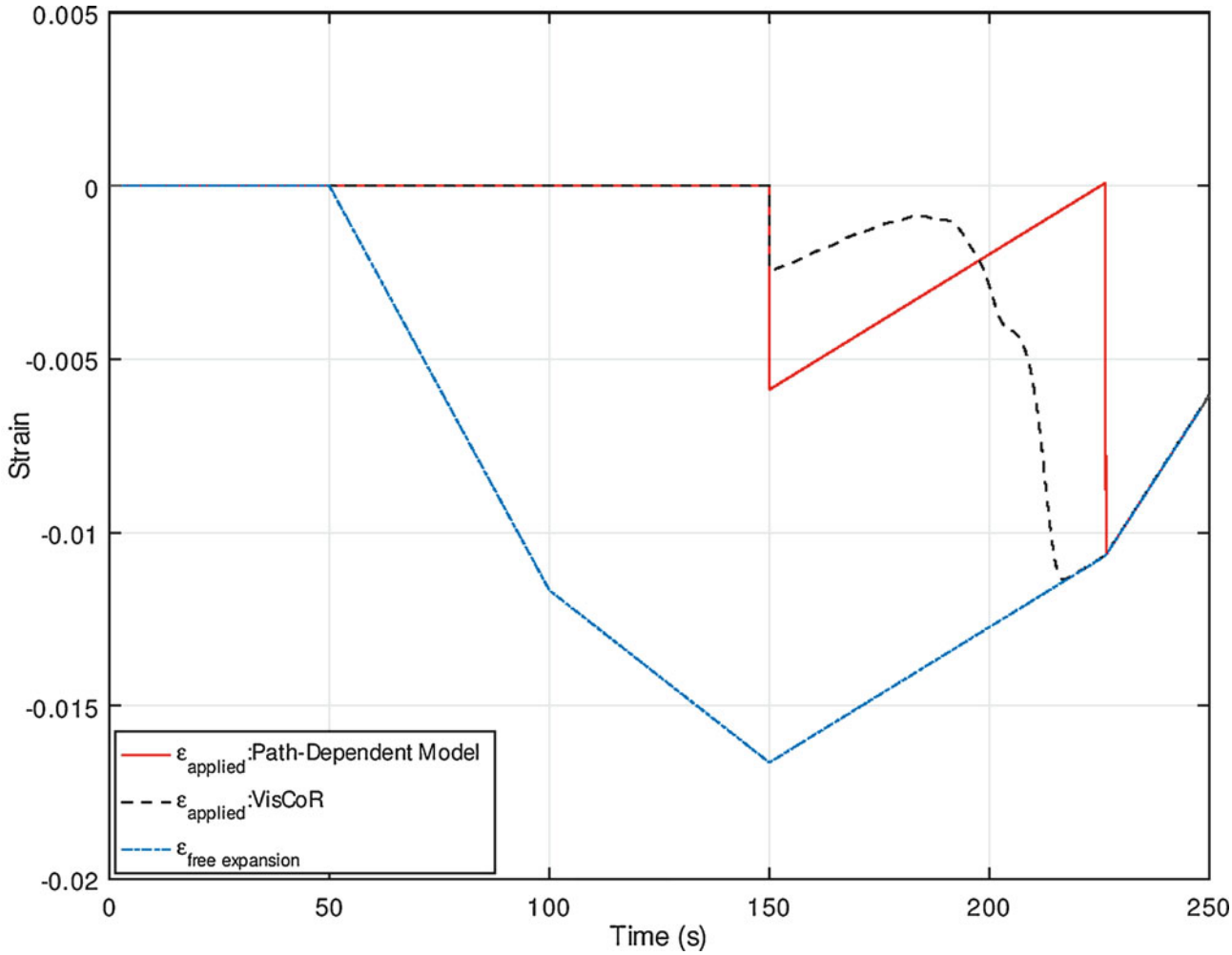

Fig. 3 Macroscopic strain development in the fully cured polymer during loading (see Fig. 1) for both constrained and unconstrained conditions. Dotted line represents the VisCoR model, solid line represents the path dependent model

place. Tensile stresses start to form due to constrained chemical shrinkage, but since stress relaxation in the rubbery state is very fast, the stress is small. The glass transition temperature, T_g increases with increasing DoC according to Eq. (52). At $t = t_{vit} = 96.6s$, (second vertical line in Fig. 1), T_g is equal to the cure temperature and the polymer transforms from a rubber state to glassy state. In the VisCoR model this transition does not require sudden "jump" of the shift factor: it changes with respect to T and DoC according to (47) and (48). The chemical shrinkage continues in the glassy state with the same *CCS*, but the stress relaxation is much slower and stresses from t=96.6 s to 100 s increase faster. At $t = t_0 = 100s$ (the third vertical line in Fig. 1) the material is fully cured and $T_g = 136^{\circ}C$. From t_0 until t=150 s the polymer is cooled with a constant rate from $T = 120^{\circ}C$ to $50^{\circ}C$. Since, see (50), shrinkage is not allowed, tensile stresses are increasing (in the VisCoR model they are partially relaxing while the temperature is still high). Since in the path-dependent model the stress is not allowed to relax, the stress values starting from t_{vit} up to the point of constraint removal at 150 s have been significantly over-predicted.

At $t = 150s$, the zero-strain condition is removed and replaced with zero stress condition, see (50). The strain, $\varepsilon_{applied}$ predicted by the VisCoR model and the path-dependent model is shown in Fig. 3. After the constraint $\varepsilon_{applied} = 0$ is removed the material is free to move, but the strain recovery at this temperature is rather slow (no strain recovery at all in the path-dependent model). The difference between $\varepsilon_{applied}$ and the free expansion strain remains large. When the temperature starts increasing again at t=150 s from 50 °C to 160 °C at t=250 s, the strain recovery becomes faster. It can be seen in the simulation with the VisCoR model that because of strain recovery, the slope of the strain increase during heating is lower than for the free thermal expansion. Accelerating strain recovery towards the free expansion strain is observable at $t = 180s$ and it is completely recovered at around $t = 218s$. In the path-dependent model, the strain is "frozen-in" until $T = T_g$ (136 °C) at $t_1 = 226s$ (fourth vertical line in Fig. 1), when the strain becomes equal to the free expansion strain.

Conclusions

A thermodynamically consistent model, called VisCoR, describing the temperature and degree of cure dependent thermo-rheologically complex material behaviour has been described, derived from Helmholtz free energy systematically using simplifying assumptions. The model is tested against the commonly used linear elastic "path-dependent" model for a curing material under different conditions (constrained curing and unconstrained recovery). It has been found that the path-dependent model, which does not account for viscoelastic relaxation, overestimates stresses that build-up during constrained curing conditions compared to the VisCoR model. Moreover, strain recovery is shown to be a much gradual process that speeds up with increasing temperature using the VisCoR model, rather than an instantaneous recovery of "frozen-in" strains as predicted by the path-dependent model.

References

1. J.M. Svanberg, Predictions of manufacturing induced shape distortions: high performance thermoset composites. Doctoral dissertation, Luleå tekniska universitet, 2002
2. M. Benavente, L. Marcin, A. Courtois, M. Lévesque, E. Ruiz, Numerical analysis of viscoelastic process-induced residual distortions during manufacturing and post-curing. Compos. A: Appl. Sci. Manuf. **107**, 205–216 (2018)
3. A. Johnston, R. Vaziri, A. Poursartip, A plane strain model for process-induced deformation of laminated composite structures. J. Compos. Mater. **35**(16), 1435–1469 (2001)
4. J.M. Svanberg, J.A. Holmberg, Prediction of shape distortions Part I. FE-implementation of a path dependent constitutive model. Compos. Part A **35**, 711–721 (2004)
5. M. Zocher, S. Grooves, D. Allen, A three-dimensional finite element formulation for thermoviscoelastic media. Int. J. Numer. Meth. Eng. **40**, 2267–2288 (1997)
6. M. Machado, U.D. Cakmak, I. Kallai, Z. Major, Thermomechanical viscoelastic analysis of woven-reinforced thermoplastic-matrix composites. Compos. Struct. **157**, 256–264 (2016)
7. Y.K. Kim, S.R. White, Stress relaxation behavior of 3501-6 epoxy resin during cure. Polym. Eng. Sci. **36**(23), 2852–2862 (1996)
8. S.L. Simon, G.B. Mckenna, O. Sindt, Modeling the evolution of the dynamic mechanical properties of a commercial epoxy during cure after gelation. J. Appl. Polym. Sci. **76**(4), 495–508 (2000)
9. D.J. O'Brien, P.T. Mather, S.R. White, Viscoelastic properties of an epoxy resin during cure. J. Compos. Mater. **35**(10), 883–904 (2001)
10. S. Saseendran, M. Wysocki, J. Varna, Evolution of viscoelastic behaviour of a curing LY5052 epoxy resin in the rubbery state. Adv. Compos. Mater. **26**(6), 553–567 (2017)
11. S. Saseendran, M. Wysocki, J. Varna, Evolution of viscoelastic behavior of a curing LY5052 epoxy resin in the glassy state. Adv. Manufact. Polymer Composites Sci. **2**(2), 74–82 (2016)
12. A. Courtois, M. Hirsekorn, N. Vernet, L. Marcin, E. Ruiz, M. Lévesque, Viscoelastic behavior of an epoxy resin during cure: characterization and modeling, in *The 10th International Conference on the Mechanics of Time Dependent Materials*, (Paris, 2016)
13. A. Ding, S. Li, J. Wang, A. Ni, L. Zu, A new path-dependent constitutive model predicting cure-induced distortions in composite structures. Compos. A: Appl. Sci. Manuf. **95**, 183–196 (2017)
14. R.A. Schapery, Nonlinear viscoelastic and viscoplastic constitutive equations based on thermodynamics. Mech. Time Depend. Mater. **1**, 209–240 (1997)
15. S. Saseendran, D. Berglund, J. Varna, *Viscoelastic model with complex rheological behavior (VisCoR): incremental formulation. Submitted to Composites Part A: Applied Science and Manufacturing (Under Review)*
16. J.T. Zhang, M. Zhang, S.X. Li, M.J. Pavier, D.J. Smith, Residual stresses created during curing of a polymer matrix composite using a viscoelastic model. Compos. Sci. Technol. **130**, 20–27 (2016)

Investigating How Microstructural Features Influence Stress Intensities in Pitting Corrosion

Patrick Brewick and Andrew Geltmacher

Abstract Despite the many advances made in material science, stainless steel and aluminum remain the structural materials best-suited for the naval fleet. While these metallic materials offer many benefits, such as high strength and good toughness, their persistent exposure to the maritime environment inevitably leads to issues with corrosion. Among the various manifestations of corrosion, pitting corrosion is of particular concern because the transition of corrosion pits to stress-corrosion cracks can lead to catastrophic failures. Traditional pitting corrosion analyses treat the pit shape as a semi-circle or ellipse and typically assume a growth pattern that maintains the original geometrical shape. However, when the underlying microstructure is incorporated into the model, pit growth is related to the grains surrounding the pit perimeter and the growth rate is proportional to crystallographic orientation. Since each grain has a potentially different orientation, pit growth happens at non-uniform rates leading to irregular geometries, i.e., non-circular and non-elliptical. These irregular pit geometries can further lead to higher stresses.

This work presents a detailed look at corrosion pit growth coupled with mechanical load through a numerical model of a two-dimensional stable corrosion pit. Real microstructural information from a sample of 316 stainless steel is incorporated into the model to analyze microstructural effects on pit growth. Through this work, stress distributions and stress intensity factors are examined for a variety of pit geometries, including comparisons of their range of values to a typical, semi-circular pit. The consequences of these stress distributions and concentration factors are discussed.

Keywords Pitting corrosion · Microstructure · Crystallographic orientation · Computational modeling · Stress intensity factor

Introduction

The evolution of corrosion pits to stress-corrosion cracks remains a scientific challenge in terms of detection, measurement, and prediction capabilities. Many corrosion design limitations are formulated in terms of general corrosion, which is easier to observe and predict than localized corrosion [1]. Thus, pitting corrosion often goes undetected until cracks have initiated and their growth is well advanced. Once initiated, pits can rapidly evolve through an autocatalytic process that results in a localized loss of material that can be hidden by the pit's corrosion products. The hidden nature of pitting damage can cause serious degradation by the time a problem is noticed [2, 3]. In particular, corrosion pits can lead to failure by becoming the initiation sites for stress-corrosion cracking [4, 5]. Some metals, such as the corrosion-resistant steels and marine-grade aluminum alloys used in existing naval platforms, achieve resistance against general corrosion through the formation of a passivation layer; unfortunately, this same layer causes the alloys to be susceptible to pitting corrosion [2, 6, 7].

Advances in material characterization have shown that pitting initiation and growth strongly depend on microstructural features (e.g., grain shape and crystallography, grain boundary character, second-phase precipitates) on the corroding surface [8–13]. Given that pitting corrosion occurs at small spatial and temporal scales, this phenomenon represents an opportunity to leverage computational models for simulation and prediction of the initiation and growth of a given pit geometry. Numerous studies have already applied computational models to various problems concerning pitting corrosion [14–16] and stress-corrosion cracking [17]; however, these studies mainly focus on kinetics at the macroscale, which fails to consider both the underlying microstructure and corrosive environment.

This study is concerned with how microstructure affects pitting corrosion, developing a computational framework to simulate corrosion pit growth that explicitly incorporates experimentally-measured microstructure data while being coupled

P. Brewick (✉) · A. Geltmacher
Multifunctional Materials Branch, Materials Science and Technology Division, Naval Research Laboratory, Washington, DC, USA
e-mail: patrick.brewick@nrl.navy.mil

M. Silberstein et al. (eds.), *Challenges in Mechanics of Time Dependent Materials, Fracture, Fatigue, Failure and Damage Evolution, Volume 2*, Conference Proceedings of the Society for Experimental Mechanics Series, https://doi.org/10.1007/978-3-030-29986-6_12

with mechanical loading. This study considers potential pitting sites on a sample of austenitic stainless steel (316L SS) and examines how the different crystallographic orientations at each site impact the variability of the stress intensity factors.

Background

Underlying Microstructure

An austenitic stainless steel (316L SS) is chosen because of its universal value as a representative of the 300 series stainless steels and the uniformity of its FCC microstructure. The material was obtained from the Sandmeyer Steel Company as 1/4" thick sheet metal in mill-annealed condition. A solution anneal was required to dissolve precipitated chromium carbides resulting from thermal exposure. To achieve this, the sample was heated at 1040 °C for 5 min followed by rapid cooling using a water quench. The chemical composition of the main components of the steel sample, as identified by the supplier, is 17% Cr, 12% Ni, and 71% Fe by mass fraction, with corresponding mole fractions of 18%, 11%, and 71%, respectively. A crystal orientation map of the underlying microstructure (383.5 µm in width by 286 µm in height) is shown in Fig. 1. A brief summary of the procedure for acquiring the microstructure data set is provided in [18]; more complete methodologies can be found in [19] and [20].

Theoretical Background on Pitting Corrosion

A simplified theoretical description of pitting corrosion can be obtained for activation-controlled corrosion with diffusive flow of the electrolyte in the pit. Under these conditions, the electrical resistance of solution is negligible and the solvent is assumed incompressible. In addition, the concentrations of the species are assumed to be below saturation, and there is zero net production of the reactants. Implementing these conditions simplifies the well-known Nernst-Planck mass balance equation to an equation relating the rate of change of concentration to the diffusive flux:

$$\frac{\partial c_i}{\partial t} = \nabla \left(D_i \nabla c_i \right) \tag{1}$$

where c_i is the concentration of the ith species, t is time, ∇ is the gradient operator, and D_i is the diffusion coefficient.

It is assumed that the individual species concentrations c_i comprising the given metal—such as iron, nickel, and chromium in the case of 316 SS—can be replaced with a representative or effective metal ionic concentration c based on the apparent density of the metal and its average molar mass [21]; an average charge number z can be similarly defined. Solving Eq. (1)

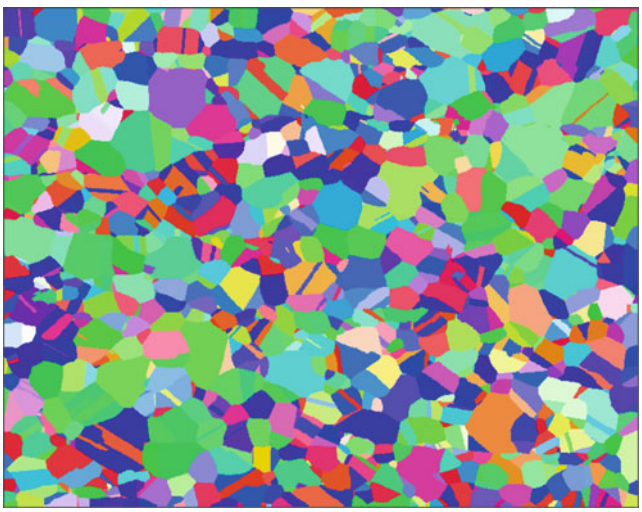

Fig. 1 2D crystal orientation map of 316 SS microstructure showing the microstructure

requires a description of boundary conditions for the effective species concentration or flux, including the flux condition on the metal-electrolyte interface representing the effect of metal dissolution. This boundary condition can be defined as a function of the dissolution current density:

$$D\nabla c \cdot \mathbf{n} = (c_{\text{solid}} - c)\,\frac{i(\eta_a)}{zFc_{\text{solid}}} \tag{2}$$

where D is the apparent diffusivity of the effective ionic concentration and $\mathbf{n}$ is the normal vector along the boundary, making $D\nabla c \cdot \mathbf{n}$ the normal component of ionic flux. Additionally, c_{solid} is the concentration of the solid metal across the interface, F is Faraday's constant, and $i(\eta_a)$ is the effective dissolution (anodic) current density of the over-potential η_a. The effective dissolution current density i is defined by the sum of anodic contributions from all species in the corroding metal, which, for 316 SS, can be written as:

$$i(\eta_a) = \sum_{k=\text{Fe,Cr,Ni}} i_k(\eta_a) \tag{3}$$

Over-potential η_a is taken as the difference between applied potential V_{app} and corrosion potential V_{corr}, i.e., $\eta_a = V_{\text{app}} - V_{\text{corr}}$.

The movement of the pit front is governed by the dissolution of metal during the pitting corrosion process. The functional form of the dissolution current density in terms of contributing potentials can be obtained from potentiodynamic experiments. While numerous functional forms are available, this study adopts a log-linear Butler Volmer relation, as shown in Eq. (4)

$$i\,(\eta_a) = i_{\text{corr}} \exp\left[\frac{zF\alpha\eta_a}{R_{\text{g}}T}\right] \qquad \text{with} \qquad i_{\text{corr}} = zFA_{\text{diss}} \exp\left[\frac{zFV_{\text{app}}}{R_{\text{g}}T}\right] \tag{4}$$

In Eq. (4), i_{corr} is the corrosion or exchange current density, A_{diss} is the dissolution affinity, α is the anodic transfer coefficient, R_{g} is the universal gas constant, and T is the current absolute temperature.

Review of Relevant Solid Mechanics

The Cauchy stress tensor $\boldsymbol{\sigma}$ is defined as

$$\boldsymbol{\sigma} = \mathbf{C} : \boldsymbol{\varepsilon} \tag{5}$$

where $\mathbf{C}$ is the 4th order elasticity tensor and $\boldsymbol{\varepsilon}$ is the strain tensor. Symmetry allows the 4th order elasticity tensor to be represented as a 6×6 matrix. As 316L SS is a crystalline material with an FCC system, its elasticity tensor can be further reduced to three independent elements, C_{11}, C_{12}, and C_{44}, with relevant values for 316 SS reported in [22, 23].

Computational Modeling Framework

Model Construction

The theoretical descriptions of pitting corrosion and solid mechanics are implemented through the finite element-based commercial software COMSOL Multiphysics. Full microstructural information is provided to a subset of the solid metallic domain within the model, as shown in Fig. 2; the remaining portions of the metallic domain are treated as homogeneous and assigned bulk properties for Young's modulus and Poisson's ratio based on [23]. The geometric dimensions and physical parameters included in the computational model are listed in Table 1 with their assigned values. The crystallographic orientation information for the microstructural region of the metallic domain is extracted from the 316 SS experimental data set. The microstructural area in the model has dimensions of 200 µm in width by 140 µm in height, which constitutes only a portion of the experimental microstructure data set. In an effort to fully explore the experimental microstructure, the location of the pit is varied by moving the center of the pit across the data set in increments of 15 µm in the x direction

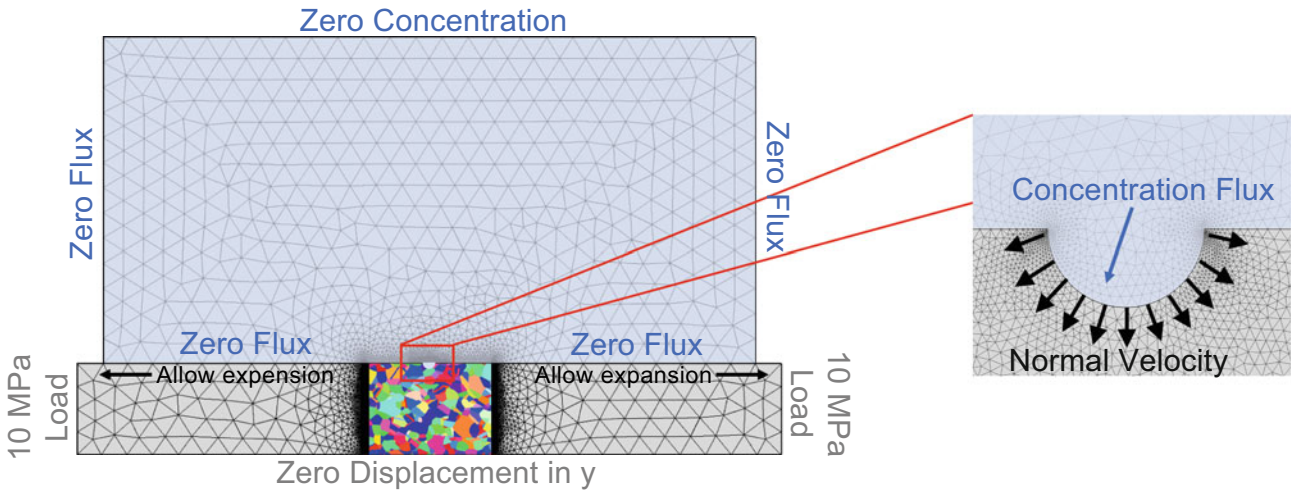

Fig. 2 An illustrated schematic of the problem domain with a close-up for the initial pit. The boundary conditions in blue are for mass transfer due to diffusion (electrolyte domain), those in gray are for the solid mechanics, and those in black are for the meshing. Note that the underlying finite element mesh is also shown

Table 1 Geometric and physical model parameters for 316 SS

Name	Value	Description
Geometric parameters		
h_e	500×10^{-6} m	Height of the electrolyte domain
h_m	140×10^{-6} m	Height of the metal domain
w	1000×10^{-6} m	Width of the both domains
r	5×10^{-6} m	Initial pit radius
Physical parameters		
α	0.65	Transfer coefficient
A_{diss}	4×10^4 mol/m^2·s	Dissolution affinity
c_{solid}	143×10^3 mol/m^3	Average steel concentration
D_0	8.5×10^{-10} m^2/s	Apparent diffusivity of metal ions
$\overline{E}_{corr}$	−0.24 V	Polycrystalline corrosion potential
E_{app}	−0.14 V	Applied potential
F	96485 C/mol	Faraday's constant
G	210 GPa	Young's modulus of steel
ν	0.33	Poisson's ratio of steel
ρ_m	7800 kg/m^3	Nominal stainless steel density
R	8.315 J/(mol K)	Universal gas constant
T	298.15 K	Current absolute temperature
z	2.19	Average charge number for steel

(width) and 20 µm in the y direction (height), with an initial location for the pit center at (100 µm, 145 µm). Using these step size increments, the pit is initiated at a total of 104 locations within the experimental microstructure, i.e., the microstructure can be used to create 104 model instances.

Incorporation of Microstructural Effects on Corrosion

This study adopts the same approach for incorporating and modeling the influence of microstructure on corrosion as discussed in Brewick et al. [18]; therefore, only a brief summary is provided herein. Within the model, it is assumed that no mass transport occurs on the metallic side of the corrosion front while the metal interfacing with the electrolyte dissolves. The influence of the metal on pit growth manifests through the definition of the anodic current density as a function of an applied over-potential (see Eq. (4)); thus, the dependence of the polarization behavior on the metal, via its crystallographic

orientation, gives rise to the influence of the microstructure on the corrosion response. A few assumptions are utilized to define this relationship.

First, following [21], the polycrystalline corrosion potential $\overline{E}_{\text{corr}}$ is assumed to be equal to $-0.24\,\text{V}$ based on experimental data for 304 SS (in 3% NaCl solution) [24]. From this assumption, one can imply the following:

$$\overline{E}_{\text{corr}} = \frac{1}{n}\sum_{j=1}^{n} {}_{j}E_{\text{corr}}^{\text{CD}} = -0.24\ \text{V} \tag{6}$$

where ${}_{j}E_{\text{corr}}^{\text{CD}}$ is the corrosion potential of the jth crystallographic orientation CD and n is the number of sampled crystal planes. Secondly, pitting potential data on face-centered cubic (FCC) aluminum [25] suggest that the [001] and [111] directions have the minimum and maximum potentials (in terms of magnitude), respectively, in with a maximum spread of 6%. It is therefore assumed that, since 316 SS has the same crystalline structure, its corrosion potential would exhibit a similar dependency on crystallographic orientation and the maximum spread or variation would be of the same order of magnitude. A variation of approximately $\pm 2.5\%$ about $E_{\text{corr}}^{\text{CD}}$ (5% maximum variation) is used in this study. It is further assumed that $E_{\text{corr}}^{[001]} = 0.975\overline{E}_{\text{corr}}$, where $E_{\text{corr}}^{[001]}$ is the corrosion potential in the [001] crystallographic direction, to ensure that the minimum potential occurs in the [001] direction. Finally, it is assumed that the potential in any crystal direction varies linearly with $E_{\text{corr}}^{[001]}$ based on its projection (using the dot product) in the [001] direction.

The determination of local potential E_{corr} on the pit front requires knowledge of the crystallographic direction along the normal at that location. Electron backscatter diffraction yields a grain map that provides the crystallographic orientation with respect to the sample reference frame at each pixel in terms of the three Euler angles (ϕ_1, Φ, ϕ_2); these data are obtained at 0.5-ţm spacing on a regular 2D grid. During the simulation, the unit normal vector at some mesh location (x, y) on the corrosion front is mapped into the local crystal coordinate system (1, 2) using the coordinate transformation:

$$\mathbf{n}_{1,2}(\phi_1, \Phi, \phi_2) = \mathbf{G}(\phi_1, \Phi, \phi_2) \cdot \mathbf{n}(x, y) \tag{7}$$

where $\mathbf{n}_{1,2}$, $\mathbf{n}$, and $\mathbf{G}$ are the unit normal vectors in crystallographic orientation space and the global coordinate space and the transformation tensor, respectively. The Euler angles at given location (x,y) are obtained through nearest neighbor interpolation of the larger data set.

Influence of Microstructure on Solid Mechanics

The elastic constants within the microstructural area of the model experience a transformation similar to that for the pitting potentials. Based on the Euler angle information, the 6×6 elastic tensor is rotated to provide the local elastic constant information. Since the transformation tensor $\mathbf{G}$ is given as a 3×3 matrix, its axis system has to be transformed into a 6×6 second-order rotation matrix $\mathbf{R}$ prior to application to the elastic tensor [26]. The local elastic tensor $\mathbf{C}_{1,2}$ is computed as

$$\mathbf{C}_{1,2} = \mathbf{R}^{\text{T}}\mathbf{C}(x, y)\mathbf{R} \tag{8}$$

where $\mathbf{C}(x, y)$ and $\mathbf{C}_{1,2}$ represent the elastic tensors in the global coordinate and crystallographic orientation spaces, respectively. Nearest neighbor interpolation of Euler angles from the underlying crystal orientation map is also employed here.

Numerical Implementation

Figure 2 provides a sample illustration of the numerical problem domain. For the mechanical boundary conditions, a tensile load of 10 MPa is applied along either vertical boundary of the solid domain, putting the sample in two-sided tension. To prevent rigid body motion, zero displacement in the y direction is prescribed along the bottom of the solid domain, and the point along the bottom of the solid domain at $x = 0$ is fixed.

The critical electro-chemical boundary conditions are those enforced on the microstructure-electrolyte interface. (Note this interface is initially composed of the semi-circular pit boundary with horizontal boundaries on either side.) The species

concentration flux condition (Eq. (2)) is enforced along the semi-circular boundary of the pit, whereas zero flux is specified along the rest of the planar metal/electrolyte interface. Similarly, the normal velocity of the front due to anodic dissolution is prescribed along the semi-circular boundary. The horizontal boundaries along the top of the solid domain allow for expansion as the pit grows but only in the global x-direction. The velocity of these boundaries is related to that of their respective pit vertices, i.e., the intersections of the horizontal boundary and pit mouth on either side.

A typical mesh for the complete problem domain (solid and electrolyte) results in approximately 92,000 elements and 440,000 degrees of freedom; there is some slight variation since a new mesh is generated for each model instance. In addition to mesh density, further consideration for both accuracy and performance is given to the numerical solver for the mesh. The multifrontal massively parallel sparse (MUMPS) direct solver is used and tolerances for relative error (10^{-6}) and scaled absolute error (10^{-4}) are prescribed. Using these settings, stable pit growth is simulated for 80 s in each model instance.

Results and Discussion

Homogeneous Case

Initially, a case with no variation in corrosion potential or elastic constants, representing the homogeneous (bulk) material without the effect of microstructure, is simulated. For this case, the corrosion potential is set as $E_{\text{corr}} = -0.24$ V and the mechanical response in the microstructural area is governed by the Young's modulus and Poisson's ratio given in Table 1. Figure 3a presents a close-up view of the evolved pit after 80 s of simulation time. Since the homogeneity promotes uniform pit growth, the pit retains its semi-circular shape with the pit radius growing uniformly in the radial direction.

Microstructure Cases

Among the 104 model instances with microstructural information, 84 were free of numerical artifacts and achieved the full 80 s of simulation time; meshing issues are primarily responsible for the few cases that failed to complete the simulation. Figure 3 displays evolved pits produced at two different locations in the microstructure. While the pit boundaries maintain aspects of their initial semi-circular shape, they clearly exhibit non-uniform growth, producing irregular changes in pit shape. Figure 3 also shows contours of the first principal stress, demonstrating that the unusual pit morphologies lead to higher stresses than the homogeneous case—note that the scale of the color bar has a slightly lower maximum value for the homogeneous case. However, the stress is still generally concentrated near the mid-line ($x = 0$) on the pit boundary.

A histogram showing the relative distribution of the maximum first principal stress is given in Fig. 4, showing that 75% of the pit locations have a maximum stress greater than that from the homogeneous case. Figure 4 also demonstrates that, while most of the maximum stress values are concentrated in the range 25–45 MPa, a few cases exceed 50 MPa. Since all model instances are subjected to the same applied load, a congruous plot can be made for stress concentrations by normalizing the maximum stress values by the nominal applied stress of 10 MPa. Thus, whether considering maximum

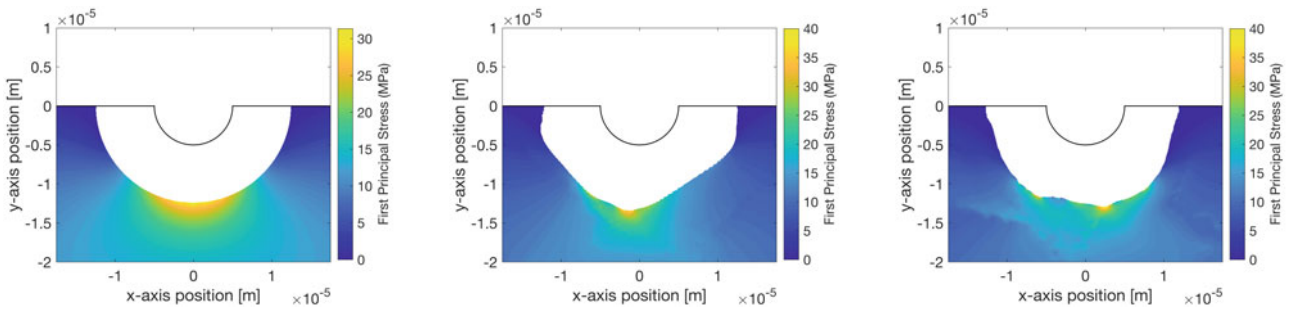

Fig. 3 Evolved pit shapes and first principal stress contours after 80 s of simulation time at several different locations in microstructure. Note that the subfigure captions refer to the coordinates of the pit center within the experimental microstructure. (**a**) Homogeneous case. (**b**) (175 ţm, 245 ţm). (**c**) (280 ţm, 225 ţm)

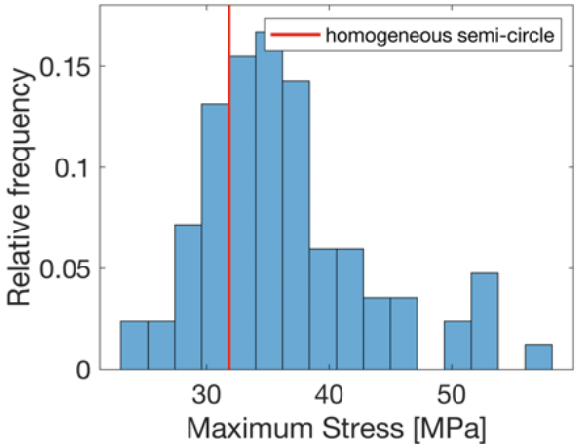

Fig. 4 Probability density plot comparing maximum stress for each evolved pit location among the 84 microstructure cases against the corresponding values for the homogeneous case

stress or stress concentrations, the microstructure cases can be shown to produce values nearly two times larger than that for the homogeneous semi-circular case.

Stress Intensity Factors

While stress intensity factors (SIFs) were originally developed in the context of cracks, corrosion pits can be treated as surface defects, and their corresponding SIFs can be computed by evaluating the J-integral along a path Γ surrounding the pit. In a two-dimensional domain, the J-integral is defined as

$$J = \int_{\Gamma} \left(W \mathrm{d}x_2 - t_i \frac{\partial u_i}{\partial x_1} \mathrm{d}s \right) \tag{9}$$

where $W(x_1, x_2)$ is the strain energy density, $\mathbf{t}$ is the surface traction vector, $\mathbf{u}$ is the displacement vector, and x_1 and x_2 are the coordinate directions. Since the J-integral is path-independent (the metallic solid domain behaves linear elastically), the SIF under mode I loading (K_I) can be evaluated for plane strain conditions as

$$K_{\mathrm{I}} = \sqrt{\frac{JE}{(1-\nu^2)}} \tag{10}$$

where E is the Young's modulus and ν is Poisson's ratio.

Using Eqs. (9) and (10), SIFs are calculated for each model instance, and the results are plotted in Fig. 5. The SIF found by evaluating the J-integral for the homogeneous semi-circular pit after 80 s of simulation time serves as a baseline for comparison. From Fig. 5 it can be observed that only about 30% of the SIFs from the evolved microstructure-influenced pits are of greater magnitude than that for the semi-circular case.

It is interesting to compare Figs. 4 and 5 because they seem to present conflicting observations in that Fig. 4 shows that the microstructure can produce much larger stress values where as Fig. 5 demonstrates that the SIFs are comparable, if not smaller, for the microstructural cases. This is significant in that it exhibits how the microstructure directly influences pit morphologies, producing irregular and non-smooth pit surfaces that lead to large stresses and high stress concentrations, but, as the same time, the impact of microstructure is more muted when considering the stress intensity factor of the sample. Thus, microstructure can be shown to produce a significant *local* effect but a much more limited *global* impact. It should be acknowledged that the maximum stress is an extremely important measure, especially as it approaches the yield stress of a given material; however, SIFs are commonly deployed tool for fracture and failure analysis.

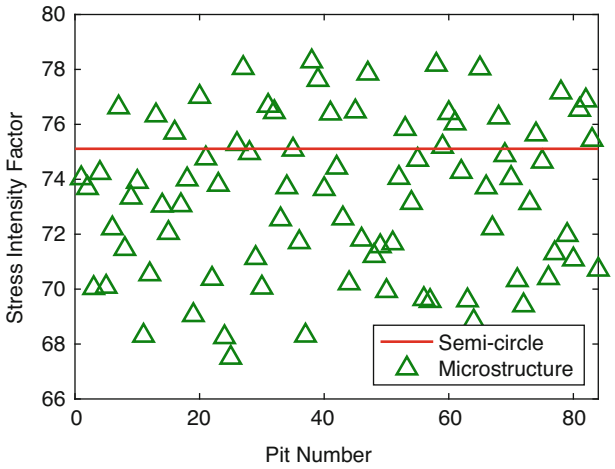

Fig. 5 Comparison of SIF from semi-circular case against those from the microstructure-sensitive cases computed using the J-integral method and the equations from with a variety of assumptions for pit radius R

Conclusions

This preliminary study emphasizes the role that microstructure plays in the pitting corrosion process. The dependence of corrosion potential on crystallographic orientation results in non-uniform current densities and, thus, non-uniform normal velocities along the pit front, which result in irregular pit morphologies. When a load is applied, it was shown that these irregular pit morphologies can yield larger stresses and stress concentrations than the idealized semi-circular case. Interestingly, the stress intensity factors (SIFs) did not evince the same trend, as the homogeneous case produced a SIF greater than nearly 70% of the microstructural cases. Thus, the influence of microstructure is shown to have a greater impact on local quantities (maximum stress) than global measures (SIFs). This suggests that bulk material and standard geometry assumptions can be appropriate for design purposes but also implies that material failures are likely microstructure dominated by microstructural features. Therefore, future studies should continue investigating how cracks initiate and propagate from corrosion pits to further the understanding of a microstructure's influence on stress-corrosion cracking.

References

1. S.M. Sharland, C.P. Jackson, A.J. Diver, A finite-element model of the propagation of corrosion crevices and pits. Corros. Sci. **29**(9), 1149–1166 (1989)
2. G.S. Frankel, Pitting corrosion of metals: a review of the critical factors. J. Electrochem. Soc. **145**(6), 2186–2198 (1998)
3. J. Bhandari, F. Khan, R. Abbassi, V. Garaniya, R. Ojeda, Modelling of pitting corrosion in marine and offshore steel structures – a technical review. J. Loss Prev. Process Ind. **37**, 39–62 (2015)
4. G.S. Chen, K.C. Wan, M. Gao, R.P. Wei, T.H. Flournoy, Transition from pitting to fatigue crack growth - modeling of corrosion fatigue crack nucleation in a 2024-T3 aluminum alloy. Mater. Sci. Eng. A **219**(1–2), 126–132 (1996)
5. B.J. Connolly, D.A. Homer, S.J. Fox, A.J. Davenport, C. Padovani, S. Zhou, A. Turnbull, M. Preuss, N.P. Stevens, T.J. Marrow, J.Y. Buffiere, E. Boller, A. Groso, M. Stampanoni, X-ray microtomography studies of localised corrosion and transitions to stress corrosion cracking. Mater. Sci. Technol. **22**(9), 1076–1085 (2006)
6. K.S. Siow, T.Y. Song, J.H. Qiu, Pitting corrosion of duplex stainless steels. Anti-Corros.Methods Mater. **48**(1), 31–36 (2001)
7. P.M. Natishan, W.E. O'Grady, Chloride ion interactions with oxide-covered aluminum leading to pitting corrosion: a review. J. Electrochem. Soc. **161**(9), C421–C432 (2014)
8. Y.S. Lim, J.S. Kim, S.J. Ahn, H.S. Kvvon, Y. Katada, The influences of microstructure and nitrogen alloying on pitting corrosion of type 316L and 20 wt.% Mn-substituted type 316L stainless steels. Corros. Sci. **43**(1), 53–68 (2001)
9. A. Di Schino, J.M. Kenny, Effect of grain size on the corrosion resistance of a high nitrogen-low nickel austenitic stainless steel. J. Mater. Sci. Lett. **21**(24), 1969–1971 (2002)
10. Z. Cvijović, G. Radenković, Microstructure and pitting corrosion resistance of annealed duplex stainless steel. Corros. Sci. **48**(12), 3887–3906 (2006)
11. A.S. Hamada, L.P. Karjalainen, M.C. Somani, Electrochemical corrosion behaviour of a novel submicron-grained austenitic stainless steel in an acidic NACL solution. Mater. Sci. Eng. A **431**(1–2), 211–217 (2006)

12. J. Guo, S. Yang, C. Shang, Y. Wang, X. He, Influence of carbon content and microstructure on corrosion behaviour of low alloy steels in a Cl− containing environment. Corros. Sci. **51**(2):242–251 (2009)
13. A. Shahryari, J.A. Szpunar, S. Omanovic, The influence of crystallographic orientation distribution on 316LVM stainless steel pitting behavior. Corros. Sci. **51**(3), 677–682 (2009)
14. N.J. Laycock, S.P. White, Computer simulation of single pit propagation in stainless steel under potentiostatic control. J. Electrochem. Soc. **148**(7), B264–B275 (2001)
15. S. Scheiner, C. Hellmich, Finite volume model for diffusion- and activation-controlled pitting corrosion of stainless steel. Comput. Methods Appl. Mech. Eng. **198**(37–40), 2898–2910 (2009).
16. A.S. Vagbharathi, S., Gopalakrishnan, An extended finite-element model coupled with level set method for analysis of growth of corrosion pits in metallic structures. Proc. R. Soc. A: Math. Phys. Eng. Sci. **470**(2168), 20140001 (2014)
17. M.R. Wenman, K.R. Trethewey, S.E. Jarman, P.R. Chard-Tuckey, A finite-element computational model of chloride-induced transgranular stress-corrosion cracking of austenitic stainless steel. Acta Mater. **56**(16), 4125–4136 (2008)
18. P.T. Brewick, N. Kota, A.C. Lewis, V.G. DeGiorgi, A.B. Geltmacher, S.M. Qidwai, Microstructure-sensitive modeling of pitting corrosion: effect of the crystallographic orientation. Corros. Sci. **129**, 54–69 (2017)
19. D.J. Rowenhorst, A. Gupta, C.R. Feng, G. Spanos, 3D crystallographic and morphological analysis of coarse martensite: combining EBSD and serial sectioning. Scr. Mater. **55**(1), 11–16 (2006)
20. G. Spanos, A.B. Geltmacher, A.C. Lewis, J.F. Bingert, M. Mehl, D. Papaconstantopoulos, Y. Mishin, A. Gupta, P. Matic, 0. Mater. Sci. Eng. A **452–453**, 558–568 (2007)
21. S. Scheiner, C. Hellmich, Stable pitting corrosion of stainless steel as diffusion-controlled dissolution process with a sharp moving electrode boundary. Corros. Sci. **49**(2), 319–346 (2007)
22. H.M. Ledbetter, Predicted single-crystal elastic constants of stainless-steel 316. Br. J. Non-Destructive Test. **23**, 286–287 (1981)
23. A. Teklu, H. Ledbetter, S. Kim, L.A. Boatner, M. McGuire, V. Keppens, Single-crystal elastic constants of Fe-15Ni-15Cr alloy. Metall. Mater. Trans. A **35**(10), 3149–3154 (2004)
24. S. Chaudhari, S.R., Sainkar, P.P. Patil, Poly(o-ethylaniline) coatings for stainless steel protection. Prog. Org. Coat. **58**(1), 54–63 (2007)
25. M. Yasuda, F. Weinberg, D. Tromans, Pitting corrosion of Al and Al-Cu single crystals. J. Electrochem. Soc. **137**(12), 3708–3715 (1990)
26. M. Moesen, L. Cardoso, S.C. Cowin, A symmetry invariant formulation of the relationship between the elasticity tensor and the fabric tensor. Mech. Mater. Int. J. **54**, 70–83, 11 (2012)

Evaluating the Influence of Size Effects on Load-Displacement Behavior and Failure in Threaded Fasteners, Part I: Experimental Testing

Thomas R. Bosiljevac, Yuriy B. Veytskin, John P. Mersch, Jeffrey A. Smith, Peter W. Grimmer, and Donald F. Susan

Abstract In an effort to enhance both the experimental testing and computational modeling of small threaded fasteners, a collaborative investigation consisting of experimental tensile testing and computational modeling was conducted to observe the effects of threaded fastener size on load-displacement behavior and failure. This paper focuses on the experimental tests performed on NAS1351N00–4, NAS1352N02–6, NAS1352N04–8, NAS1352N06–10, and NAS1352N4–24 (referred to herein as #00, #02, #04, #06 and #4, respectively) A286 fasteners. Displacement measurements were obtained from three unique sources/locations: Differential Variable Reluctance Transducers (DVRTs) inserted in the top bushing to measure the relative displacement of the bushing faces, Linear Variable Differential Transducers (LVDTs) located on the outside edge of the bushing fixtures to measure a more global response of the bushing displacement, and the stroke of the test frame. This test series clarified many ambiguities in the experimental process and further established a feasible testing method for small fasteners.

Keywords Threaded fastener · Tensile test · Fixture · Bushing · DVRT

Introduction

The engineering analysis community has become increasingly interested in the simulation of threaded fastener dependent structures and is relying on the integrity of simulations as a key component of the engineering design and qualification process. Since threaded fasteners are common components making up jointed connections of various geometrical shapes, sizes, and applications, this paper presents a renewed focus on experimental testing of threaded fastener size effects related to load-displacement behavior and failure. From this endeavor, advanced experimental testing methods related to fixturing and relative displacement measurements of the threaded fasteners have been implemented to clarify the experimental process discussed in previous papers describing the test [1–3].

Prior experimental tensile testing utilized fixturing based on the use of the NASM1312–2 method [4] using two sources of displacement measurements to characterize the threaded fasteners. The first source was the stroke associated with the test frame actuator and the second consisted of mounting LVDTs to the fixture. The compliance in the load frame in conjunction with the location of the LVDTs resulted in rethinking the experimental testing techniques related to threaded fastener behavior and response. In addition, the NASM1312–2 fixture was thought to influence the characteristics of small threaded fasteners due to the suspended weight applied to the fastener by the fixture during initial test setup and how this resulting setup-based preload might influence the load-displacement response. By improving both the proximity of the displacement sensors to the threaded fasteners and reducing the fixture weight effects during test setup provides better data validation to simulate the behavior of small threaded fasteners.

T. R. Bosiljevac (✉)
R&D S&E Mechanical Engineering, Experimental Environment Simulation, Sandia National Laboratories, Albuquerque, NM, USA
e-mail: trbosil@sandia.gov

Y. B. Veytskin
Advanced Characterization & Processing Group, Savannah River National Laboratory, Aiken, SC, USA

J. P. Mersch · J. A. Smith · P. W. Grimmer
R&D S&E Mechanical Engineering, Component Science & Mechanics, Sandia National Laboratories, Albuquerque, NM, USA

D. F. Susan
R&D S&E Mechanical Engineering, Materials Science, Sandia National Laboratories, Albuquerque, NM, USA

M. Silberstein et al. (eds.), *Challenges in Mechanics of Time Dependent Materials, Fracture, Fatigue, Failure and Damage Evolution, Volume 2*, Conference Proceedings of the Society for Experimental Mechanics Series, https://doi.org/10.1007/978-3-030-29986-6_13

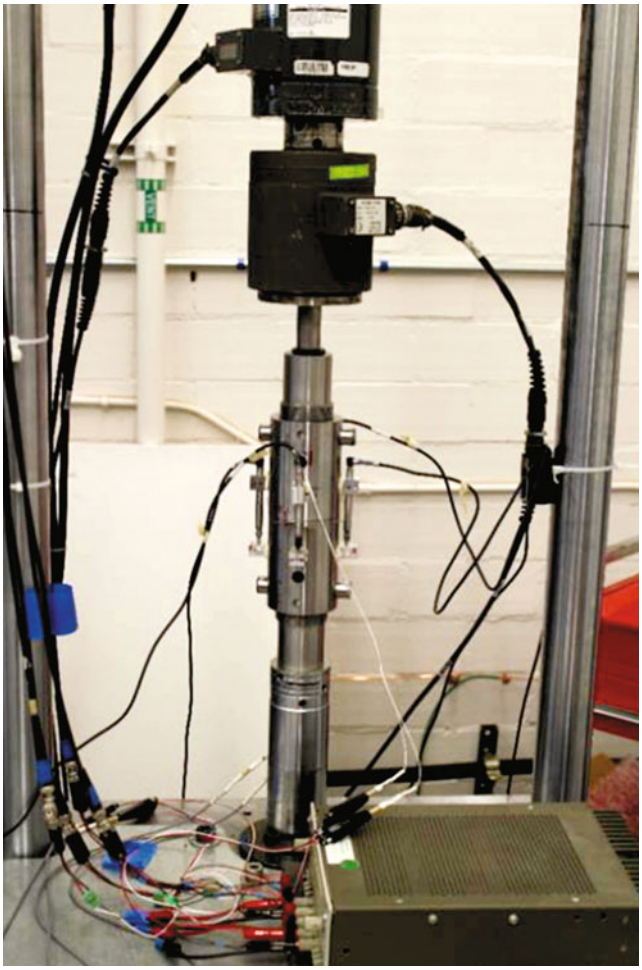

Fig. 1 Tensile test setup in 100 kN load frame

Fixturing

The new test fixture and bushing design, introduced in this paper, focused on allowing a lighter test fixture to be used while minimizing compliance issues in the load train. A view of the fixture assembly with bushings is shown in Fig. 1. Additionally, the new fixture design would allow localized displacement measurements to be obtained closer to the region around the threaded fastener for the first time. The concept was to allow quasistatic tensile tests to be performed on small threaded fasteners ranging in size from #00 to #4. The specific bushings fabricated for use in the threaded fastener test series were designed based on the NAS1351 and NAS1352 datasheets [5, 6] for A286 stainless steel fasteners #00, #02, #04, #06 and #4, respectively. The A286 threaded fasteners are shown below in Fig. 2. Calibrated measurements for each fastener specimen were measured prior to testing. The new fixture utilized a redesigned test fixture referenced in the NASM1312–2 standard and bushing combination made of 4340 steel heat treated to 42–46 Rockwell hardness (Rc).

Before each series of threaded fastener tests began, several calibration checks were run to determine the behavioral relationship between stroke, LVDTs, and DVRTs. Ideally, the relationship would be as close as possible to a 1:1 with the stroke.

Results

Trends for these tests can be difficult to evaluate in load-displacement space because the area and gage length vary amongst the different size fasteners. Therefore, the load-displacement responses were converted to stress-strain using the threaded

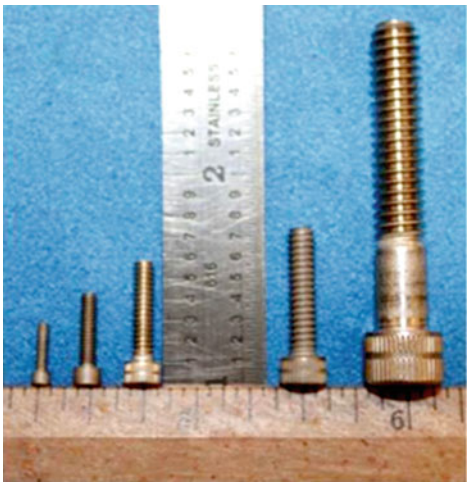

Fig. 2 A286 Threaded Fasteners [8]

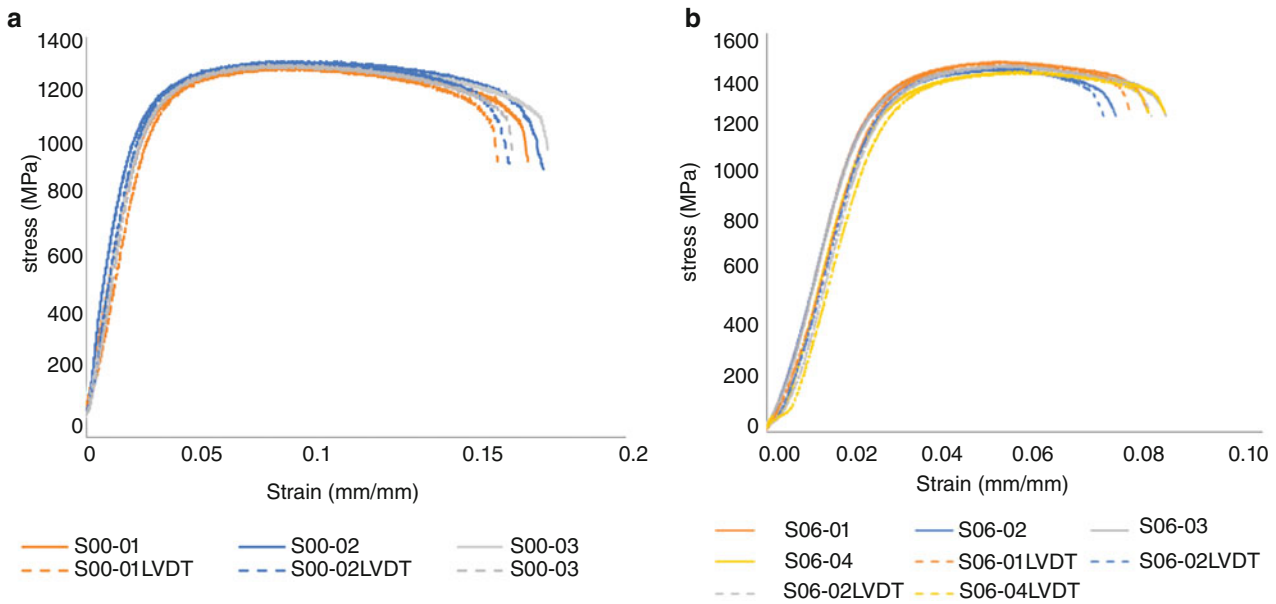

Fig. 3 LVDT and DVRT stress-strain curves for (**a**) #00 and (**b**) #06

tensile stress area calculation referenced in ASME B1.1–2003 [7] and the gage length of the tested fastener based on the cap head seat distance of each sensor bushing. The quasistatic tensile test stress-strain curves for the #00 and #06 threaded fastener sizes are shown below in Fig. 3. Each of the stress-strain curves includes strains based on the DVRT and the LVDT measurements. DVRT-related normalized displacements were obtained by taking the average displacements from only three of the four sensors (DVRT1, DVRT2 and DVRT4, respectively). The LVDT-related normalized displacements were based on taking an average from all four sensors. The DVRT stress-strain curves for each threaded fastener size are shown as a solid line, while the LVDT load-displacement curves are shown with dashed lines. The stress-strain curves provide clear insight related to the size relationship on load-displacement behavior and failure in the threaded fasteners.

Conclusion

A collaborative investigation consisting of experimental tensile testing and computational modeling [8] was conducted to observe the effects of threaded fastener size on load-displacement behavior and failure. The quasistatic tensile testing and

the forth coming microstructural investigations show a threaded fastener size relationship based upon stress-strain behavior, including ultimate tensile strength, ductility, and absorbed energy.

The placement of DVRT sensors closer to the threaded fastener being tested, in conjunction with LVDTs, has allowed localized displacements around the threaded fastener region to be measured, but the experimental testing of small fasteners using DVRTs still requires refinement regarding sensor shielding, calibration techniques, and calibration checks to further characterize and enhance the reliability of these displacement measurement techniques.

Future work should attempt to link specification and manufacturing information to the stress-strain response of a given fastener to improve blind predictions of fastener performance in the absence of direct test data on the fastener of interest.

Acknowledgement The authors would like to thank Edmundo Corona of Sandia National Laboratories for feedback and refinement to promote a collaborative atmosphere. Sandia National Laboratories is a multimission laboratory managed and operated by National Technology and Engineering Solutions of Sandia, LLC, a wholly owned subsidiary of Honeywell International, Inc., for the U.S. Department of Energy's National Nuclear Security Administration under contract DE-NA0003525.

References

1. J.P. Mersch, J.A. Smith, E.P. Johnson, *A Case Study for the Low Fidelity Modeling of Threaded Fasteners Subject to Tensile Loadings at Low and High Strain Rates, ASME Pressure Vessels and Piping Conference, PVP2017–65518* (ASME, Waikoloa, HI, 2017)
2. J.P. Mersch, J.A. Smith, E.P. Johnson, T. Bosiljevac, *Evaluating the Performance of Fasteners Subjected to Multiple Loadings and Loading Rates and Identifying Sensitivities of the Modeling Process, 2018 AIAA/ASCE/AHS/ASC Structures, Structural Dynamics, and Materials Conference* (AIAA SciTech Forum, AIAA2018-1896, Kissimmee, FL, 2018)
3. P. Grimmer, A. Barrios, M. Stossel, J. Mersch, J. Smith, J. Emery, G. Castelluccio, *Evaluation of the Nonlinear Mechanical Response of Threaded Fasteners* (NAFEMS CAASE, Cleveland, OH, 2018)
4. AIA/NAS—Aerospace Industries Association of America Inc., *English—Fastener Test Methods-Method 2- Interactions, AIA/NAS NASM1312–2*, (2012)
5. AIA/NAS—Aerospace Industries Association of America Inc., *English—Screw, Cap, Socket Head, Undrilled and Drilled, Plain and Self-Locking, Alloy Steel, Corrosion-Resistant Steel and Heat-Resistant Steel, UNRF-3A—Rev 10, AIA/NAS NAS1351*, (2016)
6. AIA/NAS—Aerospace Industries Association of America Inc., *English—Screw, Cap, Socket Head, Undrilled and Drilled, Plain and Self-Locking, Alloy Steel, Corrosion-Resistant Steel and Heat-Resistant Steel, UNRC-3A AND UNRC-2A—Rev 13, AIA/NAS NAS1352*, (2016)
7. ASME—The American Society of Mechanical Engineers, *Unified Inch Screw Threads (UN and UNR Thread Form), ASME B1.1–2003*, (2003)
8. P.W. Grimmer, J.P. Mersch, J.A. Smith, Y.B. Veytskin, D.F. Susan, *Modeling Empirical Size Relationships on Load-Strain Behavior and Failure in Threaded Fasteners 2019 AIAA/ASCE/AHS/ASC Structures, Structural Dynamics, and Materials Conference* (AIAA SciTech Forum, AIAA2019-2268, San Diego, CA, 2019)

Investigation of Dynamic Fracture Behavior of Additively Manufactured Al-10Si-Mg Using High-Speed Synchrotron X-ray Imaging

Niranjan D. Parab, Lianghua Xiong, Zherui Guo, Xianghui Xiao, Weinong Chen, Wesley Everheart, Lianyi Chen, and Tao Sun

Abstract The dynamic tensile properties of additively manufactured (AM) and cast Al-10Si-Mg alloy were investigated using high-speed X-ray imaging coupled with a modified Kolsky bar apparatus. A controlled tensile loading (strain rate = 750 s^{-1}) was applied using a Kolsky bar apparatus and the deformation and fracture behavior was recorded using the high-speed X-ray imaging setup. The recorded high-speed frames were used to identify the location of the critical flaw and to capture the dynamics of crack propagation. In all experiments, the critical flaw was located on the surface of the specimen. The AM specimens showed significantly higher crack propagation speed, yield strength, ultimate tensile strength, strain hardening coefficient, and lower ductility compared to the cast specimens under dynamic tension. The microstructures of the samples were characterized by synchrotron X-ray tomography. The correlation between the dynamic fracture behavior of the samples and the microstructure of the samples was analyzed and discussed.

Keywords Dynamic fracture · Laser powder bed fusion · Kolsky bar · High-speed X-ray imaging · Aluminum alloys

Introduction

Additive manufacturing (AM) processes selectively melt powder particles or wire feedstock in successive thin layers to build three-dimensional parts. They offer various advantages over conventional manufacturing methods: (1) ability to manufacture complex parts directly from the design, (2) on-demand manufacturing, (3) reduced inventory of spares, and (4) shortened lead time [1]. As a result of these advantages, AM of metallic materials is growing rapidly in medical, aerospace, automobile, and defense industries [2, 3]. Currently, laser powder bed fusion (LPBF) is the most popular method for manufacturing metal parts [4, 5]. Amongst the aluminum alloys, LPBF of Al-10Si-Mg has been of particular interest due to its excellent processability, light weight, high specific strength, and good corrosion resistance [6–8]. Further, the Al-10Si-Mg powder feedstock has been readily available from AM machine manufacturers and other powder vendors. Due to these advantages, Al-10Si-Mg has potential applications in aerospace, automotive, and marine industries [9, 10].

Under quasi-static loading, Al-10Si-Mg manufactured using LPBF showed higher strength and lower ductility as compared to cast or powder metallurgy counterparts [11]. Higher strength for the AM Al-10Si-Mg was attributed to the fine, hierarchical microstructure featured by the networks of eutectic Si [11]. However, it was postulated that the fracture behavior of the AM alloy was related to the high density of defects such as pores and cracks in the components [11]. The dynamic mechanical investigation of AM Al-10Si-Mg so far has been limited to compressive testing, where meso-scale

N. D. Parab (✉) · X. Xiao · T. Sun
X-ray Science Division, Advanced Photon Source, Argonne National Laboratory, Argonne, IL, USA
e-mail: nparab@anl.gov

L. Xiong · L. Chen
Department of Mechanical and Aerospace Engineering, Missouri University of Science and Technology, Rolla, MO, USA

Department of Materials Science and Engineering, Missouri University of Science and Technology, Rolla, MO, USA

Z. Guo · W. Chen
School of Aeronautics and Astronautics, Purdue University, West Lafayette, IN, USA

W. Chen
School of Materials Engineering, Purdue University, West Lafayette, IN, USA

W. Everheart
Department of Energy's Kansas City National Security Campus Managed by Honeywell FM&T, Kansas City, MO, USA

M. Silberstein et al. (eds.), *Challenges in Mechanics of Time Dependent Materials, Fracture, Fatigue, Failure and Damage Evolution, Volume 2*, Conference Proceedings of the Society for Experimental Mechanics Series, https://doi.org/10.1007/978-3-030-29986-6_14

defects such as voids and micro-cracks do not play a large role. However, under tensile loading, these defects act as stress concentration sites which leads to cracking. In this study, the meso-scale structure of additively manufactured Al-10Si-Mg is compared with the cast Al-10Si-Mg using synchrotron X-ray micro-tomography. Further, the dynamic tensile deformation and fracture behavior is captured in real time using high-speed X-ray imaging synchronized with a Kolsky bar apparatus. Irregularly shaped surface defects were identified as the crack initiation sites.

Experimental Method

The Al-10Si-Mg bar with dimension of 8 mm × 8 mm × 57 mm was manufactured using a powder bed fusion process in a commercial additive manufacturing (AM) machine (Renishaw AM 250, Renishaw PLC, Gloucestershire, United Kingdom). The dog-bone shaped tensile specimens were cut from the bar using wire electrical discharge machining (EDM). The orientation of tensile direction is parallel to the build direction of AM bar. For the cast samples, master alloy AlSi50 (99%, Fe max 0.5%, Mn max 0.15%, Ca max 0.15%, others max 0.05%), Al (99.8%) and Mg (99.99%) powders were mixed in proper composition and melted in a resistance-heating furnace. The furnace was protected by flowing argon gas. The melt was quickly poured into a stainless-steel mold in air (pour in duration <30 s). The cast ingot dimensions were 18 mm × 31 mm × 60 mm. The tension specimens were cut from the cast ingot using wire EDM. The gauge length, width, and thickness of the specimens was 4 mm, 1 mm and 0.5 mm respectively. A modified Kolsky bar setup was used to apply a controlled tensile loading and high-speed synchrotron X-ray Phase Contrast Imaging (PCI) was used to record the deformation and fracture mechanisms of the specimens. This experimental method has been used to study the failure mechanisms of various materials including carbon fiber composites [12] and high-performance fibers [13]. More details of the experimental procedure are provided elsewhere [14, 15].

Results

The stress-strain curves for both AM and cast specimens are presented in Fig. 1. The Young's moduli for both types of specimens were similar and matched previously reported values for Al-10Si-Mg AM and cast specimens [11]. The yield strength and the ultimate tensile strength for the AM specimens was significantly greater than that for the cast specimens. The fracture strain for AM specimens was smaller than the fracture strain for cast specimens. The yield and ultimate tensile strength values for the AM specimens matched the values reported earlier for the quasi-static tension experiments [16]. Further, the strain hardening coefficients derived from the dynamic experiments were higher than those reported in the literature for quasi-static experiments for both AM and cast specimens [11].

The recorded fracture sequence for a representative AM specimen is presented in Fig. 2b–i. The crack was observed to initiate from a large irregularly shaped surface flaw (lack of fusion flaw) indicated in Fig. 2b. As the specimen was subjected to tensile loading, the crack was observed to grow slowly until the strain reached a critical value. After the critical strain was

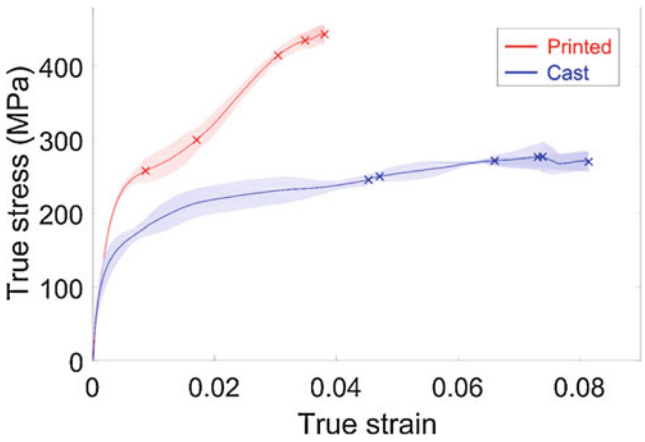

Fig. 1 Stress-strain curves for both cast and printed samples. '×' marks denote the fracture points for different specimens

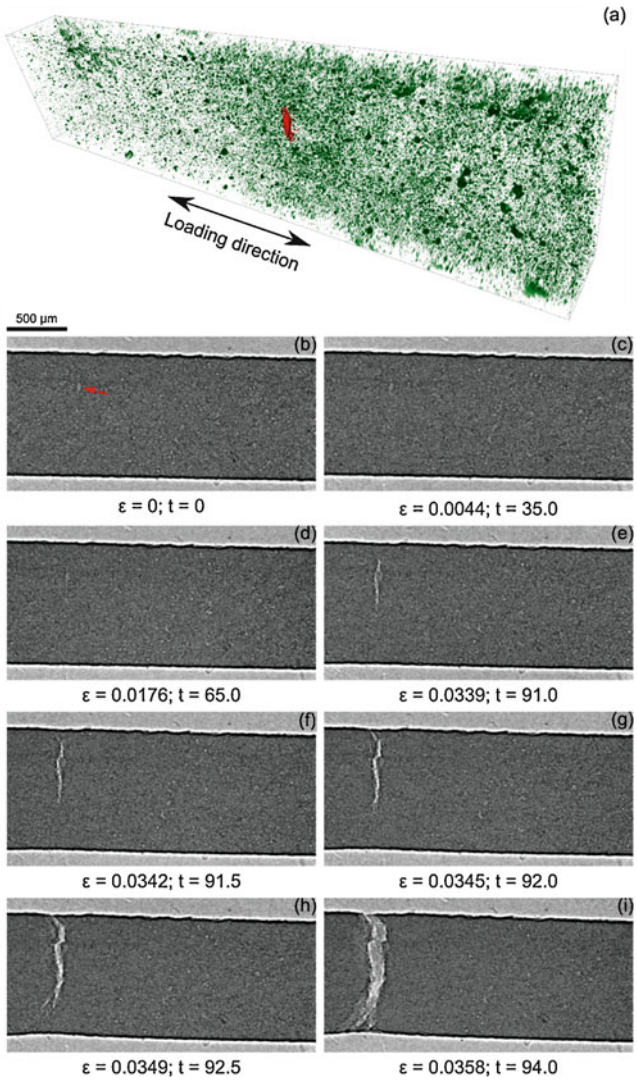

Fig. 2 (**a**) Tomographic reconstruction of the specimen volume for a representative additively manufactured sample. Green regions denote the porosity present in the specimen and red region denotes the critical flaw that initiated the fracture. Note that the critical flaw is present on the surface of the specimen. The dimensions of the presented volume are 910 μm × 422.5 μm × 3978 μm. (**b–i**) Image sequence for the dynamic tensile deformation and fracture behavior from the specimen presented in (**a**). The critical flaw is highlighted with an arrow in (**b**) All time stamps are in microseconds

reached, the crack rapidly propagated towards both ends of the sample, thus catastrophically fracturing the specimen. The crack path was relatively straight.

The fracture sequence for a representative cast specimen is presented in Fig. 3b–i. The fracture sequences for the cast specimens were similar to those of the AM specimens. The crack initiated from a large surface flaw and propagated towards both ends, thus fracturing the specimen. The critical strains leading to catastrophic crack propagation were larger for cast specimens as compared to the AM specimens.

Conclusion

The dynamic tensile properties of AM and cast Al-10Si-Mg alloy were investigated using high-speed X-ray imaging combined with a modified Kolsky bar apparatus. The meso-scale structure of both types of alloys were recorded using synchrotron X-ray tomography prior to tensile experiments. The dynamic deformation and fracture behavior of the specimens was recorded using high-speed X-ray imaging. The recorded high-speed frames were used to identify the critical flaw

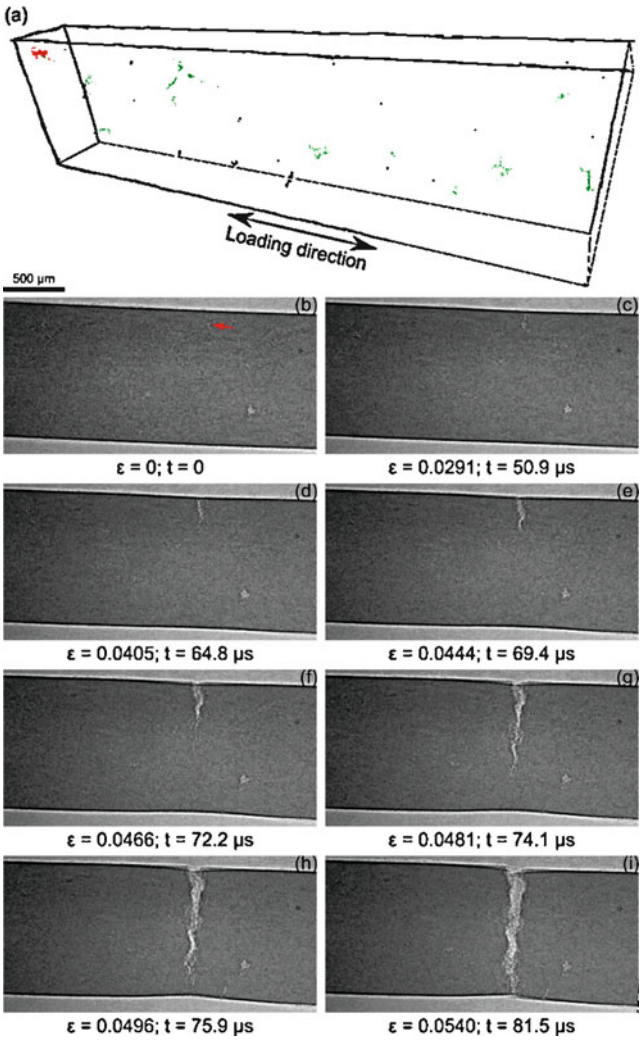

Fig. 3 (**a**) Tomographic reconstruction of the specimen volume for a representative cast sample. Green regions denotes the porosity present in the specimen and red region denotes the critical flaw that initiated the fracture. Note that the critical flaw is present on the surface of the specimen, similar to the AM specimen presented in Fig. 3. The dimensions of the presented volume are 991.25 μm × 422.5 μm × 3673.15 μm. (**b**–**i**) Image sequence for the dynamic tensile deformation and fracture behavior from the specimen presented in (**a**). The critical flaw is highlighted with an arrow in (**b**)

which acted as the crack initiation location. The AM specimens showed significantly higher yield as well as ultimate tensile strengths and lower ductility compared to the cast specimens under dynamic tension. The AM specimens also showed higher hardening compared to the cast specimens. Although the tensile strengths were significantly higher for the AM specimens, the mode I critical stress intensity factors were similar for both specimens. The dynamic fracture behavior of the specimens reported here shows the effect of meso-scale defects in both AM and cast specimens on the fracture properties of Al-10Si-Mg alloy. The reported properties will be useful in both designing parts using AM processes and developing accurate numerical models AM and cast components.

Acknowledgements This work is funded by Honeywell Federal Manufacturing & Technologies (FM&T). The authors would like to thank Alex Deriy at the APS for his help on the beamline experiments. This research used resources of the Advanced Photon Source, a U.S. Department of Energy (DOE) Office of Science User Facility operated for the DOE Office of Science by Argonne National Laboratory under Contract No. DE-AC02–06CH11357.

References

1. T. DebRoy et al., Additive manufacturing of metallic components—process, structure and properties. Prog. Mater. Sci. **92**(Supplement C), 112–224 (2018)
2. T. T. Wohlers, T. Caffrey, *Wohlers Report 2015: 3D Printing and Additive Manufcturing State of the Industry Annual Worldwide Progress Report*, (2015)
3. D.L. Bourell, Perspectives on additive manufacturing. Annu. Rev. Mater. Res. **46**(1), 1–18 (2016)
4. D.W. Rosen, Computer-aided design for additive manufacturing of cellular structures. Comput. Aided. Design Appl. **4**(5), 585–594 (2007)
5. T. Campbell, C. Williams, O. Ivanova, B. Garrett, *Could 3D Printing Change the World? Technologies, Potential, and Implications of Additive Manufacturing*, (2011)
6. N. Read, W. Wang, K. Essa, M.M. Attallah, Selective laser melting of AlSi10Mg alloy: process optimisation and mechanical properties development. Mater. Des. **65**, 417–424 (2015)
7. W. Li et al., Effect of heat treatment on AlSi10Mg alloy fabricated by selective laser melting: microstructure evolution, mechanical properties and fracture mechanism. Mater. Sci. Eng. A **663**, 116–125 (2016)
8. P. Delroisse, P.J. Jacques, E. Maire, O. Rigo, A. Simar, Effect of strut orientation on the microstructure heterogeneities in AlSi10Mg lattices processed by selective laser melting. Scr. Mater. **141**, 32–35 (2017)
9. H. Asgari, A. Odeshi, K. Hosseinkhani, M. Mohammadi, On dynamic mechanical behavior of additively manufactured AlSi10Mg_200C. Mater. Lett. **211**, 187–190 (2018)
10. M. Mohammadi, H. Asgari, Achieving low surface roughness AlSi10Mg_200C parts using direct metal laser sintering. Addit. Manuf. **20**, 23–32 (2018)
11. B. Chen et al., Strength and strain hardening of a selective laser melted AlSi10Mg alloy. Scr. Mater. **141**, 45–49 (2017)
12. Y. Nie, N.D. Parab, J.-M. Chu, T. Sun, K. Fezzaa, W.W. Chen, Crack Propagation from a Circular Defect in a Unidirectional CFRP Composite Under Dynamic Tension, in *32nd Technical Conference of the American Society for Composites*, vol. 2, (2017)
13. M. Hudspeth, B. Claus, N. Parab, B. Lim, K. Fezza, W. Chen, Mechanical Properties and Failure Processes of Ballistic Single Fibers at High Strain Rates, in *International Symposium on Fibers Interfacing the World*, (2013)
14. M. Hudspeth et al., High speed synchrotron x-ray phase contrast imaging of dynamic material response to split Hopkinson bar loading. Rev. Sci. Instrum. **84**(2), 025102 (2013)
15. W.W. Chen et al., In situ damage assessment using synchrotron X-rays in materials loaded by a Hopkinson bar. Philos. Trans. A Math. Phys. Eng. Sci. **372**(2015), 20130191 (2014)
16. N.T. Aboulkhair, I. Maskery, C. Tuck, I. Ashcroft, N.M. Everitt, The microstructure and mechanical properties of selectively laser melted AlSi10Mg: the effect of a conventional T6-like heat treatment. Mater. Sci. Eng. A **667**, 139–146 (2016)

A Simplified Investigation into Fatigue Viability of Additively Manufactured IN-718

Austin Schoening, Luke Sheridan, Onome Scott-Emuakpor, and Tommy George

Abstract Material characterization by way of fatigue testing is a common practice in materials research. This research is then applied to many different engineered devices, one of which includes the gas turbine engine. In the environment of a turbine engine the fatigue life plays a critical role in the design, operation, and maintenance of the engine. This study uses the fatigue life of two different metals (Titanium 6Al-4 V, Aluminum 6061-T6) with different cross-sectional measurements to assess the fatigue viability of another material (additively manufactured Inconel 718, or AM IN-718). The assessment of AM IN-718 fatigue life is done by normalizing all the fatigue data against respective ultimate tensile strength results obtained from monotonic tests. The data from two different gage section types for Titanium (Ti) 6Al-4 V and Aluminum (Al) 6061-T6 specimens show that the comparability of the normalized fatigue results fit within a 99% prediction interval. The viability assessment of IN-718 highlighted concerns in the material integrity, and this finding, guided by the normalized fatigue data of Ti 6Al-4 V and Al 6061-T6, led to the identification of flaws which were artifacts of poor AM process controls.

Keywords Fatigue · Additive manufacturing · Normalized stress · Life prediction · LPBF

Introduction

Additive manufacturing (AM) enables the gas turbine engine community to increase the capabilities of such engines by modifying design. In the environment of a turbine engine, the vibratory stresses induced by flow path components can, overtime, lead to failure of components by way of fatigue [1]. The concern for this type of damage, known as High Cycle Fatigue (HCF), stems from the extreme number of cycles expected during the life time of the engine. This study investigates how normalizing the fatigue data against the respective ultimate tensile strength of the material can lead to a prediction of life and be used to determine the integrity of new AM materials.

The AM process used in this study is Laser powder bed fusion (LPBF). This AM process uses a laser to melt deposited/leveled metal powder on a build plate. In this study, two builds with different layer thicknesses of 20 μm and 40 μm were manufactured using a Concept Laser™ (CL) M2 Cusing LPBF machine. The laser power, speed, and hatch spacing were held constant for both builds, and the continuous meander (CM) scan strategy was used in both builds as well. According to Sheridan [2], the CM scan strategy for the Concept Laser M2 produces parts with the smallest pore diameter, which should support higher fidelity fatigue results.

The goal of this study is to normalize fatigue of two dissimilar materials (Al 6061-T6 and Ti 6Al-4 V) and assess the viability of the LPBF AM IN-718 fatigue behavior. In order to assess fatigue behavior the maximum stress amplitude for each respective fatigue test was normalized with respect to ultimate tensile strength. Given this data, a 99% prediction interval was generated from a Ti 6Al-4 V data linear regression fit to assess if AM IN-718 could be captured within the prediction bounds. This data showed a lower fatigue life than what was expected and attributed to defects found via a fracture surface analysis using scanning electron microscopy (SEM). Also addressed in this study was the effect of significant geometry differences on fatigue behavior, namely the comparison of rectangular and circular cross-sectional area specimens. Results show a drastically different regression slope and prediction interval.

A. Schoening (✉)
Department of Mechanical Engineering, Wright State University, Dayton, OH, USA

Universal Technology Corporation, Beavercreek, OH, USA

L. Sheridan · O. Scott-Emuakpor · T. George
Air Force Research Laboratory, Wright Patterson AFB, OH, USA

M. Silberstein et al. (eds.), *Challenges in Mechanics of Time Dependent Materials, Fracture, Fatigue, Failure and Damage Evolution, Volume 2*, Conference Proceedings of the Society for Experimental Mechanics Series, https://doi.org/10.1007/978-3-030-29986-6_15

Fatigue Results

Fatigue data from Ti 6Al-4 V, Al 6061-T6, and AM IN-718 materials were generated, normalized, and are presented on the plots in Figs. 1 and 2. Shown with the Fig. 1 data (circular cross-section) is a 99% prediction interval [3] that was created from a linear regression [3] of Series 5 (Ti 6Al-4 V) data. The fatigue results for Ti 6Al-4 V and Al 6061-T6 with rectangular cross-sectional areas can be found in Fig. 2, included on the plot is a linear regression created from Series 1 (Ti 6Al-4 V) data. The regression model used in both Figs. 1 and 2 can be found in Eq. 1.

$$\ln N = A\left(\frac{\sigma_{Max}}{\sigma_{UTS}}\right) + B \tag{1}$$

Tests were completed with two types of gage sections: circular cross-sectional specimens with diameters of 6.35 mm and 5.08 mm, and rectangular cross-sectional specimens with an average width of 6.34 mm and thickness of 3.28 mm. Despite being dissimilar materials, all the normalized extruded rod Ti 6Al-4 V and Al 6061-T6 fatigue results for a circular cross section fall within the 99% prediction interval of one Ti 6Al-4 V set; however, both AM IN-718 series with layer thicknesses of 20 and 40 μm fall outside of the interval.

A correlation between two different cross-sectional areas is hard to determine, the two geometries have different data trends which make accurate prediction a challenge. Ti 6Al-4 V rectangular specimens show a deviation from the semi-log linear trend at a normalized value of 0.6–0.7 while Al 6061-T6 also shows a deviation, it is not as pronounced. It is assumed that understanding the microstructure effects on a sharp corner crack initiation is necessary for the accurate prediction of fatigue life in a rectangular cross section geometry. A corner crack initiation sight on the fracture surface of Ti 6Al-4 V can be seen in Fig. 3. Accurate prediction of a rectangular cross-section geometry is important due to the similarities these test specimens hold with blade geometries present in gas turbine engines.

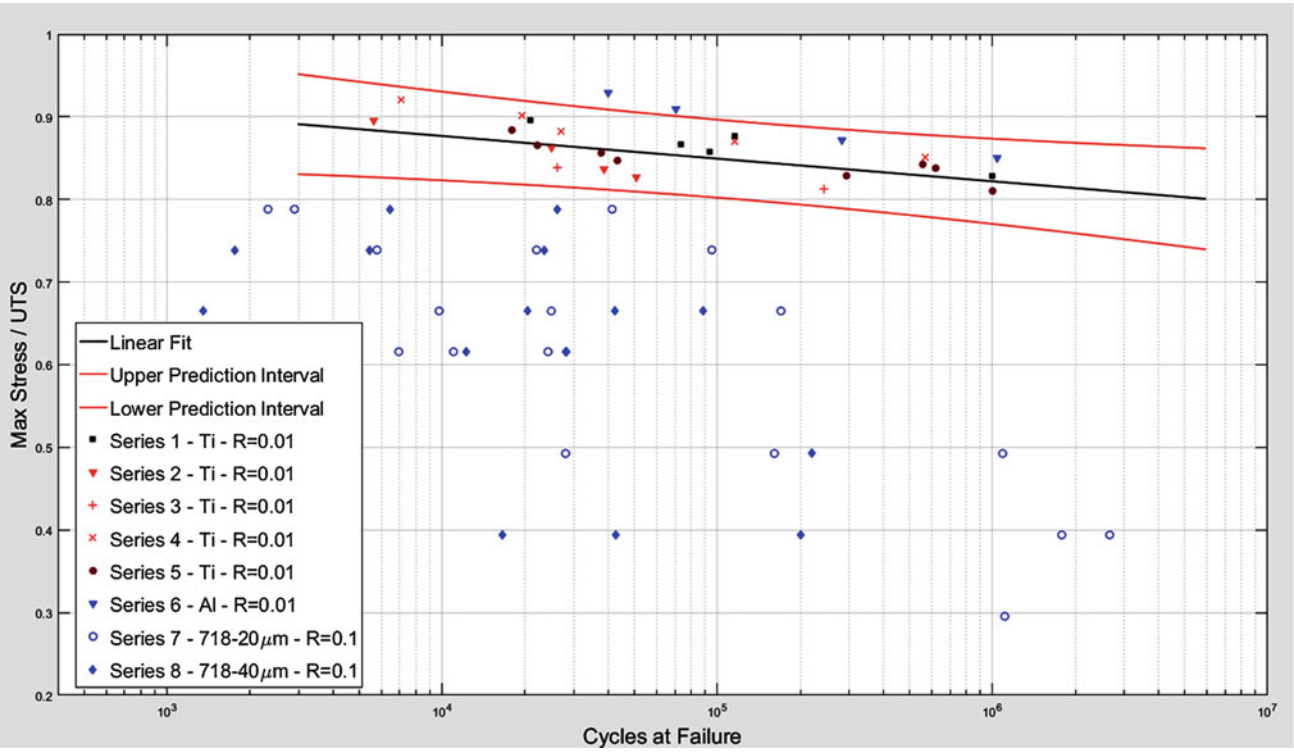

Fig. 1 Fatigue normalization plot for round specimens

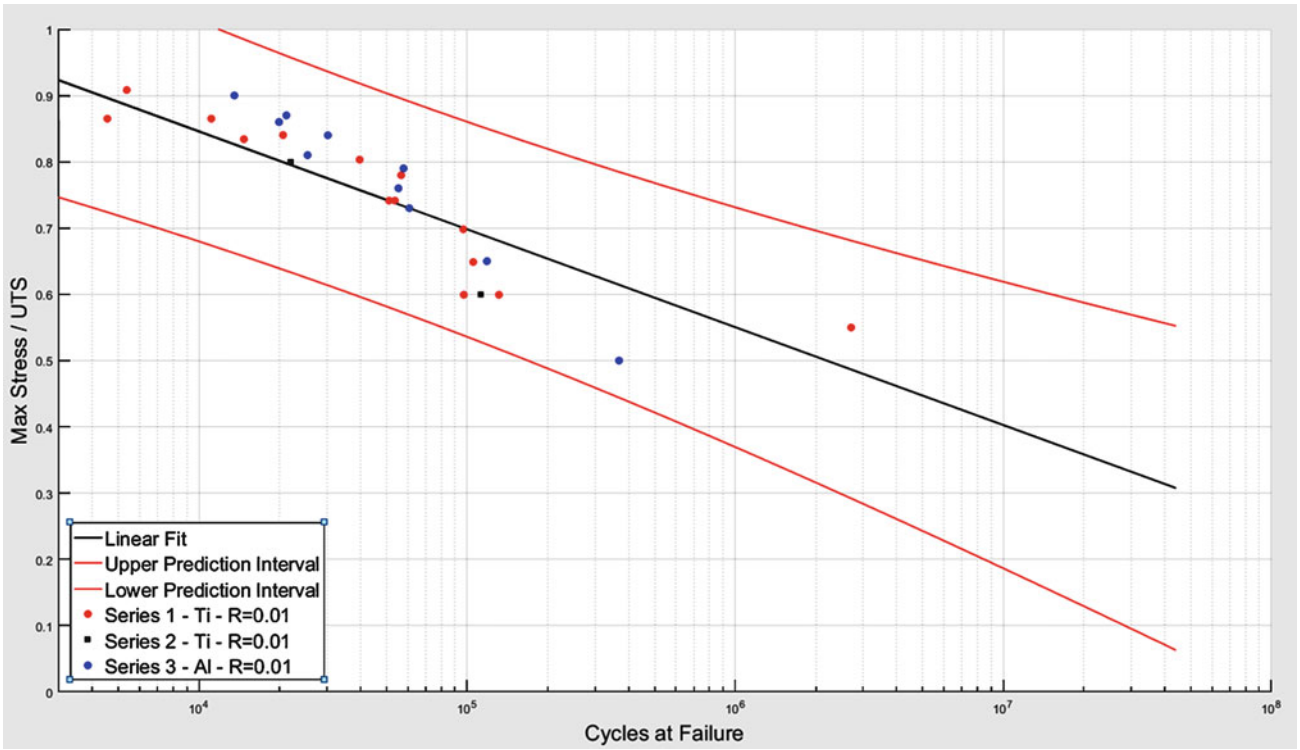

Fig. 2 Fatigue normalization plot for flat specimens

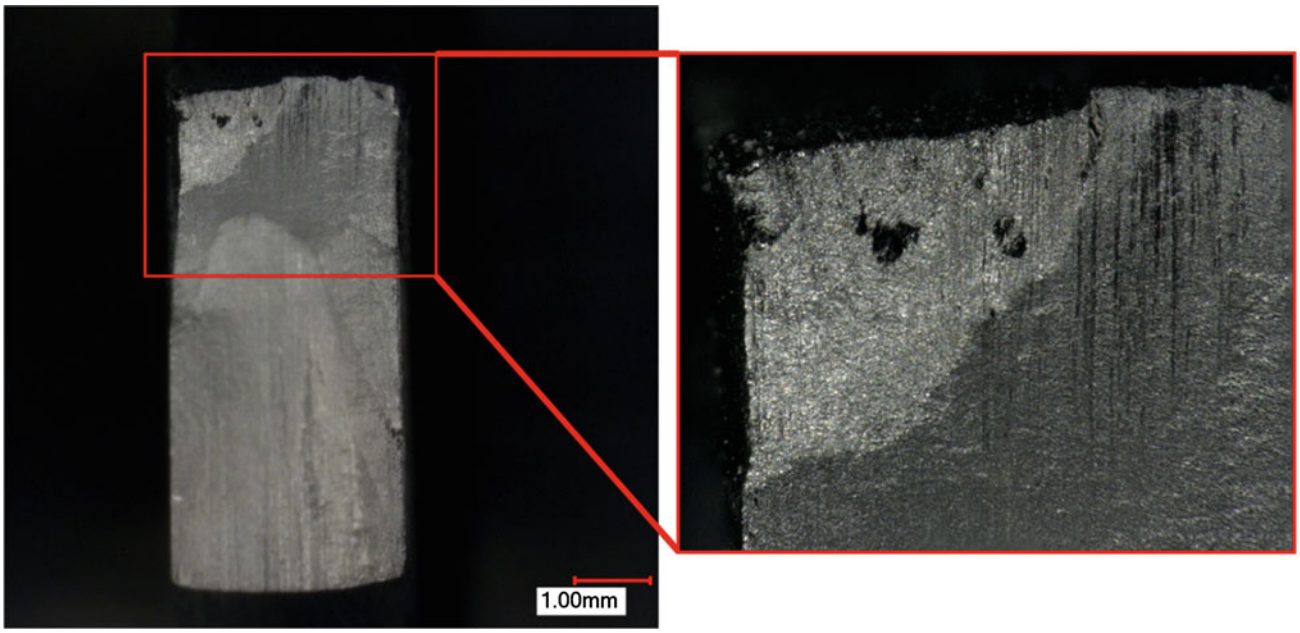

Fig. 3 Ti 6Al-4 V corner crack initiation

Fractography on AM Specimens

Fracture surface analysis of AM IN-718 with a build layer thickness of 40 μm, via scanning electron microscopy (SEM), elucidated regions which lacked in fusion and explicates the reduction in fatigue life shown in Fig. 1. This lack of fusion can be seen in Fig. 4 where SEM scans of an Inconel 718 specimen reveal a pore containing unfused and partially fused powder. Lack of fusion, often described in terms as porosity, is unfused metallic powder left from the build process.

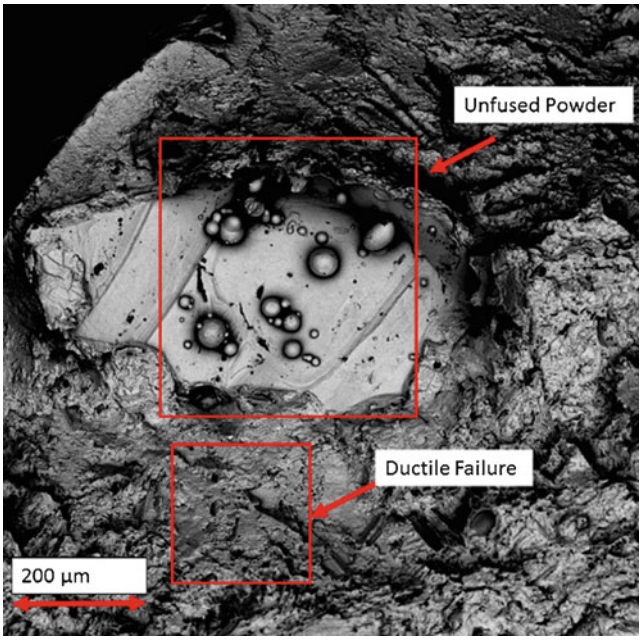

Fig. 4 Fracture surface of an AM IN-718 specimen with layer thickness of 40 µm

Process parameters such as power, speed, hatch spacing, scan strategy and layer thickness all play a role in the end result [4]. One theory states that low energy density causes a lack of fusion due to melt pool conditions [4]. It has been shown that low performance in fatigue is related to larger pore diameters [2].

Conclusion

This study uses fatigue data from two dissimilar metals to evaluate the viability of a third. Data captured in this experiment will be used to model future fatigue testing as well as predict life for other dissimilar metals. Future work will be done to create better regression and prediction models that capture a wider set of materials and geometries.

This fatigue viability analysis has shown to be a promising method to quickly evaluate AM IN-718. Future work will investigate the process parameters and help analyze the settings to find a process parameter set that allows for the creation of additive materials with less process defects and, therefore longer fatigue life. These future works will be used to test the viability of additive manufacturing as a way of creating parts for gas turbine engines.

References

1. Engine Structural Integrity Program (ENSIP), Military Handbook: MIL HDBK-1783B, United States Air Force, 15 Feb 2002
2. L. Sheridan, O.E. Scott-Emuakpor, T. George, J.E. Gockel, Relating porosity to fatigue failure in additively manufactured alloy 718. Mater. Sci. Eng. A **727**, 170–176 (2018)
3. M.H. Kutner, C.J. Nachtsheim, J. Neter, *Applied Linear Regression Models* (Mcgraw-Hill Irwin, New York, NY, 2004)
4. M. Tang, P.C. Pistorius, J.L. Beuth, Prediction of lack-of-fusion porosity for powder bed fusion. Addit. Manuf. **14**, 39–48 (2017)

A Post Mortem Analysis of the Strain-Induced Crystallization Effects on Fatigue of Elastomers

B. Ruellan, J.-B. Le Cam, E. Robin, I. Jeanneau, F. Canévet, G. Mauvoisin, and D. Loison

Abstract Natural rubber (NR) is the most commonly used elastomer in the automotive industry thanks to its outstanding fatigue resistance. Strain-induced crystallization (SIC) is found to play a role of paramount importance in the great crack growth resistance of NR (Lindley, Int J Fracture 9:449–462, 1973). Typically, NR exhibits a lifetime reinforcement for non-relaxing loadings (Cadwell et al., 1940; Ruellan et al., 2019). At the microscopic scale, fatigue striations were observed on the fracture surface of Diabolo samples tested in fatigue. They are the signature of SIC (Cadwell et al., 1940; Le Cam et al., 2013; Le Cam et al., 2004). In order to provide additional information on the role of SIC in the fatigue crack growth resistance of NR, striations are investigated through post-mortem analysis after fatigue experiments using loading ranging from −0.25 to 0.25. No striation was observed in the case of tests performed at 90 °C. This confirms that the formation of striation requires a certain crystallinity level in the material. At 23 °C, two striation regimes were identified: small striation patches with different orientations (Regime 1) and zones with large and well-formed striations (Regime 2). Since fatigue striations are observed for all the loading ratios applied, they are therefore not the signature of the reinforcement. Nevertheless, increasing the minimum value of the strain amplified the striation phenomenon and the occurrence of Regime 2.

Keywords Natural rubber · Strain-induced crystallization · Fatigue · Striation

Introduction

Elastomers are widely used in many applications for their extraordinary mechanical properties. Typically, they present damping abilities and a high fatigue resistance. The fatigue resistance of elastomers was investigated as soon as 1940 by the pioneer work by Cadwell et al. [1], Fielding [2] and 20 years later by Beatty [3]. In the case of natural rubber (NR), the strong impact of the loading ratios on the fatigue properties was demonstrated. For non-relaxing loadings (*i.e.* $R > 0$), it corresponds to a decrease in fatigue crack growth rate and an increase in tearing energy below which no crack growth occurs [4]. Since this result has not been observed for non-crystallizable rubbers, it is commonly attributed to strain-induced

B. Ruellan (✉)
Univ Rennes, CNRS, IPR (Institut de Physique de Rennes)—UMR 6251, Rennes, France

LC-DRIME, Joint Research Laboratory, Cooper Standard—Institut de Physique UMR 6251, Campus de Beaulieu, Rennes Cedex, France

Cooper Standard France, Rennes, France
e-mail: benoit.ruellan@univ-rennes1.fr

J.-B. Le Cam · E. Robin
Univ Rennes, CNRS, IPR (Institut de Physique de Rennes)—UMR 6251, Rennes, France

LC-DRIME, Joint Research Laboratory, Cooper Standard—Institut de Physique UMR 6251, Campus de Beaulieu, Rennes Cedex, France

I. Jeanneau · F. Canévet
LC-DRIME, Joint Research Laboratory, Cooper Standard—Institut de Physique UMR 6251, Campus de Beaulieu, Rennes Cedex, France

Cooper Standard France, Rennes, France

G. Mauvoisin
Laboratoire de Génie Civil et Génie Mécanique EA 3913, IUT-Université de Rennes 1, Rennes, France

D. Loison
Univ Rennes, CNRS, IPR (Institut de Physique de Rennes)—UMR 6251, Rennes, France

M. Silberstein et al. (eds.), *Challenges in Mechanics of Time Dependent Materials, Fracture, Fatigue, Failure and Damage Evolution, Volume 2*, Conference Proceedings of the Society for Experimental Mechanics Series, https://doi.org/10.1007/978-3-030-29986-6_16

crystallization (SIC). Nevertheless, the mechanisms responsible for this reinforcement are not fully understood and remain not clearly established, which is an obstacle for lifetime prediction. The presence of certain morphological patterns, namely wrenchings and striations [5], were assumed to be due to SIC. Therefore, their presence on the failure surface of NR samples should be the signature of the SIC effects in the crack growth resistance at the microscopic scale. On the one hand, the mechanisms of wrenching formation were established by Le Cam et al. [6], it revealed the role of SIC in the process of formation: highly crystallized ligaments form between elliptical zones where the crack propagates, which delay the crack propagation. On the other hand, only few studies investigated striations [5, 7–9]. Therefore, the role of SIC in their formation is not clearly understood, especially for non-relaxing loadings, where the lifetime reinforcement occurs.

Fatigue striations were investigated in four studies [5, 7–9]. The state of the art on the experiments carried out is given in [10]. A summary of this state of the art is given hereafter. First of all, the experimental conditions used in the literature to investigate fatigue striation strongly differed from one study to another. Therefore, comparing them or drawing general conclusions on fatigue striations seems complicated. The results obtained can be presented according to the sample geometry, since it was found to strongly influence the fatigue striation phenomenon.

Plane Samples

The study by Munoz et al. [9] is the one presenting the largest diversity of fatigue striations. In this study, the fatigue striation morphologies were classified according to the crack growth rate. Three striation morphologies T1, T2 and T3 were identified, they refer to morphological groups III, IV and IV in [9], respectively. They stand for striations patches whose orientation differs from one patch to another, well defined striations regrouped in different zones whose orientation also differs slightly and well-defined striations that people the sample thickness, respectively. The author showed that the occurrence of fatigue striation from typology T1 to T3 goes along with an increase in crack growth rate.

Diabolo Samples

The crack first initiates around a defect that concentrates stress. Then, it propagates by forming small wrenchings describing an ellipsoidal zone around a defect [7]. The wrenchings exhibit a similar morphology as those observed in the case of plane samples. As the crack propagates, striations eventually form before the sample breaks totally. It is to note that striations have also been observed in the case of non-relaxing loadings in [7], but damage at the macroscopic scale was quite different from that described here, since the failure occurred in a region under the insert. At the microscopic scale and on a morphological point of view, striations are separated by a distance ranging from 10 to 100 μm in [8] and from 15 to 160 μm as the crack growth rate increases in [9].

As a conclusion, only a few studies investigated fatigue striations while they could bring new information on the role of SIC on the lifetime reinforcement under non-relaxing loadings. Furthermore, the studies differed in terms of material, loading condition and sample geometry, which makes difficult any generalization to NR. Additional fatigue tests have therefore to be carried out at different loading ratios and temperatures. The next section presents these new fatigue tests. The experimental setup is first provided. Then, results are given and discussed. Concluding remarks close the paper.

Experimental Setup

Material and Sample Geometry

The material considered here is a carbon black filled natural rubber (*cis*-1,4 polyisoprene) vulcanised with sulphur. Samples tested are Diabolo samples.

Loading Conditions

The fatigue tests are performed with a uni-axial MTS Landmark equipped with a homemade experimental apparatus presented in Fig. 1. This apparatus enables us to test simultaneously and independently eight Diabolo samples, which compensates the fatigue tests duration and the dispersion in the fatigue lifetimes.

The tests are performed under prescribed displacement. The corresponding local deformation is calculated by finite element analysis (FEA) at the sample's surface in the median zone. In order to investigate the effect of temperature on the striation and fatigue properties, a Servathin heating chamber is used. The frequency is chosen in such a way that the global strain rate $\dot{\varepsilon}$ is kept constant, ranging between 1.8 and 2.4 to 2 s^{-1} for a given loading condition. In practice, the frequency ranges between 1 and 4 Hz, which limits self-heating so that no thermal damage is added to the mechanical one. Four different loading ratios $R_\varepsilon = \frac{\varepsilon_{min}}{\varepsilon_{max}}$ are used: -0.25; 0; 0.125 and 0.25. One can recall that loading ratios inferior, equal and superior to zero correspond to tension- compression, repeated tension and tension-tension, respectively.

Scanning Electron Microscopy

Second electrons images of diabolo fracture surfaces are recorded with a JSM JEOL 7100 F scanning electron microscope (SEM). In addition, the SEM is coupled with an Oxford Instrument X Max Energy Dispersive Spectrometer of X-rays (EDS) and an Aztzec software in order to determine the surface fracture composition, especially in the crack initiation zone. The fracture surfaces to be analysed are previously metallized by vapour deposition of an Au-Pd layer.

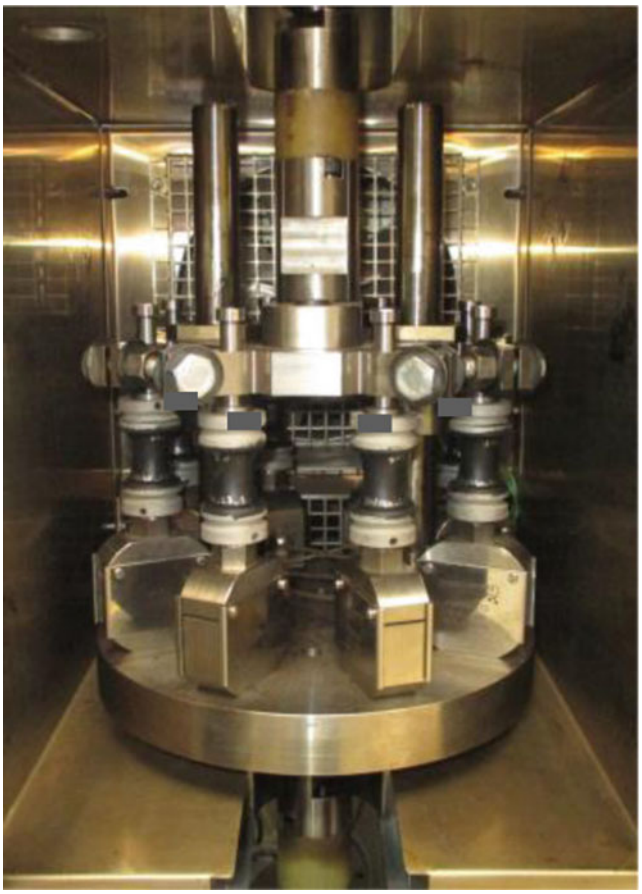

Fig. 1 Experimental setup

Results and Discussions

The failure surface was generally similar to the one described by Le Cam and co-workers [5, 7], *i.e.* the formation of fatigue striation follows the formation of wrenchings and precedes the final ligament corresponding to a catastrophic failure. Fatigue striations are first described according to their typologies. Then, the effects of the loading on the occurrence and typology of the fatigue striation are discussed.

Typology of Fatigue Striations

The analysis of the failed surfaces suggests fatigue striations form according to two regimes (see Fig. 2):

- Regime 1 corresponds to striation patches (see Fig. 2a) whose orientation can slightly deviate from the crack propagation direction. Regime 1 corresponds to the transition between full wrenching zone and full striation zones. The loading can be considered as moderate.
- Regime 2 stands for well-formed striations (see Fig. 2b) and wrenchings no longer form. It corresponds to the striation morphology identified in the literature in Diabolo samples [5, 7, 8]. Since Regime 2 is observed closed to the final ligament, the local stress can be considered as severe. It is to note that Regime 1 always precedes Regime 2 (Fig. 3).

Link Between Fatigue Striation and Loading Conditions

Fatigue striations have been linked to the loading condition in order to bring new information on the role of SIC in the crack growth resistance of NR. Classically, lifetime reinforcement occurs for non-relaxing loadings (*i.e.* $R > 0$), which can be represented in a Haigh diagram [11, 12] Erreur ! Source du renvoi introuvable presents such a diagram obtained after fatigue tests at 23 °C. The iso-lifetime curves in black highlight the lifetime reinforcement since their slope become positive under non-relaxing loadings (see [13] for more details). At the macroscopic scale, three fatigue damage modes are identified and reported in Erreur ! Source du renvoi introuvable:

– crack initiation in the surface vicinity and crack propagation in the median section until total failure,
– crack initiation in the surface vicinity and propagation of the crack by bifurcation in the median section zone,
– crack initiation and growth close to the insert area.

The fact that the two later damage modes are obtained under non-relaxing loading highlights the strong influence of the loading on the damage mechanisms.

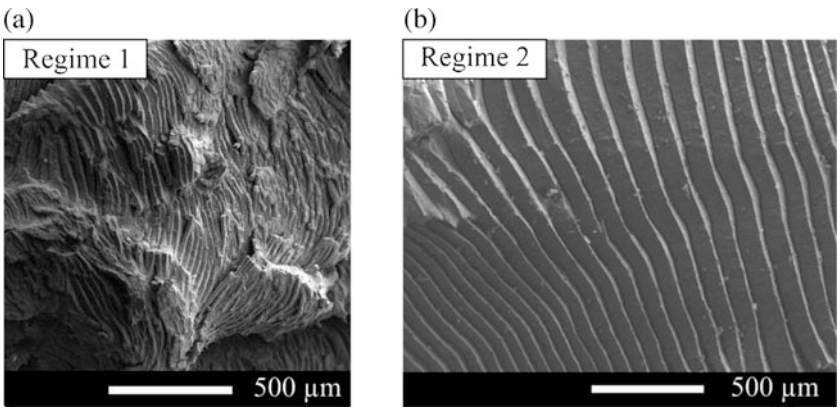

Fig. 2 SEM images of the two striation regimes (**a**) Regime 1 and (**b**) Regime 2

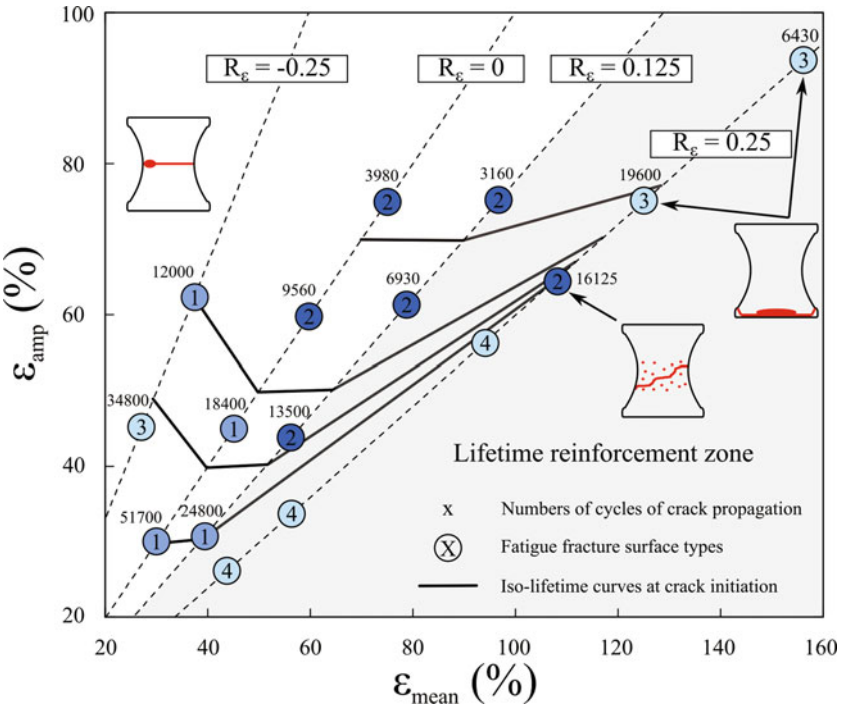

Fig. 3 Effect of the loading conditions on the fatigue life, the number of cycle of crack propagation and the macroscopic damage

At the microscopic scale, three fracture surface types are identified. They are described as follows:

- ① fracture surface with Regime 1 fatigue striation,
- ② fracture surface with Regime 2 fatigue striation. Since Regime 2 is consecutive to Regime 1, fracture surfaces noted ② also exhibit Regime 1 fatigue striations,
- ③ fracture surface without any fatigue striation.

It is to note that fracture surfaces denoted ④ correspond to experiments where no failure was observed after 1.5 million cycles. The results are described in terms of fracture surface type, according to the loading ratios R_ε:

- for repeated tension ($R_\varepsilon = 0$), fatigue striations are observed independently of the maximal strain applied: for low ε_{max}, Regime 1 appears, Regime 2 occurs as ε_{max} increases. Both striation height and distance between two striations increase with ε_{max}. It is in good agreement with the study by Munoz et al. [9].
- for non-relaxing tension ($R_\varepsilon > 0$), the same comment can be drawn as for repeated tension, however, Regime 2 appears for lower values of ε_{max}. Such loadings were found to promote SIC [13, 14] since the loading never goes back to zero during a fatigue cycle. This could therefore explain the more important occurrence of Regime 2. Note that the fact that no striation is observed for the highest ε_{max} is explained by the difference in terms of damage mechanisms: indeed, the initiation that occurred under the insert area did not allow the formation of striation.
- for relaxing tension ($R_\varepsilon > 0$), fatigue striations are also observed. However, they form at higher ε_{max}. It can be due to the fact that the crystallinity goes back to zero during such fatigue tests.

Finally, literature suggests that no crystallites remain at 90 °C under static loadings [15]. Fatigue tests performed at 90 °C revealed that no wrenchings nor fatigue striation form under such temperature. Therefore, it confirms the strong role of SIC on the formation of wrenchings and fatigue striation.

Discussion

The results presented in the present paper suggest that fatigue striations form whatever the loading applied is, even for tension-compressions tests where no lifetime reinforcement is observed. Therefore, it can be concluded that fatigue striations are the signature of SIC, but not the signature of the lifetime reinforcement. The fact that no striation was observed after

fatigue tests carried out at 90 °C could indicate that striation only form when a certain crystallinity threshold is reached. It has been shown that fatigue striation form under a wide range of loading: only Regime 1 occurs for relaxing loadings, for superior loading ratios (*i.e.* $R \geq 0$) the striation formation is found to be amplified as the loading ratio is increased. This result can be analyzed with respect to crack growth rate curves measured at different loading ratios in the study proposed by Lindley [4]. The authors showed that: (1) increasing the tearing energy (*i.e.* the loading) induces an increase of the crack growth rate: (2) increasing the loading ratio decreases the crack growth rate, for a given tearing energy and increases the tearing energy threshold below which no crack growth happens. The author deduced from this result that the crack growth resistance of NR was due to SIC. Our results are in good agreement with Lindley's for non-relaxing tension ($R = 0.25$): below a certain maximum of loading, no crack propagation occurs (fracture surface ④), above this maximum of loading, only Regime 2 striation form. Based on the result presented by Lindley, the crack growth rate at which Regime 2 occurs for $R = 0.25$ loadings should be lower than the one at which it occurs for lower loading ratios. To verify this result, the number of cycles of crack propagation N_p is also reported in Erreur ! Source du renvoi introuvable. Since the tests are carried out at approximately the same strain rate, it can be considered that N_p evolves with the inverse of the crack growth rate. Therefore, for a given amplitude of loading, since N_p increases with the loading ratio in the lifetime reinforcement zone, the crack growth rate decreases. Our results suggest that under non-relaxing loadings, the loading ratio governs the striation typology. Furthermore, the crack propagation curves can be a useful tool to quantitatively analyse the signature of SIC on the failure surface.

Conclusion

The role of SIC in the fatigue crack growth of NR is investigated using post-mortem analysis of fatigue striations. Two striation regimes occur: Regime 1 corresponding to striation patches with different orientations and Regime 2 corresponding to well defined striations. Striations are observed whatever the loading ratio applied and even for relaxing loadings, where no lifetime reinforcement occurs. Fatigue striations are therefore not the signature of the lifetime reinforcement. Nevertheless, the fatigue striation formation in Regime 2 seems to be encouraged for non-relaxing loadings, where the lifetime reinforcement occurs. For $R \leq 0$ loadings, increasing the loading (*i.e.* the tearing energy) increases the crack growth rate, which is in good agreement with the literature. For $R > 0$, the striation typology evolution could be governed by the loading ratio. Finally, no striation was observed when the temperature was increased to 90 °C. Therefore, it is concluded that the formation of striation requires the crystallinity to be above a crystallinity threshold under which no striation form.

Acknowledgements The authors thank the Cooper Standard France company for supporting this work and for fruitful discussions. The authors thank also the National Center for Scientific Research (MRCT-CNRS and MI-CNRS) and Rennes Metropole for supporting this work financially. SEM images were performed at CMEBA facility (ScanMAT, University of Rennes 1), which received a financial support from the European Union (CPER-FEDER 2007-2014).

References

1. S.M. Cadwell, R.A. Merril, C.M. Sloman, F.L. Yost, Dynamic fatigue life of rubber. Ind. Eng. Chem. Anal. Ed. **12**, 19–23 (1940). *(reprinted in Rubber Chem. and Tech. 1940;13:304-315)*
2. J.H. Fielding, Flex life and crystallisation of synthetic rubber. Ind. Eng. Chem. **35**, 1259–1261 (1943)
3. J.R. Beatty, Fatigue of rubber. Rubber Chem. Technol. **37**, 1341–1364 (1964)
4. P.B. Lindley, Relation between hysteresis and the dynamic crack growth resistance of natural rubber. Int. J. Fract. **9**, 449–462 (1973)
5. J.-B. Le Cam, B. Huneau, E. Verron, Fatigue damage in carbon black filled natural rubber under uni- and multiaxial loading conditions. Int. J. Fatigue **52**, 82–94 (2013)
6. J.-B. Le Cam, B. Huneau, E. Verron, L. Gornet, Mechanism of fatigue crack growth in carbon black filled natural rubber. Macromolecules **37**, 5011–5017 (2004)
7. J.-B. Le Cam, E. Toussaint, The mechanism of fatigue crack growth in rubbers under severe loading: the effect of stress-induced crystallization. Macromolecules **43**, 4708–4714 (2010)
8. M. Flamm, J. Spreckels, T. Steinweger, U. Weltin, Effects of very high loads on fatigue life of NR elastomer materials. Int. J. Fatigue **33**, 1189–1198 (2011)
9. L. Munoz, Etude exprimentale des mécanismes d'endommagement par fatigue dans les élastomères renforcés, PhD thesis. Université Claude Bernard Lyon 1, (2011)
10. B. Ruellan, J.-B.L. Cam, E. Robin, I. Jeanneau, F. Canévet, G. Mauvoisin, D. Loison, Fatigue crack growth in natural rubber: The role of SIC investigated through post-mortem analysis of fatigue striations. Eng. Fract. Mech. **201**, 353–365 (2018)

11. N. André, Critère local d'amorcage de fissures en fatigue dans un élastomère de type NR, PhD thesis. Ecole Nationale Supérieure des Mines de Paris, (1999)
12. N. Saintier, Prévisions de la durée de vie en fatigue du NR, sous chargement multiaxial, PhD thesis. Ecole Nationale Supérieure des Mines de Paris, (2000)
13. B. Ruellan, J.-B. Le Cam, E. Robin, I. Jeanneau, F. Canévet, Fatigue of natural rubber under different temperatures. Int. J. Fatigue **124**, 544–557 (2019). https://doi.org/10.1016/j.ijfatigue.2018.10.009
14. S. Beurrot-Borgarino, B. Huneau, E. Verron, P. Rublon, Strain-induced crystallization of carbon black-filled natural rubber during fatigue measured by in situ synchrotron X-ray diffraction. Int. J. Fatigue **47**, 1–7 (2013)
15. S. Trabelsi, Etude statique et dynamique de la cristallisation des élastomères sous tension, PhD thesis. Université Paris XI Orsay, (2002)
16. W.V. Mars, A. Fatemi, Factors that affect the fatigue life of rubber: a literature survey. Rubber Chem. Technol. **77**, 391–412 (2004)
17. J.-B. Le Cam, Endommagement en fatigue des élastomères, PhD Thesis. Ecole Centrale de Nantes, (2005)

Analysis of Crack Growth in Compressor Blade Root Subjected to Fatigue

Muktai Thomre and K. Ramesh

Abstract In the current study, experiments are performed on the aero-engine compressor blade model which is fastened to the disc using dovetail joint. Using the technique of photoelasticity, the highly stressed zone is found to be at the interface of the disc and the blade. Cyclic loading is then applied to the disc-blade assembly. Initial experimental observations showed formation of small cracks leading to crack growth and subsequent failure. In this region, a small crack is put and then the growth of crack during cyclic loading is studied till the failure of the specimen. The variation of stress intensity factor with respect to crack length and the number of cycles is evaluated for crack perpendicular to the contact length.

Keywords Dovetail Joint · Fatigue · Least squares analysis · Photoelasticity · Stress intensity factor

Introduction

Aero-engine compressor blade and disc assemblies are subjected to high thermo-mechanical loads due to high speed rotation and the fluid flow over the blades. As indicated by Shi et al. [1], there are two major causes of failure due to fatigue viz., the action of centrifugal force causing a relative motion between the contact surfaces resulting in low cycle fatigue (LCF) and the high cycle fatigue (HCF) which is caused due to the vibrational loads. Along with the loading conditions, complexities like the contact geometry, surface treatments influence the failure mode and the amount of damage incurred at the blade-disk interface [2, 3]. Consideration of these factors is important while designing such components. It is challenging to simulate these conditions experimentally as the forces are continuously varying under real working conditions. However, representative experiments could still be conducted. The experimental fixture designed by Ruiz et al. [4] can be used to simulate both the centrifugal force and the remote disc loading. Rajasekaran and Nowell [5] also developed a similar biaxial fixture for simulating the combined effect of centrifugal force and blade vibrations. However, it is relatively expensive to perform tests using these fixtures. Hence, for simplicity the HCF and LCF experiments can be performed separately [1].

The present work is focused on the analysis of low cyclic fatigue in dovetail assemblies. A suitable dovetail specimen was selected and the fatigue experiments under cyclic loading were conducted. As shown by Durelli et al. [6], it is considered that along the thickness of the dovetail assembly, the stress variation is neglected and hence the dovetail stresses could be taken as a two dimensional problem. Using this assumption the experimental technique of two dimensional photoelasticity is used to get the information about the stress field in the presence of a crack. Using digital photoelasicity [7], the fringe data from the experimental images is obtained with the help of in-house developed software DigiTFP® [8] which is then used to find stress intensity factors (SIFs) using another in-house developed software PSIF. It employs an over-deterministic non-linear least squares approach to evaluate the stress field parameters.

Experimental Model Selection

A scaled down arrangement of blade and disc which is used in an aero-engine compressor is taken for the experiments. Epoxy sheet of 6 mm thickness is cast by mixing Araldite CY 230 epoxy resin and HY 951 hardener in the ratio of 10:1 by weight. The mixture is mixed carefully and then allowed to cure in the mould for 24 h at room temperature. The specimens of the required size as shown in Fig. 1 are then machined from this cast sheet using high speed router with precautions to

M. Thomre (✉) · K. Ramesh
Department of Applied Mechanics, Indian Institute of Technology Madras, Chennai, TN, India

M. Silberstein et al. (eds.), *Challenges in Mechanics of Time Dependent Materials, Fracture, Fatigue, Failure and Damage Evolution, Volume 2*, Conference Proceedings of the Society for Experimental Mechanics Series, https://doi.org/10.1007/978-3-030-29986-6_17

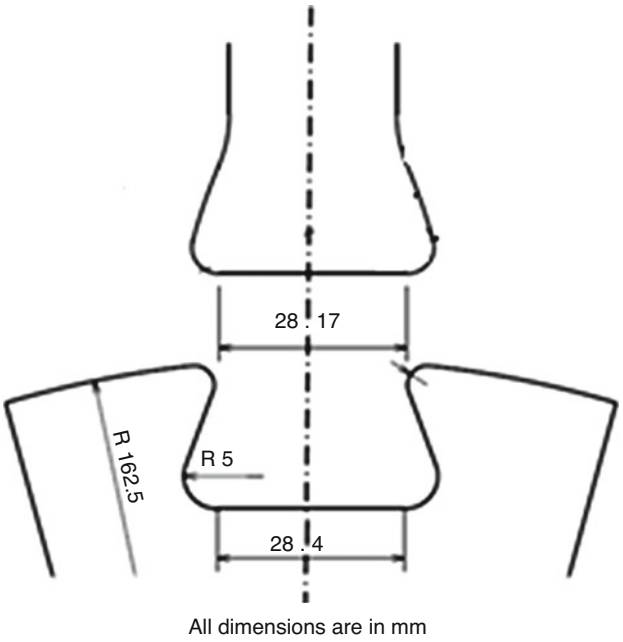

Fig. 1 Blade and Disc geometry

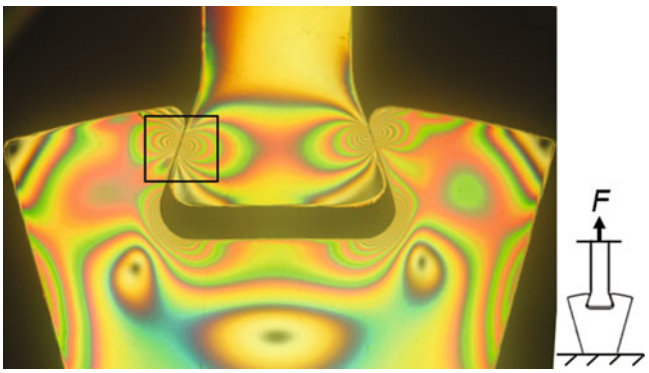

Fig. 2 Dark field isochromatics of Dovetail assembly subjected to tension

avoid excessive heating and formation of residual stresses. The material stress fringe value for the epoxy specimens is found out using a circular disc of 50 mm diameter which comes out to be 11.90 N/mm/fringe for the wavelength 546.1 nm.

Stress Distribution at the Joint

In the aero-engine, the blades are subjected to various forces like centrifugal force, bending due to fluid flowing over the blade, unsteady centrifugal forces due to shaft vibrations along with thermal stresses and hence experiencing a cycle loading. Initially, the assembly is loaded under tensile load to evaluate the stress distribution at the joint which is shown in Fig. 2. The stress concentration region as shown in Fig. 2 is taken as the region of interest for further experiments.

Experiments Using Two Dimensional Photoelasticity

Once the region of interest is evaluated, an edge crack of 2.3 mm is cut on the blade by using a saw of 0.1 mm thickness. The crack orientation is kept perpendicular to the contact length. Then this dovetail assembly is fixed to the fatigue machine using a pin joint fixture at one end. Sufficient care is taken to avoid any misalignment between the applied force and the specimen axes as it can cause bending which can affect the test results. The dovetail assembly is then subjected to sinusoidal load variation with minimum to maximum force variation as 20–750 N with frequency of 2 Hz [9]. The images are recorded in circular polariscope arrangement using a high speed color camera Delsa Genie (CR-GC00-H6400, HM series) with a frame rate of 50 fps.

Stress Intensity Factor Evaluation Using Least Squares Analysis

The fracture parameters are calculated for the crack by processing the fringe data obtained from Twelve Fringe Photoelasicity (TFP) methodology by an over-deterministic non-linear least squares approach. Using the in-house developed software PSIF which uses a multi-parameter crack tip stress field equation proposed by Atluri and Kobayashi and corrected by Ramesh et al. [10], the SIFs are evaluated. For each case, it is ensured that the convergence error is less than 0.1 as below this value the data points match well with the theoretically generated image.

Result and Discusssion

When the cyclic loading is applied, the crack experiences a mixed mode loading and a very complex fringe field is obtained as shown in Fig. 3(a). To generate a well-matched theoretically reconstructed image, the solution requires eight parameters

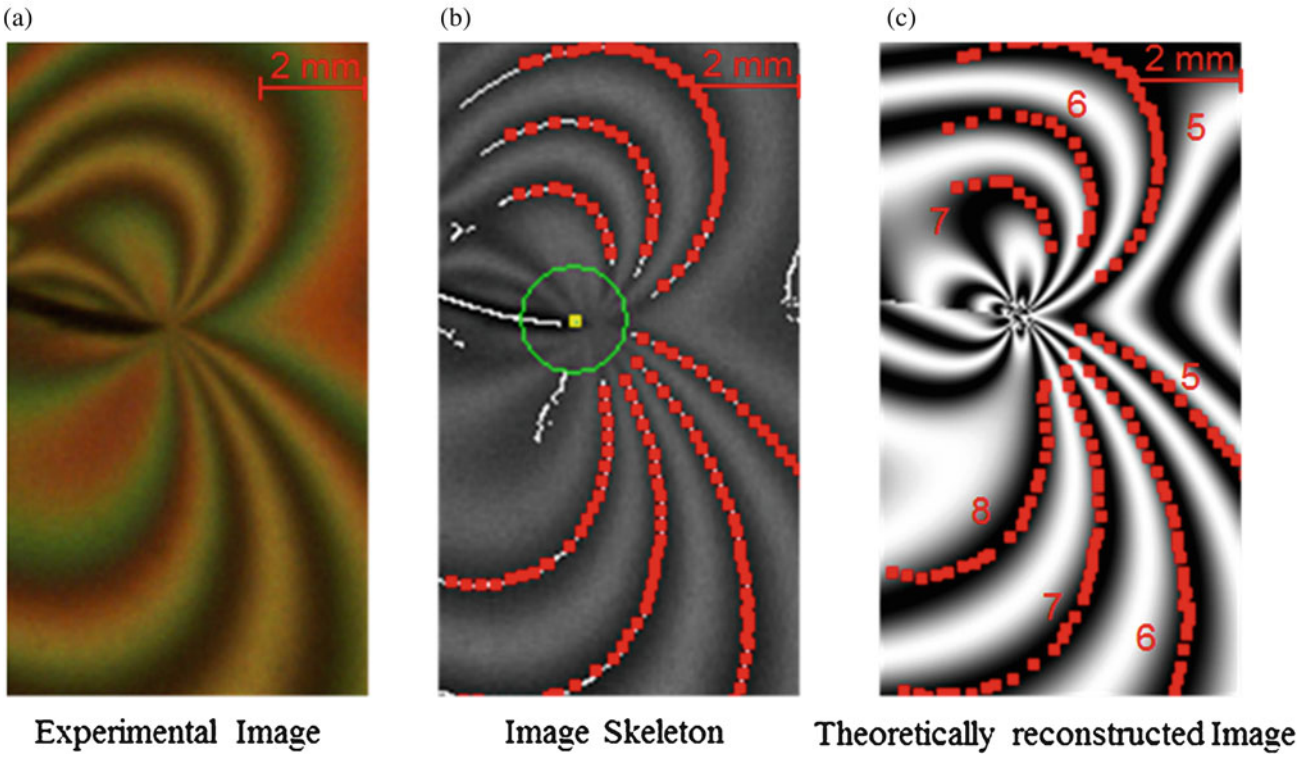

Fig. 3 (**a**) Experimentally obtained fringe pattern (**b**) Fringe skeleton for the recorded fringe pattern using TFP (**c**) Theoretically generated eight parameters solution for the crack length 42.01 mm

Table 1 Mode I and Mode II parameters used in the multi parameter solution of crack length of 42.01 mm

$A_{I1} = 2.0923$ MPa$\sqrt{}$m	$A_{II1} = -0.3774$ MPa$\sqrt{}$m
$A_{I2} = 2.7551$ MPa	$A_{II2} = 0.000$
$A_{I3} = 2.2130$ MPa(mm)$^{-1/2}$	$A_{II3} = -0.1982$ MPa(mm)$^{-1/2}$
$A_{I4} = -0.2681$ MPa(mm)$^{-1}$	$A_{II4} = 0.3210$ MPa(mm)$^{-1}$
$A_{I5} = 0.1981$ MPa(mm)$^{-3/2}$	$A_{II5} = -0.0189$ MPa(mm)$^{-3/2}$
$A_{I6} = -0.0071$ MPa(mm)$^{-2}$	$A_{II6} = 0.0197$ MPa(mm)$^{-2}$
$A_{I7} = 0.0026$ MPa(mm)$^{-5/2}$	$A_{II7} = 0.0041$ MPa(mm)$^{-5/2}$
$A_{I8} = -0.0002$ MPa(mm)$^{-3}$	$A_{II8} = -0.0017$ MPa(mm)$^{-5}$

Table 2 Variation of crack length and SIFs with no. of cycles

Sr. No.	No. of Cycle N	Time t (s)	Crack Length a (mm)	da/dN (mm/cycle)	K_I (MPa$\sqrt{}$m)	K_{II} (MPa$\sqrt{}$m)
1	2832	0	40.29	0.0065	0.1285	0.033
2	2892	30.04	42.01	0.0247	0.165	0.0299
3	2952	60.00	44.25	0.05	0.1687	0.049
4	3012	90.00	47.22	0.0497	0.1959	0.013
5	3050	109.54	49.22	0.0938	0.2014	0.011

of mode I and eight parameters of mode II as given in Table 1 which are obtained using the multi-parameter stress field equation. Using these parameters, the theoretically reconstructed image is obtained as shown in the Fig. 3c along with the stress intensity factors for mode I and mode II. It is observed that even the very complex stress field is constructed well using the multi-parameter equation. Similarly, the SIF values for remaining crack lengths are also evaluated.

With the initial crack length of 2.3 mm, the variation of crack length with number of cycles is evaluated. The variation in the crack length for the last 500 cycles with interval of 60 cycles is given in Table 2. The specimen undergoes cyclic loading and failed at 3050th cycle at the crack length of 49.22 mm measured just before failure.

It is observed that the crack is increasing from 40.29 mm to 49.22 mm in 500 cycles. Considering initial time at 40.29 mm of crack length as zero, the specimen failed in next 109.22 s. Along with the crack length, the SIFs at different cycles were also evaluated using the multi-parameter stress field equations, for each 60 cycles interval staring from crack length of 41.27 mm. As observed by Muktai and Ramesh [11], the initial stages are having mode II dominance. Further observations from the current study showed that as the crack grows, mode I is becoming more dominant and the failure is occurred due to that.

In the current study, the fatigue analysis of only one orientation is completed. The effect of cracks on the blade with different orientations subjected to fatigue is currently under progress. This will further be used to predict the life of the blades under fatigue loading.

Conclusion

The aero-engine blade experiences the cyclic loading due to the various forces. The crack perpendicular to contact length is put and the variation of crack length is found following a linear trend with the number of cycles. It is also concluded from the observations that failure is occurred due to dominance of the mode I. Also, it is found that the computerized fatigue machine is synchronized with the high speed color camera and the selected frame rate of 50 fps is sufficient enough to capture the crack propagation. Hence this procedure is standardized will be used for further experimentations.

References

1. L. Shi, D.-s. Wei, Y.-r. Wang, A.-m. Tian, D. Li, An investigation of fretting fatigue in a circular arc dovetail assembly. Int. J. Fatigue **82**, 226–237 (2016)
2. D.S. Wei, S.H. Yuan, Y.R. Wang, Failure analysis of dovetail assemblies under fretting load. Eng. Fail. Anal. **26**, 381–396 (2012)
3. P.J. Golden, A. Hutson, V. Sundaram, et al., Effect of surface treatments on fretting fatigue of Ti–6Al–4V. Int. J. Fatigue **29**, 1302–1310 (2007)
4. C. Ruiz, P.H.B. Boddington, K.C. Chen, An investigation of fatigue and fretting in a dovetail joint. Exp. Mech. **24**, 208–217 (1984)
5. R. Rajasekaran, D. Nowell, Fretting fatigue in dovetail roots: experiment and analysis. Tribol. Int. **39**, 1277–1285 (2006)
6. A.J. Durelli, J.W. Dally, W.F. Riley, Stress and strength studies on turbine blade attachment. SESA Proc **XVI**(1), 171–186 (1957)

7. K. Ramesh, *Digital Photoelasticity-Advanced Techniques and Applications* (Springer, Berlin, 2000)
8. K. Ramesh, *DigiTFP® Digital Twelve Fringe Photoelasticity* (Digital Photomechanics Lab, IIT Madras, 2017)
9. C. Ruiz, D. Novelli, Designing against fretting fatigue in aeroengines. ESIS **26**, 73–95 (2000)
10. K. Ramesh, S. Gupta, A.A. Kelkar, Evaluation of stress field parameters in fracture mechanics by photoelasicity-revisited. Eng. Fract. Mech. **56**(1), 25–45 (1997)
11. M. Thomre, K. Ramesh, Evaluation of Fracture Parameters of Cracks in Compressor Blade Root Using Digital Photoelasticity, in *Proceedings of 4th International Conference on Reliability, Safety and Hazard*, (2019)

An Automated Technique to Analyze Micro Indentation Load-Displacement Curve

N. M. Senanayake, Y. Yang, A. K. Verma, R. H. French, and J. Carter

Abstract High-throughput methods of measuring mechanical properties can accelerate materials discovery and processing route developments. These metrics of material performance get incorporated into both physics-based (ICME) and statistical machine-learning Processing-Microstructure-Properties (PMP) models. Conventional mechanical testing techniques, such as tensile testing, require large material volumes and become expensive and challenging when quantifying a statistically significant number of observations to enable process optimization thru PMP models of homogeneous materials; not to mention the added complexity of purposefully engineered inhomogeneous materials. Instrumented microhardness machines enable the extraction of indentation stress-strain curves from load-displacement curves as a proxy metric for more time/cost intensive uniaxial stress-strain curves. This versatile technique characterizes the local stress-strain behavior from small material volumes by modifying Hertz theory on the stresses between elastic solids. In this paper, an automated algorithm, written in Python (v2.7), is presented to apply modified Hertz's theory to extract the Elastic Modulus and indentation stress-strain curve from the load-displacement data. Two methods of assuming the contribution of the elastic deformation of the indenter are presented. First, the algorithm works through the assumptions made by Khosravani et al. and presents these results in comparison to a second method of assuming that the contribution of the indenter elastic deformation is sufficiently small that it is assumed constant and can be approximated from the size of the indent on the sample surface. The algorithms are compared using microhardness measurements from a nickel-base superalloy, LSHR and show that the Elastic Modulus and the yield strength values are in reasonable agreement with the reference literature. The assumptions on the effect of the indenter elastic properties has effects on the shapes of the plastic part of the curve; the Khosravani et al. method seems to underestimate the work hardening properties of the material; while the other method overestimates the work hardening properties. Therefore, utilizing both methods provides proxy measurements of the potential upper and lower bounds of the work hardening behavior beyond the yield strength of the material which could be helpful for PMP models.

Keywords Micro-indentation · Indentation yield strength · Indentation Elastic Modulus · Indentation work-hardening coefficient · Stress-strain curve · Load-unload curve

Introduction

There is interest in measuring Elastic Modulus, yield strength, and strain-hardening exponents from small volumes of materials. Typically, tensile tests [1] for measuring the yield strength and Elastic Modulus requires relatively large samples with homogenous microstructure. A reliable method for measuring these properties from small volume would reduce the cost and effort in establishing PMP models [2]. For example, process model development for additive manufacturing requires novel high-throughput assay approaches to establish PMP models [3]. The process history is inherently inhomogeneous and anisotropic, requiring small-scale testing to quantify local properties. Typically, indentation testing has been used for proxy estimates of mechanical response [4–6], but equipment instrumentation allows researchers to generate meaningful stress-strain curves [7–9].

Hertz's theory on contact mechanics [10] is used to extract the stress-strain curve from an indentation experiment. Hertz's theory is constructed for contact between elastic surfaces, and a modification (proposed by Khosravani et al. [11, 12]) is required to accommodate plasticity. The challenge of extracting stress-strain curves is to estimate the evolving contact

N. M. Senanayake (✉) · A. K. Verma · R. H. French · J. Carter
Department of Materials Science and Engineering, Case Western Reserve University, Cleveland, OH, USA
e-mail: nms105@case.edu

Y. Yang
Department of Chemical and Biomolecular Engineering, Lehigh University, Bethlehem, PA, USA

M. Silberstein et al. (eds.), *Challenges in Mechanics of Time Dependent Materials, Fracture, Fatigue, Failure and Damage Evolution, Volume 2*, Conference Proceedings of the Society for Experimental Mechanics Series, https://doi.org/10.1007/978-3-030-29986-6_18

radius between the sample and the indenter tip [13]. By measuring both the loading and unloading load-displacement curves it is possible to transition Hertz's theory from frictionless contact between two elastic solids to account for elastic-plastic interactions and approximate changes in contact area. In this paper, we propose a modified method for calculating the contact radius that incorporates measurement of the final indentation diameter.

Theory

Hertz's theory on the relationship between the applied load (P) and elastic displacement of the sample (h_e) is expressed as:

$$P = \frac{4}{3} E_{eff} \sqrt{R_{eff} {h_e}^3} \tag{1}$$

Where R_{eff} and E_{eff} are the effective radius and effective Elastic Modulus. The effective radius can be calculated by measuring the elastic displacement of the sample (h_e). The effective radius is the combination of the radius of the sample (R_s) and the indenter (R_i), which can be expressed as:

$$\frac{1}{R_{eff}} = \frac{1}{R_i} + \frac{1}{R_s} \tag{2}$$

For the indentation geometry, under purely elastic loading conditions, R_s is infinite and the effective radius it the radius of the indenter. After E_{eff} is calculated by applying R_{eff} and h_e to Eq. 1, the Elastic Modulus of the sample (E_s) can be calculated using Eq. 4:

$$\frac{1}{E_{eff}} = \frac{1-\upsilon_i}{E_i} + \frac{1-\upsilon_s}{E_s} \therefore E_s = (1-\upsilon_s)\left(\frac{1-\upsilon_i}{E_i} - \frac{1}{E_{eff}}\right)^{-1} = (1-\upsilon_s)\left(\frac{1-\upsilon_i}{E_i} - \frac{4\sqrt{R_{eff}{h_e}^3}}{3P}\right)^{-1} \tag{3}$$

Where υ_i and υ_s are the Poisson ratio for the indenter and the sample respectively, and E_i is the indenter Elastic Modulus.

Calculating the Stress-Strain Curve

The indentation stress (σ_{ind}) and strain (ε_{ind}) can be calculated from the maximum load (P) and sample displacement (h_s) and knowing the contact radius (a):

$$\sigma_{ind} = \frac{P}{\pi a^2} \tag{4}$$

$$\varepsilon_{ind} = \frac{4}{3\pi}\frac{h_s}{a} \tag{5}$$

A single loading-unloading curve in a cyclic loading-unloading experiment, Fig. 1, provides a single stress-strain point. Khosravani et al. [2] postulated that the contact radius (a) can be calculated using the value of R_{eff}:

$$a = \sqrt{R_{eff}\left(h_t - h_p\right)} \tag{6}$$

Where R_{eff} is calculated from h_t by modifying Eq. 1 to accommodate plastic deformation:

$$h_t = \left[\frac{3P}{4E_{eff}\sqrt{R_{eff}}}\right]^{\frac{2}{3}} + h_p \therefore R_{eff} = \left(\frac{3P}{4E}\right)^2 \left(h_t - h_p\right)^{-3} \tag{7}$$

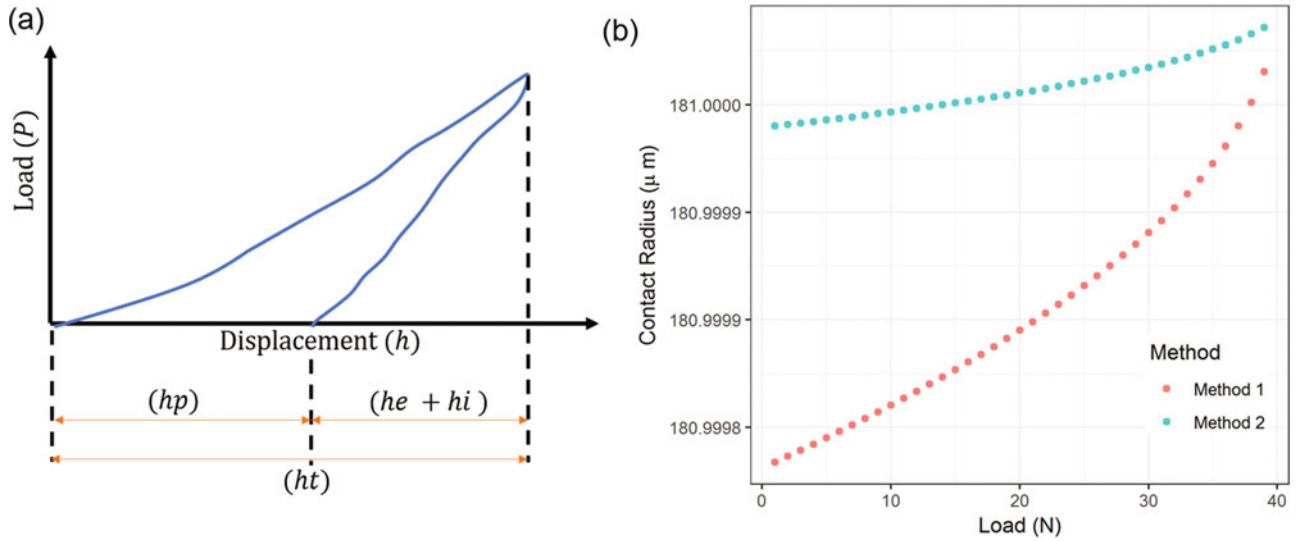

Fig. 1 (**a**) Schematic indentation load-unload curve in which the total indenter displacement (h_t) is accommodated by the sample experiencing both elastic (h_e) plastic (h_p) displacement an elastic displacement of the indenter (h_i). This schematic assumes that the elastic displacement of the indenter is zero. (**b**) The difference between the contact radii measured by methods 1 and methods 2

Where h_p is the plastic displacement extracted from the load-displacement curve by the intercept on the displacement axis after extending the unloading curve, assuming linear elasticity as shown in Fig. 1, and h_i is the elastic displacement of the indenter:

$$h_i = \frac{3\left(1 - {v_i}^2\right) P}{4E_i a} \tag{8}$$

The total displacement of the sample ($h_s = h_e + h_p$) is calculated from h_t and accounting for h_i:

$$h_s = h_t - h_i \tag{9}$$

An alternative method for solving for the contact radius proposed in this paper. In this method (method 2) contact radius for an arbitrary load is based on the geometry of the indent left on the sample surface. Assume the indent shape on the sample surface is the sector of a sphere, then the area of the curved surface is described in the following manner: $A = 2\pi R h_{pf} = \pi\left(a_f^2 + h_{pf}^2\right)$. Where h_{pf} is the plastic deformation of the sample calculated from the final loading cycle. The final contact radius, a_f, is measured from an optical image of the indent on the sample surface (Fig. 2b) and is used to calculate the radius of the indenter R. Therefore, the contact radius (a) for an arbitrary earlier loading cycle can be calculated below:

$$R = \frac{h_{pf}}{2} + \frac{2{a_f}^2}{h_{pf}} \therefore a = \sqrt{\frac{h_p}{2}\left(R - \frac{h_p}{2}\right)} = \sqrt{\frac{h_p}{2}\left(\left(\frac{h_{pf}}{2} + \frac{{a_f}^2}{2h_{pf}}\right) - \frac{h_p}{2}\right)} \tag{10}$$

A comparison of the contact radii calculated from the two methods is shown as Fig. 1b. It shows that at high loads that method 1 is predicting a larger contact radius than method 2, while at low load values method 2 is under estimating the contact radius. Similar to the first method, h_i is calculated from Eq. 8, and h_s is calculated from Eq. 9.

Method

The algorithm was validated by conducting 100 indentation tests in a 10 × 10 array on a 1 cm × 1 cm sample of a nickel-based superalloy. LSHR is a nickel-based superalloy developed by NASA Glenn [14]. Prior to indentation tests, a supersolvus heat treatment following standard conventions was conducted. After heat treatment, the samples were cut using the Allied

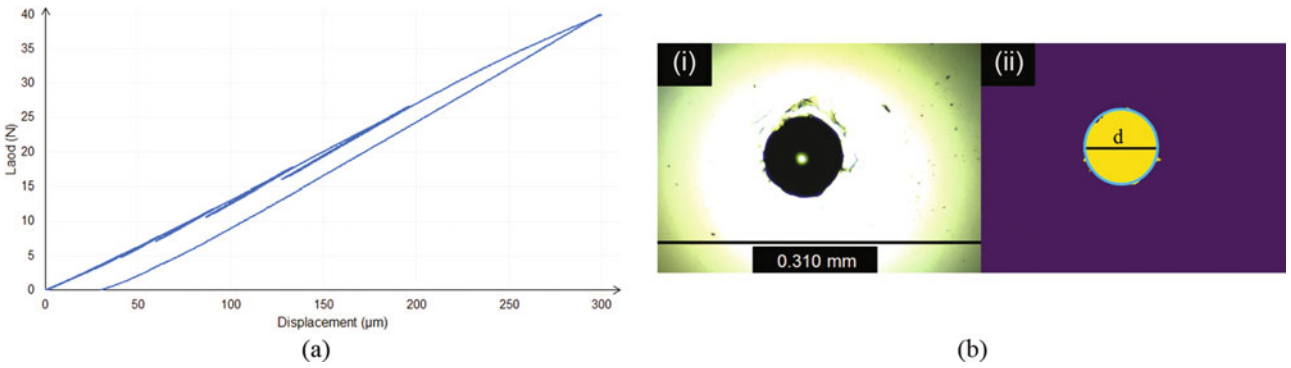

Fig. 2 (**a**) Load-Displacement curves for a single indentation experiment showing the fifteen load-unload cycles. (**b**) Optical image (1) and converted binary image (2) after noise filtering showing an overlay of the diameter of the fit minimum circumscribed circle

$A_L > A \cup A_R < A$	Region I
$A_L < A \cup A_R < A$	Region II (local maxima)
$A_L < A \cup A_R > A$	Region III
$A_L > A \cup A_R > A$	Region IV (local minima)

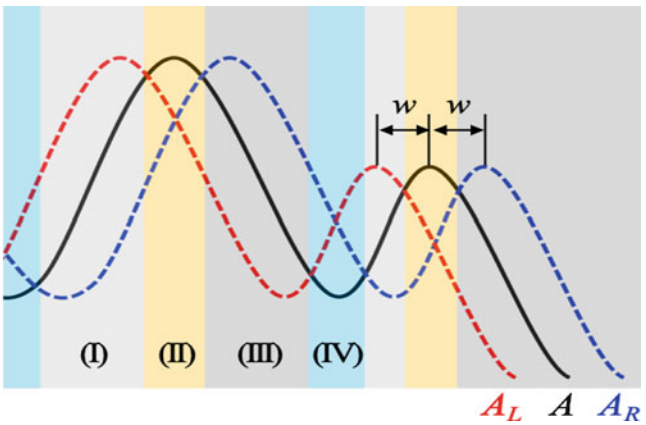

Fig. 3 (Left) Boolean Conditions implemented in the algorithm and (right) a schematic time-loading curve with left and right shift curves showing the regions to find local maxima (region II) and minima (region IV)

Techcut machine with SiC blades and polished using conventional mechanical polishing techniques to a mirror surface finish with a final polishing step with 3 μm polycrystalline diamond suspension. The mechanical properties measured via hardness indentation are comparable to the behavior presented in Gabb et al. [14].

A NANOVEA PB1000 hardness tester with a spherical diamond tip, with a 200 μm radius, was used to conduct experiments under load and unload control at a rate of 50 N/min, [2]. The resolution of the load cell was 30 mN, to a maximum load of 40 N, and the resolution on the displacement measurements was 2.2 nm, for a range of 25 mm. The initial load was 2 N and increased to 40 N in fifteen loading-unloading cycles ($\Delta P = 2.5$ N between peak loads); the minimum load in each unloading cycle was 40% of the peak load in the previous loading cycled. Figure 3a shows a representative multistep loading-unloading curve for an individual indentation experiment. The load, displacement, and time are recorded at a sufficiently high sampling rate 10-4 s to capture the peak and minimum loads. At the conclusion of the test, an optical image of the indent was captured with 1600 × 1200 pixel camera at 100× magnification (Fig. 2b).

Algorithm

The algorithms were written in Python (v2.7) using NumPy, Matplotlib, Skimage, Opencv, Pylab, Math, and Scipy libraries. The approach is as follows: ingest the load-displacement-time data and the post-experiment optical image; extract metrics from the load-displacement-time data; image processing for extraction of the final indentation radius; integrate the metrics and calculate the stress strain curves.

Data Ingestion

The algorithm ingests file pair: the load-displacement-time data and the post-deformation indent image, for a set of n indent experiments. The raw data for each indentation experiment is (1) a CSV of the metadata associated with the test parameters in a header followed by columns of data for the load and displacement at particular times; and (2) a JPEG color image of the indent on the sample surface collected at the conclusion of the experiment. The file naming convention is established to maintain the metadata associated with the sample name, measurement location, and measurement method. The filename will be a combination of letters and numbers that represent such information, during the ingestion phase this information is extracted and stored separately in an associated metadata file.

Algorithm Assumptions

The algorithm has these built-in assumptions: the polycrystalline-diamond spherical indenter tip has an Elastic Modulus (E_i) and Poisson's ratio (v_i) of 1050 GPa and 0.22 respectively and a radius of 200 μm. The transition from the purely elastic region (i.e., $R_{eff} = R_i$) to elastic-plastic region (i.e., R_{eff} is calculated from Eq. 7) in the calculation of stress and strain (Eqs. 4 and 5) is differentiated based on the unloaded threshold residual displacement value (h_p) of 0.05 μm.

Load-Displacement-Time Data Extraction

The first step in the analysis is the extraction of the peak loading positions. The load-displacement curve cannot be described by a function (i.e., it has two potential load values for the same displacement value). Thus, the algorithm uses the time-loading curve to identify the loading/unloading transition points. First, we find the local maxima region to reduce the effect of noise; noise can cause a misleading peak position. We utilized the first derivative method to find the local maxima. In order to apply the method to the entire region, we shift the original curve (A) to the left (AL) and the right (AR) with window size w use the following Boolean conditions, as shown in Fig. 3.

We then find the peak position using the first derivative of the values within each region II and IV respectively. The peaks are then labeled to subsequently extract the unloading portion of the curves. Linear elasticity is used to extract the slope of the unloading curve and to extrapolate the curve to a zero load-displacement value to find h_p for each local maxima.

Indent Image Analysis

The algorithm first separates the indented area from the background, generating a binary image using the Otsu threshold filter (skimage.filters.threshold_otsu) (Fig. 2b(1)). Next, a morphology filter (skimage.remove_small_objects) removes image noise due to lighting variations. Finally, the contact radius, a_f, is calculated from the circle circumscribed within the indented area (Fig. 2b(2)).

Data Integration and Validation

Finally, the data from the assumptions, load-displacement data, and the image analysis data are combined to solve for the values of indentation stress strain (Eqs. 4 and 5) using either the Khosravani et al. [12] method (method 1) and the method we proposed (method 2).

Results and Discussion

The indentation stress-strain curves calculated from a single multi-step loading experiment using the two methods of approximating the contact radius are plotted in Fig. 4a, b. A comparison of the values of Elastic Modulus and Yield Strength for the two methods are shown in Fig. 4c, d. As shown in these second figures, method 2 systematically under calculates both metrics as compared to the method 1 calculation of the contact radius. The calculation of the contact radius in method 2 assumes that the elastic displacement of the indenter is constant and calculated from the maximum load. This results in an over-estimation of the contact radius estimation (Fig. 1b) and in turn results in lower calculated stress (Eq. 4) and strain (Eq. 5) values in the elastic region as compared to the method 1 calculated values of contact radius. In method 1, the contact radius as a function of the indenter elastic displacement is effectively a hidden function accounted for by letting the value of R_{eff} float in values calculated from the total and plastic deformation of the sample. The differences in units between yield strength and Elastic Modulus obfuscates the fact that the relative difference between the calculated metrics for two methods are similar; i.e., the relative difference between the method 2 calculations of yield strength and Elastic Modulus are approximately 1.6% and 6.7% respectively.

The calculations of the contact radius by the two methods mostly converges at large values of applied load, as shown in Fig. 1b. Though it can be noted that the method 1 over-predicts that contact radius at the maximum load; this is noted by the crossover point in Fig. 1b at around 43 N. If the theories were self-consistent you would expect that the contact radius during

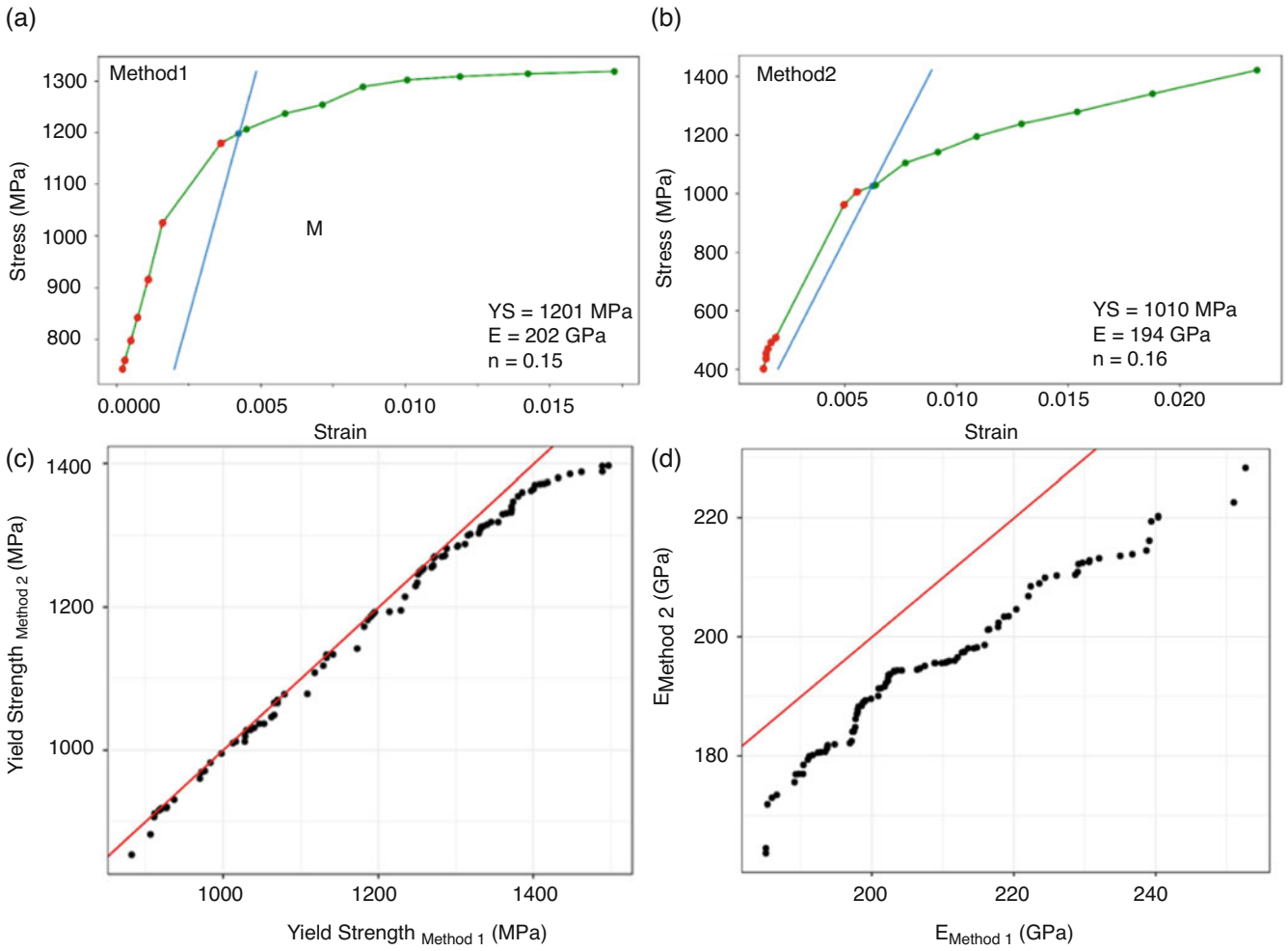

Fig. 4 Indentation stress-strain curve generated by (**a**) method 1 and (**b**) method 2. The extracted Elastic Modulus, yield strength, and strain hardening exponent (GPa, MPa, MPa) are presented for each method in the lower right of each plot. A comparison of the calculated values for the Yield Strength (**c**) and Elastic Modulus (**d**) are presented. Since all the data points lie below a line with a slope of one, it is obvious that Method 2 under-predicts compared to Method 1

Table 1 Comparison of the mechanical property metrics extracted from averaging the results after normalizing the outliers from 100 indentation stress-strain curves calculated using two methods of approximating the contact radius with the metrics extracted from uniaxial tensile testing [15]

Method	E (GPa)	σ_y (MPa)	Max Stress (MPa)	n
Method 1	208 ± 15	1203 ± 155	1376 ± 190	0.15 ± 0.02
Method 2	194 ± 13	1184 ± 168	1420 ± 186	0.16 ± 0.015
Tensile Test [14]	179–220	979–1116	1158–1558	0.17–0.20

the loading could not be greater than what was measured from the optical image. Therefore, if a more accurate measure of the work hardening behavior were required, it might be worth bounding the method 1 calculations by the method 2 calculations from P_{max}. Though not implemented in the algorithm, this could hypothetically be accommodated in the following manner:

$$a_{max} = \alpha \sqrt{R_{eff}\left(h_t - h_p\right)} = a_f \tag{11}$$

Where a fitting parameter, α, is added to Eq. 6 Such that calculated contact radius in method 1 at the max matches that contact radius, a_f, measured from the optical image. Without examining the work hardening behavior of several known materials, we can only postulate the appropriate use of the fitting parameter, i.e., should it be inside or outside of the square root.

The average mechanical property values averaged from 100 indent measurements are compared in Table 1 with the uniaxial tensile properties measured by Gabb et al. [15]. First, the assumptions of the two methods provide no appreciable differences in the output of the metrics of Elastic Modulus and the yield strength. Also, shown is that microhardness indentation can provide comparable information about the strain hardening coefficient of the materials; as calculated from the Holloman equation [16]. The maximum stress calculated from the two methods shows the obvious cross-over in the contact radius assumptions, with method 2 now over predicting the maximum stress observed compared to method 1. This crossover behavior in the calculation of the contact radius lead to identical measures of the strain hard coefficient.

The distribution of the yield-strength and Elastic Modulus values collected over 100 indents (shown in Fig. 4c, d) indicates that even though this is microhardness indentation experiment, the low load values in this regime result in the collection of pseudo-single crystal properties. The range in the measured Elastic Modulus values: 163 - 228 is consistent with the range expected from a superalloy with 40% volume of Ni_3Al when the range of observed Elastic Moduli in single crystal Nickel (139–340 GPa) [16] and Ni_3Al (112–304 GPa) [17]. This leads us to the conclusion that 100 indents are sufficient to provide a bulk measurement of the mechanical properties for inputs into a PMP model for LSHR, though this may not be the minimum number of observations necessary to accomplish such a task.

Conclusions

In this work we have performed the high-throughput indentation testing using a spherical indenter tip and instrumented equipment to collect time/load/displacement data and an optical image poste indent. We proposed an alternative method of measuring/calculating the contacting contact radius and compare the metrics extracted from the indentation stress-strain curve. The results indicate that neither method may be wholly accurate, but both provide sufficient accuracy to provide reliable metrics for our material system. An alternative method is proposed but not validated to test against materials that exhibit significant work hardening that the apparent assumptions in the two methods might be further assessed. We conclude that performing a hundred indents on our sample is sufficient to extract the necessary proxy metrics for the bulk properties needed to develop PMP models for process development activities.

Acknowledgement This work was funded by the National Science Foundation under Grant No. 1152716. Indentation experiments were conducted using equipment maintained by Dr. Martin in the CWRU Materials for Optical Research and Education (MORE) center. This work made use of the High-Performance Computing Resource in the Core Facility for Advanced Research Computing at Case Western Reserve University. Finally, the authors wish to thank NASA Glenn for providing the stress-strain curves from the room temperature tensile tests of LSHR; and for many fruitful email conversations with Prof. Kalidindi on clarification of the techniques presented in his paper.

Data Availability: The algorithms presented in this paper can be downloaded from the following git repository: https://github.com/CWRU-MSL/MicroIndetationStressStrain and/or is available from the corresponding author upon request. The repository contains necessary code and an example data set for a pair of indents on LSHR for troubleshooting.

References

1. *Standard Test Methods and Definitions for Mechanical Testing of Steel Products.* (ASTM International, 2016)
2. V.H. Baltazar Hernandez, S.K. Panda, M.L. Kuntz, Y. Zhou, Nanoindentation and microstructure analysis of resistance spot welded dual phase steel. Mater. Lett. **64**(2), 207–210 (2010)
3. T. Lookman, P.V. Balachandran, D. Xue, J. Hogden, J. Theiler, Statistical inference and adaptive design for materials discovery. Curr. Opin. Solid State Mater. Sci. **21**(3), 121–128 (2017)
4. L. Zhang et al., Characterization of local deformation behavior of Fe–Ni lenticular martensite by nanoindentation. Mater. Sci. Eng. A **527**(7-8), 1869–1874 (2010)
5. Y. Mazaheri, A. Kermanpur, A. Najafizadeh, Nanoindentation study of ferrite–martensite dual phase steels developed by a new thermomechanical processing. Mater. Sci. Eng. A **639**, 8–14 (2015)
6. T. Ohmura, K. Tsuzaki, S. Matsuoka, Evaluation of the matrix strength of Fe-0.4 wt% C tempered martensite using nanoindentation techniques. Philos. Mag. A **82**(10), 1903–1910 (2002)
7. S. Pathak, S.R. Kalidindi, Spherical nanoindentation stress–strain curves. Mater. Sci. Eng. R Rep **91**, 1–36 (2015)
8. S.R. Kalidindi, S. Pathak, Determination of the effective zero-point and the extraction of spherical nanoindentation stress–strain curves. Acta Mater. **56**(14), 3523–3532 (2008)
9. S.J. Vachhani, R.D. Doherty, S.R. Kalidindi, Studies of grain boundary regions in deformed polycrystalline aluminum using spherical nanoindentation. Int. J. Plasticity **81**, 87–101 (2016)
10. Hertz Theory—an overview | ScienceDirect Topics. [Online]. https://www.sciencedirect.com/topics/engineering/hertz-theory.
11. A. Khosravani, A. Cecen, S.R. Kalidindi, Development of high throughput assays for establishing process-structure-property linkages in multiphase polycrystalline metals: Application to dual-phase steels. Acta Mater. **123**, 55–69 (2017)
12. J.S. Weaver, A. Khosravani, A. Castillo, S.R. Kalidindi, High throughput exploration of process-property linkages in Al-6061 using instrumented spherical microindentation and microstructurally graded samples. Integr. Mater. Manuf. Innov. **5**(1), 192–211 (2016)
13. S. Pathak, J. Shaffer, S.R. Kalidindi, Determination of an effective zero-point and extraction of indentation stress–strain curves without the continuous stiffness measurement signal. Scr. Mater. **60**(6), 439–442 (2009)
14. D. Siebörger, H. Knake, U. Glatzel, Temperature dependence of the elastic moduli of the nickel-base superalloy CMSX-4 and its isolated phases. Mater. Sci. Eng. A **298**(1-2), 26–33 (2001)
15. T.P. Gabb, J. Gayda, J. Telesman, P.T. Kantzos, *Thermal and Mechanical Property Characterization of the Advanced Disk Alloy LSHR* (2005), p. 82
16. A.W. Bowen, P.G. Partridge, Limitations of the Hollomon strain-hardening equation. J. Phys. D Appl. Phys. **7**(7), 969 (1974)
17. X. Luan et al., The mechanical properties and elastic anisotropies of cubic Ni_3Al from first principles calculations. Crystals **8**(8), 307 (2018)

Mechanics and Mechanisms of Slow Crack Propagation in Brittle Hydrogels

Kimberley Mac Donald and Guruswami Ravichandran

Abstract Several experiments have reported rate dependent roughening of crack surfaces in brittle hydrogels following slow crack propagation, 0.1–1 mm/s. We conduct in-situ 2D imaging of an internal plane of propagating cracks and volumetric imaging of stationary cracks using confocal microscopy for very slow crack speeds, 0.01 mm/s, in thin brittle hydrogel specimens. We seek to better understand the mechanisms at play in these slow crack roughening events by observing both crack propagation and renucleation. Additionally, we study the crack tip region and crack shape to infer fracture toughness of the gel. Observations suggest that toughening mechanisms are at play in these surface roughening events and lead to crack arrest followed by renucleation at a "weak" point in the crack surface. Based on these observations, we hypothesize that there are two interconnected mechanisms at play: The crack is slow enough that the gel "sees" the stress concentrations at the crack tip and water is forced out of the gel while there is also time for viscoelastic and plastic processes to occur.

Keywords Brittle hydrogels · Renucleation · Slow fracture · Soft polymers · Toughening mechanisms

Introduction

Although hydrogels are not typically viewed as structural or load bearing materials, recent advances in the fields of biomedical implants, wearable electronics, and soft robotics have led to an interest in the structural and damage mechanics of such materials [1, 2]. Hydrogels exhibit extreme mechanical properties with very low stiffnesses, comparable to many biological tissues including cartilage, skin, and heart muscle, and very high deformation capacity with many able to stretch to 300% or more of their original length before breaking. This low stiffness, high stretchability combination makes these materials highly biomechanically-compatible since their properties are comparable to native biological tissue which significantly reduces the chances of irritation or rejection of wearable devices and implants respectively [3–6].

However, unlike native biological tissue, traditional hydrogels exhibit very brittle fracture behavior. Understanding the mechanics of crack formation and propagation in these brittle hydrogel materials will allow us to better understand toughening methods in such materials and structures. Additionally, it will allow us to understand the mechanisms contributing to crack surface roughening that has been observed in slowly propagating cracks in these gels. Previous studies have used fracture energy measurements with post-mortem fractography to observe the effects of crack speed on surface roughening [7, 8]. We seek to better understand the surface roughening due to slow crack propagation reported in the literature by observing these propagation events *in-situ* on the microscale.

In this report, we present an experimental method to induce very slow, O(0.01 mm/s), stable crack propagation with *in-situ*, micron scale imaging and observations of the crack propagation and renucleation. Slow, stable crack propagation is achieved by using concepts from fracking and three-dimensional imaging is performed using confocal microscopy to capture images both volumetrically and at internal planes [9]. Quantitative visualization of the mechanics at play is achieved through image analysis and correlation techniques. Observations and analyses suggest that two interconnected toughening mechanisms are at play in the surface roughening of slow cracks: The crack advances slowly enough that the gel "sees" the stress concentration which forces water out of the gel at the crack tip while there is also time for viscous elastic and plastic processes to occur.

K. Mac Donald (✉) · G. Ravichandran
Division of Engineering and Applied Science, California Institute of Technology, Pasadena, CA, USA

M. Silberstein et al. (eds.), *Challenges in Mechanics of Time Dependent Materials, Fracture, Fatigue, Failure and Damage Evolution, Volume 2*, Conference Proceedings of the Society for Experimental Mechanics Series, https://doi.org/10.1007/978-3-030-29986-6_19

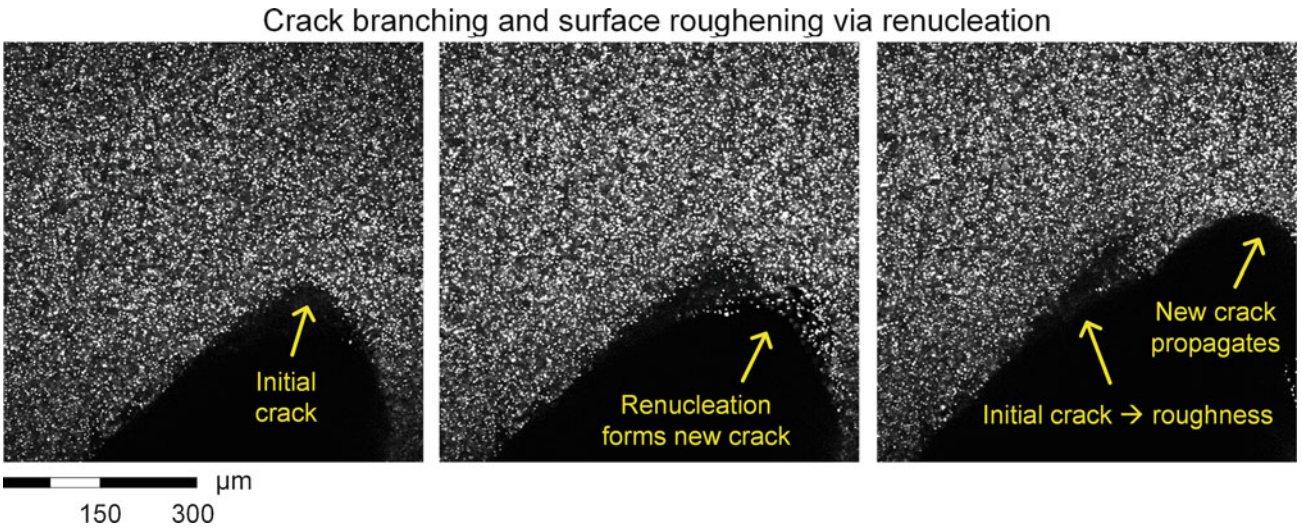

Fig. 1 Formation of crack surface roughening by renucleation: First an initial crack arrests when the stress concentration at the crack tip is no longer higher than the fracture toughness. Then renucleation occurs, forming a new crack which propagates. The initial crack tip is allowed to close and appears as a ridge (roughness) on the crack surface

Materials and Methods

This study seeks to understand the mechanisms at play in slow crack propagation in brittle hydrogels that lead to surface roughening through quantitative visualization and direct observation of crack propagation events. Microscale *in-situ* analysis and observation of crack propagation events allows for an understanding of the propagation and renucleation mechanisms beyond a post-mortem fractographic assessment.

Thin polyacrylamide-bis-acrylamide copolymer gel specimens were cast between two #0 glass coverslips where the surface tension of the water in the monomer solution allows the coverslips to self-align resulting in a relatively even gel thickness. Fracture was induced by injecting glycerol through a microfilament needle into an initial crack between the coverslips while lightly compressing the specimen in a custom designed loading device mounted on a standard microscope stage insert on an inverted laser scanning confocal microscope (LSCM) [10]. Volumetric images were taken of the initial cracks prior to propagation and of arrested cracks once propagation ceased. During crack propagation and renucleation events, 2D images were taken at an internal plane. Crack speeds achieved were less than 50 μm/s. Care was taken to ensure that cracks propagated slowly by monitoring and adjusting the injection rate of glycerol using a micro-syringe pump and that the crack remained in the frame of view by periodically adjusting the x-y coordinates of the microscope stage. However, since the glycerol is very viscous and injected via microfilament needle, there was significant friction between the glycerol and the inner wall of the needle resulting in delayed response to the pump being turned on and off. By turning the pump off once the crack began to propagate we were able to regulate the crack propagation rate. Initial observations suggest that renucleation events after the initial crack arrests contribute significantly to crack surface roughening in these slow propagation events.

Results and Discussion

Previous research has shown that when cracks propagate slowly enough through brittle hydrogel materials there is significant surface roughening that increases as the propagation rate decreases [7, 8]. In this study we seek to observe and measure slow crack propagation events in these materials in-situ in order to better understand the mechanisms that lead to this roughening. In cases where the crack renucleates near but not at the arrested crack tip, we observe significant roughening of the crack surface due to the change in location and re-orientation of the crack tip. In addition, the newly renucleated crack shows higher fracture energy than the initial crack, suggesting that toughness has increased. Fracture energy is measured assuming linear elastic fracture mechanics (LEFM) holds and measuring the crack tip opening displacement (CTOD) from the *in-situ* images. During a single propagation event we also observed some crack path meandering within the plane that may contribute to surface roughening. This meandering or local path reorientation is indicative of local changes in the effective

toughness of the gel. Fracture energy variations across different specimens are also observed and may be affected by small changes in local or global gel chemistry and specimen thickness.

The trends we observe suggest that toughening mechanisms play a significant role in fracture surface roughening for slow crack propagation in brittle hydrogels. Improving our understanding of these mechanisms, including how pressure induced fluid flow and viscous effects change material toughness, can improve our ability to design more resilient soft materials and structures for biomedical applications.

Acknowledgements This material is based upon work supported by the National Science Foundation Graduate Research Fellowship Grant No. DGE-1144469 and Designing Materials to Revolutionize and Engineer our Future (DMREF) Award No. DMS-1535083. Imaging was performed in the Biological Imaging Facility, with the support of the Caltech Beckman Institute and the Arnold and Mabel Beckman Foundation.

References

1. F. Baldi, F. Bignotti, I. Peroni, S. Agnelli, T. Ricco, On the measurement of the fracture resistance of polyacrylamide hydrogels by wire cutting tests. Polym. Test. **31**, 455–465 (2012)
2. R. Long, C.Y. Hui, Fracture toughness of hydrogels: measurement and interpretation. Soft Matter **12**, 8069–8086 (2016)
3. N. Annabi, J.W. Nichol, X. Zhong, C. Ji, S. Koshy, A. Khademhosseini, F. Dehghani, Controlling the porosity and microarchitecture of hydrogels for tissue engineering. Tissue Eng Part B Rev **16**(4), 371–383 (2010)
4. M. Whang, J. Kim, Synthetic hydrogels with stiffness gradients for durotaxis study and tissue engineering scaffolds. Tissue Eng Regen Med **13**, 126–139 (2016)
5. J.P. Gong, Y. Osada, Soft and wet materials: from hydrogels to biotissues, in *High Solid Dispersions*, ed. by M. Cloitre, (Springer, Berlin, Heidelberg, 2010), pp. 203–246
6. S. Agnelli, F. Baldi, F. Bignotti, A. Salvadori, I. Peroni, Fracture characterization of hyperelastic polyacrylamide hydrogels. Eng. Fract. Mech. **203**, 54–65 (2018)
7. T. Baumberger, C. Caroli, D. Martina, O. Ronsin, Magic angles and cross-hatching instability in hydrogel fracture. Phys. Rev. Lett. **100**(17), 178303 (2008)
8. Y. Tanaka, K. Fukao, Y. Miyamoto, Fracture energy of gels. Eur Phys J E **3**, 395–401 (2000)
9. J. Bostwick, K. Daniels, Capillary fracture in soft gels. Phys Rev Lett E. **88**(4), 042410 (2013)
10. K. Mac Donald, G. Ravichandran, An experimental method to induce and measure crack propagation in brittle polymers with heterogeneities, in *Fracture, Fatigue, Failure and Damage Evolution*, ed. by J. Carroll et al., vol. 6, (Springer, Cham, 2019), pp. 21–23

Viscoelastoplastic Damage with Maximum Rate of Dissipation-Based Growth Criterion and Tri-Component Lie Rate Decomposition

Richard B. Hall

Abstract Maximization of the rate of dissipation is applied to develop a viscoelastoplastic damaging material model with anisotropic properties and finite deformation. The thermodynamic framework suggests a new damage activation criterion based on the sum of stress and an energy release rate based on a damage-based strain measure. The framework combines the usually disjointed ideas of effective stress and damage strain kinematics to track the dimensional changes attributed to damage while retaining the physical link to load-bearing area reduction. Potential applications include large volume change oxidation of SiC CMC composites, high temperature creep and relaxation influences on damage processes in reinforced polymers and ceramics, and opening/closing of cracks via natural elastic behavior as opposed to treatments based on loading criteria.

Maximum rate of dissipation analysis is applied to develop a framework corresponding to a material model incorporating three strain elements characterized by viscoelastic, damage, and viscoplastic behaviors. A push-pull framework associates these behaviors with respective multiplicative deformation gradients with rates determined by Lie material derivatives.

Keywords Damage · Finite deformation · Viscoelastoplasticity · Lie derivatives

Kinematic/Kinetic Definitions

The present study considers materials which may undergo viscoelastoplastic damage under finite strains. The configurations and associated deformation gradients are depicted in Fig. 1, where $\mathbf{F}^c$ is viscoplastic/creep, $\mathbf{F}^d$ is damage, and $\mathbf{F}^{ve}$is viscoelastic, with $\mathbf{F} = \mathbf{F}^e\mathbf{F}^d\mathbf{F}^c$ the multiplicative decomposition of the total deformation. $\boldsymbol{\tau}$ is the Kirchhoff stress.

Denoting also $\mathbf{F}^{dc} = \mathbf{F}^d\mathbf{F}^c$for convenience and with $\mathbf{F}^e = \mathbf{F}^{ve}$ and $\mathbf{E}^e = \mathbf{E}^{ve}$ (Voigt assumption), strain measures are given by, strain measures are given by

$$\mathbf{E} = \frac{1}{2}\left(\mathbf{F}^T\mathbf{F} - \mathbf{I}\right) = \mathbf{F}^T\mathbf{e}\mathbf{F}, \quad \mathbf{e} = \frac{1}{2}\left(\mathbf{I} - \left(\mathbf{F}^e\mathbf{F}^{dc}\right)^{-T}\left(\mathbf{F}^e\mathbf{F}^{dc}\right)^{-1}\right.$$

$$\overline{\mathbf{E}}^d = \frac{1}{2}\left(\mathbf{F}^{dT}\mathbf{F}^d - \mathbf{I}\right), \quad \overline{\mathbf{e}}^c = \frac{1}{2}\left(\mathbf{I} - \mathbf{F}^{c-T}\mathbf{F}^{c-1}\right)$$

$$\tilde{\mathbf{E}}^d = \mathbf{F}^{d-T}\overline{\mathbf{E}}^d\mathbf{F}^{d-1}, \quad \tilde{\mathbf{e}}^c = \mathbf{F}^{d-T}\overline{\mathbf{e}}^c\mathbf{F}^{d-1}, \quad \tilde{\mathbf{E}}^e = \frac{1}{2}\left(\mathbf{F}^{eT}\mathbf{F}^e - \mathbf{I}\right),$$

$$\tilde{\mathbf{E}} = \tilde{\mathbf{E}}^e + \tilde{\mathbf{E}}^d + \tilde{\mathbf{e}}^c.$$

It can be noted that while $\tilde{\mathbf{E}}^e = \tilde{\mathbf{E}}^e\left[\mathbf{F}^e\right]$ and $\tilde{\mathbf{e}}^d = \tilde{\mathbf{e}}^d\left[\mathbf{F}^d\right]$, $\tilde{\mathbf{e}}^c$ has the mixed dependency $\tilde{\mathbf{e}}^c\left[\mathbf{F}^c, \mathbf{F}^d\right]$, but $\tilde{\mathbf{e}}^c = 0$ when $\mathbf{F}^c = 0$ and $\tilde{\mathbf{e}}^c$ pushes/pulls properly with the deformation.

The Lie derivatives employed for tensors associated with $\tilde{\kappa}$ are material derivatives of these tensors when pulled back to the reference configuration κ_R, then pushed back to $\tilde{\kappa}$, as illustrated by that of $\tilde{\mathbf{E}}$:

R. B. Hall (✉)
Air Force Research Laboratory, WPAFB, Dayton, OH, USA
e-mail: richard.hall.16@us.af.mil

M. Silberstein et al. (eds.), *Challenges in Mechanics of Time Dependent Materials, Fracture, Fatigue, Failure and Damage Evolution, Volume 2*, Conference Proceedings of the Society for Experimental Mechanics Series, https://doi.org/10.1007/978-3-030-29986-6_20

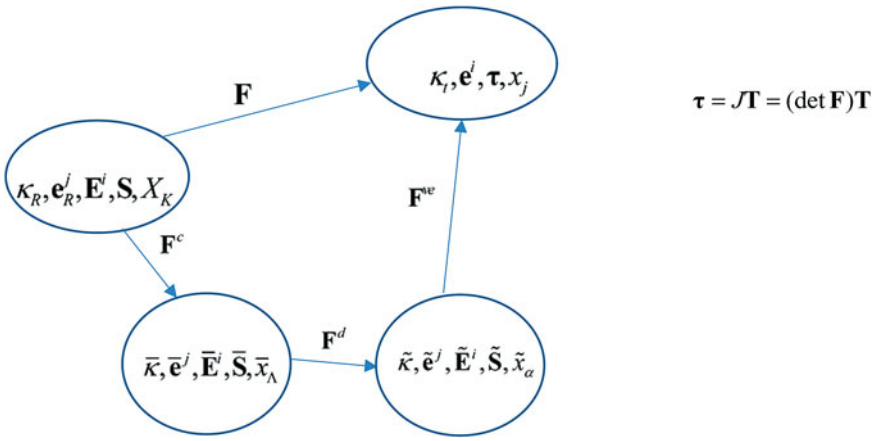

Fig. 1 Body configurations κ_R (reference), $\bar{\kappa}$, $\tilde{\kappa}$ and κ_t (current time). X_K, $\bar{x}_\Lambda$, $\tilde{x}_\alpha$, x_j are coordinates

$$\overset{\triangle}{\tilde{\mathbf{E}}} = \mathcal{L}^{dc}\tilde{\mathbf{E}} = \mathbf{F}^{dc-T}\overline{\left(\mathbf{F}^{dcT}\tilde{\mathbf{E}}\mathbf{F}^{dc}\right)}\mathbf{F}^{dc-1} = \mathbf{F}^{dc-T}\dot{\mathbf{E}}\mathbf{F}^{dc-1} = \mathbf{F}^{eT}\mathbf{d}\mathbf{F}^{e} = \tilde{\mathbf{d}} = \dot{\tilde{\mathbf{E}}} + \left(\tilde{\mathbf{l}}^{dc}\right)^T\tilde{\mathbf{E}} + \tilde{\mathbf{E}}\tilde{\mathbf{l}}^{dc}$$

$$\mathbf{d} = \frac{1}{2}\left(\left(\dot{\mathbf{F}}\mathbf{F}^{-1}\right)^T + \dot{\mathbf{F}}\mathbf{F}^{-1}\right), \quad \tilde{\mathbf{l}}^{dc} = \dot{\mathbf{F}}^{dc}\mathbf{F}^{dc-1}.$$

Stress measures and stress power combinations are given by:

$$\mathbf{S} = \mathbf{F}^{-1}\boldsymbol{\tau}\mathbf{F}^{-T} = \mathbf{F}^{dc-1}\tilde{\mathbf{S}}\mathbf{F}^{dc-T} = \mathbf{F}^{c-1}\bar{\mathbf{S}}\mathbf{F}^{c-T} \quad \tilde{\mathbf{S}} = \mathbf{F}^{e-1}\boldsymbol{\tau}\mathbf{F}^{e-T} \quad \bar{\mathbf{S}} = \mathbf{F}^{ed-1}\boldsymbol{\tau}\mathbf{F}^{ed-T}$$

$$\tilde{\mathbf{S}} \cdot \overset{\triangle}{\tilde{\mathbf{E}}} = \tilde{\mathbf{S}} \cdot \tilde{\mathbf{d}} = \boldsymbol{\tau} \cdot \mathbf{d} = \mathbf{S} \cdot \dot{\mathbf{E}}$$

with

$$\mathrm{tr}\,(\mathbf{TS}) = \mathbf{T}_{ij}\mathbf{S}_{ji} = \mathbf{T} \cdot \mathbf{S}.$$

A similar kinematic/kinetic framework with one intermediate configuration is detailed by Stumpf [1].

Thermodynamics/Constitutive Development

The reduced energy dissipation equation, assuming a split of the entropy production into mechanical and thermal components, is given by (ψ, ρ_o, η, θ, $\mathbf{q}_0$ are respectively Helmholtz energy, reference density, specific entropy, temperature, and heat flux referred to the reference configuration):

$$-\rho_0\dot{\psi} - \rho_0\eta\dot{\theta} + \tilde{\mathbf{S}} \cdot \overset{\triangle}{\tilde{\mathbf{E}}} - \mathbf{q}_0 \cdot \frac{\nabla_0\theta}{\theta} = \rho_0\theta\zeta \equiv \xi$$

$$-\rho_0\dot{\psi} + \tilde{\mathbf{S}} \cdot \overset{\triangle}{\tilde{\mathbf{E}}} = \xi^{mech}, \quad -\rho_0\eta\dot{\theta} - \mathbf{q}_0 \cdot \frac{\nabla_0\theta}{\theta} = \xi^{thermal}$$

Assuming $\psi = \tilde{\psi}\left[\tilde{\mathbf{E}}^{ve}, \tilde{\mathbf{e}}^{d}, \tilde{\mathbf{e}}^{c}\right]$ with the chain rule for $\overset{\triangle}{\psi}$ it follows:

$$\mathrm{tr}\left[\tilde{\mathbf{S}}\left(\overset{\triangle}{\tilde{\mathbf{E}}}^{ve} + \overset{\triangle}{\tilde{\mathbf{e}}}^{d} + \overset{\triangle}{\tilde{\mathbf{e}}}^{c}\right)\right] - \rho_0 \overset{\triangle}{\psi} = \xi^{mech} \geq 0$$

$$\left(\tilde{\mathbf{S}} - \tilde{\mathbf{S}}^{e}\right) \cdot \overset{\triangle}{\tilde{\mathbf{E}}}^{ve} + \left(\tilde{\mathbf{S}} + \tilde{\mathbf{Y}}\right) \cdot \overset{\triangle}{\tilde{\mathbf{e}}}^{d} + \left(\tilde{\mathbf{S}} - \tilde{\mathbf{S}}^{c*}\right) \cdot \overset{\triangle}{\tilde{\mathbf{e}}}^{c} = \xi^{mech} \geq 0$$

$$\tilde{\mathbf{S}}^{e} = \rho_0 \left(\frac{\partial \tilde{\psi}}{\partial \tilde{\mathbf{E}}^{ve}}\right)^{T} \quad \tilde{\mathbf{Y}} = -\rho_0 \left(\frac{\partial \tilde{\psi}}{\partial \tilde{\mathbf{e}}^{d}}\right)^{T} \quad \tilde{\mathbf{S}}^{c*} = \rho_0 \left(\frac{\partial \tilde{\psi}}{\partial \tilde{\mathbf{e}}^{c}}\right)^{T}$$

Based on the dissipation relation, the following are adopted as inelastic activation criteria:

$$\left(\tilde{\mathbf{S}} - \tilde{\mathbf{S}}^{e}\right) \cdot \overset{\triangle}{\tilde{\mathbf{E}}}^{ve} = \xi^{ve} \geq 0, \quad \left(\tilde{\mathbf{S}} + \tilde{\mathbf{Y}}\right) \cdot \overset{\triangle}{\tilde{\mathbf{e}}}^{d} = \xi^{d} \geq 0, \quad \left(\tilde{\mathbf{S}} - \tilde{\mathbf{S}}^{c*}\right) \cdot \overset{\triangle}{\tilde{\mathbf{e}}}^{c} = \xi^{c} \geq 0$$

$$\xi^{mech} = \xi^{ve} + \xi^{d} + \xi^{c}$$

The second activation criterion is noteworthy. $\tilde{\mathbf{e}}^{d}$ is a strain-based measure of damage; $\tilde{\mathbf{Y}}$ is thus called here the *damage strain* energy release rate, and appropriately reflects the loss of stored energy occurring with damage. The combination of $\tilde{\mathbf{Y}}$with the stress $\tilde{\mathbf{S}}$ is thus thermodynamically implied to drive damage in accordance with the dissipation eq.

A Lagrange function is defined for application of assumed maximization of the rate of dissipation (cf. [2, 3]), where $s = \left\{\tilde{\mathbf{E}}^{ve}, \tilde{\mathbf{e}}^{d}, \tilde{\mathbf{e}}^{c}\right\}$is the state and λ is a Lagrange multiplier constraining the assumed dissipation function $\tilde{\xi}^{mech}\left[\overset{\triangle}{\tilde{\mathbf{E}}}^{ve}, \overset{\triangle}{\tilde{\mathbf{e}}}^{d}, \overset{\triangle}{\tilde{\mathbf{e}}}^{c}; s\right] = \tilde{\xi}^{ve}\left[\overset{\triangle}{\tilde{\mathbf{E}}}^{ve}; s\right] + \tilde{\xi}^{d}\left[\overset{\triangle}{\tilde{\mathbf{e}}}^{d}; s\right] + \tilde{\xi}^{c}\left[\overset{\triangle}{\tilde{\mathbf{e}}}^{c}; s\right]$ to obey the derived dissipation equation:

$$\Phi = \tilde{\xi}^{mech}\left[\overset{\triangle}{\tilde{\mathbf{E}}}^{ve}, \overset{\triangle}{\tilde{\mathbf{e}}}^{d}, \overset{\triangle}{\tilde{\mathbf{e}}}^{c}; s\right] - \lambda\left\{\left(\tilde{\mathbf{S}} - \tilde{\mathbf{S}}^{e}\right) \cdot \overset{\triangle}{\tilde{\mathbf{E}}}^{ve} + \left(\tilde{\mathbf{S}} + \tilde{\mathbf{Y}}\right) \cdot \overset{\triangle}{\tilde{\mathbf{e}}}^{d} + \left(\tilde{\mathbf{S}} - \tilde{\mathbf{S}}^{c*}\right) \cdot \overset{\triangle}{\tilde{\mathbf{e}}}^{c} - \tilde{\xi}^{mech}\left[\overset{\triangle}{\tilde{\mathbf{E}}}^{ve}, \overset{\triangle}{\tilde{\mathbf{e}}}^{d}, \overset{\triangle}{\tilde{\mathbf{e}}}^{c}; s\right]\right\}$$

Maximization of Φ leads to

$$\mu \frac{\partial \tilde{\xi}^{ve}}{\partial \overset{\triangle}{\tilde{\mathbf{E}}}^{ve}} = \tilde{\mathbf{S}} - \tilde{\mathbf{S}}^{e}, \quad \mu \frac{\partial \tilde{\xi}^{d}}{\partial \overset{\triangle}{\tilde{\mathbf{e}}}^{d}} = \tilde{\mathbf{S}} + \tilde{\mathbf{Y}}, \quad \mu \frac{\partial \tilde{\xi}^{c}}{\partial \overset{\triangle}{\tilde{\mathbf{e}}}^{c}} = \tilde{\mathbf{S}} - \tilde{\mathbf{S}}^{c*}, \quad \mu = \frac{1+\lambda}{\lambda}$$

Assuming simple quadratic dissipation relations for each of $\tilde{\xi}^{ve}, \tilde{\xi}^{d}, \tilde{\xi}^{c}$ leads to the following integrable relations:

$$\overset{\triangle}{\tilde{\mathbf{E}}}^{ve} = \mathbf{N}^{v-1}[s]\left(\tilde{\mathbf{S}} - \tilde{\mathbf{S}}^{e}[s]\right) \quad \overset{\triangle}{\tilde{\mathbf{e}}}^{d} = \mathbf{H}^{d-1}[s]\left(\tilde{\mathbf{S}} + \tilde{\mathbf{Y}}[s]\right) \quad \overset{\triangle}{\tilde{\mathbf{e}}}^{c} = \mathbf{K}^{c-1}[s]\left(\tilde{\mathbf{S}} - \tilde{\mathbf{S}}^{c_*}[s]\right)$$

Conclusion

The described model corresponds to a Voigt viscoelastic element in combination with damage and viscoplastic elements. The stress employed in the above relations is obtained via an effective stress continuum damage argument, e.g [4]. A fourth-order damage measure connected to the damage strain $\tilde{\mathbf{e}}^{d}$ permits memory of the accrued damage state while $\tilde{\mathbf{e}}^{d}$fluctuates with deformation. Work continues on further defining the detailed constitutive relations and computational implementations.

References

1. H. Stumpf, Theoretical and computational aspects in the shake down analysis of finite elastoplasticity. Int. J. Plast. **9**, 583–602 (1993)
2. K.R. Rajagopal, A.R. Srinivasa, Mechanics of the inelastic behavior of materials: part II—inelastic response. Int. J. Plast. **14**, 969–995 (1998)
3. K.R. Rajagopal, A.S. Srinivasa, On thermomechanical restrictions of continua. Proc. R. Soc. Lond. A **460**, 631–651 (2004)
4. S. Murakami, *Continuum Damage Mechanics* (Springer, New York, ISBN 978-94-007-2665-9, 2012)

Validation of Free-Free Vibration Test Method for Fatigue and Damping Characterization of Thin Structures

Thaddeus Crowe, Phil Johnson, Onome Scott-Emaukpor, Dhananjay Kumar, and Tommy George

Abstract A modular vibration-based fatigue test capability that significantly minimizes the effects of boundary conditions has been developed. The system utilizes a specimen with boundary conditions on its node lines, which isolates the gage section for deflection as a free-free beam in its first bending mode. The thin specimen is suspended inside an electromagnet by 6 lbs. monofilament fishing line, and permanent magnets are bolted to the bottom of the specimen. The alternating current inside of an electromagnet attracts and repels the permanent magnets rapidly (~55 Hz for a 0.016? thick specimen), causing the beam to cycle in first bend. This testing capability is ideal for generating and assessing fatigue life of thin specimens requiring large deflections for failure. Understanding and characterizing fatigue behavior of thin components is important, especially since the emergence of additive manufacturing (AM) for small, fatigue susceptible components. An alternate solution is to suppress the vibratory susceptibility of the component. Therefore, the importance of thin coatings capable of providing damping to components is on par with fatigue characterization. In this study, 0.4 mm cold-rolled Titanium (Ti) 6Al-4 V specimen were fatigued and compared to published data. Also, a thin damping coating (titanium nitride, or TiN) was applied to a few Ti 6Al-4 V specimens to assess the performance. Both the fatigue and damping assessments are necessary to validate the free-free test method.

Keywords Damping · Fatigue · Thin-walled structures · In-situ test · Turbine engine · Aerospace

Introduction

Turbine engine blades that experience vibration during operation are susceptible to high amplitude responses, resulting in a shorter life of the blade. Vibration of these engine components are not represented well with standard low frequency axial fatigue tests because blades often experience high frequency vibration bending [1]. Accurately characterizing high cycle fatigue (HCF) behavior is critical in keeping the engine working as planned. Therefore, new fatigue test methods are necessary for assessing turbine engine blade HCF capabilities.

Using AM for turbine engine applications can positively affect small systems. Specifically, AM can be used to manufacture small parts with complex cooling configurations for improved engine performances. Small cooled parts that can improve engine performance will likely have thin walls that are susceptible to vibration, and as a result fatigue failure [2]. To assess the fatigue behavior of these thin parts, a test method that removes the effects of boundary conditions and allows for larger part deflection is required. In addition, the method should be able to characterize damping treatments as an alternative HCF mitigation approach.

A vibration-based test method capable of assessing fatigue life of thin specimens requiring large deflections and damping treatments of thin components has been developed. To validate this test method, cold-rolled Ti 6Al-4 V specimens were fatigued to failure. Also, in an attempt to decrease susceptibility to cyclic failure, TiN coating was applied on Ti 6Al-4 V

T. Crowe (✉)
Ohio University, Russ College of Engineering, Athens, OH, USA

Universal Technology Corporation, Dayton, OH, USA

P. Johnson
Universal Technology Corporation, Dayton, OH, USA

O. Scott-Emaukpor · T. George
Air Force Research Laboratory, Wright Patterson AFB, OH, USA

D. Kumar
Department of Mechanical Engineering, North Carolina A&T State University, Greensboro, NC, USA

M. Silberstein et al. (eds.), *Challenges in Mechanics of Time Dependent Materials, Fracture, Fatigue, Failure and Damage Evolution, Volume 2*, Conference Proceedings of the Society for Experimental Mechanics Series, https://doi.org/10.1007/978-3-030-29986-6_21

specimens to assess damping performance. The step test method was used to generate fatigue data, and damping performance was determined by conducting sine sweeps and applying the half power bandwidth method. The results for Ti 6Al-4 V fatigue behavior and TiN damping are discussed with the details of the free-free vibration bending test method.

Current State of Standardized Fatigue

There are two standard fatigue methods commonly used for fatigue design; axial loading (ASTM E466 and E606) and rotation bending (ISO 1143). As stated previously, turbine engine components are susceptible to vibration fatigue loading at high frequencies that can cause HCF failure. Therefore, standard axial tests that operate at 20–100 Hz are poor representatives of the engine case.

Currently, cantilever beam shaker test is the preferred method used to characterize the capability of damping coatings (ASTM E756). This test has a large amount of energy dissipation at the boundary condition that can add unnecessary uncertainty to the assessment of damping coating capability. Though the cantilevered beam test is a reliable way of characterizing coatings for damping, improvements in the form of a new test method can eliminate the boundary conditions effects.

Free-Free Experimental Test Method

In order for the free-free fatigue test method to be considered a reliable and practical approach, the process must be modular and repeatable. The preliminary setup begins with the specimen suspended inside the electromagnet by monofilament fishing wire (6 lbs./0.010? avg. dia.) at the first bending mode nodal line, and the wire is tightly strung between two fixed poles. A standalone computer is connected to a Polytec PSV-500 Scanning Laser Vibrometer controller and head that is directed to the surface of the specimen. Using the PSV 9.2 Acquisition software, a two-dimensional alignment is performed with several points to calibrate the position of the laser to the local point with highest velocity: a linear pattern of points run down the specimen and a scan is performed with the vibrometer. After the scan, the Polytec PSV-500 is replaced with a OFV-505 single point laser vibrometer head, and the laser is aligned to the maximum point. Also at max displacement, a Micro-Measurements CEA-06-06UW-350 strain gage is glued on the back side of the specimen. Magnet wires from the gage are soldered into a junction box that outputs to a Vishay Measurements Group signal conditioning Amplifier. To ensure strain accuracy, an Agilent 34401A 6 1/2 digit multimeter is used to calibrate the amplifier. After calibration, the signal is sent via BNC cable to the Vibration Research VR9500 controller for data acquisition via VibrationVIEW software.

A VR9500 controller that is attached to a standalone computer is used for the free-free test method. The associated VibrationVIEW software is responsible for setting and controlling test parameters such as, drive voltage, sweep range, and step-test information for fatigue assessment. The controller outputs the voltage needed to drive the test into an Audio Source monoblock amplifier. The alternating current from the amplifier is then sent to a 14 gage copper coil which creates a magnetic field with an alternating charge: negative to positive. The suspended specimen inside magnetic field is attracted and repelled by the associated charge, and the specimen deflects in free-free first bending mode. The test setup is captured by Fig. 1.

A failure mode, effects, and critical analysis (FMECA) was conducted to prove this test is safe without monitoring. The FMECA identifies possible safety hazards and associated mitigation measures. With the VR9500 controller built-in shutdown limits, there is confidence that this test can operate safe and autonomously.

Validation of Results

The step test procedure is followed when fatiguing to failure with vibration bending [1]. This procedure is composed of a series of increasing sinusoidal resonance dwells. Each step is for a given number of cycles (Nstep) and consecutively increases amplitude each step until failure. Traditionally, failure is conceptualized during the test by noting the change in frequency vis-. . . -vis for a control velocity amplitude [2–7]. For example, if the natural frequency shifts .1%, failure is recognized [6, 8]. For the free-free test, however, failure is quickly detected due to instantaneous instability of the cycling mechanism. The stress amplitude at failure achieved by the step test method is determined by fitting between the step at which it failed and the previous step [1, 9]. The failure stress amplitude (Sa) of Nstep cycles to failure is characterized in

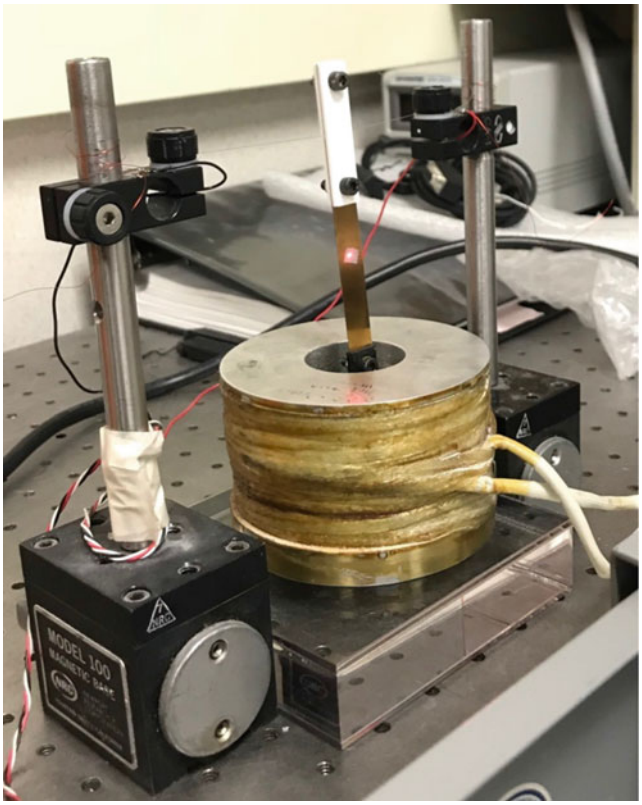

Fig. 1 Free-free fatigue test setup

Eq. 1. Validation of this test procedure against steady sinusoidal dwell fatigue life results have been achieved for aluminum, titanium, and nickel-based alloys [4, 5, 7, 10].

Determining the damping properties of metallic coating has two steps [11]. First, the nominal Ti 6Al 4 V specimen is tested; second, the Ti 6Al 4 V specimen is coated with 2?m TiN and the now the two-part system is retested. The vibration test used for this method is a slowly swept sinusoidal excitation. To compare the control specimen and the coated specimen, the quality factor of damping (Q) was needed. Q was calculated with the half power bandwidth method; where natural frequency is divided by the difference in upper and lower frequency at a frequency response of 0.707 of maximum. The TiN coating used on the specimen is traditionally used for anodes in lithium ion batteries and electrodes in supercapicitors. The reason TiN was chosen for damping is because it has a magnetostrictive capability under applied strains that could benefit vibration suppression [11, 12] (Fig. 2).

Concluding Results

Fatigue data of thin Ti 6Al-4 V specimens (0.4 mm) at 105 cycles is compared to previously published data from 3.2 mm to 4 mm thick specimens in Fig. 3 [2, 13]. As shown in the figure, there is a large scatter in the results of the thin specimen. The inconsistency in data could be from defects such as pores and rolling marks. Since the thin specimen has less material thickness than the other known specimen, the significance of the defects is much greater. These results validate the necessity for free-free testing.

The coating performance of TiN was determined on two coated Ti-64 specimens (2?m on one side, 2?m on two side). The results listed in Table 1 show that TiN did not provide significant damping to the system, but the test method was proven repeatable. The deviation of system Qs are relatively small based off four repeated tests (loading and unloading each trial). More work is required to better understand TiN damping capability.

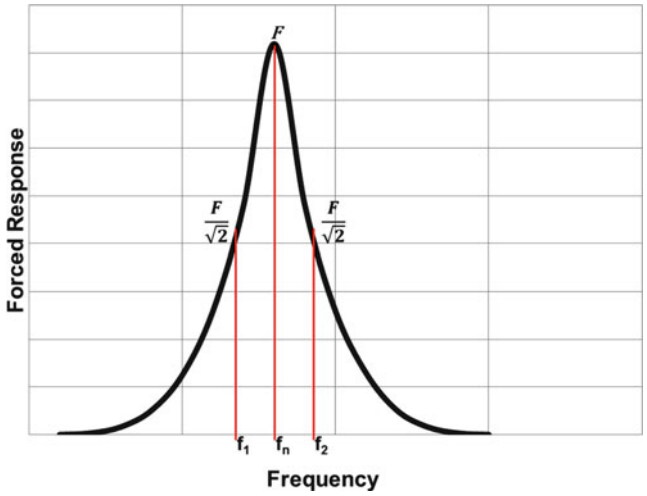

Fig. 2 Half power bandwidth method for measuring damping capability

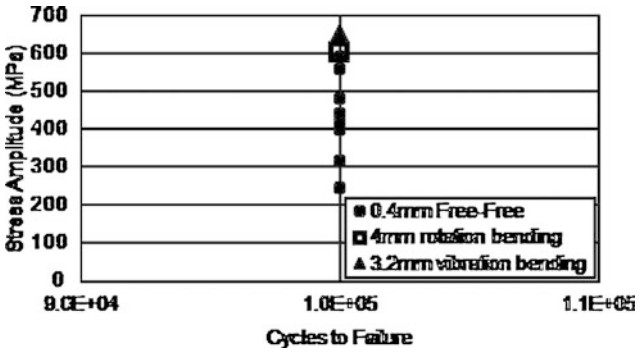

Fig. 3 TI 6AL-4 V bending fatigue comparison

Table 1 TiN damping performance results

Specimen	Mean System Q (#)	Rel. STD (%)
Bare	74.2	45
One Sided TiN	53.9	4.38
Two Sided TiN	51.3	0.92

References

1. T. Nicholas, *High Cycle Fatigue: A Mechanics of Materials Perspective* (Elsevier, Oxford, UK, 2006)
2. O. Scott-Emuakpor, T. George, E. Henry, C. Holycross, J. Brown, *As-Built Geometry and Surface Finish Effects on Fatigue and Tensile Properties of Laser Fused Titanium 6Al-4V? Proceedings ASME Turbo Expo*, 2017, paper No. GT2017–63482
3. O. Scott-Emuakpor, M.-H.H. Shen, T. George, C. Cross, An energy-based uniaxial fatigue life prediction method for commonly used gas turbine engine materials? ASME J. Eng. Gas Turbines Power **130**(6), 15 (2008)
4. O. Scott-Emuakpor, J. Schwartz, T. George, C. Holycross, C. Cross, J. Slater, Bending fatigue life characterization of direct metal laser sintering nickel alloy 718? Fatigue Fract. Eng. Mater. Struct. **38**(9), 1105–1117 (2015)
5. O. Scott-Emuakpor, C. Holycross, T. George, J. Beck, J. Schwartz, M.-H.H. Shen, J. Slater, J., *Material Property Determination of Vibration Fatigued DMLS and Cold-Rolled Nickel Alloys,? ASME/Turbo Expo*, Dusseldorf, Germany, 16–20 June 2014, paper No. GT2014–26247
6. J. Bruns, A. Zearley, T. George, O. Scott-Emuakpor, C. Holycross, Vibration-based bending fatigue of a hybrid insert-plate system? J. Exp. Mechan. **55**(6), 1067–1080 (2015)
7. O. Scott-Emuakpor, T. George, C. Cross, J. Wertz, M.-H.H. Shen, A new distortion energy-based equivalent stress for multiaxial fatigue life prediction? Int. J. Nonlinear Mechan. **47**(3), 29–37 (2012)
8. J. Bruns, *Fatigue Crack Growth Behavior of Structures Subject to Vibratory Stresses? Society of Experimental Mechanics Annual Conference*, Greenville, SC, 2–6 June 2014
9. D.C. Maxwell, T. Nicholas, A rapid method for generation of a haigh diagram for high cycle fatigue? J. Fatigue Fract. Mechan. **29**, 626–641 (1998)

10. R. Bellows, S. Muju, T. Nicholas, Validation of the step test method for generating Haigh diagrams for Ti-6Al-4V? Int. J. Fatigue **21**(7), 687–697 (1999)
11. American Society for Testing and Materials, E756–05: Standard Test Method for Measuring Vibration-Damping Properties of Materials,?ÿASTM Book of Standards, 2010; Vol. 04.06, ASTM International, West Conshohocken, PA
12. P. Torvik, B. Langley, *Properties of Hard Coatings with High Damping,? AIAA Joint Propulsion Conference and Exposition*, Orlando, FL, 27–29 July 2015
13. M. Janecek et al., The very high cycle fatigue behaviour of Ti-6Al-4V alloy? Proc. Int. Symp. Phys. Mater. **128**(4), 497–502 (2015)

Improved Measurement for High-Cycle Fatigue Examination

Samantha D. Burton, Emma E. German, Brandon A. Furman, Casey M. Holycross, Onome Scott-Emuakpor, and Ryan B. Berke

Abstract This research analyzes a novel high-throughput method for vibration-based fatigue testing. This method builds off previous research by Bruns and Zearley, where a carrier plate assembly containing a test specimen vibrates to failure. This method redesigns an aluminum carrier plate to simultaneously load three, instead of one, test specimens in parallel. The redesign was selected, using SolidWorks modal analysis, based on its ability to concentrate cyclic stress on the specimens, rather than on the plate, to extend the life of the plate. For experimental validation, the redesigned plate assembly was fatigued with an electrodynamic shaker following the same procedures as Bruns' and Zearley's assembly. The assembly was monitored with stereo digital image correlation to detect mode shape. Although the assembly exhibited the same mode shape as simulation experiments, fatigue tests could not be completed due to the large accelerations required to generate relatively small strains. Additional work is needed to identify other multi-insert designs capable of exerting larger fatigue strains.

Keywords High cycle fatigue · Vibration-based testing · High-throughput techniques · Stereo digital image correlation

Introduction

Fatigue plays a critical role in turbine, engine, and aircraft design. With fatigue strength occurring beneath ultimate and yield strength, fatigue makes machines vulnerable to unexpected failures [1]. Furthermore, with fatigue cracks occurring at microscopic levels, which limits immediate detection, extensive preventative maintenance costs are also involved. Hence, using fatigue properties to govern machine design significantly mitigates vulnerabilities and costs. Various fatigue testing methods (e.g. servo-hydraulic [2], rotating beam [3]) are used to obtain fatigue properties; however, high-cycle fatigue (HCF) measurements can be costly and time-consuming—a single axial fatigue stress operating at 40 Hz requires almost 70 h to accumulate enough cycles (on the order of 10^7) to generate a single point on an S-N curve [4]. Additionally, due to statistical variability in fatigue measurements, such tests must often be repeated for a given set of operating conditions [5].

To address excessive testing time, George et al. [6] developed a vibration-based fatigue testing method in which a square plate is cantilevered at one end and excited to its fourth resonant mode at about 1600 Hz using a mechanical shaker. Thus, the vibration-based method completes the same number of cycles about 40 times faster compared to an axial load frame oscillating at 40 Hz. Bruns and Zearley later modified the technique to test smaller bending specimens inserted into a reusable carrier plate, thus drastically reducing material waste [7]. More recently, Scott-Emuakpor et al. improved the repeatability of fatigue measurements made using the Bruns-Zearley assembly by replacing the rectangular insert specimen with a specimen having an hourglass-shaped gauge region [8]. Images of each plate and specimen design are shown in Fig. 1. Vibrational testing methods are comparatively faster and more representative of the fatigue that occurs in gas turbine engines [9].

In this new work, the carrier-insert assembly was further modified to promote high-throughput testing. The new assembly includes multiple insert specimens which are shared by a common carrier plate, thus allowing each specimen to be tested in parallel. The specimen which experiences the highest stress fails first, but in the meantime the remaining specimens accumulate the same number of cycles at reduced stress levels. This drastically increases the throughput of the technique by dividing the total testing time by the number of parallel specimens.

S. D. Burton · E. E. German · B. A. Furman · R. B. Berke (✉)
Utah State University, Mechanical and Aerospace Engineering, Logan, UT, USA
e-mail: ryan.berke@usu.edu

C. M. Holycross · O. Scott-Emuakpor
Air Force Research Laboratory, Wright-Patterson AFB, OH, USA

M. Silberstein et al. (eds.), *Challenges in Mechanics of Time Dependent Materials, Fracture, Fatigue, Failure and Damage Evolution, Volume 2*, Conference Proceedings of the Society for Experimental Mechanics Series, https://doi.org/10.1007/978-3-030-29986-6_22

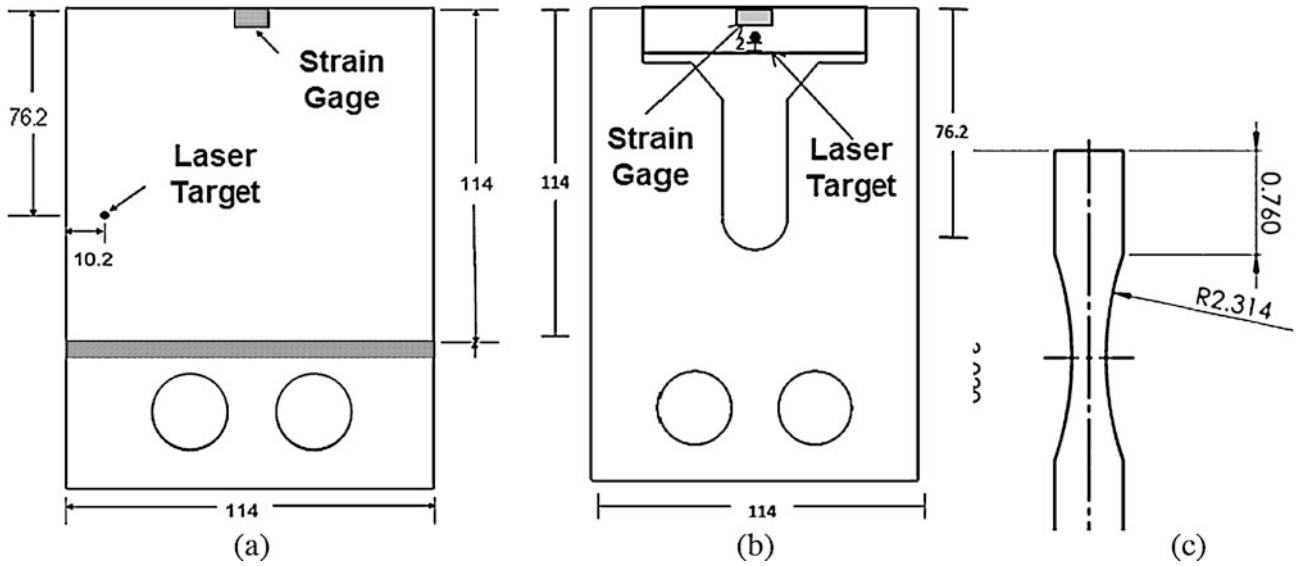

Fig. 1 (**a**) Cantilevered plate by George et al. (units in mm); (**b**) Revised plate by Bruns, Zearley, et al. (units in mm); and (**c**) Modified hourglass insert by Scott-Emuakpor et al. (units in in)

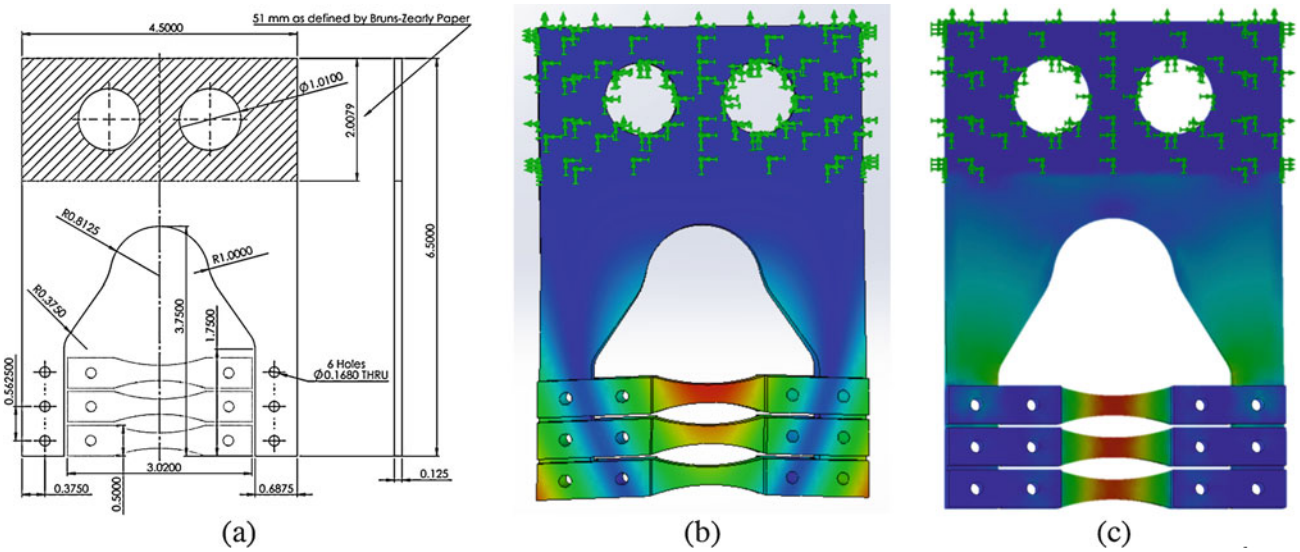

Fig. 2 (**a**) Dimensions of the three-insert design (units in in); (**b**) simulated mode shape of the design's fourth resonant mode; and (**c**) simulated von mises stress distribution of the design's fourth resonant mode. The shaded, upper portion of the assembly is clamped

Determination of Carrier Plate Geometry

An initial multi-insert assembly was designed to accommodate three specimens. In designing the three-insert plate, previous FEA results from Scott-Emuakpor [8] were first replicated using SolidWorks. From the replicated results, dimensions of the single-insert carrier plate were systematically modified to accommodate three specimens. The internal shape of the plate was manipulated over several iterations to (1) reduce the relative stress on the carrier plate in proportion to the inserted specimens while (2) ensuring that the general mode shape was consistent with the vibration-based test method of Scott-Emuakpor. The final design before manufacturing, shown in Fig. 2(a), has the same outer dimensions as the single-insert plate [7] and the same tab and specimen dimensions as the hourglass specimens. The relevant mode shape and its corresponding stress distribution are shown in Fig. 2(b) and (c). Significant plate stresses were located at the regions of transition between the clamped tabs and the plate's main body, thus, focus was primarily spent on reducing the stresses at the transition regions. Note that the dimensions for the plate were adjusted minimally for convenience in manufacturing.

Initial Tests

The system was manufactured and set up with the following specifications. The carrier plate and insert specimens were made of 0.122 in. thick 6061-T6 Aluminum. The inserts were secured to the carrier plate at each end by a pair of rectangular tabs which were also 6061-T6 Aluminum. These tabs were half as thick as the carrier and inserts. A stud clamping torque of 170 N-m was used to fix the three-insert plate (hashed region in Fig. 2) to the mounting block of a 20,000 lb. Unholtz-Dickie electrodynamic shaker. A bolt clamping torque of 6.2 N-m was used to fix the plate to the specimens via the connecting tabs. Each insert was polished to a mirror-like finish and then speckled with black and white VHT Flameproof paint to perform digital image correlation (DIC). The black paint pattern was applied using a stamp rolling kit from Correlated Solutions Inc. to a white background.

The strain in each insert specimen was monitored throughout testing in three ways. First, a Micro-Measurements CEA-05-062UW-350 strain gauge was applied to each insert and connected to a Vishay 2310B signal amplifier to monitor axial strain in real time. However, as strain gauges have limited fatigue lives of their own, the gauges routinely fail mid-test before the specimen has failed. Second, to maintain consistent strain levels after a strain gauge has failed, the assembly was additionally monitored by a Polytec OFV 505 laser vibrometer which was positioned 76.2 mm from the free edge of the plate. Although the vibrometer measures out-of-plane displacement, not strain, there exists a linear relationship between displacement and strain which can be exploited to maintain consistent loading after a strain gauge has failed [10]. Third, the assembly was additionally monitored throughout testing by a pair of Photoron SA-Z high speed cameras to compute full-field displacements via stereo-DIC. The cameras each recorded 1-MP images at a rate of 20,000 frames per section. The images were post-processed using Vic-3D to compute full-field strains. For test control and data acquisition, the assembly was additionally monitored by an Endevco charge-type accelerometer mounted to the shaker body. Together, the vibrometer and accelerometer were used to assess whether the plate was in resonance. Resonance was maintained via feedback control from a Vibration Research VR9500 controller.

While performing the first calibration procedure for the three-insert plate, DIC showed that the plate exhibited a mode shape similar to Fig. 2's FEA analysis. However, large base excitations were required to induce relatively small strains. For example, to achieve deformation on the order of 100 $\mu\varepsilon$, accelerations near 30 g's were required. Such accelerations, when extrapolated to meaningfully high fatigue strains, exceeded the shaker's specifications. To compensate, the assembly was modified by removing the innermost specimen, resulting in a two-insert assembly. The revised assembly exhibited two relevant modes, simulated using ANSYS in Fig. 3.

Both modes produce bending in both specimens, but in mode 3 strains are higher on the inner specimen while in mode 4 strains are higher in the outer specimen. A revised test plan was devised to take advantage of the two relevant modes:

1. First, the assembly should be loaded in mode 3 until the outer specimen fails at a strain level of 3000 $\mu\varepsilon$. Meanwhile, the inner specimen accumulates damage at a reduced strain level. The failed outer specimen should be removed and replaced with a fresh specimen.

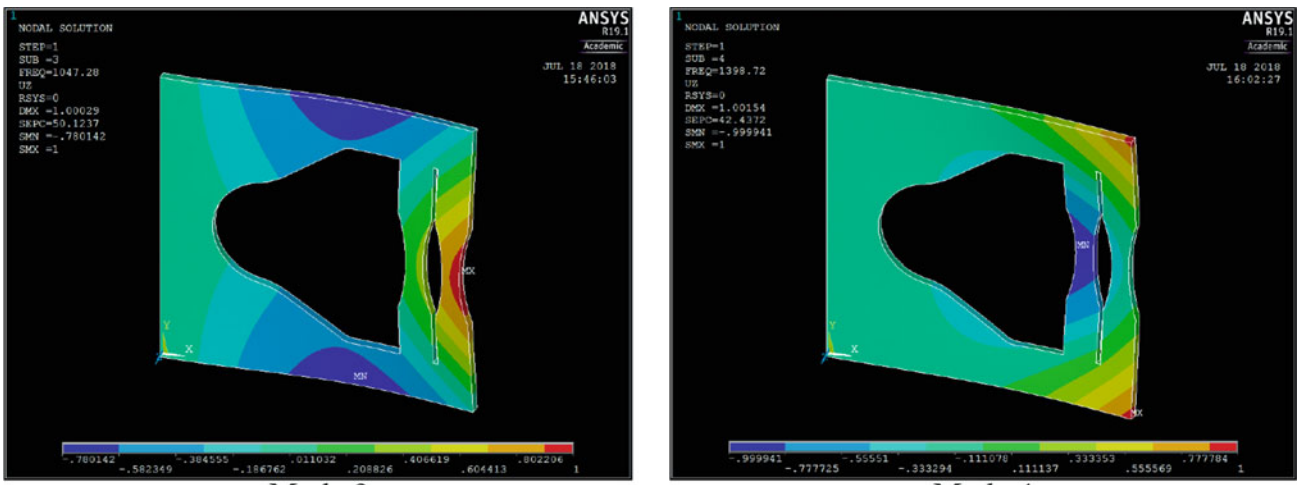

Fig. 3 Displaced mode shapes of the two relevant modes for the two-insert assembly. Note that the tabs and fasteners which secure the inserts to the carrier are not modeled. The left edge of the model is clamped

Table 1 Strains measured at various amplitudes of excitation for the two resonant modes depicted in Fig. 3

	Low Amp	>>	>>	High Amp
Mode 4 (995 Hz)				
Gauge 1 (Outer specimen)	372 με (89%)	525 με (88%)	783 με (89%)	969 με (89%)
Gauge 2 (Inner Specimen)	416 με	594 με	878 με	1084 με
Mode 3 (866 Hz)				
Gauge 1 (Outer specimen)	447 με	781 με	1032 με	1235 με
Gauge 2 (Inner Specimen)	398 με (89%)	686 με (88%)	893 με (86%)	1057 με (86%)

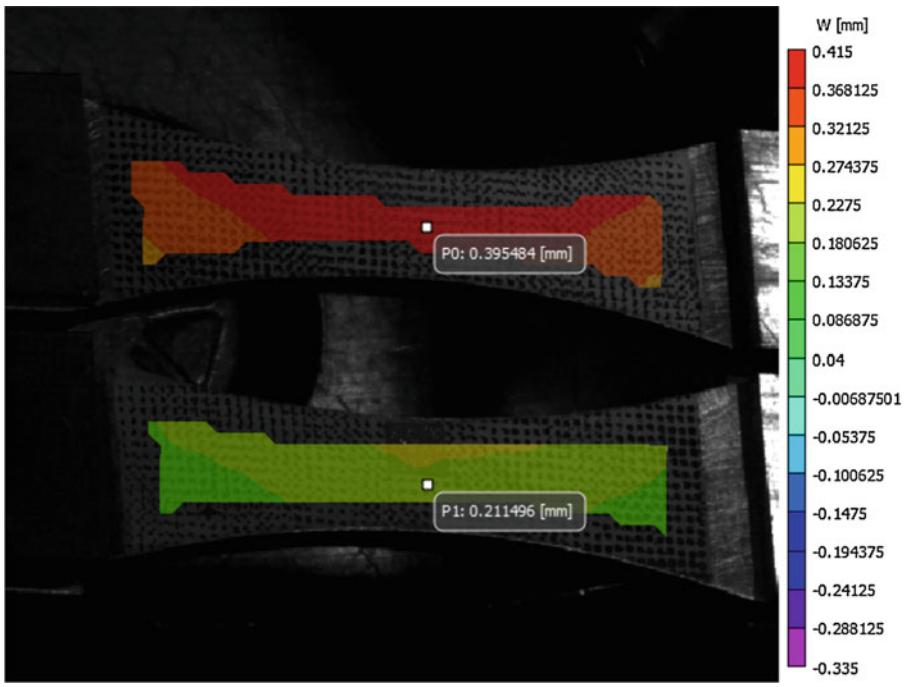

Fig. 4 Peak out-of-plane displacement measured in Mode 4 using Stereo-DIC

2. The assembly should then be loaded in mode 4 such that the inner specimen continues to accumulate damage at the same strain level it experienced earlier. Meanwhile, the new outer specimen accumulates damage at an even lower strain level. The failed inner specimen should be removed and replaced with a fresh specimen.
3. Future load steps should continue to alternate between modes 3 and 4 until enough specimens have failed to populate an S-N curve.

The ANSYS simulations in Fig. 3 (which do not account for the tabs or fasteners which secure the inserts to the carrier plate) predict that in both modes, the strain in the lower strain specimen is about 56–60% of the strain in the higher strain specimen. However, in physical testing the strain gauges reported that the strain in the lower strain specimen was closer to 86–89% of the higher strain specimen. The gauge readings from initial low-amplitude tests are summarized in Table 1. The peak displacements from the final Mode 4 test, obtained using stereo-DIC, are shown in Fig. 4.

The two-insert plate did not survive testing long enough to produce meaningful fatigue results. During the initial calibration period to identify the linear relationship between strain gauge and laser vibrometer readings, a visible crack developed at the bolt hole where the third insert specimen was removed. The cracked carrier plate is shown in Fig. 5. We have since ordered and machined a new carrier plate without the additional bolt hole, but further testing still needs to be run using the new carrier plate.

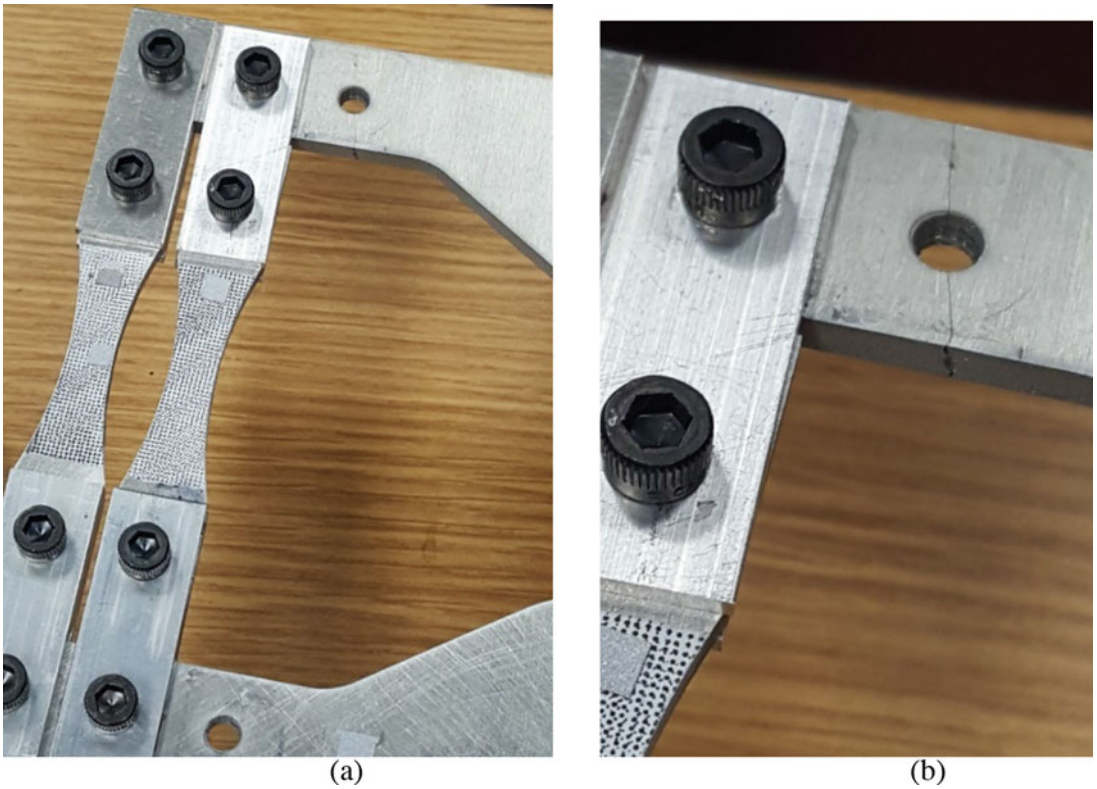

Fig. 5 (**a**) Photograph of the modified two-insert assembly; and (**b**) close-up of the crack near the bolt hole where the third specimen was removed

Revised Geometry

In the above two-insert assembly, the lower strain specimen experiences 88% of the strain in the higher strain specimen, as measured by strain gauges. Using the strain-life equation, the difference in fatigue life can be estimated:

$$\varepsilon_a = \frac{\sigma_f{}'}{E}\left(2N_f\right)^b + \varepsilon_f{}'\left(2N_f\right)^c$$

where $E = 68.9$ GPa is Young's modulus, $\sigma_f{}' = 654$ MPa is the fatigue strength coefficient, $b = -0.1$ is the fatigue strength exponent, $\varepsilon_f{}' = 4.2957$ is the fatigue ductility coefficient, $c = -1.0072$ is the fatigue ductility exponent, and $2N_f$ is the number of load reversals, making $N_f = 10^7$ the number of cycles [11]. This amounts to a fatigue life which is about 3.5× more cycles compared to the life of a higher-strain specimen.

With such a large difference in fatigue life, a high-throughput experiment involving the above two-insert assembly would fail 3.5× higher-strain specimens in the time it would take to fail 1 lower-strain specimen. From the perspective of the higher-strain specimen this allows greater statistical characterization of that strain level, but from the perspective of testing multiple strain levels to populate an S-N curve this is not very high-throughput.

To improve throughput in future tests, new inserts were devised to bring the expected fatigue lives of the two specimens closer together. Instead of the hourglass-shaped gauge regions shown in previous figures, the new inserts have half-hourglass-shaped gauge regions with their straight edges placed close together, as shown in the simulated mode shapes in Fig. 6. The ANSYS simulations predict that the lower-strain specimen will experience about 78–80% strain compared to the higher-strain specimen. For comparison, simulations of the full-hourglass specimens predicted about 56–60% strain in the lower-strain specimen but in practice the physical strains were measured to be 86–89%, so physical strains in the half-hourglass specimens are expected to be even higher.

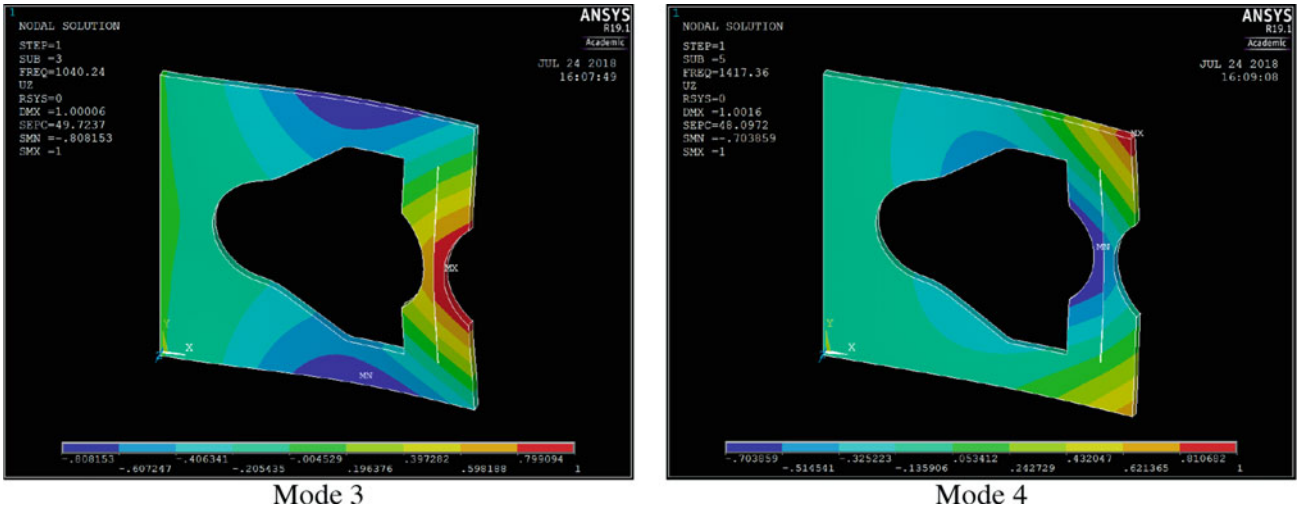

Fig. 6 Displaced mode shapes of the two relevant modes with the updated half-hourglass inserts. The tabs and fasteners which secure the inserts to the carrier plate are still not modeled

Discussion

As aforementioned, the purpose for the three-insert plate was to develop a high-throughput fatigue testing procedure. Though the shaker's specifications prevented multiple-specimen testing, assembly alterations could allow successful three-specimen testing. These alterations include adjusting the geometry of the three-insert assembly to promote fatigue bending at lower accelerations. Once a three-insert assembly has been successfully debugged, future designs should incorporate even more inserts to improve throughput further. Additionally, the procedures for any multi-insert assembly should be adjusted to accommodate damage accumulation at multiple strain levels, for example incorporating a damage accumulation model such as Miner's Rule [1].

One key limitation of multi-insert fatigue assemblies is the reliance on many strain gauges. Every time a specimen is removed and replaced, minor differences in specimen dimensions and clamping conditions can produce slight changes in the overall assembly's resonant response. Thus, in order to assess how much strain is applied to each insert specimen, new strains must be measured for each insert every time the assembly is altered. However, since the fatigue life of each gauge is typically less than the life of the specimen that it monitors, failed strain gauges must be scraped off and new gauges must be applied to each specimen in the assembly. This adds significant time and material costs.

To reduce dependency on strain gauges, one promising alternative is high-speed stereo-DIC. Since DIC is non-contacting, it can continue to monitor strain long after strain gauges have failed. However, DIC has several key limitations of its own. First, under current computing capabilities, full-field DIC remains a post-processing technique, and thus cannot monitor strain in real time. Therefore, at least one strain gauge is still needed to establish strain levels at the start of each loading step. That gauge must still be calibrated against a laser vibrometer to ensure constant excitation for the duration of the step. Second, the measurement resolution of DIC is much coarser compared to strain gauges. A typical strain gauge can resolve down to single micro-strains, while DIC operates more on the order of hundreds or thousands of micro-strains [12]. DIC strain measurements are also computed from multiple subsets worth of displacement data, and thus tend to span a larger gauge area compared to some strain gauges [13].

Furthermore, because the carrier-insert assembly oscillates out-of-plane with respect to the camera sensors, there is considerable blurring which interferes with the DIC calculation. Some of the blur is motion blur, which can be mitigated by reducing the exposure time on the cameras but produces darker images. Some of the blur is due to poor depth of field, which can be mitigated by reducing the aperture on the lenses but also produces darker images. The relative contributions to DIC measurement error of motion blur versus poor depth of field remain unknown. Unless a very bright light source is used, some blurring is inevitable.

Summary and Conclusion

In this research, high-throughput fatigue testing was attempted, where a single-insert plate was modified to accommodate three insert specimens while mitigating stress on the plate. Experimental testing indicated that meaningfully high fatigue strains were not achievable with this three-insert configuration. In response, the three-insert plate and procedure were modified for a two-insert plate by removing one of the specimens. Calibration was successfully executed; however, the two-insert plate failed during testing. From the failed results, a new two-insert assembly was devised, featuring half-hourglass specimens. Preliminary FEA results indicate the feasibility of the new design, but further testing remains. Once demonstrated, this and other related high-throughput techniques have the potential to greatly reduce fatigue testing times. This will allow larger populations of samples to be more quickly characterized, allowing for better stochastic consideration of fatigue.

Acknowledgements This work was sponsored in part by the AFRL Summer Faculty Fellowship Program.

References

1. R. Budynas, J.K. Nisbett, *Shigley's Mechanical Engineering Design*, 10th edn. (McGraw-Hill, New York, NY, 2014)
2. J. Wertz, M.-H.H. Shen, O. Scott-Emuakpor, T. George, C. Cross, An energy-based torsional-shear fatigue lifing method. Exp. Mech. **52**(7), 705–715 (2012)
3. L.R. Krishna et al., Enhancing the high cycle fatigue life of high strength aluminum alloys for aerospace applications. Fatigue Fract. Eng. Mater. Struct. **42**(3), 698–709 (2019)
4. O.E. Scott-Emuakpor, H. Shen, T. George, C. Cross, An energy-based uniaxial fatigue life prediction method for commonly used gas turbine engine materials. J. Eng. Gas Turbines Power **130**(6), 062504–062504–15 (2008)
5. O. Scott-Emuakpor, T. George, T. Letcher, M.-H.H. Shen, C. Cross, Incorporation of a probabilistic monotonic strain energy analysis to a lifting method. J. Fail. Anal. Prev. **12**(1), 109–115 (2012)
6. T.J. George, J. Seidt, M.-H. Herman Shen, T. Nicholas, C.J. Cross, Development of a novel vibration-based fatigue testing methodology. Int. J. Fatigue **26**(5), 477–486 (2004)
7. J. Bruns, A. Zearley, T. George, O. Scott-Emuakpor, C. Holycross, Vibration-based bending fatigue of a hybrid insert-plate system. Exp. Mech. **55**(6), 1067–1080 (2015)
8. O. Scott-Emuakpor, T. George, C. Holycross, C. Cross, Improved Hybrid Specimen for Vibration Bending Fatigue, in *Fracture, Fatigue, Failure and Damage Evolution*, vol. 8, (Springer, Cham, 2017), pp. 21–30
9. O. Scott-Emuakpor, J. Schwartz, T. George, C. Holycross, C. Cross, J. Slater, Bending fatigue life characterisation of direct metal laser sintering nickel alloy 718. Fatigue Fract. Eng. Mater. Struct. **38**(9), 1105–1117 (2015)
10. O. Scott-Emuakpor, T. George, C. Cross, J. Wertz, M.-H. Herman Shen, A new distortion energy-based equivalent stress for multiaxial fatigue life prediction. Int. J. Non-Linear Mech. **47**(3), 29–37 (2012)
11. R.J. Bucci, Selecting aluminum alloys to resist failure by fracture mechanisms. Eng. Fract. Mech. **12**(3), 407–441 (1979)
12. E. Byrne, M. Simonsen, "Vic-3D application note: resolution and accuracy." [Online]. http://www.correlatedsolutions.com/support/index.php?/Knowledgebase/Article/View/8/1/resolution-and-accuracy. Accessed 21 Feb 2019
13. P. Reu, Virtual strain gage size study. Exp. Tech. **39**(5), 1–3 (2015)

Application of Linear Viscoelastic Continuum Damage Theory to the Low and High Strain Rate Response of Thermoplastic Polyurethane

H. Chen and C. R. Siviour

Abstract This paper outlines an empirical correlation method combining quasi-static tests in tension and compression, and high strain-rate tests in compression, with dynamic mechanical analysis and time-temperature superposition. A generalized viscoelastic model incorporating continuum damage is calibrated. The results show that a model calibrated using data from quasi-static compression and dynamic mechanical analysis can be used to adequately predict both the quasi-static tensile and the compressive high strain rate response.

Keywords Polyurethane · Dynamic mechanical analysis · Viscoelasticity · Viscoelastic damage · High strain-rates

Introduction

Thermoplastic elastomers are widely used in engineering and industry. They benefit from advantageous properties such as flexibility, durability and property recovery after deformation, but simultaneously dependent on effects of polymer networks, temperature, strain rate and loading history [1]. As segmented block co-polymer, microphase-separated structures offer polyurethanes a wide range of mechanical properties, which can strongly depend on the applied strain rate (or frequency) and temperature, as well as pressure. In common with all polymers, TPUs have a well-known equivalence, known as time-temperature superposition principle (TTS), which allows empirical mechanical behavior between rubbery and glassy states to be formulated in terms of time and temperature respectively [1–3].

Rate dependence in polyurethanes has been studied using direct measurements over the range of strain rates from 10^{-3} s^{-1} to 10^{4} s^{-1} [4, 5], to understand the material hardening, fracture, voids and crack behaviors with increasing strain rates [6, 7]. Developments including high-speed photography [8–10], have allowed low-impedance materials to be studied at high strain rates up to 10,000 s^{-1} [11]. From a mechanical point of view, there is evidence of substantial softening during cyclic loading, in particular a loss of stiffness that can be correlated to the maximum stress achieved in prior loadings, the so-called Mullins effect [12, 13]. In terms of the possible changes in molecular configurations, various physical interpretations and macromolecular models have been reviewed recently by refining strain energy density into material responses [13–16]. A typical approach is to adopt damage continuum mechanics into phenomenological models [17].

In this study, we calibrated the temperature and frequency dependence of a commercial polyurethane, and explored large strain quasi-static compression responses, to further predict the high strain rate behavior of the material. Dynamic mechanical analysis (DMA) was first executed to understand the viscoelastic behavior as a function of temperature and frequency, producing a master curve as a function of frequency through TTS. A linear viscoelastic continuum damage model based on the Boltzmann superposition integral and a strain based damage criterion was reviewed, and the model parameters were fitted to the data from quasi-static compression experiments and the dynamic mechanical analysis. This model was further used to predict the response in tensile experiments, and most importantly, high strain rate compression experiments. The study in this paper thus provides an applicable methodology to characterize temperature and strain rate dependent mechanical properties of rubbers, including prediction of high rate behavior from data obtained in low rate tests.

H. Chen (✉) · C. R. Siviour
Department of Engineering Science, Solid Mechanics and Materials Engineering, University of Oxford, Oxford, UK
e-mail: huanming.chen@eng.ox.ac.uk

M. Silberstein et al. (eds.), *Challenges in Mechanics of Time Dependent Materials, Fracture, Fatigue, Failure and Damage Evolution, Volume 2*, Conference Proceedings of the Society for Experimental Mechanics Series, https://doi.org/10.1007/978-3-030-29986-6_23

Linear Viscoelastic Damage Theory

The most general model of viscoelasticity is based on physical rheology, without involving any explicit model of chemical composition or molecular variation. The Generalized Maxwell model was used to establish the physical phenomenology of the viscoelasticity under investigation. The stress relaxation function and modulus can be written as:

$$E(t) = E_0 + \sum_{i=1}^{M} E_i \exp\left(-\frac{t}{\tau_i}\right) \tag{1}$$

where E_i denotes elastic modulus from spring elements; $\tau_i = \eta_i/E_i$ is the effective stress relaxation time of each Maxwell element.

For time-varying strains, stress-strain relations in viscoelastic materials can be represented by the cumulative instantaneous stress relaxation behavior as a function of the entire loading history, derived as the Boltzmann superposition principle:

$$\sigma(t) = \int_0^t E(t-s)\,\dot{\varepsilon}(s)ds \tag{2}$$

Continuum damage mechanism is employed to develop a simple isotropic damage mechanism, which incorporates softening behavior under deformation and leads to a progressive degradation in storage modulus in a monotonic test with increasing amplitude [17]. The range of structural transformations or degradation during material deformation might include de-bonding, chain breakage, spherule fracture, and lamellae slippage in both micro- and macro-morphology. The model is driven from the free energy which is uncoupled into a volumetric and deviatoric response. In the model, all damage is summarized as an isotropic damage-dominated energy dissipation leading to potential energy degradation from non-equilibrium viscous stress, expressed as:

$$S = \overline{g}(\varepsilon_{Max})\frac{\partial \psi^0(\varepsilon)}{\partial \varepsilon}, \quad \text{where } \varepsilon_{Max} = \max_{s\in(-\infty,t]} \sqrt{2\psi^0(\varepsilon(s))} \tag{3}$$

$$\overline{g}(x) = \beta + (1-\beta)\frac{1-e^{-x/\alpha}}{x/\alpha}, \quad \beta \in [0,1], \alpha \in [0,\infty) \tag{4}$$

where S is the stress tensor and $\varepsilon(s)$ is the strain tensor. $\overline{g}(x)$ represents the integrated continuum damage parameter, empirically formulated by fitting coefficients α and β; x is the magnitude of true strain in the continuous process [17].

The process integrating isotropic damage behavior through the Boltzmann superposition integral is proportional to instantaneous stored strain energy, with empirical softening behavior emerging from linear viscoelasticity to present material damage affecting the inherent local modulus. The response with a constant strain rate can be simplified as:

$$\sigma(t) = \int_0^t E(t-s)\,\overline{g}(\varepsilon)\,\dot{\varepsilon}(s)ds \tag{5}$$

Method and Results

Rheological Model

Experiments were performed on a DMA machine (TA Q800), in which a beam (35 × 10 × 5 mm) was tested in dual-cantilever configuration under cyclic deformation. The machine outputs complex modulus (E' and E''), loss tangent (tanδ), stress, temperature and frequency. Isothermal frequency sweeps were performed at 2 °C intervals between −50 °C and 80 °C, and frequencies 0.5, 2, 5 and 10 Hz. The displacement amplitude was 30 μm. From the output values of moduli against loading frequency at each temperature (Fig. 1b), a master curve of frequency dependence was produced in Fig. 1a. Two approximately tangential lines at high and low temperatures can be fitted: these intersect at the same point on the temperature axis and indicates the glass temperature, T_g, of about −27 °C, as TTS correlates mechanical behavior on

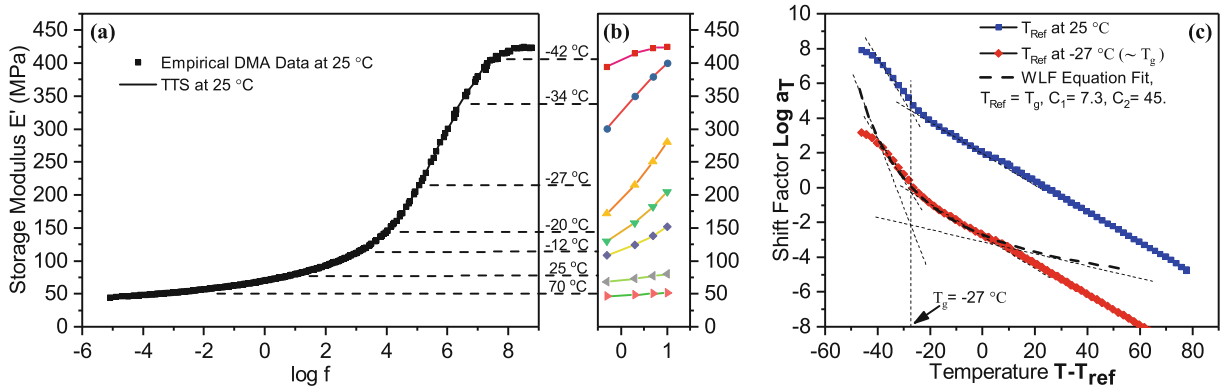

Fig. 1 (**a**) A continuous plot of E′ vs. log f. generated by applying TTS on E′ vs. log f curves (**b**) at different temperatures. (**c**) Shift factor vs. temperature at reference temperatures of 25 °C and −27 °C; WLF equation for curve at T_g with parameters $C_1 = 7.3$, $C_2 = 45$

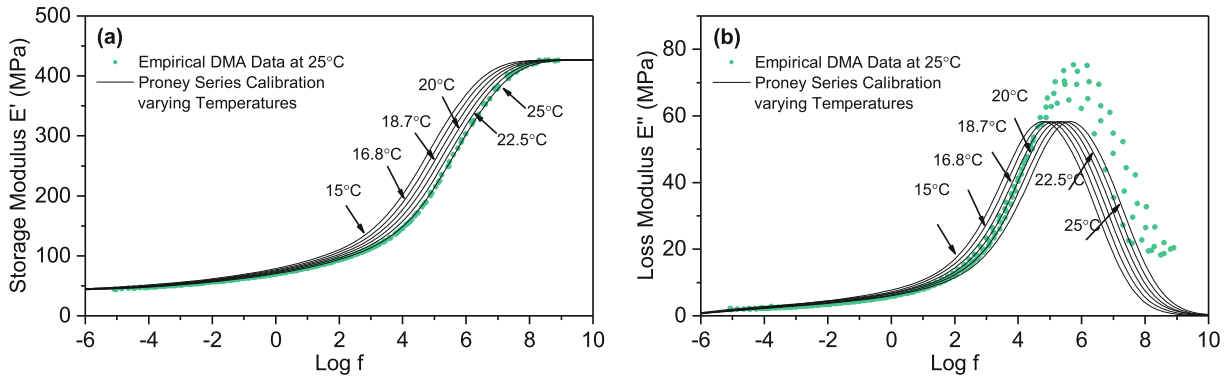

Fig. 2 (**a**) Storage modulus E′, (**b**) Loss modulus E″ vs. log frequency for various reference temperatures

temperature and frequency dependence by shifting factors. For interest, the Williams-Landel-Ferry (WLF) equation [1] obeys the empirical data around this point.

$$\log a_T = -\frac{C_1 (T - T_s)}{C_2 + (T - T_s)} \tag{6}$$

where C_1 and C_2 are constants, T_S is the reference temperature in which the TTS process implemented.

Figure 2 above displays the plot of both storage E′ and loss E″ moduli against frequency obtained from empirical DMA data by applying TTS at reference temperature 25 °C. The next step is using Alfrey Approximation to parameterize the Prony series of Generalized Maxwell Model [1]. Certain calibration results of the Generalized Maxwell Model were investigated by applying TTS at different reference temperatures.

Phenomenological Damage Model

Quasi-static experiments allow the damage model to be calibrated. Tests with monotonic loadings were executed in a commercial screw-driven testing machine (Instron 5982). For tensile experiments, TPU strips (dimension of 5 × 10 × 200 mm) were used, whilst in compression cylinders (dimension of 5 mm diameter × 5 mm length) were tested. Force was recorded by a load cell, whilst strain was directly from the digital image correlation (DIC) technique. The DIC analysis results showed that the true strain rates achieved were 0.08, 0.008, 0.0008 s^{-1} in tension; and 0.09, 0.009 and 0.0009 s^{-1} in compression. In general linear viscoelastic continuum theory, the damage is mainly dependent on the strain magnitude, independent of the change in loading rate and loading direction. The comparison between inherent and empirical local stiffness is to introduce how resultant phenomenological softening occurred. The calibration of damage factor $\overline{g}(\varepsilon)$ was determined by comparing

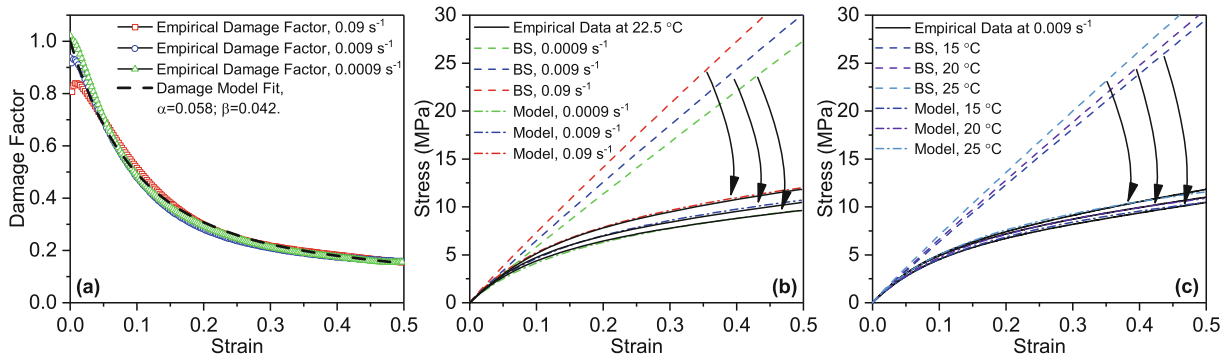

Fig. 3 (**a**) Damage factor and parameters $\alpha = 0.058$, $\beta = 0.042$ was determined by carrying out Boltzmann superposition (BS) for compression at 22.5 °C, for model predictions varying temperatures (**b**) and strain rates (**c**) respectively

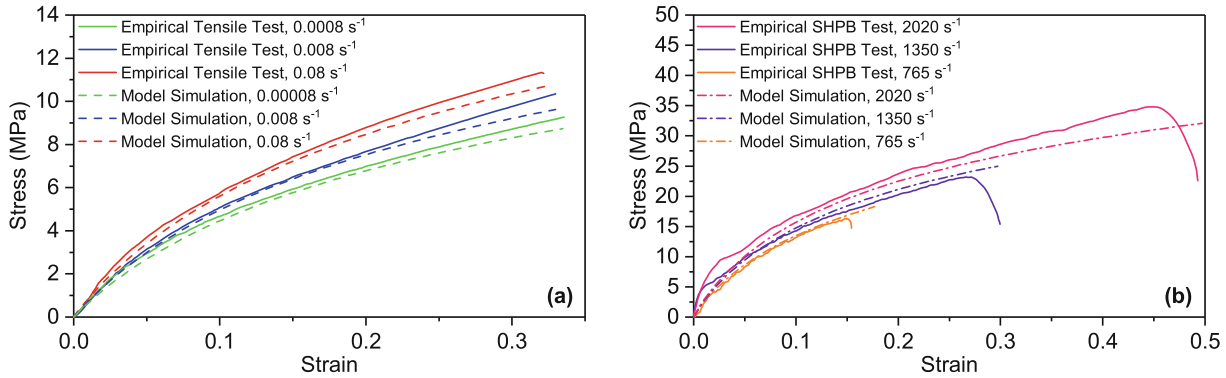

Fig. 4 The calibration data for tensile tests (**a**) with constant temperature at 16.8 °C varying strain rates 0.08 s^{-1}, 0.008 s^{-1} and 0.0008 s^{-1}; for high strain rates tests in SHPB (**b**) with constant temperature at 18.7 °C varying strain rates 765 s^{-1}, 1350 s^{-1} and 2020 s^{-1}

the ratio of local stiffnesses between stress-strain responses using the Boltzmann superposition principle obtained from DMA and experimental data, in particular the empirical data and simulation calibrated under same temperatures and rates (Fig. 3).

Model Application to Low Rate Tension and High Rate Compression

The model was then used to predict the response of the material in tension. Owing to experimental constraints, the Boltzmann superposition integral was first which is recalculated at a temperature of 16.8 °C for three rates of 0.08, 0.008 and 0.0008 s^{-1}. The parameters α and β remain constant as they are independent of temperature and rate strain rates. A comparison of model output and experimental data is shown in Fig. 4a. A further prediction of the results from SHPB experiments was performed, at temperature of 18.7 °C and strain rates up to 2000 s^{-1}, results are shown in Fig. 4b.

Discussion and Conclusion

A viscoelastic constitutive model with effects of continuum damage has been shown to provide a characterization of the mechanical behavior of thermoplastic polyurethane under uniaxial loading from low to high strain rates. A specific viscoelastic damage model upon phenomenological damage criteria obtained from compression experiments was capable of characterizing both tensile and high strain rate experiments. The material showed a strong dependence on both temperature and frequency from DMA. The TTS principle grouping with Prony series was applicable to calibrate materials behaviors, and WLF relationship was applicable for DMA data.

The behavior of material softening resulting from the material damage has been investigated. The responses contributed damage effects from strain magnitude and characterized by one set of factor parameters: α and β. Both temperature and rate

dependences in comparison of model simulation and experiments were well modelled. There is a small difference between compression and tensile experiments, which may be affected by experimental errors (*e.g.* frictional boundary) and unevenly stresses when the material is deformed. Additionally, the model is able to predict experimental data in high strain rates but exhibited insufficient stiffness development for strain rates over 2000 s^{-1}.

Further examination of the implementation is to test the linear viscoelastic damage theory in a wider range of strain rates and a study of recovery upon cyclic loading with increasing amplitude of strains may also involve. More specific configuration and characterization of filler structure in TPUs will be investigated in particular on the local stiffness degradation and hysteresis behaviors.

Acknowledgements This material is based upon work supported by the Air Force Office of Scientific Research, Air Force Material Command, USAF under Award No. FA9550-15-1-0448. We thank Dr. Nick Hawkins, Mr. Akash Trivedi, Dr. Igor Dyson, Mr. Richard Duffin and Mr. Wolfgand Mix from University of Oxford who provided insight and expertise for the research.

References

1. D.W. Ward, I.M. Hadley, *An Introduction to the Mechanical Properties of Solid Polymers* (John Wiley & Sons Ltd, Hoboken, NJ, 1997)
2. J. Qiao, A.V. Amirkhizi, K. Schaaf, S. Nemat-Nasser, G. Wu, Dynamic mechanical and ultrasonic properties of polyurea. Mech. Mater. **43**(10), 598–607 (2011)
3. C.M. Roland, J.N. Twigg, Y. Vu, P.H. Mott, High strain rate mechanical behavior of polyurea. Polymer (Guildf). **48**(2), 574–578 (2007)
4. J.E. Field, S.M. Walley, W.G. Proud, H.T. Goldrein, C.R. Siviour, Review of experimental techniques for high rate deformation and shock studies. Int J Impact Eng **30**(7), 725–775 (2004)
5. C.R. Siviour, High strain rate characterization of polymers. AIP Conf. Proc. **1793**, 060029 (2017)
6. J.T. Fan, J. Weerheijm, L.J. Sluys, High-strain-rate tensile mechanical response of a polyurethane elastomeric material. Polymer (UK) **65**, 72–80 (2015)
7. C.M. Roland, Mechanical behavior of rubber at high strain rates. Rubber Chem. Technol. **79**(3), 429–459 (2006)
8. M.J. Kendall, C.R. Siviour, Experimentally simulating adiabatic conditions: approximating high rate polymer behavior using low rate experiments with temperature profiles. Polymer (UK) **54**(18), 5058–5063 (2013)
9. W. Chen, F. Lu, B. Zhou, A quartz-crystal-embedded split Hopkinson pressure bar for soft materials. Exp. Mech. **40**(1), 1–6 (2000)
10. B. Song, W. Chen, Split Hopkinson pressure bar techniques for characterizing soft materials. Lat. Am. J. Solids Struct. **2**(2005), 113–152 (2005)
11. S.H. Yoon, C.R. Siviour, The incremental virtual fields method and prestretching method applied to rubbers under uniaxial medium-strain-rate loading. Strain **53**(3), 1–20 (2017)
12. L. Mullins, Effect of stretching on the properties of rubber. Rubber Chem. Technol. **21**(2), 281–300 (1948)
13. J. Diani, B. Fayolle, P. Gilormini, A review on the Mullins effect. Eur. Polym. J. **45**(3), 601–612 (2009)
14. R. Diaz, J. Diani, P. Gilormini, Physical interpretation of the Mullins softening in a carbon-black filled SBR. Polymer (Guildf). **55**(19), 4942–4947 (2014)
15. F. Clément, L. Bokobza, L. Monnerie, On the Mullins effect in silica-filled polydimethylsiloxane networks. Rubber Chem. Technol. **74**(5), 847–870 (2001)
16. E.M. Arruda, M.C. Boyce, A three-dimensional constitutive model for the large stretch behavior of rubber elastic materials. J. Mech. Phys. Solids **41**(2), 389–412 (1993)
17. J.C. Simo, On a fully three-dimensional finite-strain viscoelastic damage model: formulation and computational aspects. Comput. Methods Appl. Mech. Eng. **60**(2), 153–173 (1987)

Shear Property Characterization for Agarose Gel

D. W. Millar, M. M. Mennu, K. Upadhyay, A. M. Knapp, and P. G. Ifju

Abstract Hydrogels are hydrophilic polymer networks. They have a defined geometry, which gives them solid like characteristics. Hydrogels also exhibit liquid like nature since certain soluble molecules diffuse through the hydrogel matrix. These characteristics of hydrogel make it extremely difficult to determine the mechanical properties through conventional methods. A new in-plane shear test method that incorporates 3D printed parts and digital image correlation (DIC) was developed. 3D printed parts were used as loading fixture to ensure the appropriate grip on the hydrogel. DIC was used to measure the properties and validate the test methodology. It was identified that shear modulus could be calculated to within 5% coefficient of variation at about 20% strain. Future research will identify ways to increase the limit of the stress-strain curve for calculating shear properties.

Keywords Agarose · Digital image correlation · Hydrogel · Shear testing

Introduction

Hydrogels are cross-linked polymeric network materials that swell in an aqueous medium. A swollen hydrogel is soft, nonlinearly elastic, and has a porous microstructure; these characteristics are similar to that of many biological tissues, and thus hydrogels are used as tissue engineering scaffolds [1], biological implants [2], contact lenses, et cetera.

The mechanical behavior of hydrogels changes significantly with a number of factors such as the applied maximum strain level, deformation mode, loading rate, and microstructural parameters such as gel concentration and mesh size. Characterization under such different loading conditions is especially difficult for these materials because of their fragile and slippery surfaces, which makes it impossible to use traditional contact based strain-measuring devices for them, such as clip extensometers, strain gages, etc. Existing literature mainly consists of simpler tests such as uniaxial compression and tension, which, although shed light to the uniaxial deformation mode, is incomplete from a constitutive modelling perspective, which requires data from all three primary deformation modes [3, 4]. Experiments that can accurately capture the shear mode of deformation during a single-pulse loading (not oscillatory) are thus much needed.

The aim of this study is to develop an in-plane direct shear test for hydrogels that not only induces large strain deformation in the material, but also results in a very small coefficient of variation, thus ensuring excellent repeatability. To this end, custom 3D printed single lap shear fixtures are developed in which individual lap plates contain cylindrical rod-like projections to hold the specimen that has been molded between the two lap plates. Four design parameters are adjusted to achieve 16 test lap plate designs (Fig. 1), which are further investigated in order to select the optimal gripping method. Two-dimensional digital image correlation (DIC) is used to obtain full-field strain maps of the deformed region; shear stress versus average nominal shear strain response is investigated.

Materials and Methods

A novel testing fixture was proposed to grip Agarose hydrogel and allow for shear strain levels past current established amounts. The goal was to design fixtures with pegs that the test material would solidify around and act as anchors during tensile testing. The test area of Agarose would be formed by space left between mirroring brushes. When considering the

D. W. Millar · M. M. Mennu (✉) · K. Upadhyay · A. M. Knapp · P. G. Ifju
Department of Mechanical and Aerospace Engineering, University of Florida, Gainesville, FL, USA
e-mail: mmennu@ufl.edu

M. Silberstein et al. (eds.), *Challenges in Mechanics of Time Dependent Materials, Fracture, Fatigue, Failure and Damage Evolution, Volume 2*, Conference Proceedings of the Society for Experimental Mechanics Series, https://doi.org/10.1007/978-3-030-29986-6_24

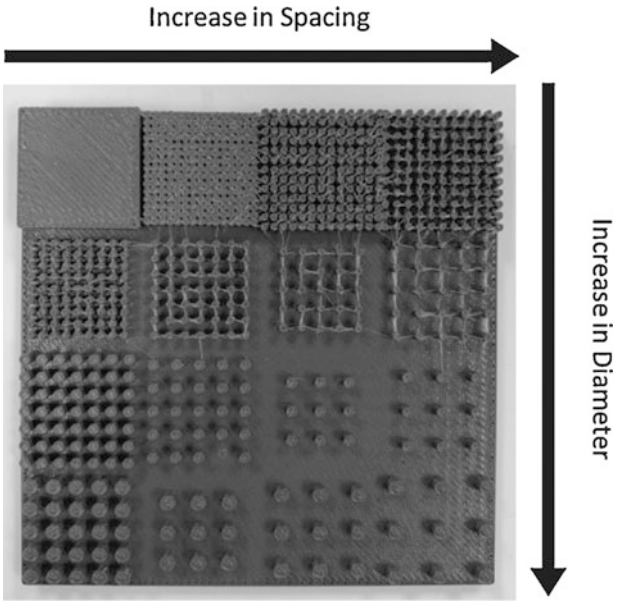

Fig. 1 3D printed parameter sweep of peg spacing and peg diameter for 0 degree pegs with 2 mm extension

peg geometry, four factors were considered: (1) peg extension (varying from 1.0 to 4.0 mm in increments of 1.0 mm), (2) peg angle (varying from 0° to 45° in increments of 15°), (3) peg spacing (varying from 1.5D to 3.0D in increments of 0.5D; D represents current peg diameter), and (4) peg diameter (varying from 0.5 to 2.0 mm in increments of 0.5 mm). Models of patterns were 3D printed using a Fortus 360 mc.

Once the models of the 16 variations of the above listed factors were printed (Fig. 1), selection of the most appropriate model was needed. After comparing the failure method of Agarose to that of common brittle materials, it was found that the pegs angled at either 0° or 45° would result in the most appropriate failure mode data. Furthermore, one of the biggest factors when selecting the designs to use was the quality of the print job. Since the brushes were small, the resolution of the machine used needed to be clean enough as to not interfere with the gripping of the Agarose gel. When comparing the known requirements to the actual printed results, it was determined that two models met the criteria: (1) 0° pegs, 3 mm extension, 1.5 mm diameter, and 1.5D spacing; and (2) 45° pegs, 3 mm extension, 1.5 mm diameter, and 1.5D spacing.

Designing original brushes and updating for current testing: With the testing patterns selected, a design apparatus needed to be designed and printed to connect the brush patterns to the TestResources® 311 machine. When designing the brush apparatus, it became necessary to focus on the test area of the Agarose with respect to the direction of the load being applied. Due to the nature of the test (i.e. keeping the hydrogel suspended between two brushes), rotational effects were suspected to occur. Because of this, the brushes were designed so the load being applied occurred along the same centerline as the test area to eliminate potential rotational effects. The brushes were designed around this main requirement, and the final product of the two testing apparatuses can be seen below (Fig. 2).

Agarose gel powder (cat. No. BP1356, Fisher Scientific, Belgium) was mixed with distilled water to make hydrogels of 2.5% (wt./solvent volume) concentration; the detail procedure can be found in [5]. All quasi-static (10^3 s^{-1}) mechanical tests were conducted on a servo-mechanical universal test frame (TestResources® 311) using a 250 lbf load cell. Tension tests were conducted using the Agarose hydrogel specimen solidified between two brush pegs placed in a clevis pin fixture to avoid any induced moments that translate to impose pure shear strain on the test material.

Digital image correlation technique was used to capture strain data during the shear testing procedure. Since out-of-plane deformation is negligible, a commercial software, 2D VIC (Correlated Solutions), was used for calculating strain data on the agarose gel. Two cameras were set up, one on each side of the shear strain specimen. This was implemented to reduce the variability in strain and acquire an average strain from both sides. This eliminated errors in measurement that would be seen only from one side of the specimen. One necessary procedure for calculating strains is speckle patterning the surface of the hydrogel. This was achieved through chalk powder (50–150 μm speckle size) grinded from a regular chalk with fine grade sandpaper. The two brushes were be slightly compressed together using rubber bands. Several samples were tested under quasi-static strain rate of 1.95 mm/min while images of the test area were recorded every second. The stress-strain data from the TestResources® 311 and 2D VIC(Correlated Solution) were analyzed and compared against each other and current accepted stress-strain data established by Dr. Subhash et al.

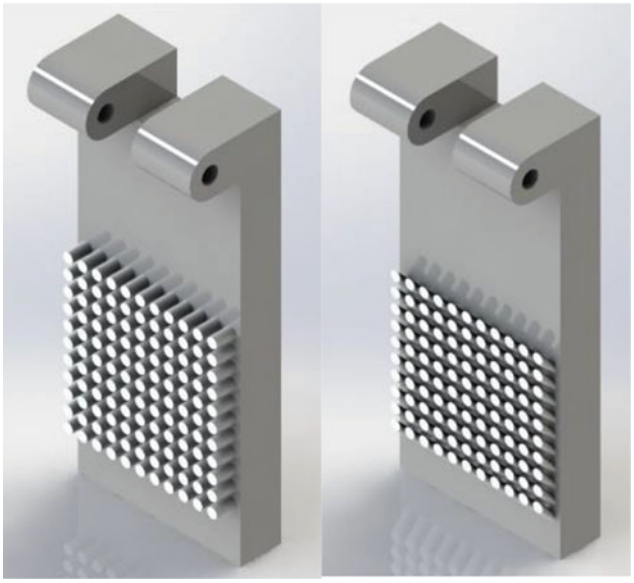

Fig. 2 Brush apparatus models incorporating design (**a**) 0° pegs, 3 mm extension, 1.5 mm diameter, and 1.5D spacing pegs (left), and design (**b**) 45° pegs, 3 mm extension, 1.5 mm diameter, and 1.5D spacing pegs (right)

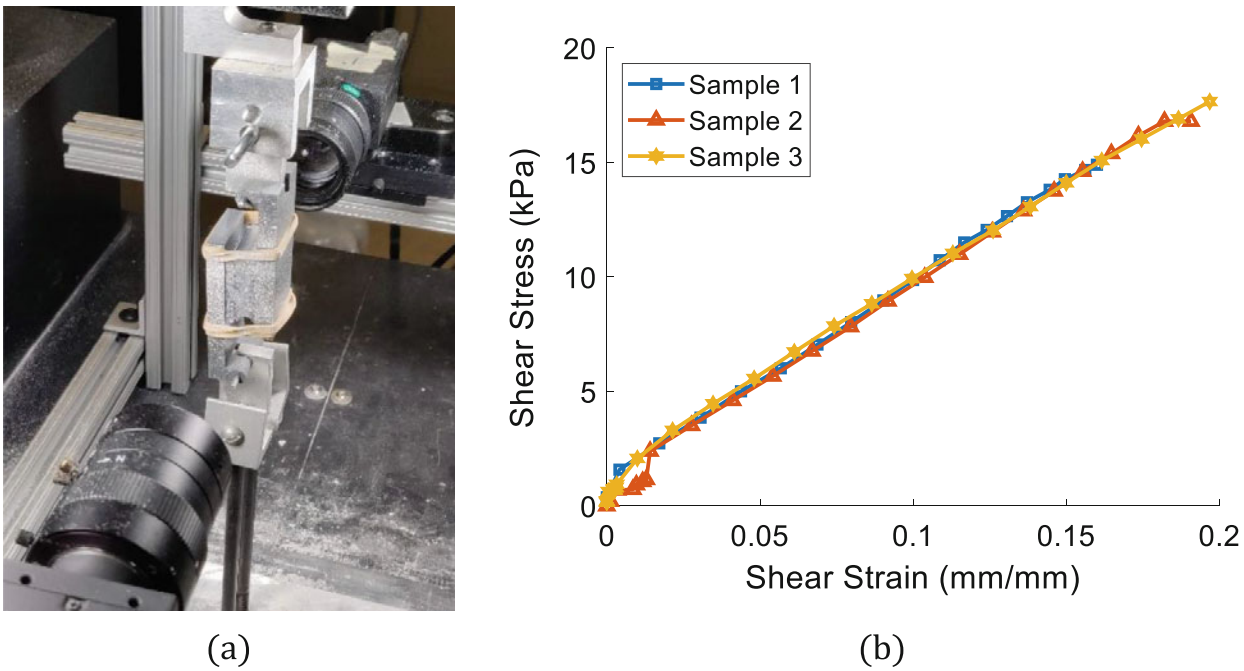

Fig. 3 (**a**) DIC setup, (**b**) Stress-Strain Curves for 2.5% concentration agarose gel

Results and Discussion

After running three quasi-static shear tests, the stress-strain curve was obtained for 2.5% concentration agarose gel as shown in Fig. 3. The result shows consistency in material properties for each sample. The mean shear modulus for the samples was determined to be 86.9 kPa. Further statistical analysis proves that shear modulus can be calculated with a coefficient of variation less than 5%. This result show matching curves with current stress-strain data obtained in [4].

After concluding three trials, it was noted that improvements to the testing procedure should be made in order to observe more desirable behavior from the Agarose. During some of the trials, it was observed that the Agarose would slowly peel off of the lower, stationary brush instead of stretch and break within the test area. To eliminate this behavior, the gage length

between the two brushes should be decreased from the current 6.5 mm gage length used. This improvement will help ensure the failure will occur within the test area between the brushes instead of along the tops of the brushes.

Conclusion

A simple design based on 3D printed parts combined with DIC techniques has been proven to be a viable technique for acquiring material properties from simple quasi-static loading cases. This method allows for increased accuracy and repeatability of strain results by implementing a technique of averaging strains along the gauge length of the specimen on both sides of the sample. This method can also be extended to comparing the relationship between the concentration of agarose gel and the material property with current theoretical models.

References

1. A. Sasson, S. Patchornik, R. Eliasy, D. Robinson, R. Haj-Ali, Hyperelastic mechanical behavior of chitosan hydrogels for nucleus pulposus replacement-experimental testing and constitutive modeling. J. Mech. Behav. Biomed. Mater. **8**, 143–153 (2012)
2. E. Caló, V.V. Khutoryanskiy, Biomedical applications of hydrogels: a review of patents and commercial products. Eur. Polym. J. **65**, 252–267 (2015)
3. R.W. Ogden, G. Saccomandi, I. Sgura, Fitting hyperelastic models to experimental data. Comput. Mech. **34**(6), 484–502 (2004)
4. K. Upadhyay, G. Subhash, D. Spearot, Thermodynamics-based stability criteria for constitutive equations of isotropic hyperelastic solids. J. Mech. Phys. Solids **124**, 115–142 (2019)
5. G. Subhash, Q. Liu, D.F. Moore, P.G. Ifju, M.A. Haile, Concentration dependence of tensile behavior in agarose gel using digital image correlation. Exp. Mech. **51**(2), 255–262 (2011)

High Temperature Low-Cycle Fatigue and Creep-Fatigue Behavior of Fe-25Ni-20Cr Austenitic Stainless Steel

Zeinab Alsmadi, Abdullah S. Alomari, N. Kumar, and K. L. Murty

Abstract Preliminary investigation on mechanical properties of a Nb-strengthened and nitrogen-stabilized Fe-25wt.%Ni-20Cr (Alloy 709) advanced austenitic stainless steel suggests that it might be a potential candidate for Sodium-Cooled Fast Reactor (SFR), which has higher technology readiness level for deployment. However, the creep-fatigue deformation behaviour is unknown for this alloy. To understand high temperature creep-fatigue interaction of the Alloy 709, strain-controlled low-cycle fatigue (LCF) tests were performed at strain amplitudes ranging from 0.15% to 0.6% with fully reversible cycle of triangular waveform at 750 °C in air following ASTM standard E2714–13. In addition, different hold times of 1, 10, 30 and 60 min were introduced at the maximum tensile strain to investigate the effect of the creep damage on the fatigue-life at strain amplitude of 0.5% at 750 °C. During continuous cyclic loading, fatigue life is found to decrease with increase in strain amplitude. The creep-fatigue life and the number of cycles to crack initiation are found to decrease with increasing hold time indicating the rapid initiation and propagation of cracks. The fractographs of the samples deformed at 0.5% strain amplitude indicated that fatigue might have been the dominant mode of deformation whereas, for the sample deformed at the same strain amplitude with different hold times, both fatigue and creep have contributed to the overall deformation of the alloy. Further studies are underway to carry out creep-fatigue tests at different hold times, strain ranges, and temperatures as well as microstructural characterization of the samples following deformation.

Keywords Austenitic stainless steel · Gen-IV nuclear reactor · Mechanical properties · Creep-fatigue · Plastic deformation

Introduction

The structural material of SFR should have superior mechanical properties that can withstand high temperatures, high corrosive environments and high radiation doses such as austenitic stainless steel, which is corrosion-resistant and has good creep properties due to its high nickel and chromium content. For example, Fe-25Ni-20Cr austenitic stainless steel (known as Alloy 709) contains 20% chromium and 25% nickel; it is stabilized by nitrogen and strengthened by niobium. Therefore, it is of great importance to understand the plastic deformation of this alloy and predict how it will behave under typical SFR operating conditions.

Creep-fatigue interaction is expected to be a contributor to the damage mode for many components such as reactor cladding, pressure vessels and gas turbines operating at high temperatures in next-generation nuclear reactors [1–5]. In this paper, the creep-fatigue interaction of the Alloy 709 is investigated by conducting strain-controlled fatigue tests at 1% total strain range, 2×10^{-3} s^{-1} strain rate (0.1 Hz) and 750 °C with hold times of 60, 600, 1800 and 3600 s at the tensile strain. Also, low-cycle fatigue (LCF) tests were performed at strain amplitudes ranging from 0.15% to 0.6% with fully reversible cycle of triangular waveform at 750 °C in air for baseline information. All tests were conducted as described in the ASTM standard E2714–13 [6].

Z. Alsmadi (✉) · A. S. Alomari · K. L. Murty
Department of Nuclear Engineering, North Carolina State University, Raleigh, NC, USA
e-mail: zalsmad@ncsu.edu

N. Kumar
Metallurgical and Materials Engineering, The University of Alabama, Tuscaloosa, AL, USA

M. Silberstein et al. (eds.), *Challenges in Mechanics of Time Dependent Materials, Fracture, Fatigue, Failure and Damage Evolution, Volume 2*, Conference Proceedings of the Society for Experimental Mechanics Series, https://doi.org/10.1007/978-3-030-29986-6_25

Table 1 Chemical composition (wt%) of Alloy 709

Element	C	Mn	Si	P	S	Cr	Ni	Mo	N	Ti	Nb	B	Fe
Wt%	0.07	0.91	0.44	<0.014	<0.000	19.93	24.98	1.51	0.148	0.04	0.26	0.0045	Bal.

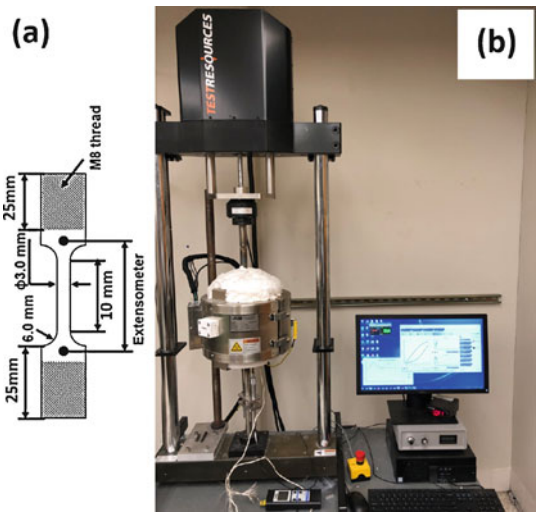

Fig. 1 (**a**) The sample geometry. (**b**) The Experimental set-up

Experimental Setup

The material investigated here is received in the form of plate that had undergone hot-rolling followed by solution-annealing heat-treatment at 1100 °C and water quenching. The chemical composition of the alloy is given in Table 1. Parallel-gage test specimens were used for low-cycle fatigue and creep-fatigue tests with 3 mm diameter gage section and 10 mm gage-oriented length along rolling direction as shown in Fig. 1a.

The creep-fatigue and low-cycle fatigue tests were carried out using an electro-dynamic creep-fatigue machine (Model 810LE3) from TestResources. To enable high temperature testing, a furnace from Applied Test Systems was used and the temperature during the test was controlled using a K-type thermocouple wrapped around the gage section of the cylindrical test sample. The strain was measured and controlled using an extensometer mounted on the grip-section of the sample with a Linear Variable Differential Transducer (LVDT) attached to it (Fig. 1b).

For microstructural examination, scanning electron microscope (SEM) was used after the fractured samples were cleaned in acetone. The fractography was carried out in the FEI Quanta 3D FEG (Fig. 2). As shown in Fig. 2a, when no hold time is introduced, a triangle waveform is produced while a trapezoidal waveform is produced with imposed hold times (Fig. 2b). Also shown in Fig. 2 are the corresponding variation of the stress and hysteresis loops during loading cycles.

Results and Discussion

Low-Cycle Fatigue

Figure 3 shows the strain amplitude vs. number of reversals ($2N_f$) in log-log scale in which the curve is comprised of low-cycle fatigue (LCF) ($N < 5 \times 10^5$) at high strain ranges and high-cycle fatigue (HCF) ($N > 5 \times 10^5$) at low strain ranges. LCF is controlled by ductility and HCF is controlled by strength. Therefore, the plastic curve appears at larger strain amplitudes than the elastic curve, which means that the high ductility of the material is important if good resistance to large strain ranges (LCF) is to be obtained, and a high tensile strength is important when exposures in the low strain ranges (HCF) are to be encountered [7]. Also,

The strain amplitude versus number of cycles results follow the characteristic slopes equation as follows:

$$\frac{\Delta\varepsilon}{2} = 6.143\left(2N_f\right)^{-0.36} + 0.9696\left(2N_f\right)^{-0.15} \tag{1}$$

where $\frac{\Delta\varepsilon}{2}$ is the strain amplitude and N_f is the number of cycles to failure.

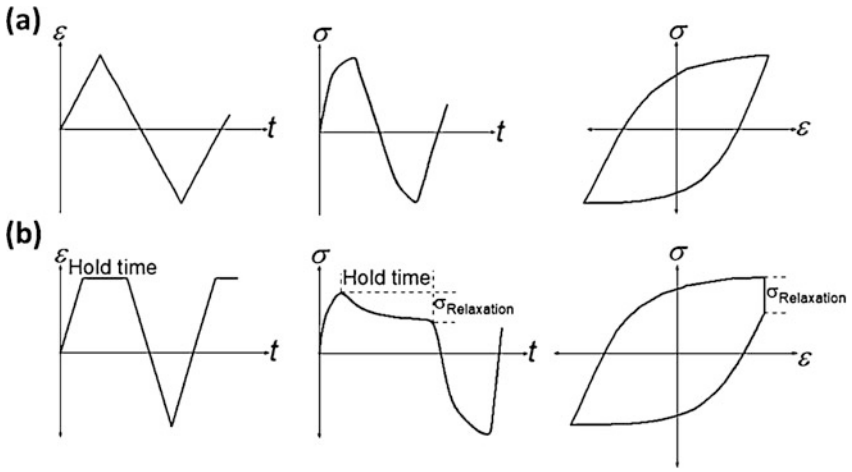

Fig. 2 Schematic of loading cycle of the strain-controlled creep-fatigue test showing strain–time, stress–time and stress–strain curves (**a**) without hold time and (**b**) with hold time imposed at the peak tensile strain

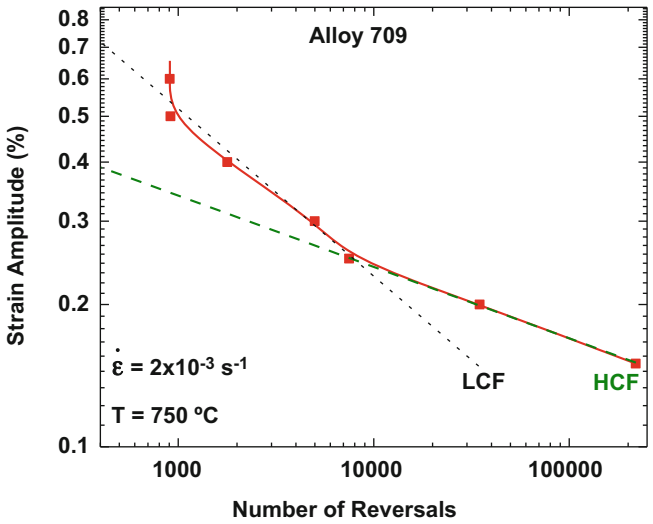

Fig. 3 Strain amplitude vs. number of reversals in log-log scale showing both LCF and HCF parts

Creep- Fatigue

Peak stresses during tension and compression parts of the loading cycles were plotted as a function of number of cycles at 0, 60, 600, 1800 and 3600 s hold times as shown in Fig. 4a. In continuous cyclic loading, the alloy exhibits rapid rate of cyclic softening behavior. While with imposing hold time, the rate of cyclic hardening becomes more pronounced with increasing hold time. The change of the cyclic behavior is linked with the microstructure and can be due to (a) dislocation-dislocation, (b) dislocation–precipitate and (c) dislocation–solute atom interactions [8].

At 1% strain range, the second cycles of creep-fatigue hysteresis loop for the Alloy 709 at different hold times are shown in Fig. 4b and it is found that the increase in the inelastic strain with hold time was introduced by means of transformation from elastic strain caused by stress relaxation during hold times. Therefore, it predicts the occurrence of creep damage at high temperatures [4, 8, 9]. In Fig. 4c, it is shown that creep-fatigue life of the alloy decreases with increasing hold time, in which failure is defined by 90% drop of the maximum tensile stress.

Tensile stress relaxation as a function of time during holding period is shown in Fig. 4 for typical mid-life stress relaxation response curves of the Alloy 709 for 60, 600, 1800 and 3600 s hold times. As shown in Fig. 4, all the stress relaxation curves

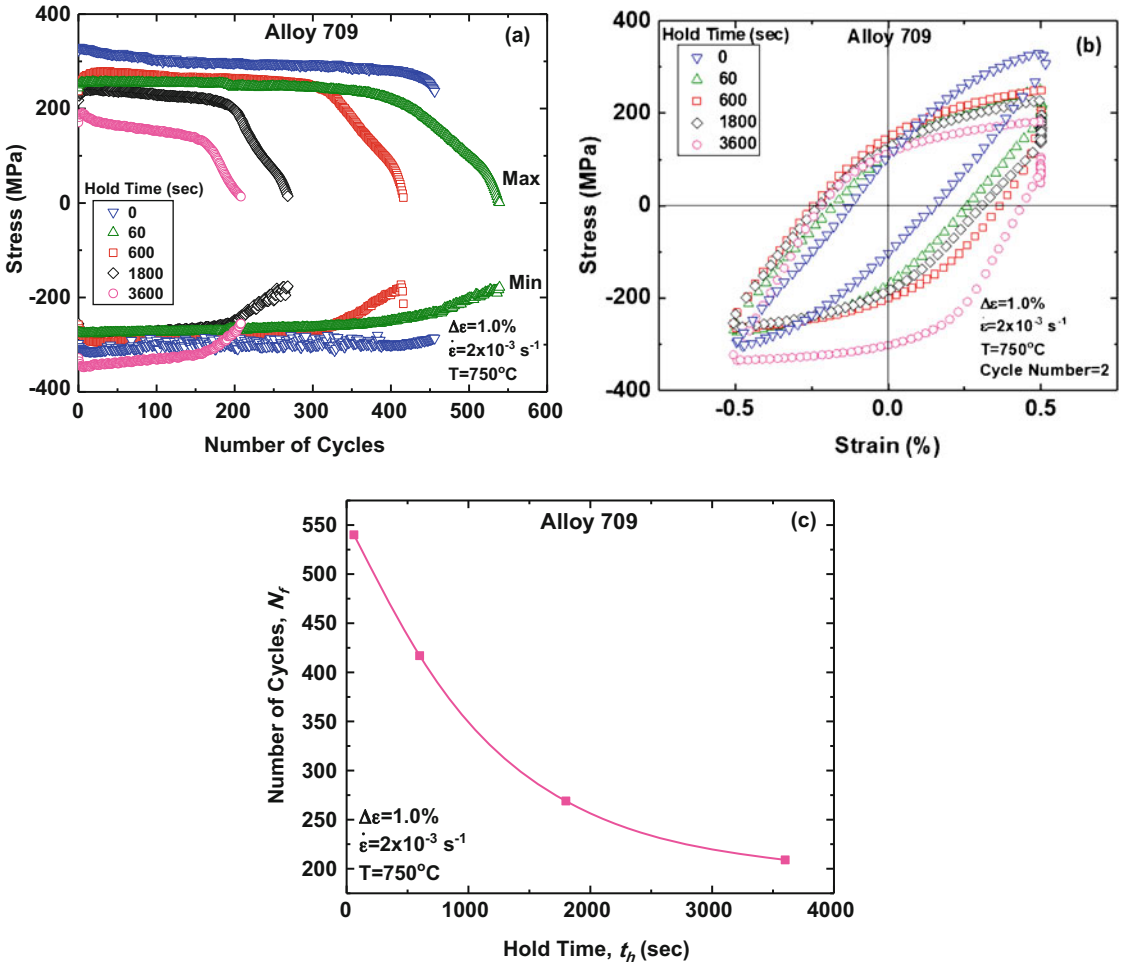

Fig. 4 (**a**) Maximum and minimum stresses vs. number of cycles to failure at 1% strain range and different hold times. (**b**) Hysteresis loops for the creep-fatigue tests of the Alloy 709 at 1% strain range and different hold times showing the second cycles, respectively. (**c**) Number of cycles to failure vs. hold time at 1% strain range of Alloy 709

show a rapid drop in stress at the beginning followed by a relatively stable state of stress relaxation. The stress relaxation curve during hold time can be fitted to a power-law Eq. (3) as shown in Fig. 5:

$$\sigma = b_o(t + t_o)^{b_1} \tag{2}$$

where b_o, t_o and b_1 and are fitted parameters.

In the ASME Code, Section III, Subsection NH, creep-fatigue life is evaluated by a linear summation of fractions of cyclic and creep damages given by [3, 4, 10]:

$$\sum_j \left[\frac{n}{N_d}\right] + \sum_k \left[\frac{\Delta t}{T_d}\right] \leq D \tag{3}$$

where n and N_d are the number of cycles of type j and the allowable number of cycles of the same cycle type, respectively; and Δt and T_d are the actual time at stress level k and the allowable time at that stress level, respectively; D is the allowable combined damage fraction which is usually assumed to be equal to one. The first term accounts for fatigue damage, D_f, and the second term accounts for creep damage, D_c, in terms of time-fraction. Creep damage fraction is calculated using

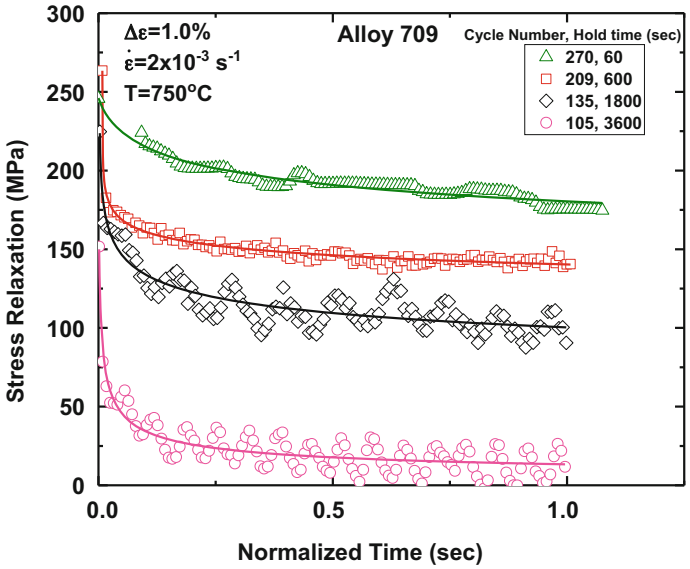

Fig. 5 Stress relaxation of Alloy 709 with time at 1% strain range at different hold times at mid-life cycle

time-fraction method based on a linear correlation between the rupture time (t), temperature (T), and applied stress (σ) using Larson-Miller Parameter (LMP) as employed by Wright et al. [3]:

$$LMP = T\left(\log(t) + C\right) \tag{4}$$

where C is the Larson-Miller constant (~20). A linear equation in semi-log scale describes the creep data using LMP:

$$LMP = a_o + a_1 log(\sigma) \tag{5}$$

where a_o and a_1 are the fitting parameters, σ is stress (MPa). Therefore, creep damage can be calculated as follow:

$$D_k^c = \frac{b_o^{-m}}{A\left(1 - b_1 m\right)}\left((t_h + t_o)^{1-b_1 m} - (t_o)^{1-b_1 m}\right) \tag{6}$$

where t_h is the stress relaxation hold time in seconds. A and m are the fitting parameters in the Larson-Miller parameter as a function of stress. The creep damage in Eq. (3) is calculated at the half-life cycle and then multiplied by the corresponding creep-fatigue life. Creep-fatigue interaction diagram for the Alloy 709 is shown in Fig. 6, where creep damage is plotted as a function of the fatigue damage at different hold times. Also shown here is the ideal failure criterion of linear damage summation. There is not enough data of creep-fatigue for the Alloy 709 that allow us to determine the creep-fatigue damage envelope for this alloy and thus more studies are underway to accomplish that.

The point of macro-crack initiation and failure was determined following the approach applied by Totemeier et al. [11], where the absolute value of the ratio of peak tensile stress to compressive stress is plotted against cycle number as shown in Fig. 7a. Therefore, macro-crack initiation is defined as the point at which the stress ratio deviated from linearity while failure is defined as a 20% drop in stress ratio from the point of deviation. Figure 7b shows the number of cycles to crack initiation and failure at different holding times in which the number of cycles to crack initiation and failure decreases with increased hold time, indicating rapid rates of crack initiation and propagation with intervening creep.

In order to investigate the damage mechanisms responsible for the final fracture of Alloy 709 subjected to creep-fatigue tests, detailed observations of specimen free and fracture surfaces using both Optical and Scanning and Transmission Electronic Microscopy (SEM/TEM) were carried out. The fractographs of the fracture surface of Alloy 709 after low-cycle fatigue (LCF) test at 1.0% strain range (Fig. 8a) showed multiple crack nucleation sites, striations, ductile failure under shear stress and dimple features while the fracture surface after creep-fatigue test at 1.0% strain range and 3600 s hold time (Fig. 8b) exhibited much lower density of striations indicating that the intervening creep damage. Also, the density of cracks is shown to increase with holding time, where typical intergranular and transgranular cracks are observed.

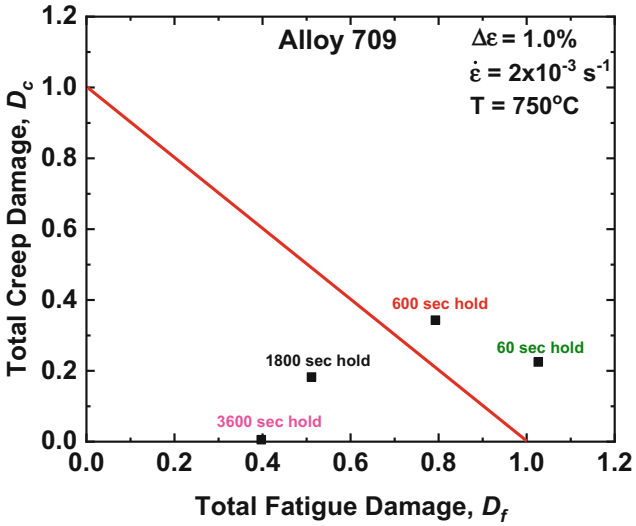

Fig. 6 Creep-fatigue interaction diagram based on linear damage summation. The red solid line shows the ideal failure criterion of linear damage summation

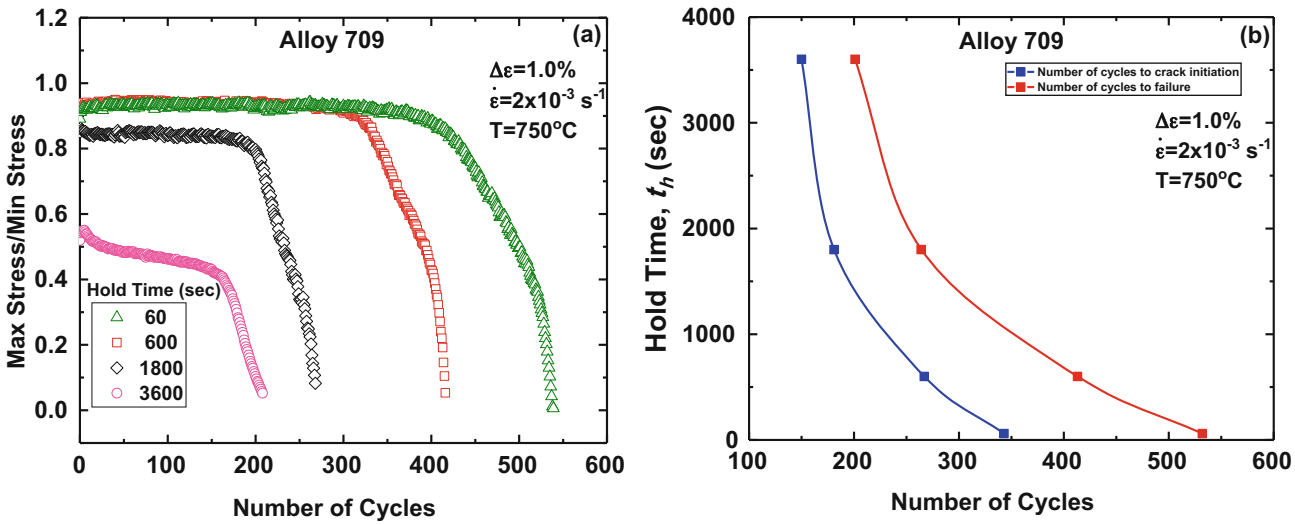

Fig. 7 (**a**) Peak tensile and compressive stress ratio for creep-fatigue test of the Alloy 709 at 1% strain range versus number of cycles for different hold times. (**b**) The number of cycles to crack initiation and failure at 1% strain range versus hold time

Conclusion

Strain-controlled low-cycle fatigue (LCF) tests were performed at strain amplitudes ranging from 0.15% to 0.6% with fully reversible cycle of triangular waveform at 750 °C in air. Different hold times of 1, 10, 30 and 60 min were introduced at the maximum tensile strain to investigate the effect of the creep damage on the fatigue-life at strain amplitude of 0.5% at 750 °C. During continuous cyclic loading, fatigue life is found to decrease with increase in strain amplitude.

The creep-fatigue life and the number of cycles to crack initiation are found to decrease with increasing hold time indicating the rapid initiation and propagation of cracks due to intervening creep. The fractographs of the samples deformed at 0.5% strain amplitude indicated that fatigue is the dominant mode of deformation with classic transgranular cracks while, for the samples deformed at the same strain amplitude with different hold times, both fatigue and creep have contributed to the overall deformation and fracture of the alloy. Further studies are underway to carry out creep-fatigue tests at different hold times, strain ranges, and temperatures as well as microstructural characterization of the samples following deformation.

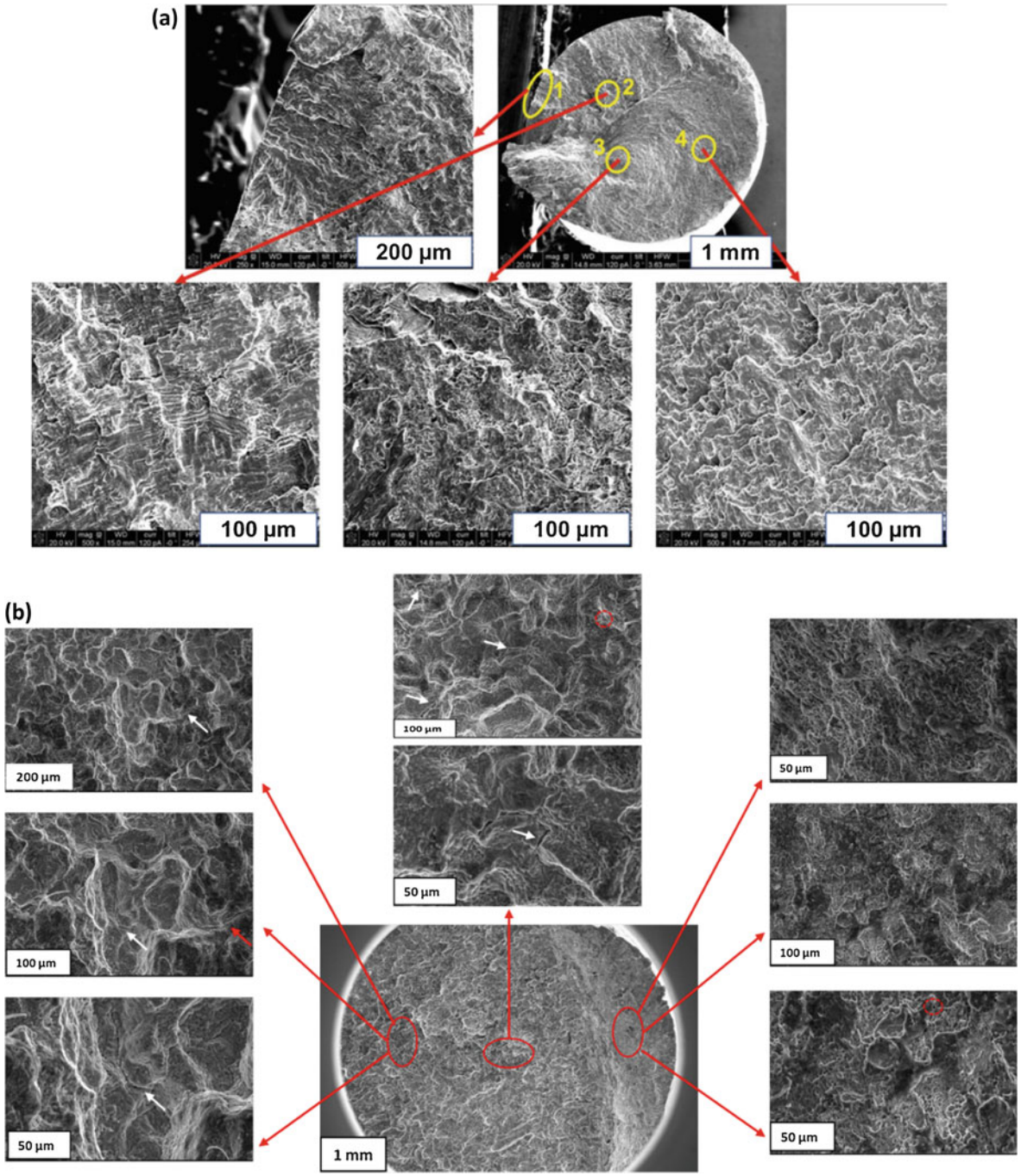

Fig. 8 (**a**) Fractographs of the fracture surface of Alloy 709 after LCF test at 1.0% strain range showing different microscopic features representative of different modes of failure. (**b**) Fractographs of the fracture surface of Alloy 709 after creep-fatigue tests at 1.0% strain range and hold times of 3600 s

Acknowledgements The authors gratefully acknowledge the financial support from the Nuclear Energy University Programs (NEUP/ Project #15-8582) of the Department of Energy for this work. Thanks are due to Dr. Sam Sham of ANL for the materials and various discussions. The authors would also like to acknowledge the use of microscopy facility at Advanced Instrumentation Facility at North Carolina State University, Raleigh, USA.

References

1. K.L. Murty, I. Charit, *An Introduction to Nuclear Materials: Fundamentals and Applications* (Wiley-VCH, Weinheim, 2013)
2. X. Zhang et al., Creep–fatigue endurance of 304 stainless steels. Theor. Appl. Fract. Mech. **71**, 51–66 (2014)
3. J.K. Wright, et al., Determination of the creep fatigue interaction diagram for alloy 617, Proceedings of the ASME 2016 Pressure Vessels and Piping Conference, Vancouver, Canada, p. 255 (2016)
4. R.T. Dewa et al., High-temperature creep-fatigue behavior of alloy 617. Metals **8**, 103 (2018)
5. R.Z. Wang et al., Creep-fatigue behaviors and life assessments in two nickel-based superalloys. J. Press. Vessel. Technol. **140**, 13 (2018)
6. ASTM Standard E2714-13, *Standard Test Method for Creep-Fatigue Testing* (ASTM International, West Conshohocken, PA, 2013)
7. X. Chen, Z. Yang, M.A. Sokolov, D.L. Erdman, K. Mo, J.F. Stubbins, Effect of creep and oxidation on reduced fatigue life of Ni-based alloy 617 at 850 oC. J. Nucl. Mater. **444**, 393–403 (2014)
8. M.C. Carroll, L.J. Carroll, Developing dislocation subgrain structures and cyclic softening during high- temperature creep–fatigue of a nickel alloy. Metall. Mater. Trans. A **44**, 3592–3607 (2013)
9. M. Kolluri, P. ten Pierick, T. Bakker, Characterization of high temperature tensile and creep-fatigue properties of Alloy 800H for intermediate heat exchanger components of (V)HTRs. Nucl. Eng. Des. **284**, 38–49 (2015)
10. J.K. Wright, *Draft ASME Boiler and Pressure Vessel Code Section III, Division 5, Section HB, Subsection B, Code Case for Alloy 617 and Background Documentation* (INL, Idaho Falls, ID, 2015). https://doi.org/10.2172/1245056
11. T. Totemeier, H. Tian, Creep–fatigue-environment interactions in inconel 617. Mater. Sci. Eng. A **468-470**, 81–87 (2007)

Thermo-Mechanical Characterization of Polyurea Hybrid Blend Variants

V. Alizadeh and A. V. Amirkhizi

Abstract Polyurea (PU) is a microphase-segregated elastomer synthesized through bulk polymerization of isocyanates and amines. Polyurea has previously been shown to be an excellent medium in absorbing energy from blast and shock waves, especially when layered with metallic components. The focus of the present work is to evaluate the thermo-mechanical properties of polyurea considering three different hybrid blend formulations. Hybrid polyurea specimens are synthesized by reacting a blend of diamines of long and short chains (Versalink P-1000 and P-250) with weight ratios of 70:30% and 80:20%, with Isonate 143 L and compared with a previously studied blend of 76:24%. This original blend formulation has been shown to have mostly similar properties to a standard PU formulation that uses medium length chain diamines (VP-650) and the same overall hard domain proportion. However, the blend formulation shows wider transition and loss spectra. Thermal phase transition and conductivity measurements are performed to better comprehend the thermal characteristics of the proposed blend formulations. Storage and loss moduli DMA master-curves along with high strain rate data at room temperature using split Hopkinson pressure bar (SHPB) will be presented. The high strain rate experiments are conducted in unconfined and confined configurations to asses shear and bulk responses of material. The overall objective of this approach is to propose fine-tuned blend formulations that can provide a balanced stiff and tough elastomeric response.

Keywords Polyurea · Hybrid formulation · Master curves · Thermo-mechanical characterization · High strain rate

Introduction

Mechanical properties of polyurea strongly depend on the phase segregation and hydrogen bonding, which can be controlled by the molecular structure of selected prepolymers, i.e. amines and isocyanates. Urea linkages are formed by copolymerization reaction of isocyanate and amine which connects the amine soft segments (SS) with isocyanate hard segments (HS). Due to the presence of thermodynamic incompatibility between HS and SS, partial phase separation can occur despite the existence of covalent bonds [1, 2]. Reversible crosslinking, as a result of hydrogen bonds between hard segments, allows hard domain to self-assemble into nanostructured morphologies. This has become an adjustable tool for organizing soft matter at the nanometer scale. Numerous applications of block copolymers have been proposed, given the diverse array of structures that can be achieved. Synthetic chemistry i.e. type of the diisocyanate, diamine, molecular weight of the SS, and H-bonding [3] can tune the size, shape, and arrangement of patterns, which in turn affect the macroscopic mechanical, rheological, and optical properties of the polyurea elastomers [4] and still provides the high flexibility, tensile strength, chemical resistance, high tear toughness, and high chemical resistance as well as the low flammability and durability. In addition, polyurea demonstrates high shear resistance, resilience and generally better thermal properties such as high melting point and high temperature stability.

Polyurea Synthesis

In the present work, PU was synthesized, by reacting oligomeric poly(tetramethylene oxide) (PTMO) diamines (Versalink, Air Products) with aromatic 4,4′-Methylenediphenyldiisocyanate (Isonate 143 L Modified MDI, Dow Chemicals). Two Versalink prepolymers, P-1000 and P-250, were used in which 1000, and 250 refer to the molecular weight of the PTMO

V. Alizadeh · A. V. Amirkhizi (✉)
Department of Mechanical Engineering, University of Massachusetts, Lowell, MA, USA
e-mail: alireza_amirkhizi@uml.edu

M. Silberstein et al. (eds.), *Challenges in Mechanics of Time Dependent Materials, Fracture, Fatigue, Failure and Damage Evolution, Volume 2*, Conference Proceedings of the Society for Experimental Mechanics Series, https://doi.org/10.1007/978-3-030-29986-6_26

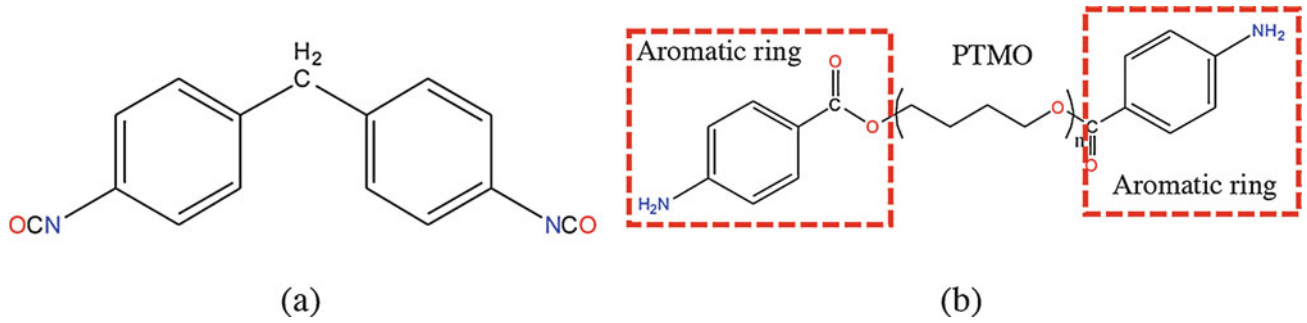

Fig. 1 (**a**) Isonate 143 L and (**b**) Versalink

repeating units. The synthesis follows step growth polymerization in bulk. Based on manufacturer's recommendations, stoichiometric ratio of isocyanate to amine was augmented with an additional 5% of Isonate 143 L to compensate for any loss due to moisture and to provide light chemical crosslinking. Figure 1 shows the Isonate 143 L along with the Versalink amine. A hybrid polyurea specimen, PU-HB05, has been previously synthesized by reacting a blend of VP-1000:VP-250 with weight ratios of 76:24% (56:44% mole ratio), with Isonate 143 L. This weight ratio was calculated in order to ensure the total proportion of hard to soft segments of PU-HB05 match that of the polyurea made using Versalink P-650 which has ~45% hard segment ratio. To calculate the hard segment ratio (hard segment weight over the total weight) we assumed that (a) PTMO chain of Versalink participates in soft segment (SS) formation, (b) aromatic ring with carbonyl functional group in Versalink, goes in hard segment (HS) formation, and (c) isocyanate completely participates in HS formation. Blends of VP-1000:VP-250 for PU-HB05–20% and 30% have weight ratios of 80:20% and 70:30%, respectively. Reduction of VP-1000:VP-250 ratio can increase the hard segment ratio due to introduction of more stiffer, short chain VP-250 within the long chain VP-1000 (~43% for PU-HB05–20% and ~47% for PU-HB05–30%).

DSC and MDSC

For DSC measurements two heating cycles were performed. The temperature range was from −80 to 200 °C while the cooling and heating rates were 10 °C/min. Midpoint inflection method was used to calculate glass transition temperature (T_g). To measure the specific heat capacity and thermal conductivity, MDSC approach was utilized. Heat capacity of samples were estimated between −40 and 40 °C with temperature increments of 5 °C, modulation amplitude and period of 1 °C and 80 s, respectively. Samples used to estimate specific heat capacity had 0.4 ± 0.05 mm thickness and their diameter were 4 ± 0.2 mm. Thermal conductivity measurements were performed at −25, 0, and 25 °C with modulation on samples of diameter $d = 4 \pm 0.2$ mm and height $l = 4 \pm 0.2$ mm.

Frequency Domain Master Curves

Master curves construction is based on the time-temperature superposition principle, which is applicable to thermo-rheologically simple polymers though it is a relatively good approximation in many practical cases. According to this concept, increasing temperature is analogous to decreasing the frequency or strain rate. This provides a great advantage as polymer characteristics at high and low frequencies or short and long-time scales may be inferred from experiments at low and high temperatures. The obtained graphs at multiple temperatures over a narrow range of frequency, need to be shifted horizontally and vertically to approximate the response of the polymer at a desired reference temperature. The procedure of building master curves in this study follows [5]. First, the vertical shifting is performed based on absolute temperature scaling of entropic elasticity at equilibrium state (and ignoring density changes). This is followed by the determination of horizontal shift and construction of the master curves for both storage and loss moduli. To obtain the master curves for the storage and loss moduli, DMA experiments were performed using TA-Q800 in single cantilever bending configuration. The frequency table included 0.5, 1, 2, 5, 10, and 20 Hz and temperature range was from −80 to 50 °C in 5 °C steps. The narrow band frequency graphs at each temperature were then shifted along the frequency axis to construct the master curve. The reference temperature (T_0) for these master curves was 25 °C and the shifting factors were calculated based on the average

of storage and loss shift data. WLF parameters were also obtained for $T_0 = 25$ °C and $T_0 = T_g + 50$ °C, where the glass temperatures (T_g) were estimated according to the observed pick of the loss modulus master curve.

High Strain Rate Characterization

Split Hopkinson pressure bar test (SHPB) is used to study the dynamic or inelastic flow of materials at strain rate of 100–15,000/s. SHPB system used in this study consists of a gas gun, striker bar, an incident bar, a transmission bar, strain gages, and data acquisition setup. Figure 2 shows the SHPB apparatus. The striker bar, incident bar, and transmission bar are made of the same material (Al-7075) and have the same cross section with diameter of 12.7 mm. They stay elastic throughout the test. The sample to be tested is sandwiched between the incident and transmission bars. The impact of striker bar to the incident bar generates an elastic compression wave, which travels along the incident bar and then loads the sample. Once the wave reaches the sample, a part of the wave is transmitted through the specimen to the transmission bar (transmitted wave) and a part is reflected (reflected wave) back to the incident bar. The incidence, transmitted, and reflected waves are recorded by the strain gages mounted at the same distance from the sample on the corresponding bars.

Under axial compression, cylindrical specimens tend to expand in radial direction due to Poisson's effect if unconfined. Such a test generally measures the shear response of polymeric materials. A confinement tube can prevent this and allow for the measurement of bulk volumetric mechanics of such specimens [6]. The sample in this case has the same diameter as the SHPB bars and is in full contact with the confinement tube, whose inner diameter is also nominally the same as the sample diameter. To get more accurate estimates of deviatoric and triaxial components of stress, a hoop strain gage may be applied to the outside of the confinement tube that can indirectly measure the transverse strain and stress components. The radial stress is needed inside the tube while the hoop strain measured on the outside surface. A finite length tube may be simulated with a uniformly distributed inside pressure equal to the unknown radial stress over a cylindrical surface with the same length as the sample. A linear implicit axisymmetric finite element analysis similar to [6] gives the approximate relationship,

$$\sigma_r = \xi E_{\text{tube}} \varepsilon_\theta, \tag{1}$$

where ξ is a constant obtained using the FEA, σ_r is the induced radial stress due to sample expansion, and ε_θ is the outside hoop strain measured with the aid of the strain gauge attached at the center of the outer surface of the confinement tube.

Due to the radial inertia in the bars, the shape of the pulse changes slightly as it travels along its length. Therefore, the values measured at the location of strain gages may need correction to represent what the sample experienced. This process is referred to as dispersion correction and may be found discussed in detail in [7]. Furthermore, due to the finite time of travel across the length of the sample, the assumption of dynamic equilibrium (uniform stress across the length and zero acceleration) may be improved. Without this assumption, an average state of stress and corrected average strain rate in the sample may be derived based on,

$$\sigma(t) = \frac{A_0}{2A} E_0 \left[\varepsilon_I(t) + \varepsilon_R(t) + \varepsilon_T(t)\right], \quad \dot{\varepsilon}(t) = -\frac{c_0}{L}\left[-\varepsilon_I(t) + \varepsilon_R(t) + \varepsilon_T(t)\right], \tag{2}$$

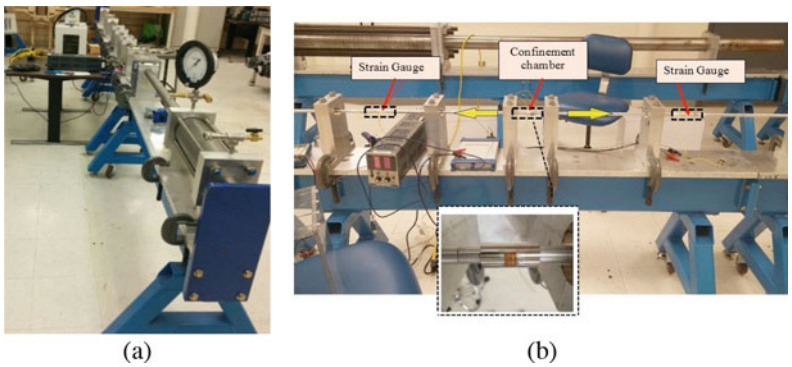

Fig. 2 (**a**) The SHPB apparatus in its entirety, (**b**) the uniaxial strain condition (confined) setup with the confinement tube

Table 1 Material and geometric properties of the SHPB setup

Properties	Values
Material	AL-7075
Modulus (GPa)	69
Density (kg/m^3)	2768
Poisson's Ratio	0.33
Striker Length (in)	6[a] and 12[b]
Incident and Transmission Bars Length (ft)	4
Diameter (in)	0.50
Wave Speed (m/s)	5494
Tube Material	Maraging Steel-C350
Tube Modulus (GPa)	200
Tube Poisson's Ratio	0.29
Tube Inner and Outer Diameter	0.50 and 0.75
Sample length (in)	0.08[a] and 0.20[b]
Sample Diameter (in)	0.25[a] and 0.50[b]

[a]Unconfined test
[b]Confined test

where E_0, A_0 and c_0 are the Young's modulus, cross-sectional area and sound speed of the split-Hopkinson bars, respectively. $\varepsilon_I(t)$, $\varepsilon_T(t)$, and $\varepsilon_R(t)$ are the measured incident, transmitted and reflected strain signals in the bars, and A and L are the cross-sectional area and length of the sample, respectively. Table 1 shows the material and geometric parameters of SHPB setup.

Conclusions and Summary

The focus of this effort was to evaluate the effect of chain length and dispersed hard segment content as well as its morphology on the thermo-mechanical properties of PU. Therefore, two new polyurea hybrid blend formulations were introduced, PU-HB05-20% and PU-HB05-30%, to be compared with a previously studied PU-HB05-24%. Results showed stiffer response for 30% formulation while the magnitude of loss was not changed substantially. There was not much of a difference observed between the three above mentioned hybrid blend formulations for heat capacity and thermal conductivity.

Acknowledgements This work has been conducted at the Department of Mechanical Engineering, University of Massachusetts, Lowell, and has been supported through ONR grant N00014-16-1-2458 to the University of Massachusetts, Lowell.

References

1. I.W. Hamley, *The Physics of Block Copolymers* (Oxford University Press, New York, USA, 1998), p. 424
2. F.S. Bates, G.H. Fredrickson, Block copolymer thermodynamics: theory and experiment. Annu. Rev. Phys. Chem. **41**(1), 525–557 (1990)
3. R. Bonart, X-ray investigations concerning the physical structure of cross-linking in segmented urethane elastomers. J. Macromol. Sci. B **2**(1), 115–138 (1968)
4. I.W. Hamley, Ordering in thin films of block copolymers: fundamentals to potential applications. Prog. Polym. Sci. **34**, 1161–1210 (2009)
5. Z. Jia, A.V. Amirkhizi, W. Nantasetphong, S. Nemat-Nasser, Experimentally-based relaxation modulus of polyurea and its composites. Mech. Time Depend. Mater. **20**(2), 155–174 (2016)
6. A.V. Amirkhizi, J. Isaacs, J. McGee, N.L. De Lauriston, S. Nemat-Nasser, Constitutive modeling and experiments on polyurea, in *Proceedings of the 2005 SEM Annual Conference and Exposition on Experimental and Applied Mechanics, Portland, OR*, (2005), pp. 465–466
7. J.C. Gong, L.E. Malvern, D.A. Jenkins, Dispersion investigation in the split Hopkinson pressure bar. J. Eng. Mater. Technol. **112**(3), 309 (1990)

Milled Carbon Fiber Polyurea Elastomeric Composites

V. Alizadeh and A. V. Amirkhizi

Abstract Polyurea is one of the widely used materials in the coating industry and is well known to form a mechanically robust elastomeric network. Due to its toughness and ease of application, it has been studied as a potential protective coating in cavitation erosion conditions. The temperature rise within the polyurea under such harsh loading conditions can lead to significant softening and rapid failure of the coating, while in slightly lower intensity situations the coating may not show any signs of damage. Therefore, controlling the temperature rise due to dissipative heating may lead to better and more reliable coatings. Reinforcing the polyurea with milled carbon fibers not only has the benefit of increasing its thermal conductivity (hence distributing localized heating to larger volumes), it could also increase its stiffness, while maintaining its elastomeric nature (in contrast with continuous fiber composites). The milled fibers may be dispersed within the polyurea matrix in 3D randomly oriented arrangements or may be aligned parallel to the coated surface in very thin layers. The aim of this study is to investigate the thermal and mechanical behavior of such composites. The matrix polyurea specimen is synthesized by reacting a mixture of medium length diamine (Versalink P-650) with isocyanate 143 L. Thermal phase transition (DSC) and thermal conductivity measurements (using MDSC) are performed to accurately measure the thermal properties of such composites. DMA tests are conducted to construct the storage and loss moduli master curves. Stress-strain curves under uniaxial loading at high strain rates are obtained using split Hopkinson pressure bar (SHPB). Results show a significant increase in thermal conductivity and stiffness. The presented study assesses the feasibility of improving elastomer-based coatings for protection against harsh cavitation erosion conditions.

Keywords Polyurea · Carbon fibers · Split Hokinson Pressure Bar · Thermal conductivity · Dynamic properties

Introduction

Polyurea (PU) is currently used as one of the robust material choices in the coating industry, owing to its fast curing in the absence of catalyst at a wide range of temperature and humidity conditions and without significantly affecting its microstructure and properties. Application of polyurea elastomeric coating to the interior of the walls of retrofitted buildings was able to prevent the failure, collapse, and fragmentation of the structure [1]. Further use of polyurea with fabrics like carbon woven materials, Kevlar, and E-glass demonstrated the improved energy dissipation and shock resistance properties under dynamic and impulsive loadings both in air and water [2, 3]. Experimental studies showed that the polyurea coating temperature is increasing under repetitive loads such as those induced by bubble collapse observed in cavitation erosion phenomenon [4]. Introducing carbon fibers within the polyurea matrix can enhance its thermal conductivity which may lead to better performance under the aforementioned loading conditions [5]. Moreover, increase in stiffness while maintaining the elastomeric nature of the composite is another advantage of such approach, which are expected to improve shock resistivity of these particulate composites.

The goal of this study is to investigate thermo-mechanical properties of the reinforced polyurea with milled carbon fiber particulates. Two different volume ratios for carbon fibers, 10% and 30%, are studied and results are discussed. Experimental methods used to determine the thermal properties of the reinforced polyurea are differential scanning calorimetry (DSC) and modulated DSC (MDSC) and provide glass transition temperature, specific heat capacity, and thermal conductivity. Extraction of mechanical properties involves quasi-static and high strain-rate tests using DMA and SHPB, respectively. SHPB tests includes both uniaxial stress and uniaxial strain configurations.

V. Alizadeh · A. V. Amirkhizi (✉)
Department of Mechanical Engineering, University of Massachusetts, Lowell, MA, USA
e-mail: alireza_amirkhizi@uml.edu

M. Silberstein et al. (eds.), *Challenges in Mechanics of Time Dependent Materials, Fracture, Fatigue, Failure and Damage Evolution, Volume 2*, Conference Proceedings of the Society for Experimental Mechanics Series, https://doi.org/10.1007/978-3-030-29986-6_27

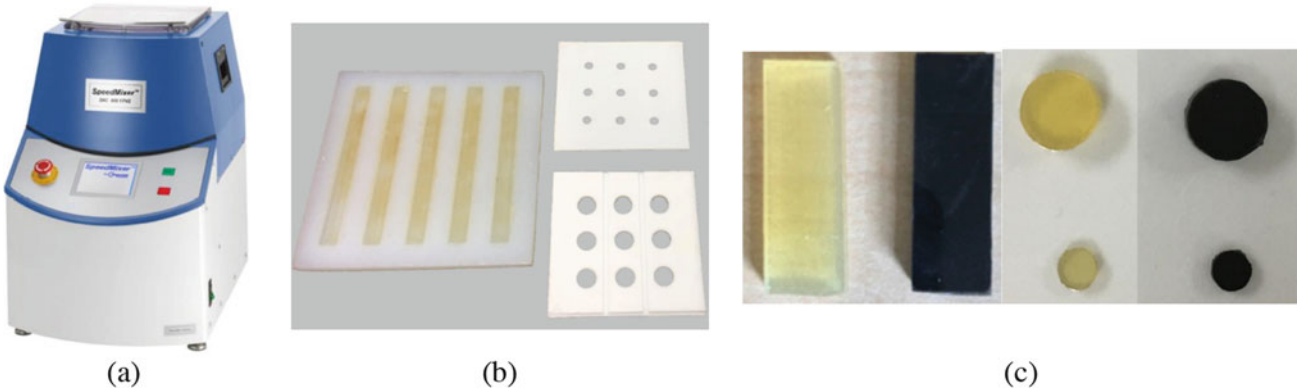

Fig. 1 (**a**) FlackTek DAC-600.1 VAC-P speed mixer, (**b**) Teflon molds for DMA and SHPB tests, (**c**) Polyurea samples for DMA and SHPB tests (the black samples have milled carbon fiber inclusions)

Fig. 2 Differential scanning calorimetry (DSC) instrument

Sample Fabrication

The matrix polyurea specimen is synthesized by reacting a mixture of medium length diamine Versalink P-650 (VP-650) (Air Products) and isocyanate 143 L (Dow Chemicals) at room temperature. Versalink amine was preheated for 5 h to dry and remove water then stored with molecular sieves to maintain low level of moisture. First the VP-650 is mixed with carbon fibers (Zoltek PX30) at 1000 rpm for 2 min and degassed under vacuum (−900 mbar) at room temperature using FlackTek DAC-600.1 VAC-P speed mixer. Then the homogeneous VP-650 and carbon fibers compound was mixed with isocyanate. The mixture was cast in Teflon molds and kept in desiccator for 24 h. Samples were then heat cured at 80 °C under vacuum for 24 h to achieve complete cure and network formation. Figure 1 depicts the speed mixer used along with the Teflon molds and polyurea samples.

Differential Scanning Calorimetry (DSC)

Thermal phase transition of polyurea was investigated using TA-Q800 DSC instrument. The heat flow was measured over the temperature range of −80 to 200 °C. The operation was performed in heating and cooling cycles at 10 °C/min rate. This test method was used to determine polyurea glass transition temperatures and enthalpies of fusion. Transitions were investigated using midpoint inflection method to calculate T_g. Figure 2 shows the DSC instrument used for this study.

Thermal Conductivity Measurements

Thermal conductivity is a crucial factor in energy dissipation applications. Modulated DSC (MDSC) approach is suitable for the determination of thermal conductivity (k) of polyurea samples if k lies in the range of 0.1–1 W/mK. In MDSC tests samples are exposed to a cyclic (sinusoidal modulation) thermal profile superposed on a linear ramp. The resultant experimental data after deconvolution gives reversing (heat capacity) and non-reversing components of the heat flow. For small samples, whose temperatures are uniform throughout the test, this provides a very good partition of the two components. However, for a large sample the assumption of temperature uniformity is not reasonable, and the heat flow is affected by the thermal conductivity within the material. After determining the specific heat capacity, C_p, using a small sample, a much taller cylindrical sample is tested similarly to measure its apparent heat capacity C. The cylindrical sample is exposed to a temperature modulation at one end, while the other end can only be heated by the conduction through its height. Therefore, the measured apparent heat capacity is lower in comparison with the specific value. The observed thermal conductivity of the sample k_o may be estimated as [6],

$$k_o = \frac{8lC^2}{C_p m d^2 p}, \tag{1}$$

where, C_p is the specific heat capacity of the material, p is the modulation period, and l, d, m, C, are the cylindrical sample's length, diameter, mass, and apparent heat capacity, respectively. To account for the heat loss through the material (from the sides) a correction (calibration) factor D need to be defined. The corrected thermal conductivity can be calculated as,

$$k = \frac{k_0 - 2D + \sqrt{{k_o}^2 - 4Dk_o}}{2}; \quad D = \sqrt{k_o k_{ro}} - k_r, \tag{2}$$

where, k_{ro} and k_r are the observed and actual thermal conductivities of a reference material. Polystyrene has been used for this reference measurement. In the present work, the reversing heat capacity of samples were estimated between −40 and 40 °C using MDSC with temperature increments of 5 °C, modulation amplitude and period of 1 °C and 80 s, respectively. Thermal conductivity measurements were performed at −25, 0, and 25 °C with modulation on samples of diameter $d = 4 \pm 0.2$ mm and height $l = 4 \pm 0.2$ mm.

Dynamic Mechanical Analysis (DMA)

Dynamic mechanical tests were performed in a single cantilever bending configuration (single beam cantilevered at both ends) with beam length of 17 ± 0.25 mm in temperature step mode with a frequency table of 0.5, 1, 2, 5, 10, and 20 Hz at a temperature step of 5 °C/min from −80 to 50 °C. The isothermal time for each step was 3 min and the initial amplitude was set at 15 μm. The width and thickness of the samples used for DMA were 11.7 ± 0.05 and 4 ± 0.25 mm, respectively.

Split Hopkinson Pressure Bar (SHPB)

A quick opening of the compressed gas valve launches the striker bar, which travels down and impacts the incident bar. The impact generates an elastic compression wave, which travel along the incident bar and then loads the sample. Once the wave reaches the sample, a part of wave is transmitted through the specimen to the transmission bar (transmitted wave) and a part is reflected (reflected wave) back to the incident bar. The incidence, transmitted, and reflected waves are recorded by the strain gages mounted at the same distance from the sample on the corresponding bars. The stress and strain rate within the sample are generally estimated as,

$$\sigma(t) = \frac{A_0}{A} E_0 \varepsilon_T(t), \quad \dot{\varepsilon}(t) = -\frac{2c_0}{L} \varepsilon_R(t), \tag{3}$$

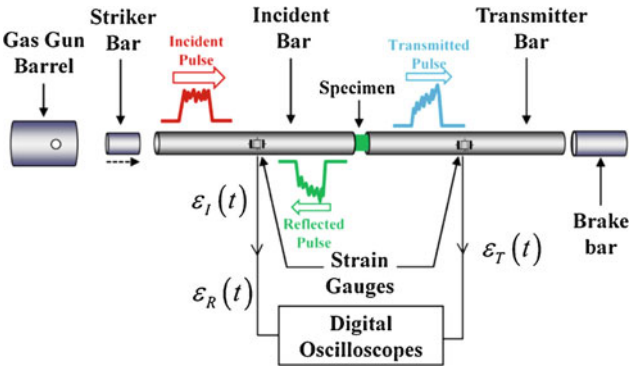

Fig. 3 Schematic view of the SHPB apparatus

where E_0, A_0 and c_0 are the Young's modulus, cross-sectional area and sound speed of the split-Hopkinson bars, respectively. $\varepsilon_T(t)$ and $\varepsilon_R(t)$ are the measured transmitted and reflected strain signals in the bars and A and L are the cross-sectional area and length of the sample.

Samples were tested under uniaxial stress compression (unconfined) at different strain rates from 3000 to 12,000/s at room temperature. They were also tested under nearly uniaxial strain compression (confined) at strain rate of around 3500/s. The variation in the strain rate is accomplished by varying the striker bar impact velocity. For the nearly uniaxial strain tests, samples have 12.7 $\pm$ 0.1 mm diameter with 5 $\pm$ 0.1 mm length. The uniaxial stress loading configuration samples have 6.5 $\pm$ 0.1 mm diameter and 2 $\pm$ 0.1 mm length.

Conclusions and Summary

Results showed that introducing carbon fibers within the polyurea structure can increase heat capacity and thermal conductivity of the polyurea matrix quite substantially. Polyurea having higher volume ratios of carbon fiber inclusions shows more resistance to temperature elevations (higher heat capacity) and higher heat diffusion (higher thermal conductivity). DMA and SHPB results also show much higher stiffness at low and high strain rate loading conditions while the loss is not affected comparatively.

Acknowledgements This work has been conducted at the Department of Mechanical Engineering, University of Massachusetts, Lowell, and has been supported through ONR grant N00014-16-1-2458 to the University of Massachusetts, Lowell.

References

1. K.J. Knox, M.I. Hammons, T.T. Lewis, J.R. Porter, F.P. Branch, Polymer materials for structural retrofit, in *Force Protection Branch, Air Expeditionary Forces Technology Division*, (Air Force Research Laboratory, Tyndall AFB, Florida, 2000), pp. 5–17
2. J.E. Crawford, Modeling blast-resistant protection systems composed of polymers and fabric. Model. Perform. Eng. Struct. Mater **III**, 61–75 (2002)
3. J. E. Crawford and S. Lan, Design and implementation of protective technologies for improving blast resistance of buildings, in: *Enhancing Building SecuritySeminar*, 2005
4. J.-K. Choi, P. Marlin, G. L. Chahine, Experimental and numerical study of polyurea failure under cavitation, in: *Fifth International Symposium on Marine Propulsion*, 2017
5. V. Alizadeh, A. Amirkhizi, Modeling of cavitation erosion resistance in polymeric materials based on strain accumulation, in *Challenges in Mechanics of Time-Dependent Materials, Volume 2, Conference Proceedings of the Society for Experimental Mechanics Series*, (Springer, Cham, 2019), pp. 61–63
6. S.M. Marcus, R.L. Blaine, Thermal conductivity of polymers, glasses and ceramics by modulated DSC. Thermochim. Acta **243**(2), 231–239 (1994)